

PRACTICAL APPLICATIONS OF INFRARED, RAMAN AND NUCLEAR
MAGNETIC RESONANCE SPECTROSCOPIC TECHNIQUES FOR QUALITATIVE,
QUANTITATIVE AND STRUCTURAL ANALYSIS OF PHARMACEUTICAL
DRUGS, CEMENTITIOUS MATERIAL AND ORGANIC MOLECULES
CONTAINING PHOSPHOROUS

A DISSERTATION IN
Chemistry
and
Geosciences

Presented to the Faculty of the University
of Missouri-Kansas City in partial fulfillment of
the requirements for the degree

DOCTOR OF PHILOSOPHY

by

Sudhaunshu Shrikant Purohit

B.Sc., University of Mumbai, 2004

M.Sc., University of Mumbai, 2007

M.S., University of Kentucky, 2010

Kansas City, Missouri

2016

© 2016
SUDHAUNSHU S. PUROHIT
ALL RIGHTS RESERVED

PRACTICAL APPLICATIONS OF INFRARED, RAMAN AND NUCLEAR
MAGNETIC RESONANCE SPECTROSCOPIC TECHNIQUES FOR QUALITATIVE,
QUANTITATIVE AND STRUCTURAL ANALYSIS OF PHARMACEUTICAL
DRUGS, CEMENTITIOUS MATERIAL AND ORGANIC MOLECULES
CONTAINING PHOSPHOROUS

Sudhaunshu Shrikant Purohit, Candidate for Doctor of Philosophy

University of Missouri Kansas City, 2016

ABSTRACT

The study of the interaction between matter and electromagnetic radiation which procreated the wide branch named as Spectroscopy has gained tremendous attention since the last century. Atoms and molecules respond to electromagnetic radiation to produce their unique spectra which can be used to detect, identify and quantify valuable information about the substance under study. Since, its conception, spectroscopy has been widely used in physical and analytical chemistry and has ramified various techniques depending on the different types of radiation. This dissertation focuses on implementation of various spectroscopic techniques such as Infrared, Raman and Nuclear Magnetic Resonance (NMR) spectroscopy in order to determine theoretical, conformational, qualitative and quantitative properties of different molecules under study.

Understanding the physical structure of a molecule is fundamental for function, dynamic, and mechanism studies. Infrared and Raman spectroscopy are two of the most widely used and powerful techniques for the accurate determination of molecular symmetry and conformational stability. They provide information of molecular vibrations and the two techniques complement each other to yield more complete information about the molecular structure than when they are evaluated separately. One of the focus of this dissertation is the determination of the structural parameters, conformational stability, vibrational assignments and *ab initio* calculations of organic molecules containing five membered ring and phosphorous by utilizing infrared and Raman spectral techniques. The findings of my spectroscopic, structural, and theoretical studies are based on infrared and/or Raman spectra of gas, liquid, solid as well as variable temperature xenon solutions, and microwave spectrum which are supported by *ab initio* and DFT calculations.

Nearly four decades ago the potential of Nuclear Magnetic Resonance (NMR) spectroscopy for the quantitative analysis of organic chemicals was first demonstrated. Along with solution state NMR, for past two decades solid state NMR spectroscopy has also come to the forefront of quantitative analytical techniques in pharmaceutical research, as, both of these techniques have been successfully applied to the study of polymorphism in pharmaceutical drugs at both the qualitative and quantitative levels. The investigation of our research presented in this dissertation was initiated by selecting AIDS, the predominant pandemic of twenty-first century and Tenofovir (TFV), a well-tested antiretroviral drug that has proven its mettle against HIV/AIDS. In order to be able to accurately quantify the amount of drug being delivered in human body is a crucial requirement of any drug development process. We specifically focused on phosphorous containing drugs and hence,

a part of this dissertation describes about the development and implementation of a general ^{31}P qNMR method to achieve direct, real time quantification of *in vitro* drug release. We have effectively utilized both solution state and solid state ^{31}P qNMR spectroscopic techniques to establish the kinetics of drug release and to determine the encapsulation efficiency of nano-formulation for a particular drug under study, respectively. The *in vitro* drug release profile has been studied in various human body fluids such as simulated vaginal & seminal fluids, plasma etc. depending on the drug under study. The results of method validation parameters for TFV in simulated vaginal & seminal fluid and human plasma obtained by using ^{31}P solution state qNMR spectroscopy are presented in this dissertation.

Another chapter of this dissertation explains the analysis of calcined clay as supplementary cementitious material, obtained from Ghana, a West African nation, which does not have an abundance of commonly used SCMs such as fly ash, silica fume, metakaolin, and slag. However, the abundance of clay minerals in the country could provide a sustainable alternative with respect to SCMs application. Qualitative techniques such as Thermal Gravimetric Analysis (TGA) and Forrier Transform Infrared Spectroscopy (FTIR), and quantitative tools like Nuclear Magnetic Resonance (NMR) are able to provide meaningful characterizing of thermally activated clays. In this study, clay from Ghana was thermally activated at temperatures of 600, 700, 800, 900 and 1000°C. The main objective was to characterize calcined clay using TGA, FTIR, NMR, and their relation to pozzolanic activity to best understand the potential of this abundant resource to alleviate cement supply burdens.

The faculty listed below, appointed by the Dean of the School of Graduate Studies have examined a thesis titled “Practical Applications of Infrared, Raman and Nuclear Magnetic Resonance Spectroscopic Techniques for Qualitative, Quantitative and Structural Analysis of Pharmaceutical Drugs, Cementitious Material and Organic Molecules Containing Phosphorous” presented by Sudhaunshu Shrikant Purohit, candidate for the Doctor of Philosophy, and certify that in their opinion it is worthy of acceptance.

Supervisory Committee

Nathan A. Oyler, Ph.D., Committee Chair
Department of Chemistry

Fedor Rudakov, Ph.D.
Department of Chemistry

David Van Horn, Ph.D.
Department of Chemistry

James B. Murowchick, Ph.D.
Department of Geosciences

Jejung Lee, Ph.D.
Department of Geosciences

CONTENTS

ABSTRACT	iii
LIST OF TABLES	viii
LIST OF ILLUSTRATIONS	xi
ACKNOWLEDGMENTS	xiv
DISSERTATION OUTLINE.....	xvii

Chapter

1. INTRODUCTION.....	1
2. QUANTITATIVE ANALYSIS OF PHOSPHOROUS CONTAINING DRUG MOLECULES ENCAPSULATED IN pH-SENSITIVE NANOPARTICLE FORMULATIONS TO ESTABLISH DRUG LOADING AND DRUG RELEASING PROFILE BY UTILIZING ³¹ P SOLID STATE AND SOLUTION STATE NUCLEAR MAGNETIC RESONANCE SPECTROSCOPIC TECHNIQUES.....	11
3. ANALYSIS OF CALCINED CLAY AS A SUPPLEMENTARY CEMENTITIOUS MATERIAL: A CASE STUDY OF CLAY FROM GHANA.....	80
4. INFRARED AND RAMAN SPECTRAL STUDIES TO OBTAIN STRUCTURAL PARAMETERS, CONFORMATIONAL STABILITY, VIBRATIONAL ASSIGNMENTS AND <i>AB INITIO</i> CALCULATIONS OF ORGANIC MOLECULES CONTAINING FIVE MEMBERED RING AND PHOSPHOROUS.....	104
REFERENCE LIST 1.....	10
REFERENCE LIST 2.....	75
REFERENCE LIST 3.....	103
REFERENCE LIST 4.....	205
VITA.....	208

TABLES

Table	Page
2.1. Considerations and limitations in dialysis method of drug quantitation.....	30
2.2. Accuracy (mean recovery) data for the ³¹ P-NMR method in VFS, SFS, and human plasma.....	44
2.3. Precision data for the ³¹ P-NMR method in VFS, SFS, and human plasma.....	44
2.4. Robustness analysis data for ³¹ P-qNMR method in VFS, SFS, and human plasma....	45
2.5. <i>In vitro</i> drug release kinetics models parameters of TFV loaded chitosan nanofibers.	49
2.6. Independent and dependent variables and their levels in custom design.....	71
3.1. Solid State NMR spectra indicating position and peak areas of respective peaks of ²⁷ Al and ²⁹ Si. Peak areas are calculated considering Raw Clay as a control.....	91
3.2. Mortar mix proportion for strength activity index of calcined clays at 7 and 28 days...	96
4.1. Calculated ^a and observed frequencies (cm ⁻¹) for 1-bromo-1-silacyclopentane <i>twist</i> (<i>C₁</i>) form.....	117
4.2. Calculated ^a frequencies (cm ⁻¹) for 1-bromo-1-silacyclopentane <i>twisted</i> (<i>C₁</i>) form.	119
4.3. Calculated ^a frequencies (cm ⁻¹) for 1-bromo-1-silacyclopentane <i>twisted</i> (<i>C₁</i>) form.	121
4.4. Calculated electronic energies (hartree) and energy differences (cm ⁻¹) for the <i>twisted</i> (<i>C₁</i>), <i>envelope-axial</i> (<i>C_s</i>), <i>envelope-equatorial</i> (<i>C_s</i>), and <i>planar</i> (<i>C_s</i>) forms of 1-bromo-1-silacyclopentane.....	126
4.5. Structural parameters (Å and degree), rotational constants (mhz) and dipole moment (debye) for 1- ⁷⁹ bromo-1-silacyclopentane <i>twisted</i> (<i>c₁</i>) form.....	127
4.6. Symmetry coordinates of 1-bromo-1-silacyclopentane.....	130
4.7. Observed and calculated ^a frequencies (cm ⁻¹) and potential energy distributions (P.E.D.s) for the <i>Gt</i> (<i>C₁</i>) conformer of 2-cyanoethylphosphine.....	147
4.8. Observed and calculated ^a frequencies (cm ⁻¹) and potential energy distributions (P.E.D.s) for the <i>Tt</i> (<i>C_s</i>) conformer of 2-cyanoethylphosphine.....	149
4.9. Observed and calculated ^a frequencies (cm ⁻¹) and potential energy distributions (P.E.D.s) for the <i>Tg</i> (<i>C₁</i>) conformer of 2-cyanoethylphosphine.....	150
4.10. Observed and calculated ^a frequencies (cm ⁻¹) for the <i>Gg</i> (<i>C₁</i>) conformer of 2-cyanoethylphosphine.....	152

4.11. Structural parameters (\AA and $^\circ$) and rotational constants (MHz) for the <i>Gt</i> , <i>Tt</i> and <i>Tg</i> conformer of 2-cyanoethylphosphine.....	160
4.12. Temperature and intensity ratios of the conformational bands of 2-cyanoethylphosphine from the Raman spectra of the liquid.....	161
4.13. Calculated energies (hartree) and energy differences ^a (cm^{-1}) for the five conformers of 2-cyanoethylphosphine.....	164
4.14. Symmetry coordinates for 2-cyanoethylphosphine w.r.t. <i>Tt</i> conformer.....	165
4.15. Comparison of rotational constants (MHz) obtained from ab initio MP2(full)/6-311+G(d,p) predictions, experimental values from microwave spectra, and from the adjusted r_0 structural parameters for 2-cyanoethylphosphine.....	168
4.16. Observed and calculated ^a frequencies (cm^{-1}) and potential energy distributions (P.E.D.s) for the <i>tTt</i> (C_{2h}) conformer of 1,2-diphosphinoethane.....	178
4.17. Observed and calculated ^a frequencies (cm^{-1}) for the <i>g'Tt</i> (C_1) conformer of 1,2-diphosphinoethane.....	180
4.18. Observed and calculated ^a frequencies (cm^{-1}) for the <i>g'Tg'</i> (C_2) form of 1,2-diphosphinoethane.....	181
4.19. Observed and calculated ^a frequencies (cm^{-1}) for the <i>g'Tg</i> (C_i) form of 1,2-diphosphinoethane.....	182
4.20. Observed and calculated ^a frequencies (cm^{-1}) for the <i>tG'g'</i> (C_1) form of 1,2-diphosphinoethane.....	183
4.21. Observed and calculated ^a frequencies (cm^{-1}) for the <i>tG't</i> (C_2) form of 1,2-diphosphinoethane.....	184
4.22. Temperature and intensity ratios of the conformational bands of 1,2-diphosphinoethane from the Raman spectra of the liquid.....	194
4.23. Calculated energies (hartree) and energy differences ^a (cm^{-1}) for the ten conformers of 1,2-diphosphinoethane.....	195
4.24. Structural parameters (\AA and $^\circ$) and rotational constants (MHz) for the <i>g'Tt</i> , <i>g'Tg'</i> , <i>tG'g'</i> , and <i>tG't</i> conformer of 1,2-diphosphinoethane.....	196
4.25. Symmetry coordinates for the <i>tTt</i> conformer of 1,2-diphosphinoethane.....	198
4.26. Comparison of rotational constants (MHz) obtained from ab initio MP2(full)/6-311+G(d,p) predictions, experimental values from microwave spectra, and from the adjusted r_0 structural parameters for 1,2-diphosphinoethane.....	201

ILLUSTRATIONS

Figure	Page
2.1 Tenofovir molecule.....	25
2.2 Dialysis membrane method of quantitative <i>in vitro</i> drug release analysis from drug formulations in biological media. (A) Initial state. (B) Equilibrium state.....	28
2.3 Membrane partitioning in dialysis method of quantitative <i>in vitro</i> drug release analysis from drug formulations in biological media.....	31
2.4 Linearity assay of the ³¹ P-NMR method in: (A) VFS. (C) SFS. (E) Human plasma. Representative ³¹ P-NMR peak of TFV in: (B) VFS. (D) SFS. (F) Human plasma..	42
2.5 Specificity analysis of the ³¹ P-NMR analysis: (A) TFV in VFS. (B) Blank VFS. (C) TFV in SFS. (D) Blank SFS. (E) TFV in plasma. (F) Blank plasma. (G) TFV with OPA in water.....	43
2.6 (A) Coaxial electrospinning chitosan nanofibers fabrication assembly setup. (B) Surface morphology of chitosan NFs; scale bar, 5 μm. (C) Size distribution histogram of chitosan NFs determined by image analysis software and averaged using at least 100 measurements per group.....	46
2.7 Percent cumulative drug release (% w/w) profile of TFV loaded chitosan NFs analyzed by solution state ³¹ P-NMR and UV-Vis spectroscopy assay in A] VFS, B] SFS, and C] Human Plasma.....	48
2.8 Illustration of the layer by layer preparation of core dissolved (C ⁻ MSN) and core containing (C ⁺ MSN) mannose sensitive nanoparticles (MSN). CaCO ₃ core particle is coated with 6 layers including a PEI layer initiator.....	58
2.9 ³¹ P solid state NMR spectra of C ⁻ MSN, C ⁺ MSN. Tenofovir appears at 15.7 ppm and the spinning side bands are indicated by asterisks.....	62
2.10 FTIR spectra of glycogen, Con A, CaCO ₃ -PSS core particle, C ⁺ MSN, C ⁻ MSN and Con A/glycogen agglutinate.....	64
2.12 Tenofovir release profile from C ⁺ MSN in the presence of methyl α-D-mannopyranoside (1000 μg/ml) and HIV-1 rgp120 (100-1000 μg/ml). Data from each time point is triplicated (n=3).....	65

2.13 Schematic preparation scheme of the TCS coated multilayer MPs.....	70
2.14 Drug Loading Analysis of MPs using ^{31}P SS NMR Spectroscopy. A single peak for TFV appears at 15.7 ppm. Spinning side bands are shown by Asterisks.....	72
2.15 FT-IR spectra of oppositely charged TCS and Alginate coatings (n=3).....	73
3.1 DTA results of powdered clay.....	86
3.2 FTIR spectra of raw clay and clays calcined at temperatures 600-1000°C.....	88
3.3 ^{27}Al SS MAS NMR spectra of raw clay and clays calcined at temperatures 600-1000°C. The spinning side-bands are indicated by Asterisk.....	92
3.4 ^{29}Si SS MAS NMR spectra of raw and calcined clays.....	94
3.5 Strength activity index of calcined pozzolan.....	96
3.6 ^{27}Al SS MAS NMR spectra of hydrated cement '20 Clay Pozzolan' at 3 days...98	
3.7 ^{27}Al SS MAS NMR spectra of hydrated cement '20 Clay Pozzolan' at 7 days...99	
3.8 ^{27}Al SS MAS NMR spectra of hydrated cement '20 Clay Pozzolan' at 28 days.....	100
4.1 Comparison of experimental and calculated infrared spectra of 1-bromo-1-silacyclopentane: (A) observed IR spectrum of gas; (B) observed IR spectrum of solid; (C) simulated IR spectrum of <i>twist</i> (C_I) conformer.....	115
4.2 Comparison of experimental and calculated Raman spectra of 1-bromo-1-silacyclopentane: (A) observed Raman spectrum of liquid; (B) simulated Raman spectrum of <i>twist</i> (C_I) conformer.....	116
4.3 Planar (C_s) conformer of 1-bromo-1-silacyclopentane showing atom numbering and internal coordinates.....	129
4.4 Comparison of experimental and calculated infrared spectra of 1-bromo-1-silacyclopentane: (A) observed infrared spectrum of solid; (B) simulated infrared	

spectrum of <i>twist</i> conformer; (C) simulated infrared spectrum of <i>envelope-axial</i> conformer; (D) simulated infrared spectrum of <i>envelope-equatorial</i> conformer...	131
4.5 Comparison of experimental and calculated infrared spectra (990-1200 cm^{-1}) of 1-bromo-1-silacyclopentane: (A) simulated spectra of <i>twist</i> (C_1) conformer at 0.5 cm^{-1} and 4.0 cm^{-1} resolutions; (B) observed infrared spectrum of the gas showing typical B-, A- and A/C-type band contours at 1157, 1080 and 1033 cm^{-1} , respectively, measured at 0.5 cm^{-1} resolution.....	132
4.6 Raman spectra (0-1550 cm^{-1}) showing the polarized and the depolarized bands for 1-bromo-1-silacyclopentane.....	133
4.7 Infrared spectra (3200-400 cm^{-1}) of 2-cyanoethylphosphine: (A) liquid; (B) amorphous solid; (C) crystalline solid; (D) simulated IR spectrum of <i>Gauche-trans</i> conformer; (E) simulated IR spectrum of <i>Trans-trans</i> conformer.....	145
4.8 Raman spectra (3050-50 cm^{-1}) of 2-cyanoethylphosphine: (A) liquid; (B) solid; (C) simulated Raman spectrum of <i>Gauche-trans</i> conformer; (D) simulated Raman spectrum of <i>Trans-trans</i> conformer.....	146
4.9 <i>Trans-trans</i> (C_s) conformer of 2-cyanoethylphosphine showing atom numbering and internal coordinates.....	156
4.10 Newmann projections of the five conformers of 2-cyanoethylphosphine.....	159
4.11 Newmann projections of the ten conformers of 1,2-diphosphinoethane.....	175
4.12 Comparison of experimental and calculated infrared spectrum of 1,2-diphosphinoethane: (A) observed spectrum of gas; (B) observed spectrum of amorphous solid; (C) observed spectrum of crystalline solid; (D) simulated spectrum of <i>tTt</i> form; (E) simulated spectrum of <i>g'Tt</i> form.....	190
4.13 Comparison of experimental and calculated Raman spectrum of 1,2-diphosphinoethane: (A) observed spectrum of liquid; (B) observed spectrum of solid; (C) simulated spectrum of <i>tTt</i> form; (D) simulated spectrum of <i>g'Tt</i> form.....	191
4.14 <i>tTt</i> conformer of 1,2-diphosphinoethane showing atom numbering and internal coordinates.....	193

ACKNOWLEDGEMENTS

My debts of gratitude to all the academic institutions I have yet attended and which have contributed principally in my career by providing me a platform to gain education. It includes my school, I.E.S. Raja Shivaji Vidyalaya, Ramnarain Ruia College (University of Mumbai), University of Kentucky and University of Missouri Kansas City. I hereby take this opportunity to present my cordial gratitude to the many individuals who offered extremely valuable suggestions as well as criticism which eventually molded my personality and career.

First of all, I must express my sincere appreciation towards my research advisor Prof. Nathan A. Oyler as my journey as a Ph.D. student would be way tough in the absence of tremendous guidance and support I have received from him at every level. I also thank all of the members of my advisory committee which includes, Prof. Fedor Rudakov, Prof. David Van Horn, Prof. James Murowchick and Prof. Jejung Lee for their timely supervision and genuine suggestions through the course of my Ph.D. research.

I would also like to thank Prof. James Durig, Prof. Fedor Rudakov, Prof. David Atwood, Prof. Fitzgerald Bramwell and Prof. Kiran Mangaonkar for providing me an opportunity to work in their research laboratories on various projects and gain a lot of research experience and scientific knowledge throughout my tenure as a graduate student.

This list would be left incomplete if not mentioned with names such as Mr. and Mrs. Karmarkar and Mr. Yogesh Patil for their help as a teacher during my high school days. I am quite thankful to Mr. Nitin Shukla for providing me with financial aid in the early years of my grad school. I also present my immense respect for my dear colleagues and friends Prof. Alexandru Spataru, Prof. Ericka Sanner, Dr. Amol Date, Mrs. Prajakta

Date, Dr. Tanmoy Dutta, Dr. Bhushan Deodhar, Mr. Nitin Salvi and Mr. Clark Harrison for their unconditional and incessant love and support throughout my strenuous graduate years. I also recognize my friends and colleagues Mr. Thuong Nguyen and Mr. John Self for their instantaneous help when I really needed it in my impromptu difficult situations. I am thankful to my friends, colleagues and roommates Mr. Kuldeep Shetye and Mr. Dattatray Sawant. My association with my friends and colleagues Dr. Vivek Agrahari, Dr. Jianing Meng, Mr. Fohona Coulibaly and Dr. Mark Bediako have always been extremely pleasant with whom I spent a lot of time discussing on various projects on pharmacy and cement material. I also thank Cipla LTD., Metropolitan Community College and Swinney Recreation Center, UMKC and all of their staff for providing me an opportunity to work with them.

I also present my cordial gratitude towards, Mr. Shirsavkar, Mrs. Sagvekar and Mr. Rao for their unremitting spiritual support to make me withstand the harsh realities of graduate life. I extend my genuine acknowledgments to my elder cousins Dr. Padmakar Tillu, Mr. Vipin Paranjape and our family friends Mrs. Mangal Joshi, Mrs. Harcharan Kaur Kahan, and Mrs. Meena Kanade. I certainly cannot miss my step-grandmother Mrs. Vasudha Patwardhan for her relentless love and affection towards me for past more than 20 years. She has always been a beacon of hope and positivity for me.

I present my cordial gratitude towards Dr. Jerry Singh the president of RTI Laboratories for entrusting me and offering me an excellent opportunity to work with them. I express my sincere respect and appreciation for his help and guidance and also providing me with a very healthy work environment which contributes in my progress.

Finally, I would like to acknowledge my parents Mr. Shrikant Purohit, Miss. Asha Gaikawai and Mr. Nitin Patwardhan with deep gratitude and respect for their tremendous love and sustained support throughout all these years. They have been always with me when I needed them the most. I would like to conclude with presenting my gratefulness to the God almighty without whom I would not be able to achieve this degree.

This Ph.D dissertation is dedicated to my parents,

Mr. Shrikant Purohit, Miss. Asha Gaikawari,

and

Mr. Nitin Patwardhan

for their unconditional love and support throughout my life and academic career.

Dissertation Outline

This dissertation includes the results obtained from the research that involved the implementation of spectroscopic techniques such as infrared, Raman and NMR and were utilized in diverse research projects.

Chapter-2 discusses about the extensive use of both solid state and solution state NMR spectroscopy for both qualitative and quantitative determination of phosphorous containing drug (Tenofovir) encased in pH sensitive nano-particle shell and its subsequent release profile when in contact with human body fluids such as vaginal & seminal fluids and human plasma.

Chapter-3 describes the implementation of solid state NMR as analytical tool for both qualitative and quantitative determination of bonding between Aluminum and Silicon sheets of calcined Ghanaian clay samples which are used as supplementary cementitious material in construction.

Chapter-4 on the other hand, focuses on infrared and Raman spectral studies to obtain structural parameters, conformational stability, vibrational assignments and *ab initio* calculations of organic molecules containing five membered ring and phosphorous.

Chapter 1

INTRODUCTION

The physical evolution of humans may have followed natural law of selection but the technological development can certainly be attributed to their curious minds, always engaged in discovering answers in a scientific manner. The logically inquisitive nature of humans, when was channeled to acquire knowledge in a systematic and organized manner was able to produce outstanding discoveries which in turn have immensely transformed our civilization and improved the way of life. The scientific revolution in 19th century, introduced the technology which cleared the pathway for advancements in instrumentation techniques that allowed the acquisition of more sensitive data than that was previously possible. Although, the availability of more data should help the scientific community in solving a problem; the usefulness of the conclusions reached is only realized if the data is interpreted as carefully and correctly as possible. Thus, the necessity of effective analytical tools which can efficiently be able to carry out both qualitative and quantitative analysis of the substance under study, eventually, led to the discovery of techniques such as Chromatography and Spectroscopy. The end of the nineteenth and beginning of the twentieth centuries was marked by significant efforts to quantify and explain the origin of spectral phenomena. This particular dissertation includes the implementation of few spectroscopic techniques which have aided me to contribute in the analysis of pharmaceutical, organic, cement samples at their molecular level.

Spectroscopy in general can be explain as the study of the interaction of electromagnetic radiation with matter. Much of the scientific knowledge of the structure of the universe, from stars to atoms, can be derived from interpretations of the interaction of

radiation with matter. Spectroscopy is widely used in Chemistry because atoms and molecules have unique spectra by which the spectroscopic data is often represented. It is a powerful and sensitive form of chemical analysis, as well as a method of probing electronic and nuclear structure and chemical bonding. A spectrum is a plot of the response of interest as a function of wavelength or frequency, which can be used to detect, identify and quantify information about the atoms and molecules¹. Spectroscopy is a sufficiently broad field where many sub-disciplines exist, each with numerous implementations of specific spectroscopic techniques. The various implementations and techniques can be classified in several ways. In many applications, the spectrum is determined by measuring changes in the intensity or frequency of the energy. Spectroscopic techniques are also distinguished by the type of radiative energy involved in the interaction. Understanding the physical structure of a molecule is fundamental for function, dynamic, and mechanism studies. Many methods, such as solution state and solid state Nuclear Magnetic Resonance (NMR) spectroscopy, X-ray crystallography, and molecular spectroscopy (IR/Raman), have been applied so far to study the molecular structures. In this very dissertation, I have utilized various spectroscopic techniques such as Infrared spectroscopy, Raman spectroscopy and Nuclear Magnetic Resonance (NMR) spectroscopy in order to determine theoretical, qualitative and quantitative properties of different molecules under study.

The field of molecular structure determination has thrived from improvements in instrument design. The molecular structure is the orientation of atoms of molecules within free space. Conformational stability is a part of molecular structure which also includes bond lengths, bond angles, torsional angles etc. It is quite important to determine the

orientation of a molecule in space with respect to the rest of the molecule. The study of these quantitative elements is important as they provide information about the various forces acting upon the molecule, eventually defining molecular geometry. Chemical formula of a molecule all by its own does not provide the complete understanding of the real world system as the intermolecular forces exhibit strong influence on the bulk properties of the system. The study of conformational geometry is important because properties such as melting/boiling points, conductance etc. are dependent on the crystal structure of the molecule which further depends on conformational geometry. In order to be able to investigate motion and structure at the molecular level, determination of spatial orientations or conformers that are present in various physical states is critical. For a molecule with more than one conformer it is essential to determine the most stable conformer, energy difference between the conformers and energy necessary for interconversion between the conformers.

Infrared and Raman spectroscopy are two of the most widely used and powerful techniques for the accurate determination of molecular symmetry and conformational stability. They provide information of molecular vibrations and the two techniques complement each other to yield more complete information about the molecular structure than when they are evaluated separately. The distinctive spectral features (vibrational frequency, band intensity, gas phase band envelope and rotational fine structure and Raman depolarization ratio, *etc.*) are unique fingerprints of the functionality and the organic molecules; in addition, they provide invaluable information about the symmetry and structure of individual conformations.

A large amount of information on the structure, bonding, and conformational stability of small molecules has become available through studies of their rotational and vibrational spectra. Vibrational spectroscopy has become an important method for the elucidation of molecular structure through the investigation of inter and intra-molecular forces of a molecule, as well as, the relative stability of the different molecular conformations, because the spectra can be investigated in all stages of aggregation (vapors, liquids, solutions, amorphous and crystalline solids, and in inert matrices at high pressure). Thus, infrared and Raman spectroscopy can provide reliable data for the determination of conformational stability, especially if the molecule has at least one element of symmetry^{2,3}. Usually, the molecules selected for vibrational analysis are relatively simple ones which often contain one or more elements of symmetry and are capable of producing different conformations upon internal rotation.

One of the focus of this dissertation is the determination of the structural parameters, conformational stability, vibrational assignments and *ab initio* calculations of organic molecules containing five membered ring and phosphorous by utilizing infrared and Raman spectral techniques. The findings of my spectroscopic, structural, and theoretical studies are based on infrared and/or Raman spectra of gas, liquid, solid as well as variable temperature xenon solutions, and microwave spectrum which are supported by *ab initio* and DFT calculations. The *ab initio* calculations are performed with the Gaussian 03 program⁴ with Gaussian-type basis functions. The energy minima with respect to nuclear coordinates are obtained by the simultaneous relaxation of all geometric parameters by the gradient method of Pulay⁵. Several basis sets as well as the corresponding ones with diffuse functions are employed with the Møller-Plesset perturbation method⁶ to the second

order with full electron correlation (MP2(full)) along with the density functional theory by the B3LYP method. By utilizing the information, acquired through the experimental and theoretical studies carried out in the research laboratory, I have accomplished the following results for the molecules under study. Spectra obtained from infrared and Raman experiments are used in the vibrational studies to assign fundamental frequencies for all possible conformers as well as for the identification of the conformers. The MP2(full)/6-31G(d) calculations are used to predict the force constants, frequencies, infrared intensities, Raman activities, band contours, potential energy distributions and depolarization values to support the vibrational assignment. Raman spectrum of liquid is used to obtain the experimental depolarization values. Determination of enthalpy difference values is carried out by using variable temperature, infrared or Raman spectra of xenon solutions or the liquid. From these experimentally obtained ΔH values, the order of the stability of the conformers are determined. The experimentally determined enthalpy values are used to evaluate the quality of the predicted values of energies by *ab initio* and density functional theory calculations obtained from various basis sets up to aug-cc-pVTZ. Also % abundance of each conformer are determined by experimentally obtained ΔH values. The r_0 structural parameters can be obtained from utilizing the experimentally determined rotational constants from previously published microwave data or data obtained from my research. The experimentally determined values are then compared with the estimated values obtained from adjusted MP2(full)/6-311+G(d,p) calculations for the respective conformers. These physiochemical data should provide significant trends and affects to better understand the major factors controlling the relative stabilities of the conformers as well as the relative values of the structural parameters.

NMR spectroscopy, first discovered in 1938 is a non-destructive analytical tool which has been successfully applied to study molecular structure, sample purity, and reaction mechanisms at the atomic level. The application and development of NMR spectroscopy has demonstrated the great contribution of this technique on compound identification and has enabled a more thorough understanding of molecular structure and dynamics.

Solid-State Nuclear Magnetic Resonance (SS NMR) has become one of the best techniques to determine molecular structure via inter/intra-molecular interactions. Unlike the well-known solution state NMR, solid-state NMR primarily elucidates the structural information by chemical shift anisotropy and dipolar coupling regardless of the solubility, crystallinity, and amorphousness of the target samples. The fascinating development of solid-state NMR methods in the past thirty years has contributed greatly to the level of our understanding of molecular structure and molecular interactions both quantitatively and qualitatively. This method has been applied in studying lyophilized samples, non-crystalline solids, insoluble aggregates, and biopolymer frozen solutions to determine their physical, chemical, and biological properties.

The story of evolution of human civilization would feel unfinished if the devastating role played by diseases is left untold. To name with, epidemics such as plague factually demonstrated a potential to cause mass extinction of human population. The dispersal of a majority of life threatening diseases has been put to leash as the development in medical sciences since the early twentieth century introduced a large number of lifesaving drugs. Nevertheless, even today diseases like AIDS, Hepatitis, Cancer, Alzheimer etc. are few notorious names to mention with where, therapy is still far from

curing the disease and a successful vaccine is yet to be developed, which renders, implementation of precautionary measures to prevent from infection to be the best strategy for survival. Since the beginning of current century, scientific community has been incessantly researching to invent and develop not only an effective drug against these diseases but also an efficient drug delivery system to administer the drug in infected human body. Years of tenacious research has finally yielded in the development of a means to resolve problems associated with delivery of therapeutic compound to the target site. We are now aware of a variety of drugs that are being effectively used against these diseases as a part of preventive treatment and to our surprise majority of these drugs contain phosphorous.

Nearly four decades ago the potential of NMR spectroscopy for the quantitative analysis of organic chemicals was first demonstrated⁷⁻⁹ whereas, the first quantitative measurements have been described in the literature in 1963^{10,11}. Even though, most of these early qNMR studies have been performed with solution state NMR technique, for past two decades solid state NMR spectroscopy has come to the forefront of quantitative analytical techniques in pharmaceutical research. The Food and Drug Administration (FDA) has also recognized the need for solid state NMR characterization of drug substances as approximately 80–90% of pharmaceutical products on the market exist in the solid form. The possibility of decrease in stability and increase in interaction with excipients of active pharmaceutical ingredient (API) due to its alteration, caused by the extreme conditions of processing the formulation into dosage form makes it critical to study pharmaceutical compounds in the solid state both at the bulk level and for the final dosage form^{12,13}. Thus,

SS NMR spectroscopy has also been successfully applied to the study of polymorphism in pharmaceutical drugs at both the qualitative and quantitative levels.

To be able to accurately quantify the amount of drug being delivered in human body is a crucial requirement of any drug development process. We cleverly decided to make use of a ^{31}P atom present in these drugs and hence, in this dissertation we are primarily focusing on the development and implementation of a general ^{31}P qNMR method to achieve direct, real time quantification of *in vitro* drug release. We have effectively utilized both solution state and solid state ^{31}P qNMR spectroscopic techniques to establish the kinetics of drug release and to determine the encapsulation efficiency of nano-formulation for a particular drug under study, respectively. Taking into account the principles of ^{31}P qNMR, the proposed method rather can be extensively applied to all the drug molecules that contain phosphorous, signifying a subsequent huge scope of this method. The *in vitro* drug release profile has been studied in various human body fluids such as simulated vaginal and seminal fluids, human plasma etc. depending on the drug under study.

The investigation of our research presented in this dissertation was initiated by selecting AIDS, the predominant pandemic of twentieth century and Tenofovir (TFV), a well-tested antiretroviral drug that has proven its mettle against HIV/AIDS. To study this specific disease-drug pair, we have used a specific type of spray dried, mucoadhesive, pH sensitive nano-formulation, successfully developed by Zhang T. et al.¹⁴ that served as an encasing for TFV. The respective nano-formulation has proved to be efficient in administering TFV in human body through the epithelial cells of human genitals. Previously, Zhang C. et al.¹⁵ developed and implemented ^1H qNMR spectroscopic method to quantify the amount of TFV being delivered whereas, we are introducing ^{31}P qNMR

spectroscopic method for quantification purposes. The results of method validation parameters for TFV in simulated vaginal & seminal fluid and human plasma obtained by using ^{31}P solution state qNMR spectroscopy are presented in this dissertation. The encapsulation efficiency of the respective nano-formulation encasing TFV in solid form was estimated by integrated ^{31}P (144.597 MHz) Bloch decays and is also well conversed herein. FTIR spectroscopy has been extensively used to aid in determining the structural components of the nano-formulations used.

Another chapter of this dissertation explains the analysis of calcined clay as supplementary cementitious material, obtained from Ghana, a West African nation, which does not have an abundance of commonly used SCMs such as fly ash, silica fume, metakaolin, and slag. However, the abundance of clay minerals in the country could provide a sustainable alternative with respect to SCMs application. Qualitative techniques such as Thermal Gravimetric Analysis (TGA) and Forrier Transform Infrared Spectroscopy (FTIR), and quantitative tools like Nuclear Magnetic Resonance (NMR) are able to provide meaningful characterizing of thermally activated clays. In this study, clay from Ghana was thermally activated at temperatures of 600, 700, 800, 900 and 1000°C. The main objective was to characterize calcined clay using TGA, FTIR, NMR, and their relation to pozzolanic activity to best understand the potential of this abundant resource to alleviate cement supply burdens.

In this study, clay from Ghana was thermally activated at temperatures of 600, 700, 800, 900 and 1000°C. The main objective was to characterize calcined clay using TGA, FTIR, NMR, and their relation to pozzolanic activity to best understand the potential of this abundant resource to alleviate cement supply burdens.

References

- (1) Crouch, S; Skoog, D. *ref 1*; Australia: Thomson Brooks/Cole, 2007.
- (2) Durig, J. R.; Durig, D. T.; Durig, B. R.; Sullivan, J. F. *J. Mol. Struct.* **1985**, *126*, 83.
- (3) van der Veken, B. J.; Durig, J. R. *Elsevier, Amsterdam* **1986**, *15*.
- (4) Frisch, M. J.; Trucks, G. W.; Schlegel, H. B.; Scuseria, G. E.; Robb, M. A.; Cheeseman, J. R.; Montgomery, Jr., J. A.; Vreven, T.; Kudin, K. N.; Burant, J. C.; Millam, J. M.; Iyengar, S. S.; Tomasi, J.; Barone, V.; Mennucci, B.; Cossi, M.; Scalmani, G.; Rega, N.; Petersson, G. A.; Nakatsuji, H.; Hada, M.; Ehara, M.; Toyota, K.; Fukuda, R.; Hasegawa, J.; Ishida, M.; Nakajima, T.; Honda, Y.; Kitao, O.; Nakai, H.; Klene, M.; Li, X.; Knox, J. E.; Hratchian, H. P.; Cross, J. B.; Bakken, V.; Adamo, C.; Jaramillo, J.; Gomperts, R.; Stratmann, R. E.; Yazyev, O.; Austin, A. J.; Cammi, R.; Pomelli, C.; Ochterski, J. W.; Ayala, P. Y.; Morokuma, K.; Voth, G. A.; Salvador, P.; Dannenberg, J. J.; Zakrzewski, V. G.; Dapprich, S.; Daniels, A. D.; Strain, M. C.; Farkas, O.; Malick, D. K.; Rabuck, A. D.; Raghavachari, K.; Foresman, J. B.; Ortiz, J. V.; Cui, Q.; Baboul, A. G.; Clifford, S.; Cioslowski, J.; Stefanov, B. B.; Liu, G.; Liashenko, A.; Piskorz, P.; Komaromi, I.; Martin, R. L.; Fox, D. J.; Keith, T.; Al-Laham, M. A.; Peng, C. Y.; Nanayakkara, A.; Challacombe, M.; Gill, P. M. W.; Johnson, B.; Chen, W.; Wong, M. W.; Gonzalez, C.; Pople, J. A. Gaussian 03, Revis. E.01, Gaussian, Inc., Wallingford, CT **2004**.
- (5) Pulay, P. *Mol. Phys.* **1969**, *17*, 197.
- (6) Møller, C.; Plesset, M. S. *Phys. Rev.* **1934**, *46*, 618.
- (7) Shoolery, J. N. *Prog. NMR Spectrosc.* **1977**, *11*, 79.
- (8) Greenhalgh, R.; Shoolery, J. N. *Anal. Chem.* **1978**, *50*, 2039.
- (9) Wayne, R. S.; Stockton, G. W.; Wilson, L. A.; Miyamoto, J.; Kearney, P. C. *Proc. Int. Congr. Pest. Chem.* **1982**, *4*, 381.
- (10) Jungnickel, J. L.; Forbes, J. W. *Anal. Chem.* **1963**, *35*, 938.
- (11) Hollis, D. P. *Anal. Chem.* **1963**, *35*, 1682.
- (12) Otsuka, M.; Matsumoto, T.; Kaneniwa, N. *J. Pharm. Pharmacol.* **1989**, *41*, 665.
- (13) Connors, K. A.; Amidon, G. L.; Stella, V. J. *New York John Wiley Sons.* **1986**.
- (14) Zhang, T.; Sturgis, T. F.; Youan, B. B. *Eur. J. Pharm. Biopharm.* **2011**, *79*, 526.
- (15) Zhang, C.; Zhang, T.; Oyler, N.; Youan, B.-B. *J. Pharm. Sci.* **2014**, *103*, 1170.

Chapter 2

QUANTITATIVE ANALYSIS OF PHOSPHOROUS CONTAINING DRUG MOLECULES ENCAPSULATED IN pH-SENSITIVE NANOPARTICLE FORMULATIONS TO ESTABLISH DRUG LOADING AND DRUG RELEASING PROFILE BY UTILIZING ^{31}P SOLID STATE AND SOLUTION STATE NUCLEAR MAGNETIC RESONANCE SPECTROSCOPIC TECHNIQUES

Introduction

The story of evolution of human civilization would feel unfinished if the devastating role played by diseases is left untold. Since, the dawn of the civilization in the known history, human race has been afflicted by several infectious and autoimmune diseases. To name with, epidemics such as plague factually demonstrated a potential to cause mass extinction of human population. The beginning of 20th century introduced a new era where significant development in medical sciences promised greater life expectancy as either cure or acute preventive therapies were invented to triumph over large number of medical conditions. The dispersal of a majority of life threatening diseases has been put to leash as the development in medical sciences since the early 20th century introduced a large number of lifesaving drugs. In spite of these achievements, to the date, a therapy is still far from curing the life-threatening diseases such as AIDS, hepatitis, cancer, Alzheimer etc. These are few notorious names to mention a successful vaccine is yet to be developed, which renders, implementation of precautionary measures to prevent from infection to be the best strategy for survival. These diseases affect people not only physically, but also emotionally, as contracting and living with a disease can alter one's personality as well as perspective on life. Hence, scientific community has been engaged

in intense research to invent measures, if not cure, to prevent the infection from these diseases and cease the further spread of the disease in human body after being diagnosed.

Since the beginning of current century, scientific community has been incessantly researching to invent and develop not only an effective drug against these diseases but also an efficient drug delivery system to administer the drug in infected human body. Hats off to the perseverance of scientific community as now we are aware of quite a few number of drugs which have proven ability against these diseases. Years of tenacious research has finally yielded in the development of a means to resolve problems associated with delivery of therapeutic compound to the target site. We are now aware of a variety of drugs that are being effectively used against these diseases as a part of preventive treatment. It is rather interesting to know that majority of these drugs contain phosphorous atom and we have ingeniously come up with a plan to take an advantage of this ^{31}P atom for the quantitative measurements of the drug under study. In this research, we have projected the use of nuclear magnetic resonance spectroscopy as an analytical tool that aided us to quantify the amount of drug being delivered by conducting *in vitro* studies. Our major objectives enlisted the development of a quantitative NMR method that can be further implemented to determine the amount of drug released from its placebo-encasing in the simulated human body fluids. As a matter of fact, it is not only the drugs but also their delivery systems in human body that are exclusively being researched and are under development.

The extensive research in the field of nanotechnology has provided scientific community with a plausible solution to overcome the problems faced while developing suitable drug delivery system. Nano-formulations are now being synthesized using numerous types of materials which are designed to release the encased drug strictly when

triggered by change in the pH of the surrounding media. Hence, it is also quintessential to understand the encapsulation capacity of these nano-formulations in their solid form. Modern research showed that the problems such as limited effectiveness, poor bio-distribution, and lack of selectivity encountered during conventional ways of application of drug can be overcome by controlling drug delivery¹. Recent developments in nanotechnology revealed nanoparticles (structures smaller than 100 nm) to have a great potential as drug carriers, as drug molecule encapsulated in nano-formulation can be delivered directly to the site of action. Liposomes, solid lipids nanoparticles, dendrimers, polymers, silicon or carbon materials, and magnetic nanoparticles are the examples of nano-carriers that have been tested as drug delivery systems. The nanostructures exhibit unique physicochemical and biological properties due to their small size². Properties such as an enhanced reactive area as well as an ability to cross cell and tissue barriers made nanoparticles a favorable material for biomedical applications. Nano-carriers have effectively proven potential applications in solubilizing poorly soluble drug candidates, reducing drug toxicity, prolonging circulation times, controlling drug release kinetics, drug targeting, and monitoring drug delivery to enhance therapeutic efficacy³⁻⁷. Thus, in recent years interest in nanoparticle drug delivery systems has grown dramatically as they have shown improvement in the pharmacological and therapeutic properties of conventional drugs. Nevertheless, *in vivo* delivery process exhibited the challenges such as minimal drug leakage during the initial period and triggered drug release at the target site which were needed to overcome.

Pharmacokinetics and pharmacodynamics are undoubtedly the main pillars that must be thoroughly studied while designing any drug. Pharmacokinetics deals with the

quantitative aspect of drug handling by a body which in turn defines the temporal relationship between dose of the drug to be administered and a respective drug concentration in the body. On the other hand, pharmacodynamics establishes relationship between drug concentration at the pharmacological receptor and its respective pharmacological response. The new drug designed to be considered useful as a medicine must be capable of being delivered to its site of action achieving concentrations sufficient to initiate and maintain the appropriate pharmacological response. ADME, stands for absorption, distribution, metabolism and excretion, describes the qualitative process by which the body handles the drug as soon as it is administered in the body. The thorough knowledge of ADME provides a systematic podium to understand relationship between pharmacokinetics and pharmacodynamics. The studies of ADME process have suggested that once the administered drug reaches to equilibrium within the body, the time profile of drug-plasma concentration is observed to be quite parallel to that of drug-tissue concentration if not of absolutely equal magnitude. This makes the issue of time required to achieve equilibrium, rather critical in establishing relationship between pharmacokinetics and pharmacodynamics. Hence, learning pharmacokinetics is vital when launching new drug-body profile as it offers a quantitative outline for the prospective optimization of therapeutic dosage treatments⁸.

Also, prior to the actual administration of a drug in human body the quality control of drug delivery system is an extremely important step which makes understanding the factors influencing drug release, from both *in vivo* and *in vitro* perspective, quintessential. Hence, a variety of meaningful *in vitro* drug release testing methods were developed and implemented to predict the *in vivo* pharmacokinetics and performance specifications.

Methods introduced in earlier years such as ultrafiltration and ultracentrifugation incorporated significant errors in measurement and proved to be inefficient^{9,10}. The most prevalently used method to establish the kinetics of drug release from nanoparticles was dynamic dialysis where the amount of drug released from nanoparticle was assumed to be directly proportional to the disappearance of drug from donor compartment and its appearance in receiver compartment. Also, the elimination of the additional step of separating nanoparticles from free drug at various time points during the kinetic study surpassed the popularity of dynamic dialysis over ultrafiltration and ultracentrifugation. Soon, potential sources of errors discovered in the experimental data obtained, put the authenticity and reliability of dynamic dialysis method to question. The rate of the drug release in receiving chamber was attributed to the driving force for drug transport across the dialysis membrane and its barrier properties. The driving force on the other hand was influenced by the reversible drug binding to the nano-carrier and the issue of drug partitioning between the phases present in dispersed systems¹¹⁻¹⁵. The idea of compensating for the misinterpretation of release rate of dialysis method by implementing the reverse dialysis method was also proven to be not so effective due to its poor sensitivity and specificity^{16,17}. Even though, the methods such as HPLC and LCMS utilized for the quantification of drug released in receiving chamber proved to be highly accurate¹⁸⁻²¹, the experimental demonstration of the practical limitations incorporated within the dialysis method rendered it to be far from being tagged flawless²². Thus, the demand for an ideal solution compelled scientific community to search for the direct, accurate, and if possible, real time method for the detection and quantification of drug molecule.

Facts discussed so far, motivated us to develop qNMR method which can effectively establish kinetic release profile of the phosphorous containing drug under study, encapsulated in nano-formulation. We planned to initiate the pharmacokinetics studies of the drug under consideration, *in vitro*, imitating the *in vivo* scenario. This provided us sufficient information about the actual performance of the drug before being tested on animals or humans.

Nuclear magnetic resonance (NMR) spectroscopy is perhaps the most important, powerful, and widely used form of spectroscopy in both academic and industrial research since its discovery in early 1950s. It probes atomic environments based on the different resonance frequencies exhibited by nuclei in a strong magnetic field. An increase of sensitivity due to stronger static magnetic fields allowed not only independent and intrinsically reliable determination of chemical purity but also the determination of amount of substance in the sample under study by utilizing NMR spectroscopy. NMR is an effective spectroscopic tool for quantitative analysis, as the intensity of a resonance line is directly proportional to the number of resonant nuclei or spins. In contrast to chromatography, quantitative NMR (qNMR) employs a universal reference standard as an internal standard for majority of chemical products assayed, as NMR response can be made the same for all chemical components including an internal standard by optimizing certain instrumental parameters. Thus, qNMR competes effectively with chromatographic methods by avoiding a need for a reference standard for each analyte while maintaining higher standards of sensitivity, speed, precision, and accuracy. These facts enabled qNMR to find applications in various fields like Physics, Chemistry, Bio-Chemistry, Pharmacy, Food Science, Medicine & Veterinary²³⁻²⁶.

Nearly four decades ago the potential of NMR spectroscopy for the quantitative analysis of organic chemicals was first demonstrated^{27,28} whereas, the first quantitative measurements have been described in the literature in 1963^{29,30}. Even though, most of these early qNMR studies have been performed with solution state NMR technique, for past two decades solid state NMR spectroscopy has come to the forefront of quantitative analytical techniques in pharmaceutical research. The Food and Drug Administration (FDA) has also recognized the need for solid state NMR characterization of drug substances as approximately 80–90% of pharmaceutical products on the market exist in the solid form. The possibility of decrease in stability and increase in interaction with excipients of active pharmaceutical ingredient (API) due to its alteration, caused by the extreme conditions of processing the formulation into dosage form makes it critical to study pharmaceutical compounds in the solid state both at the bulk level and for the final dosage form^{31,32}. Thus, SSNMR spectroscopy has also been successfully applied to the study of polymorphism in pharmaceutical drugs at both the qualitative and quantitative levels.

In pharmaceutical research, NMR spectroscopy has been primarily used in classical organic chemistry framework as typical investigation focused on (i) structural determination and chirality studies of drug substances, (ii) studies that included cellular metabolism and proteins. Quantitative NMR being universal and highly specific, proved to be a remarkably successful analytical tool in structural analysis. A systematic validation of qNMR method, performed in a manner consistent with the Good Laboratory Practice guidelines of the United States and international government regulatory agencies, have been reported^{33–35}. United States Pharmacopoeia³⁶ and the British Pharmacopoeia³⁷ have also reported the general qNMR as a primary ratio method of measurement in which the

analyte can be correlated directly to the calibration standard and hence to be compendial. The widespread acceptance of NMR for quantitative measurements can be attributed to specific advantages like, (i) the possibility to determine structures at a molecular level, (ii) no need for intensity calibrations in case of determination of ratios (signal area is directly proportional to the number of nuclei), (iii) relatively short measuring times, (iv) its non-destructive character, (v) no prior isolation of the analyte in a mixture, which means rather easy sample preparation and handling and (vi) the possibility of a simultaneous determination of more than one analyte in a mixture.

We have absolutely focused our study on the phosphorous containing drugs as our research plan included the development of qNMR method that will target ^{31}P nuclei in the drug under study for the quantification purposes. Solution state qNMR technique will be utilized to establish the kinetics of the drug release in the simulated human body fluids whereas, solid state qNMR spectroscopic technique will help us determine the encapsulation efficiency of the nano-formulation. The concomitant theoretical discussion to corroborate our hypotheses is presented herein.

Finally, through these quantitative analysis, we aim to provide medical field with a better understanding of the drug loading and drug releasing profiles of the large number of phosphorus containing drugs. To summarize our broader perspective, we strongly believe that our results will aid scientific community, build improved versions of drug delivery systems that will further decrease the probability of infection or spreading of the disease in human body. In due course, the use of more efficient drug delivery systems will result in saving greater number of human lives. We are quite determined to take the battle to the doorsteps of the life threatening diseases such as AIDS, hepatitis B, cancer, Alzheimer and

thus, we are confident that our research contribution will benefit significantly to the entire human society.

General Research Approach

We envisioned and meticulously designed this research project with certain objectives in mind, presented as follows-

1] Development and validation of a method for quantitative analysis of drug molecules containing ^{31}P nuclei utilizing solid state and solution state NMR spectroscopic techniques: We focused our study on phosphorus containing drug molecules which have proven their effectiveness against AIDS. A method was required to be developed and validated that would aid us in carrying out direct and real time quantitative analysis of the drug by using nuclear magnetic resonance spectroscopic technique which will target the ^{31}P nuclei in the molecule under study.

2] Application of solution state NMR spectroscopic technique to establish kinetics of drug release from nano-formulation in various body fluids: It is crucial to establish the profile of drug release from its nano-formulation encasing *in vitro* and hence, solution state qNMR spectroscopy was implemented to serve the purpose. The release study was carried out in several human body fluids such as vaginal & seminal fluids, plasma etc.

3] Application of solid state NMR spectroscopic technique to determine the encapsulation efficiency of a drug and nano-formulation pair: A variety of nano-formulations was used to encase the drugs under study and hence, we were also interested to learn the actual amount of a drug that gets encased in certain type of nano-formulation. Solid state NMR spectroscopy was put to use to determine the encapsulation efficiency of the nano-formulation.

4] Investigation of phosphorus containing drugs that have proven ability in the treatment of the four direst diseases of current era by utilizing proposed qNMR spectroscopy: We commenced our studies by choosing to investigate a phosphorous containing drug- Tenofovir (TFV) which has been widely utilized in the treatment against AIDS. We have taken into consideration the proven effectiveness of a specific type of spray dried, mucoadhesive, pH sensitive nano-formulations that will serve as an encasing for TFV. We are interested in learning the rate of *in vitro* release of TFV in various human body fluids as well as the amount of TFV in solid form, encapsulated in the nano-formulation during the various stages of encapsulation process. We have been effectively implementing both solution state and solid state NMR spectroscopic techniques. The respective results obtained on *in vitro* release of TFV in vaginal simulated fluid (VFS) are discussed herein. Results obtained on encapsulation efficiency of a particular nano-formulation under study with respect to TFV are also presented.

Previously, Zhang et al.³⁸ developed and validated for the first time ¹H solution state NMR method to perform a real-time detection and quantification of Tenofovir. The drug release profile was established in VFS and VSFS by integrating the two peaks ($\delta = 8.00$ & 8.09 ppm) generated from the aromatic protons in Tenofovir to quantify its respective amount. Their results have demonstrated a good sensitivity as well as specificity that allowed the direct quantification of *in vitro* Tenofovir release from a spray-dried mucoadhesive and pH-sensitive MS formulation based on polymethacrylate salt without the membrane diffusion technique.

Taking into consideration of our own research interests both solution state and solid state NMR spectroscopic techniques were utilized in order to obtain quantitative

measurements of Tenofovir which is at the core of our studies. Hence, in this study we implemented a real time ^{31}P solution state NMR method to be a simple, rapid and precise way to quantify the *in vitro* release of Tenofovir from an encapsulated nanoparticle formulation. We also quantified Tenofovir in a solid form encapsulated inside of nanoparticle formulation by utilizing ^{31}P solid state NMR spectroscopic method in order to obtain encapsulation efficiency. The presence of a single phosphorous atom in Tenofovir was put to the advantage of our analysis. A single peak produced in NMR spectra, exclusively indicative of this phosphorous with natural isotopic abundance of 100% allowed high signal-to-noise (S/N) ratio and thus will be directly proportional to the amount of Tenofovir.

One of the very important fundamental aspect of qNMR is that the signal intensity for a compound X (I_x) is directly proportional to the number of nuclei (N_x) producing the NMR signal³⁴.

$$I_x = K_s N_x \quad (K_s \text{ is an independent spectrometer constant}).$$

Usually the NMR signal of a single substance consists of several resonance lines. However, Tenofovir is observed to produce a specific single resonance line corresponding to its single phosphorous atom at $\delta = 15.7$ ppm. Therefore, either the raw integrated signal (I_x) or a ratio of relative integrated peak areas for two compounds X and Y (I_x/I_y) could be used to quantify a molecular concentration. If multiple ^{31}P NMR experiments are performed, K_s being a spectrometer constant across the spectrum, the relative integrated signal area is equivalent to the concentrations. In our project, the integrated peak area of the phosphorous in Tenofovir was used to estimate the amount of drug.

The determination of relative area ratios I_x/I_y is the easiest way to obtain quantitative results. For ^{31}P single pulse NMR experiments with correct acquisition parameters K_s is the same constant for all resonance lines within the same spectrum, such that it cancels for the ratio-

$$\frac{I_x}{I_y} = \frac{N_x}{N_y}$$

The molar ratio N_x/N_y of two compounds X and Y can be calculated straightforward using-

$$\frac{n_x}{n_y} = \frac{I_x N_y}{I_y N_x}$$

Consequently, the amount fraction of a compound X in a mixture of m components is given by-

$$\frac{n_x}{\sum_{i=1}^m n_i} = \frac{I_x/N_x}{\sum_{i=1}^m I_i/N_i}$$

without any need to consider the solvent signal in which the mixture is dissolved as the only sample preparation step. For the purity determination of a substance an internal standard with known purity is needed. The purity of the analyte P_x can be calculated as follows-

$$P_x = \frac{I_x N_{std} M_x m_{std}}{I_{std} N_x M_{std} m} P_{std}$$

Here, M_x and M_{std} are the molar masses of the analyte and the standard, respectively, 'm' the weighed mass of the investigated sample, m_{std} and P_{std} are the weighed mass and the purity of the standard and N_{std} and I_{std} correspond to the number of spins and the integrated signal area of a typical NMR line of the standard, as described above.

In our study, integrations of the ^{31}P peak of TFV will be used to quantify the amount of TFV in various media under study. The linewidth of NMR signal directly depends on T_2 (spin-spin relaxation time) which varies from different molecules ($\text{Linewidth} = (T_2)^{-1}$). T_2 is usually very small for large molecules such as polymers or proteins, which gives rise to very broad peaks. Therefore, if TFV would be free in the solution, the phosphorous signal could be easily detected. However, if TFV would be encapsulated inside the polymer, the peak generated from TFV will be very broad because of the slow tumbling.

This whole project was a collaborative effort that was carried out congenially by Department of Chemistry, UMKC and School of Pharmacy, UMKC. Syntheses of spray dried, mucoadhesive, pH sensitive nano-formulations took place at School of Pharmacy, UMKC whereas, Department of Chemistry, UMKC was responsible for the quantitative solid state and solution state NMR spectroscopic experimentation to establish kinetics of drug release and encapsulation efficiency.

PROJECT-1

Real-Time Analysis of Tenofovir Release in Biological Fluids Using Quantitative Phosphorus (³¹P) Nuclear Magnetic Resonance Spectroscopy

Introduction

AIDS undoubtedly remains the deadliest epidemic of our time. WHO/UNAIDS/UNICEF global report of 2011 has estimated an average of 2.7 million new infections and 1.8 million AIDS related deaths in 2010 whereas, the report of 2013 estimated 35.3 (32.2–38.8) million people living with HIV in 2012. Since its discovery, AIDS has yet caused an estimated 37 million deaths worldwide³⁹. HIV is a single stranded RNA retrovirus responsible for AIDS. It uses reverse transcriptase enzyme to replicate single stranded DNA in a host cell through the process of reverse transcription. Body fluids such as semen, vaginal fluid and blood are the crucial media for transmitting HIV. There is yet no cure or vaccine invented. The five major types of drugs are usually used in combination, to treat HIV infection. One of these types of drugs known as ‘reverse transcriptase inhibitors’ (RTI) have been specifically designed to disrupt the process of reverse transcription and thereby suppresses the growth of HIV. A study has shown that combinations comprising of three drugs from at least two different types can slow the course of the disease and may lead to a near normal life expectancy. This type of combination treatment is referred as anti-retroviral therapy (ART), combination anti-retroviral therapy (cART) or highly active anti-retroviral therapy (HAART)⁴⁰. Since 2001, expanded access to antiretroviral therapy and declining incidences of HIV infection have led to a steep fall globally by 33% in the number of adults and children dying from HIV-related causes³⁹.

Reverse transcriptase inhibitors, further categorized in three forms consist of their respective nucleoside and nucleotide analogues (NRTI & NtRTI) and non-nucleoside reverse transcriptase inhibitor (NNRTI). In 1987, US FDA approved the first effective therapy against HIV which was the nucleoside reverse transcriptase inhibitor⁴¹. Since then number of drugs have been synthesized under RTI class. Tenofovir (TFV), a drug marketed by Gilead Sciences (trade name Viread) belongs to the category of NtRTI has proven to be effective against HIV as it blocks the reverse transcriptase enzyme^{42,43}. It is administered as the fumarate salt of its disoproxil prodrug called as Tenofovir disoproxil fumarate (TDF) and alafenamide prodrug called as Tenofovir alafenamide fumarate (TAF).

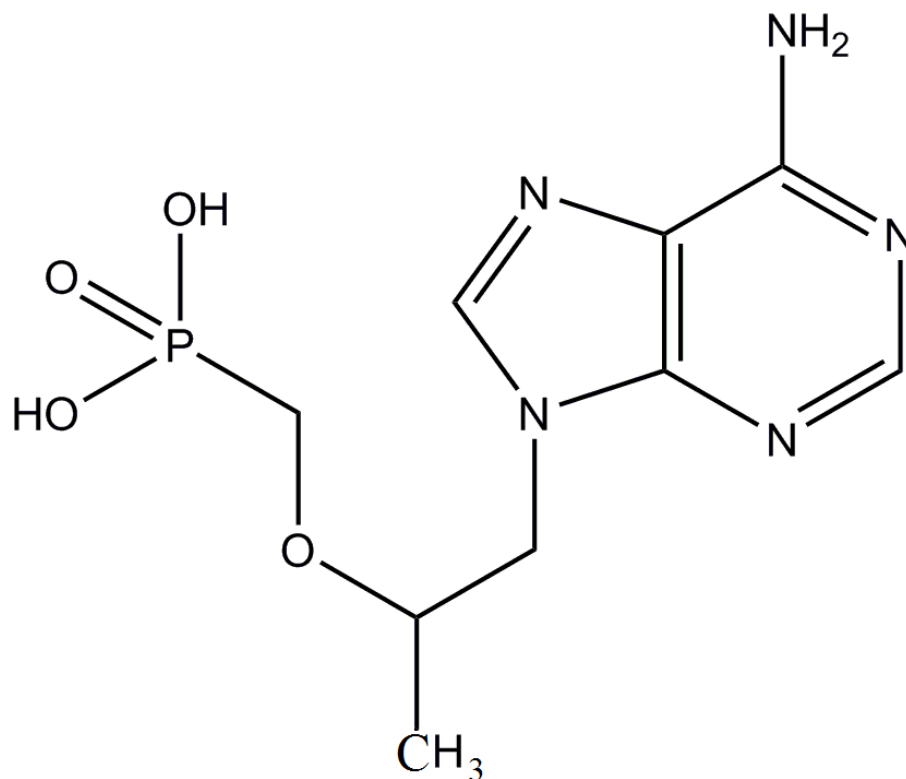


Figure 2.1. Tenofovir molecule.

The recommended oral dose (tablet form/powder form) of {[(2R)-1-(6-amino-9H-purin-9-yl)propan-2-yl]oxy}methyl phosphonic acid, also known as Tenofovir in adults is 300 mg/day. Tenofovir gets eliminated from patient's body by renal elimination. Pharmacokinetic studies following oral administration have shown the oral bioavailability of Tenofovir to be 39% along with food and 25% in fasted state based on urinary recovery data and intravenous data in patients⁴⁴. Certain adverse effects such as lactic acidosis and liver problems are commonly incorporated with oral route with typical symptoms including stomach and muscle pain, nausea, headache, diarrhea and flatulence⁴⁵. The treatment of HIV disease was realized to be quite difficult considering the problems associated with delivery of therapeutic compound to the target site. As oral administration of Tenofovir proved to be less efficient as a drug delivery method, the urgent need for alternative pre-exposure prophylaxis (PrEP) methods is a self-indicative of antiretroviral therapy being still far from curing the disease and a successful HIV vaccine is yet to be developed.

The idea of PrEP methods though started with the oral application of antiretroviral drugs was later focused on the vaginal/rectal application of anti-HIV substances, known as microbicides which are currently the principal focus for HIV prevention strategies^{46,47}. To the date a great variety of HIV microbicides candidates have been studied and tested in clinical trials for their safety and microbicidal effects⁴⁸⁻⁵¹. Infections caused by HIV and other enveloped viruses and sexually transmitted pathogens can be prevented by these microbicides which are the agents used topically within the vagina or rectum. In terms of formulation, a lot of the emphasis has been put on to the first generation gel formulation. According to some of the recent studies Tenofoir is approved as a microbicide in its

effectiveness and safety for the prevention of HIV infections and its formulations as solid-lipid nanoparticles, vaginal gel, and vaginal ring have already been developed⁵²⁻⁵⁷.

Recently, 1% vaginal gel formulation of Tenofovir has been developed. It has been proven effective in clinical trials as, HIV incidence was reduced by 54% in the high gel adherence (>80%) group⁵². In the light of this promising results emanated the prospect of a possible total protection against HIV, if a sustainable concentration of the active drug can be maintained. Unfortunately, this topical gel formulation was observed to suffer from several disadvantages such as leakage, poor patient compliance and the most significant one being its low retention time within the vaginal cavity. Thus, the coital dependence not only proved to limit the effectiveness, acceptability and adherence of aqueous gel system but also demanded a high dosing frequency⁵². These limitations compelled a microbicide formulation that could be administered in a coital independent fashion to become an ideal prevention strategy against sexually-acquired HIV.

The requirement to overcome the practical limitations pushed the scientific study in a direction to prepare a formulation that essentially possess high vaginal retention time and can release a high dose of microbicide when sexual intercourse occurs. Nano-formulations such as hydrogels, mucin like polymers and spray dried mucoadhesive microspheres based on polymethacrylate salt were invented and reported. These topical microbicide formulations designed for vaginal delivery are site retentive, pH and temperature sensitive, non-cytotoxic and non-immunogenic to vagina epithelium and vaginal flora and can be triggered to burst release in the presence of human semen⁵⁸⁻⁶³. Collectively, these data presented potentially effective strategy for intravaginal delivery of microbicides for the prevention of HIV transmission. Impressive facts discussed so far thus

pushed us to choose Tenofovir which contains single phosphorus atom to obtain the *in vitro* kinetic release profile in seminal & vaginal fluids, plasma and blood along with its encapsulation efficiency in various nano-formulations by implementing ^{31}P -qNMR spectroscopy.

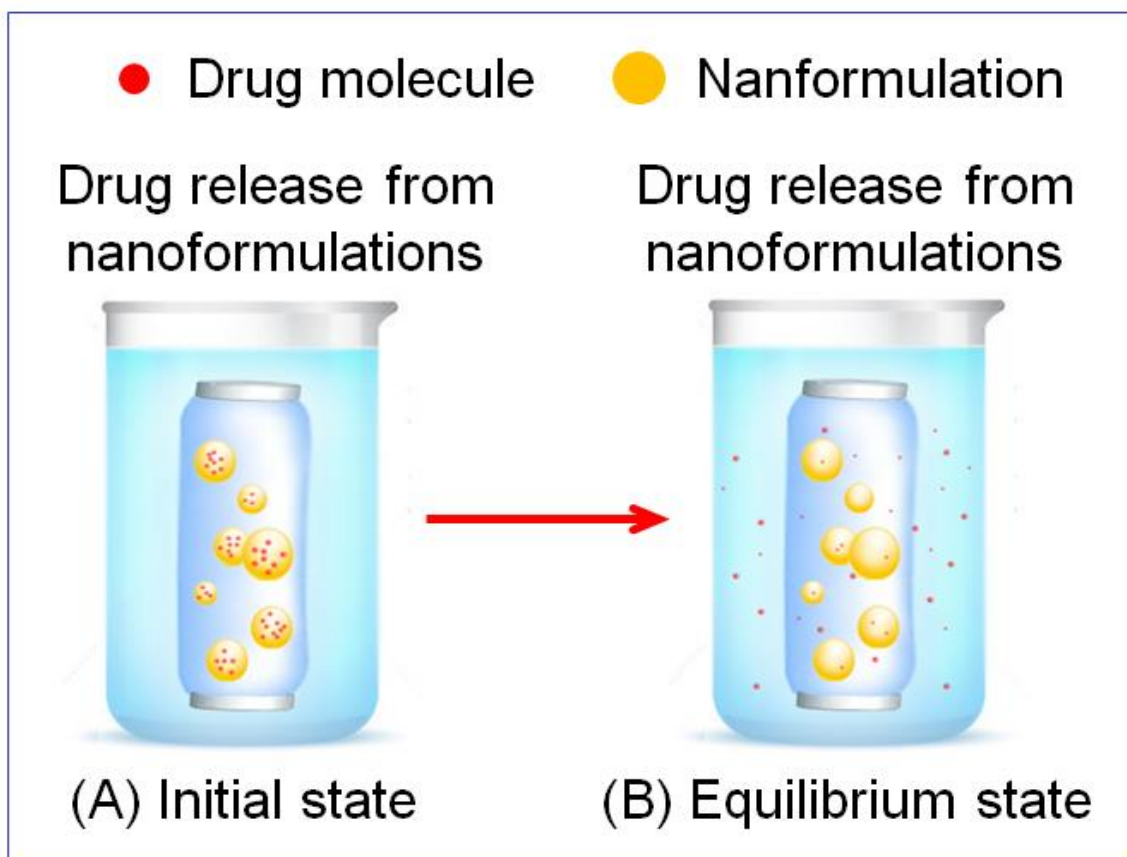


Figure 2.2. Dialysis membrane method of quantitative *in vitro* drug release analysis from drug formulations in biological media. (A) Initial state. (B) Equilibrium state.

Accurately quantifying the amount of drug being delivered in the human body is a crucial requirement of any drug development process. Most quantitative techniques such as liquid chromatography (LC) and UV-Vis spectrometry require a dialysis membrane to separate the free drug released from their formulations and to determine the drugs in biological fluids. In the dialysis method, the drug formulation is enclosed in a dialysis bag with appropriate molecular weight cutoff (MWCO) membrane in the donor compartment (Figure 2). A sink condition has to be maintained to separate the drug in donor compartment with respect to the receiving compartment. The amount of drug detected in the receiving compartment is generally considered as the amount of drug released from the drug formulations. However, the experimental results of release quantification methods utilizing dialysis membrane can be misleading since most of the times donor compartment does not satisfy the sink condition⁶⁴⁻⁶⁶. In addition, dialysis method is not capable of direct and real-time quantification of the drug release kinetics. Moreover, in dialysis approach the drug release is governed by the partition between two phases separated by the dialysis membrane⁶⁴⁻⁶⁶ (Figure 3). There are some further limitations of the dialysis membrane method (Table 1) that makes it a less than ideal choice in drug quantification and depending on the drug/carrier systems, significant errors may be introduced. For example, there are several process parameters such as diffusion coefficients, pH, temperature, time, concentration, volume of release media, dialysis membrane surface area and thickness, molecular charges, and stirring speed that can potentially affect the dialysis rate⁶⁴⁻⁶⁶ and the quantification of *in vitro* drug release kinetics. Hence, there is a critical need for developing a direct, real-time, and specific method for the quantification of drug release kinetics in bulk and in its nanoformulations.

Table 2.1 Considerations and limitations in dialysis method of drug quantitation.

Parameters	Consideration	Limitation
Volume of the release media	Volume of media inside the dialysis membrane should be at least 6- to 10-fold less to provide a driving force for drug transport to the outside and maintaining sink conditions.	Concentration gradient between the inside and outside of the dialysis bag may affects the observed release rate.
	Outer media must be agitated to prevent the accumulation of polymer degradants, especially for the protein formulations.	Agitation can affects the release kinetics of drug formulations.
	Two/three media changes over the period of 12-24 hrs.	Time to equilibrate is prolonged if the bulk media is not stirred due to the formation of unstirred water layer).
Dialysis membrane surface	Appropriate membrane surface molecular weight cutoff and surface area must be selected.	Achievement of equilibration with the outer media is slow if membrane surface area is small or too quick if surface area is very large.
Drug diffusion process	Two step process: diffusion of drug from the carrier to the interior of the dialysis membrane and then to the reservoir.	Due to two diffusion barriers, the measured drug release kinetics is slower, and depending on the drug/carrier systems, significant errors may be introduced.
	Dialysis bag with a higher drug concentration require a longer time for the drug to diffuse out of the bag.	Cannot be used if the drug binds to the polymer or dialysis membrane.
Process variables	Several process variables has to be optimized including the pH, temperature, time, concentration, volume, stirring speed, sampling time).	Many process factors affecting the dialysis rate (diffusion coefficients, pH, temperature, time, concentration, volume, membrane surface area, thickness, molecular charges, stirring speed).

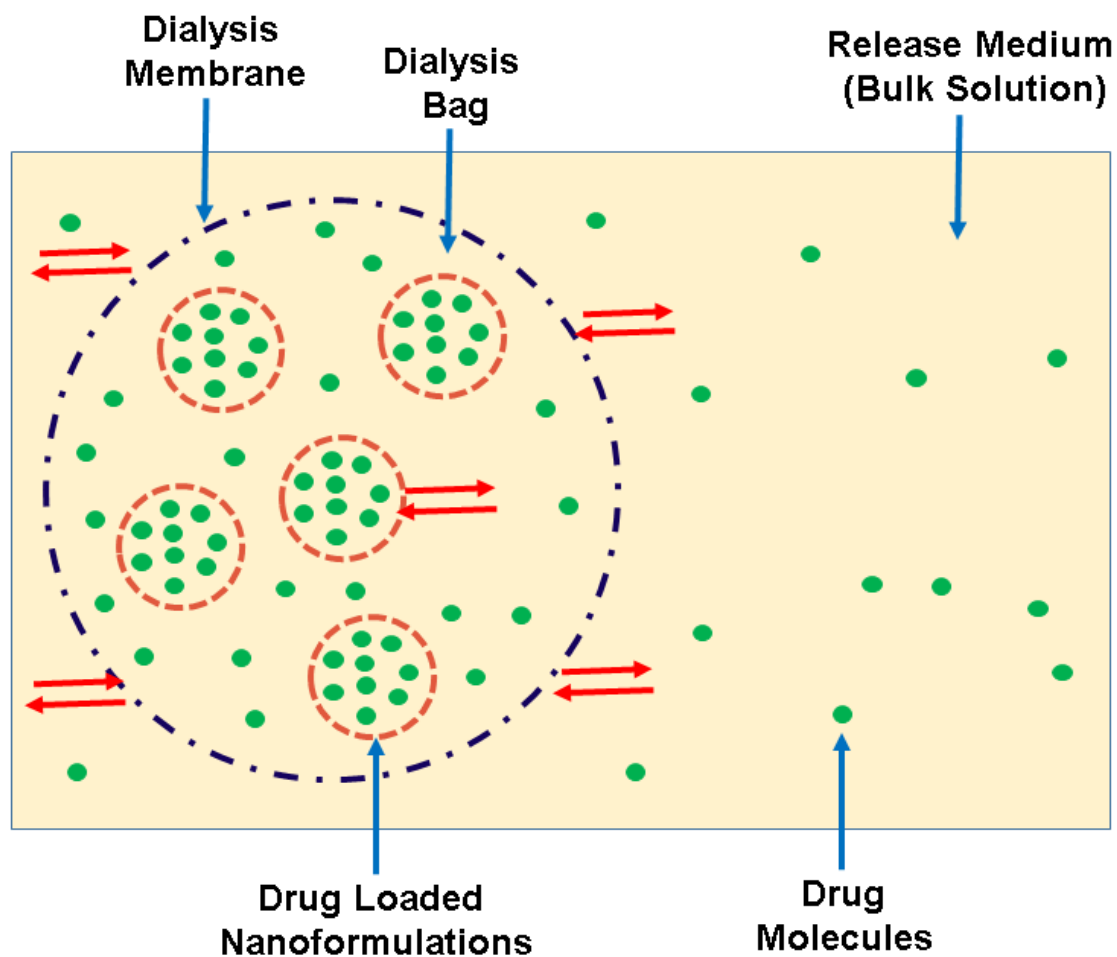


Figure 2.3. Membrane partitioning in dialysis method of quantitative *in vitro* drug release analysis from drug formulations in biological media.

Recently, Zhang et al., have published a proton (^1H) NMR method³⁸ to quantify an anti-HIV topical vaginal microbicide drug (Tenofovir: TFV) in vaginal fluid simulant (VFS) and in a mixture of vaginal and seminal fluid simulant (VSFS) buffers. The authors have compared the NMR method with the dialysis membrane method to analyze the drug release pattern by high performance liquid chromatography (HPLC) assay. Although, the ^1H -NMR method was fully validated and well analyzed, the requirement of using deuterated solvents

in ^1H -NMR spectroscopy makes this method less economic and not easily feasible routinely in biological fluids analysis.

Carbon NMR (^{13}C -NMR) spectroscopy is another commonly used NMR approach. The width of the ^{13}C -NMR spectrum is wider than that of the ^1H -NMR spectrum. This is due to the fact that the carbon resonance is 0-220 ppm relative to the tetramethylsilane (TMS) standard, while the resonance of protons is 0-12 ppm. It thus makes it possible to be able to identify the distinguishable peaks of each carbon atom. However, most of the drugs and release media components contain more than one carbon, some of these carbons are in very similar environments. As a result, the overlap of the ^{13}C signal is inevitable, especially in the relatively large compound. Also, if ^1H -NMR is compared with ^{13}C -NMR while considering their respective NMR active nuclei then the abundance of ^{13}C is very low (~1.1%) and the use of higher sample concentrations or amount is required. The implementation of ^{13}C -NMR spectroscopy thus proves to be a drawback as it is less economical in routine analysis especially for *in vivo* assays⁶⁷.

The ^{31}P -qNMR is an excellent technique for studying phosphorus containing compounds and typically gives rise to single sharp peak that corresponds to the single phosphorous atom being a part of the drug molecule and is the case in most of the drugs. The ^{31}P nucleus is useful in NMR spectroscopy due to its relatively high gyromagnetic ratio (17.235 MHz T^{-1}) in comparison to that of ^{13}C (10.705 MHz T^{-1})^{67,68}. Furthermore, ^{31}P has a 100% natural isotopic abundance⁶⁷. Moreover, like the ^1H nucleus, the ^{31}P nucleus has a nuclear spin of $1/2$, which makes spectra relatively easy to interpret. The major advantage of ^{31}P -qNMR compared to ^1H NMR is that there is no need of expensive deuterated solvents, which simplifies the sample preparation process.

Therefore, considering the above aspects, in this study, a rapid, specific, and direct ^{31}P -qNMR method for the real-time quantification of TFV in vaginal fluid simulant (VFS), semen fluid simulant (SFS), and human plasma was developed and validated. TFV is a nucleotide reverse-transcriptase inhibitor under the category of antiretroviral drugs. It is a weakly acidic, water-soluble, stable, and low molecular weight (MW: 287.213 Da) drug^{69,70}. TFV is a Food and Drug Administration (FDA) approved microbicide (in its pro-drug form) and has been proven to prevent HIV transmission through the vagina⁵². The developed NMR method of TFV was further applied for the real-time quantification of TFV in its nanofiber (NF) based formulations in these biological fluids.

Experimental and Theoretical Methods

1] Chemicals

Tenofovir (TFV) was purchased from Beijing Zhongshuo Pharmaceutical Technology Development Co. Ltd. (Beijing, China). Chitosan (MW 50-190 kDa), thioglycolic acid, poly (ethylene oxide) (MW 900 kDa), were purchased from Sigma Aldrich (St. Louis, MO, USA). Sodium triphosphate penta-basic (TPP) was from Thermo Fisher Scientific (Pittsburgh, PA, USA). Poly (DL-lactide) was obtained from Purac Biomaterials (Lincoln, IL, USA). Pooled normal human plasma was purchased from Innovative Research, Inc., (Novi, MI, USA). Deionized water for all the experiments was obtained through a Millipore Milli Q water purification system (Millipore Corp., Danvers, MA, USA). All other chemicals were of analytical grades and used as obtained from the suppliers. The pH of all the solutions was adjusted using either hydrochloric acid (HCl) or sodium hydroxide (NaOH) solutions prepared accordingly and measured using a

SevenEasy pH meter (Mettler Toledo, Schwerzenbach, Switzerland) under ambient temperature conditions (23-24°C).

2] Preparation of Multilayer Microparticles (MPs)

2a] Synthesis of Hyaluronic Acid Nanofibers (HA-NF)

The respective microparticles were synthesized by a published method⁶³.

2b] Synthesis of Chitosan Nanofibers (TCS-NF)

The TFV loaded chitosan NFs were prepared by using a coaxial electrospinning method^{71,72}. Chitosan is a water-soluble, linear amino-polysaccharide, which is composed of 2-amino-2-deoxy- β -D-glucan combined with glycosidic linkages. Chitosan exhibits many advantages in formulation development, including biocompatibility, biodegradability, and low-immunogenicity^{73,74}. Chitosan-thioglycolic acid conjugate was synthesized by introducing thioglycolic acid to chitosan via amide bond formation mediated by a carbodiimide⁷³. Briefly, Chitosan-thioglycolic acid conjugate was mixed with PLA in a ratio of 1:1 (w/w) and used as the shell material. A blend of TFV and PEO was used as the core material. A coaxial spinneret was used to allow for the injection of core solution into the shell solution at the tip. An electrospinning system was used for NF production. The core and shell composite solutions were placed in two glass syringes (Becton, Dickinson and Company, NJ, USA), and pushed by two syringe pumps (Cole-Parmer Instrument Company, IL, USA) with the feeding rate of 0.05 ml/h for the two solutions. A high voltage power supply (Gamma High Voltage Research, Inc., FL, USA) was used to provide a voltage of 15 kV to the nozzle. The chitosan NFs were collected onto an aluminum collector connected to the ground electrode. The NFs mat was peeled from

the collector, vacuum dried at room temperature and stored in a vacuum desiccator until further uses.

3a] Quantitative Solution State ^{31}P -qNMR Spectroscopic Analysis of TFV

The experimental procedure for solution state ^{31}P -qNMR spectroscopy were carried out on a Varian (Palo Alto, California) 400 MHz spectrometer with a Varian two channel probe. The V_{nmrj} software (version 2.2) was used to process the data. Preliminary analyses were performed to get the optimized NMR conditions. Typically, the spectra were acquired with a 45° pulse length that was $5.05 \mu\text{s}$. The relaxation delay and the number of scans were seen at 5 sec and 256, respectively. Relaxation delay is considered to be one of the most important parameters in qNMR assays and in order to make most nuclei fully relaxed, 5 times of the maximum T_1 (Spin-lattice relaxation time) is required. The T_1 of the phosphorous atom of TFV was 5 s that typically requires up to 25 s ($5 \times T_1$) for relaxation delay time. However, as the experimental parameters were fixed between all spectra (specifically the number of scans), the effect of short relaxation delay was consistent in all experiments, eventually making the integral calculations also consistent. The short relaxation delay was primarily applied because of the limited acquisition time between for each experiment during the *in vitro* drug release study. Shimming (adjusting the resolution of the NMR signals by optimizing the homogeneity of the magnetic field) was applied to every sample in order to obtain a similar linewidth in each spectrum. Baseline correction, phase adjustment, and integral calculation was carried out manually using MestReNova Lite 5.2.5-4731 software (Escondido, California). The assay was performed in triplicate at 37°C and spinning speed of 20 Hz. Kinetics experiments were applied where intensities of

the ^{31}P peak of TFV was utilized to quantify the amount of TFV released from nano-formulations. The total time for one release experiment was 12 hours.

The linewidth of NMR signal directly depends on T_2 (spin-spin relaxation time) which varies for different molecules (Linewidth = $(T_2)^{-1}$). T_2 is usually very small for large molecules such as polymers or proteins, which gives rise to very broad peaks. Therefore, if the drug is free in the solutions, the phosphorous signal can be easily detected. However, if drug is encapsulated inside the polymeric formulations, the peak generated from drug could be very broad because of the slow tumbling. The NMR spectra of free TFV was observed to produce a specific single resonance line corresponding to its single phosphorous atom at ~15 ppm. The integrated peak area of the phosphorous atom in TFV was used to estimate its amount.

3b] Sample Preparation for Solution State ^{31}P -qNMR Spectroscopic Analysis

VFS (pH 4.2) and SFS (pH 7.6) will be prepared individually according to published method^{75,76}. Serial dilutions of stock solution with the same diluents will lead to the sample solutions in the concentration range of 0.1–5 mM for ^{31}P NMR analysis. TFV samples were prepared at the concentrations of 0.1 - 5.0 mM in VFS, SFS, and human plasma. However, a commercially available human plasma was used. A stock solution of TFV (1 M) in respective biological fluids was diluted with the same fluids to yield the solutions in the above concentrations range. The samples were analyzed by taking 500 μL of each sample in a 5-mm outer diameter NMR tubes (Wilmaad-LabGlass, Vineland, NJ, USA) and analyzed using the ^{31}P -qNMR method. Orthophosphoric acid (OPA: 85% v/v) was used as the external reference compound.

4] Method Validation for Solution State ³¹P-qNMR Spectroscopic Analysis

Seven different samples with TFV concentrations from 0.075 to 5 mM were selected to construct the standard curves of the method. Three concentrations (0.2, 0.75, and 5 mM) were utilized to validate the method according to International Conference of Harmonization (ICH Q2:R1) guidelines⁷⁷. The variation within the ³¹P NMR peak areas were presented as percentage of relative standard error (%RSE) for each validation parameters.

4a] Specificity

Specificity is typically a required precondition for qNMR and is hence always tested prior to the other validation parameters. The specificity of the method measures the proportion of positives that are identified correctly, it was determined by analyzing the potential interference of formulation/biological fluid components peaks to the TFV peak. The ³¹P NMR spectrum of standard TFV solution in VFS/SFS/human plasma was compared with that of drug-free VFS/SFS/human plasma as well as TFV loaded nanoformulations suspended in these biological fluids to ensure the specificity of the NMR method. All the measurements were carried out at 37°C temperature.

4b] Linearity and Calibration Curve

Linearity is the ability of the method to elicit test results that are directly proportional to the analyte concentration within a given concentration range. A calibration plot was prepared in the concentration range of 0.2 - 5.0 mM in VFS, SFS, and 0.3 - 5.0 mM in human plasma by analyzing the peak areas of ³¹P in each TFV solution. The intercept, slope, and correlation coefficient (*R*) values were determined by linear regression analysis. All the measurements were carried out at 37°C temperature.

4c] Limit of Quantification (LOQ) and Limit of Detection (LOD)

The LOQ and LOD values represent the lowest quantity of a substance that can be distinguished from the absence of that substance, and the concentration at which quantitative results can be reported with a high degree of confidence within a stated confidence limit, respectively⁷⁷. The LOQ and LOD values were determined using the signal-to-noise (S/N) ratios of 10:1 and 3:1, respectively. All the measurements were carried out at 37°C temperature.

4d] Precision and Accuracy

Precision and accuracy represent the level of measurement that yields consistent results (no random errors) and true result (no systematic errors) when repeated, respectively. Accuracy is the percent of therapeutic molecule recovered by the assay. Accuracy of the ³¹P-qNMR method was calculated for three quality control (QC) samples (0.2 mM, 0.75 mM, and 5.0 mM) in VFS, and SFS, and 0.3 mM, 0.75 mM, and 5.0 mM in human plasma. The results were reported as percent mean recovery. Precision was assessed using the same QC samples and reported as percent relative standard error (%RSE). The intra-day (within-day) and inter-day precision and mean recovery (over a period of one week) were determined. All the measurements were carried out at 37°C temperature.

4e] Robustness

The robustness of an analytical assay is its ability to remain unaffected by small variations in the assay parameters. The following changes in the solution state ³¹P-qNMR method parameters were examined: temperature (in °C), relaxation delay (in seconds), and 45° pulse width (in μs). The variation in the ³¹P NMR peak area of TFV at the concentration

of 5.0 mM was calculated and the acceptance criteria of %RSE < 2% was considered for each parameter.

4f] Repeatability

Repeatability expresses the precision of the method under the same operating conditions over a short time interval. The repeatability of the method was performed by analyzing three QC concentrations of TFV (n = 3), three times a day in VFS, SFS and human plasma.

5] Analysis and Characterization

5a] Real Time *in vitro* Drug Release Analysis of Chitosan NFs using ³¹P-qNMR (Direct) Method

Chitosan NFs loaded with TFV at the concentration of 1 mg/mL were dispersed in VFS, SFS and human plasma. The samples were prepared in NMR glass tubes and analyzed by taking 1 mL of each sample using the solution state ³¹P-qNMR method at 37°C with a spinning speed of 20 kHz. The data were collected at different time points in real time measurements up to 12 hours. The percent drug release profile of TFV was measured using a calibration curve of TFV.

5b] *In vitro* Drug Release Analysis of Chitosan NFs using Dialysis Membrane (Indirect) Method

Chitosan NFs at the concentration of 1 mg/mL in VFS, SFS and human plasma were added in the dialysis bag (Spectra/Por Float-A-Lyzer G2, MWCO 3.5-5 KD, Spectrum Laboratories Inc. Rancho Dominguez, CA, USA) were placed into a dialysis tube containing 20 ml of release media. The whole system was kept at 37°C water bath with a shaking speed of 60 rpm. At predetermined time intervals, up to 12 h, 1 mL of the sample

was taken out and replaced by fresh release media to maintain the sink conditions. The concentration of TFV in the dialysis solution was determined by the UV-Vis spectroscopy at the wavelength of 259 nm. Each experiment was run in triplicate ($n = 3$) together with a blank control. The percent cumulative drug release profile of TFV was measured using a calibration curve of TFV in the concentration range of 1 - 10 $\mu\text{g/mL}$ ¹⁸.

5c] *In vitro* Drug Release Kinetics of NFs

The drug release data of TFV loaded chitosan NFs were analyzed by using various *in vitro* kinetic models^{69,78}. The previously described Microsoft Excel add-in DDSolver program⁷⁹ was used for the data modeling. The kinetic models used were zero-order, first-order, Higuchi, Korsmeyer-Peppas, Hixson-Crowell, Weibull and, Quadratic models. The criteria for selecting the most appropriate model were based on the coefficient of determination, (R^2) and the Akaike information criterion (AIC)⁷⁹. The Akaike Information Criterion is a measure of goodness of fit based on maximum likelihood. The selection of an appropriate model was based on a higher R^2 values and lower AIC value.

5d] Statistical Data Analysis

The experimental values were generally presented as mean \pm standard deviation (SD) of triplicate determinations ($n = 3$) unless otherwise mentioned.

Results and Discussion

1] Solution state ³¹P-qNMR Method Validation for TFV Analysis

³¹P had a relatively high gyromagnetic ratio and an isotopic abundance of 100%. Thus ³¹P q-NMR spectroscopy was an analytical technique. ³¹P NMR shifts were primarily dominated by the paramagnetic shielding tensor includes the radial expansion (related to

charge), energies of excited states, and bond overlap. The solution state ^{31}P -qNMR method of TFV was developed and validated according to the ICH guidelines⁷⁷.

The NMR method was found to be linear over the tested concentration range in VFS (Figure 4A), SFS (Figure 4C), and human plasma (Figure 4E) with the R value > 0.999 , (Figure 4). The TFV peaks in VFS, SFS, and human plasma were shown in Figure 4B, Figure 4D, and Figure 4F, respectively. The LOD values of the developed solution state ^{31}P -qNMR method were found to be 0.075 mM (VFS), 0.1 mM (SFS), and 0.2 mM (human plasma), whereas, the LOQ values were 0.2 mM for VFS and SFS, and 0.3 mM for human plasma, respectively. The ^{31}P -qNMR peak of TFV was observed at ~ 15.7 (Figure 5A), ~ 15.1 (Figure 5C), ~ 13.7 (Figure 5E), and ~ 15.7 (Figure 5G) in VFS, SFS, plasma and water, respectively.

Specificity analysis demonstrated the lack of interference peaks between the signal of interest (^{31}P peak of TFV) and any other peak from the components of the VFS (Figure 5B), SFS (Figure 5D), human plasma (Figure 5F), and OPA (Figure 5G), respectively. The chemical shifts in the TFV NMR peak were slightly different (varied between 15.7 to 13.7 ppm) in different biological fluids which might be due to the interactions between the spins of phosphorus groups present in each biological fluids and the associated shielding and deshielding effects. Overall, the results showed that the TFV peak was well separated from all three biological fluid components (Figure 5). The components present in the VFS didn't have any phosphorus groups and that could be the reason no other peak has been observed in the ^{31}P NMR spectra of the blank VFS (Figure 5B). The components present in the VFS didn't have any phosphorus containing groups^{75,76} and that is the reason no other peak has been observed in the ^{31}P NMR spectra of the blank VFS (Figure 5B). However, the

presence of sodium phosphates in SFS^{75,76} showed a peak at ~1.7 ppm (Figure 5D) in blank SFS which had an interaction with the TFV phosphorus group and has been shifted to ~1.25 ppm (Figure 5C). The presence of inorganic hydrogen and dihydrogen phosphates in the plasma⁸⁰ showed the NMR peaks at ~2.5 ppm and in between 0-(-2) ppm (Figure 5F). These peaks have been shifted little bit in the presence of TFV and also had a significant effect on the chemical shift value of TFV (~13.7 ppm) (Figure 5G).

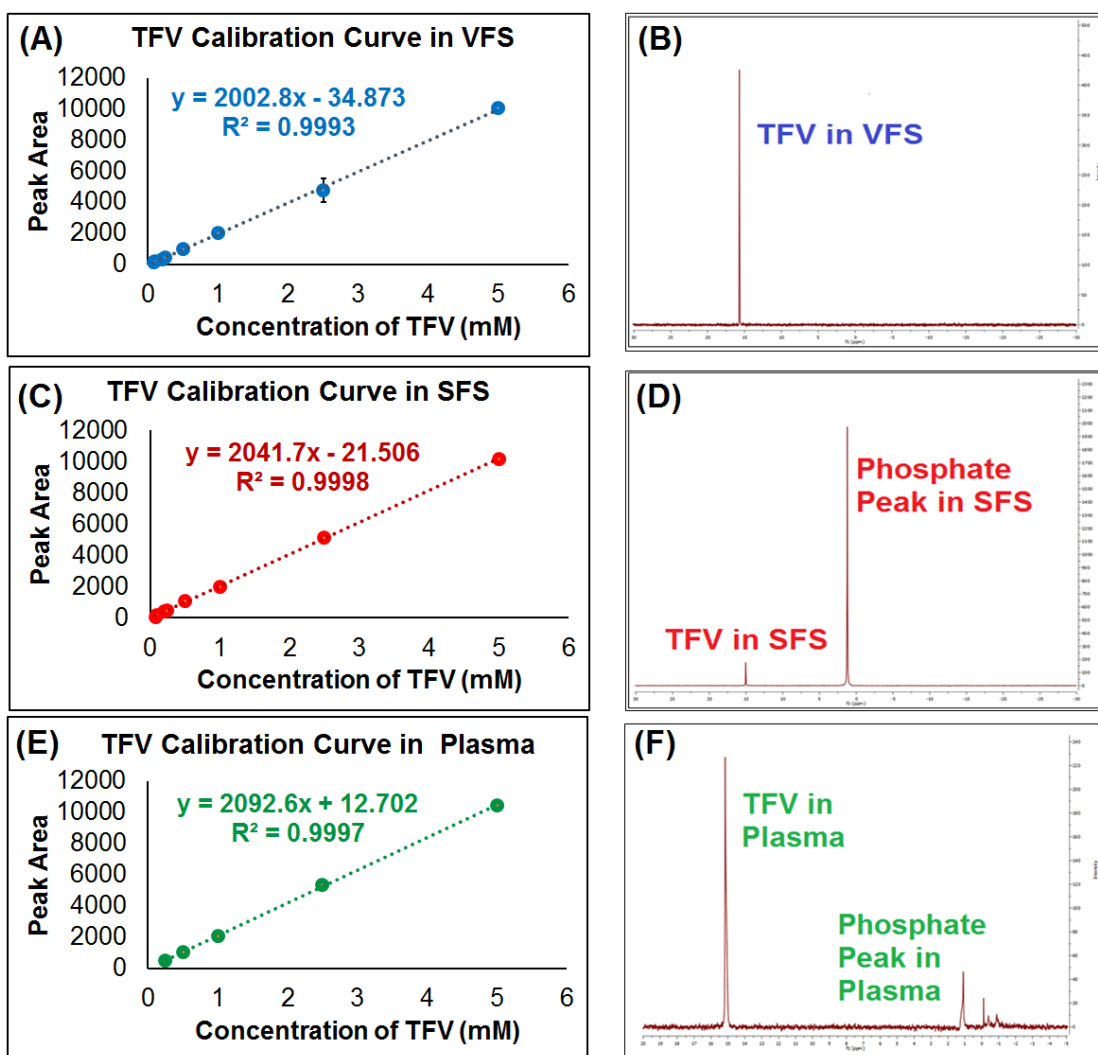


Figure 2.4. Linearity assay of the ³¹P-NMR method in: (A) VFS. (C) SFS. (E) Human plasma. Representative ³¹P-NMR peak of TFV in: (B) VFS. (D) SFS. (F) Human plasma.

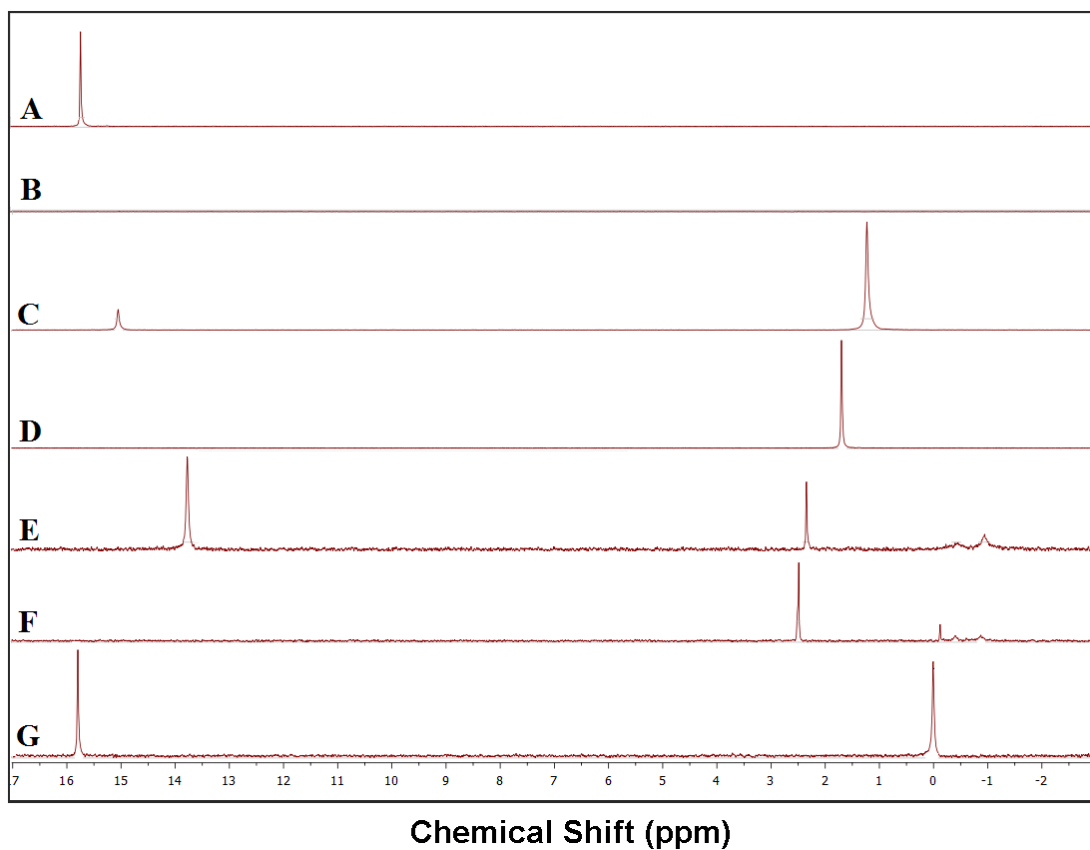


Figure 2.5. Specificity analysis of the ^{31}P -NMR analysis: (A) TFV in VFS. (B) Blank VFS. (C) TFV in SFS. (D) Blank SFS. (E) TFV in plasma. (F) Blank plasma. (G) TFV with OPA in water.

The results of the repeatability showed that the NMR method was reproducible and showed the consistent results in terms of the ppm value and area of TFV (data not shown). The method was accurate with a percent mean recovery value between 90% to 110% (Table 2) and precise as the %RSE values for intra-day, and inter-day precision were less than 2% for all the QC samples tested in VFS, SFS, and human plasma (Table 3). The %RSE for each robustness parameters and tested concentration of 5.0 mM was found to be < 2% (Table 4) and the developed solution state ^{31}P -qNMR method was considered robust.

Table 2.2. Accuracy (mean recovery) data for the ^{31}P -NMR method in VFS, SFS, and human plasma.

Biological Media	Concentration (mM)	Mean recovery \pm RSE (%) (n = 3)		
		Intra-day		Inter-day
		Within-a day	Day-2	Day-3
VFS	0.20	102.8 \pm 2.7	102.1 \pm 1.7	101.2 \pm 1.7
	0.75	96.0 \pm 2.3	99.6 \pm 0.9	97.6 \pm 1.9
	5.00	103.5 \pm 0.2	103.8 \pm 0.3	103.6 \pm 0.3
SFS	0.20	94.7 \pm 1.6	98.9 \pm 1.3	96.1 \pm 1.4
	0.75	95.6 \pm 1.2	101.6 \pm 1.5	93.8 \pm 1.6
	5.00	106.5 \pm 0.3	107.9 \pm 0.2	105.9 \pm 0.2
Human Plasma	0.30	105.2 \pm 2.9	104.6 \pm 2.1	103.5 \pm 2.4
	0.75	96.7 \pm 1.9	96.7 \pm 1.9	94.8 \pm 1.5
	5.00	99.9 \pm 1.8	99.9 \pm 1.8	99.3 \pm 1.9

Table 2.3. Precision data for the ^{31}P -NMR method in VFS, SFS, and human plasma.

Biological media	Concentration (mM)	Precision as %RSE (n = 3)		
		Intra-day		Inter-day
		Within-a day	Day-2	Day-3
VFS	0.20	1.65	1.65	1.04
	0.75	0.44	0.44	1.14
	5.00	0.11	0.11	0.16
SFS	0.20	1.70	1.70	1.49
	0.75	1.25	1.25	1.63
	5.00	0.31	0.31	0.19
Plasma	0.30	1.64	1.22	1.37
	0.75	1.11	1.11	0.81
	5.00	1.05	1.05	1.09

Table 2.4. Robustness analysis data for the ³¹P-qNMR method in VFS, SFS, and human plasma.

Biological Media (TFV Conc. 5mM in each)	Robustness Parameters								
	Temperature (°C)			Relaxation Delay (sec)			45° Pulse Width (µs)		
	% RSE (n = 3)			% RSE (n = 3)			% RSE (n = 3)		
	35	37	39	4.8	5.0	5.2	4.85	5.05	5.25
VFS	0.30	0.43	0.34	0.22	0.43	0.15	0.12	0.43	0.28
SFS	0.17	0.21	0.22	0.24	0.21	0.24	0.15	0.21	0.27
Plasma	0.91	0.98	0.72	0.70	0.98	0.79	0.81	0.98	0.64

2] Application of the developed solution state ³¹P-qNMR method in quantitative real time *in vitro* TFV release analysis from chitosan NFs

The developed solution state ³¹P-qNMR method was applied for the real-time quantification and release profile of TFV from the above chitosan based NFs formulation using electrospinning method (Figure 6A). The SEM images revealed that the chitosan based NFs were successfully formulated (Figure 6B). The mean diameter of NFs was 158.51 ± 59.20 nm (n = 100) (Figure 6C). The drug loading (DL), and yield of chitosan NFs was 14.20 ± 2.12 % w/w, and 63.18 ± 1.16 % w/w, respectively, (n = 3).

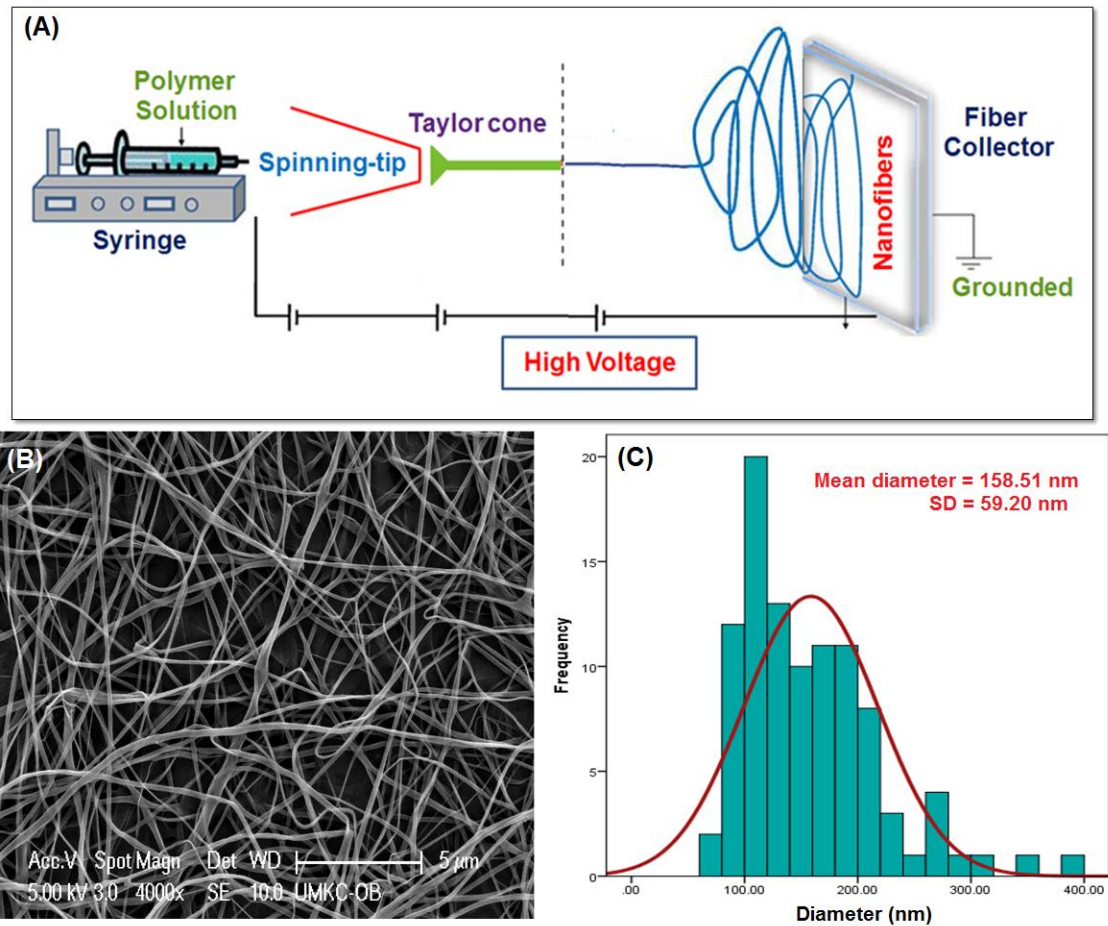


Figure 2.6. (A) Coaxial electrospinning chitosan nanofibers fabrication assembly setup. (B) Surface morphology of chitosan NFs; scale bar, 5 μm. (C) Size distribution histogram of chitosan NFs determined by image analysis software and averaged using at least 100 measurements per group.

The results of the drug release data modeling showed that ~75%, ~72%, and ~70% w/w drug release was observed in case of NMR method in VFS (Figure 7A), SFS (Figure 7B), and human plasma (Figure 7C), respectively. To evaluate the magnitude of potential interference of the dialysis membrane with the quantification of the drug release from

nanoformulations, the concentration of TFV release from the chitosan NFs in the receiving compartment was measured using UV-Vis method. The results showed that only ~47%, ~52%, and ~52% w/w of TFV release was observed using UV-Vis method in VFS (Figure 7A), SFS (Figure 7B), and human plasma (Figure 7C), respectively. The relatively lower drug release (approximately 20% less) observed by UV-Vis method might be due to the interference of dialysis membrane with drug transport to the release media. From the results, it was reasonably speculated that TFV did not achieve equilibrium during the release period analyzed by dialysis membrane method. Therefore, the data obtained for a drug release using the dialysis method will not be accurate if the formulation has a burst release profile and the amount of drug measured in the receiving compartment will be significantly underestimated. The in vitro kinetic modeling of NFs showed that it followed Korsmeyer-Peppas model mostly expect in VFS where it follow the first order model in case of NMR measurements (Table 5). First order model described the amount of drug released by unit of time diminish. Korsmeyer-Peppas model represented drug release from a polymeric system, the value of n characterizes the mechanism of drug release from the formulation. As NF is a cylindrical system, when $n < 0.45$ corresponds to a Fickian transport, $0.45 < n < 0.89$ to non-Fickian diffusion mechanism⁸¹. In all of the three release media, the release mechanism seemed to be different when the release kinetic is determined by NMR and UV-Vis. Therefore, it is misleading to refer to the dialysis membrane method, where further demonstrated the importance of developing a real-time quantification method.

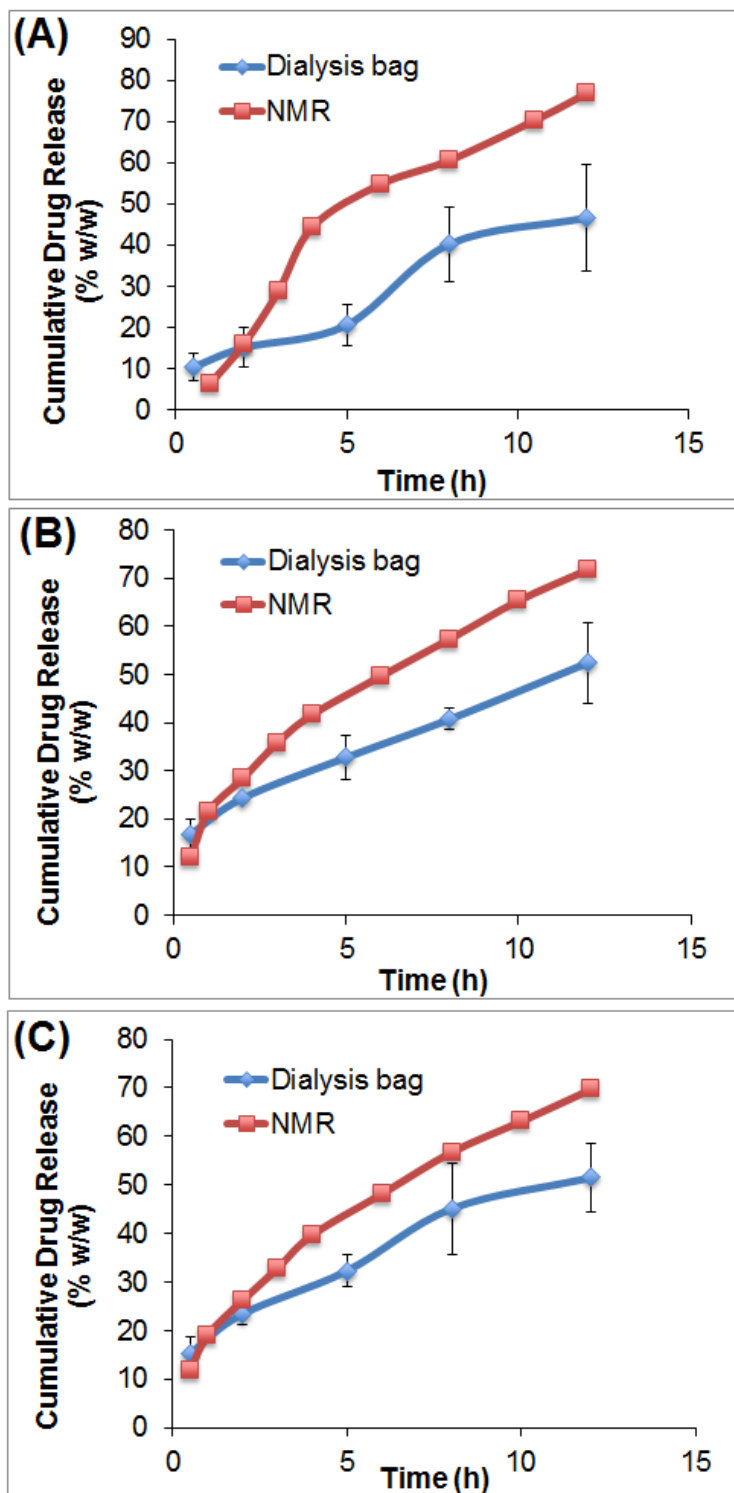


Figure 2.7. Percent cumulative drug release (% w/w) profile of TFV loaded chitosan NFs analyzed by solution state ^{31}P -NMR and UV-Vis spectroscopy assay in A] VFS, B] SFS, and C] Human Plasma.

Table 2.5. *In vitro* drug release kinetics models parameters of TFV loaded chitosan nanofibers.

Biological fluid	Kinetic model	NMR			UV-Vis		
		Parameters	R^2 *	AIC**	Parameters	R^2 *	AIC**
VFS	Zero-order	$k_0=7.227$	0.8763	52.7264	$k_0=2.366$	0.8261	21.8931
	First-order	$k_1=0.121$	0.9759	39.6561	$k_1=0.027$	0.8600	20.8996
	Korsmeyer-Peppas	$k_{KP}=13.608$	0.9544	46.7385	$k_{KP}=5.323$	0.9235	19.8759
		$n=0.711$			$n=0.634$		
	Higuchi	$k_H=20.810$	0.8915	51.6773	$k_H=7.010$	0.9008	19.1790
Weibull	$\alpha=9.077$	0.9772	41.2043	$\alpha=18.888$	0.9200	20.1049	
		$\beta=1.050$			$\beta=0.692$		
SFS	Zero-order	$k_0=7.029$	0.6530	65.2748	$k_0=4.958$	0.3047	33.3906
	First-order	$k_1=0.120$	0.9078	53.3421	$k_1=0.071$	0.5532	31.1992
	Korsmeyer-Peppas	$k_{KP}=20.106$	0.9976	22.4483	$k_{KP}=18.767$	0.9700	19.6941
		$n=0.511$			$n=0.393$		
	Higuchi	$k_H=20.537$	0.9973	21.4897	$k_H=15.149$	0.9314	21.8282
Weibull	$\alpha=4.789$	0.9936	31.3369	$\alpha=4.824$	0.9551	21.7076	
		$\beta=0.697$			$\beta=0.473$		
Plasma	Zero-order	$k_0=6.801$	0.7160	63.3986	$k_0=5.040$	0.4397	33.0646
	First-order	$k_1=0.112$	0.9306	50.7188	$k_1=0.073$	0.6776	30.3012
	Korsmeyer-Peppas	$k_{KP}=18.414$	0.9991	13.9156	$k_{KP}=17.921$	0.9804	18.2931
		$n=0.537$			$n=0.423$		
	Higuchi	$k_H=19.793$	0.9960	25.0033	$k_H=15.346$	0.9629	19.4869
Weibull	$\alpha=5.335$	0.9961	26.7440	$\alpha=5.147$	0.9717	20.1428	
		$\beta=0.725$			$\beta=0.517$		

* Coefficient of determination. ** Akaike Information Criterion.

Comparing the NMR assay and indirect UV-Vis assay of drug release quantitation, NMR method appeared to have three distinct advantages: Firstly, the NMR method is a direct and real-time quantification method, where dialysis membrane was not required. If the *in vitro* profile was determined using an indirect method, such as UV-Vis or LC assay, the concentration of the drug in the release media might be underestimated due to the interactions between drug molecules and the dialysis membrane and the two step process. When it is converted to the *in vivo* study, the real blood concentration of drug would be lower than the predicted blood concentration, and therefore, led to a potential toxic effect. Secondly, the NMR method allowed for more data points to be collected in real-time quantitation scenario which provided a more accurate and dynamic measurement of release profile. Thirdly, no specific sample preparation method was required, thus saving valuable research time. The UV-visible spectroscopy measurements based on the Beer-Lambert Law and absorbance can only be related to drug concentration if molar absorptivity was determined or known for a drug molecules^{82,83}. Conversely, it is well known that the phosphorus atom plays an important role in physiological processes since it is part of genetic materials (DNA) as well as of ATP. Thus, solution state ³¹P-qNMR method for phosphorus quantitation can also be widely applied in the analysis of other biological agents. Moreover, the direct proportionality of the analytical response and concentration is a major advantage of NMR over UV-Vis and LC assays for quantitative analysis of therapeutic molecules. In addition, the UV-visible spectroscopy measurements based the Beer-Lambert Law and absorbance can only be related to drug concentration if

molar absorptivity was determined or known for a drug molecules. However, with q-NMR method, the information about molar absorptivity was not needed.

PROJECT-2

Layer by Layer Engineering of HIV-1 rgp120 Responsive Nanomicrobicide:

Physico-Chemistry and Biological Responses

Introduction

Since its discovery in 1983, Human Immunodeficiency Virus infection and Acquired Immune Deficiency Syndrome (HIV/AIDS) has remained a scientific mystery, given that a complete eradication, strategy is yet to be found. Owing to the Highly Active Antiretroviral Therapy (HAART), which decreases the risk of opportunistic infections and maintains the immune system function, HIV patients can now live longer. However, sexual transmission of HIV, which account for 75 to 85 % of the overall HIV infections, is still a major hurdle in the complete eradication of HIV. In addition to having multiple sexual partners and the lack of male circumcision, another major reason for the increase in HIV transmission is that 6 out of 10 people living with HIV do not know their HIV positive status making them a risk to their sexual partners^{84,85}. Therefore, there is a crucial need to develop a topical drug delivery system capable of preventing HIV sexual transmission. Recently, various microbicide drug delivery strategies (gels, films, rings, etc.) have been proposed, attempting to address this need with limited success. Semisolid dosage forms (gels) which are the most common microbicide drug delivery systems, present major challenges of messiness, leakage and lack of controlled release⁴⁶. Besides their lack of retention, which constantly leads to leakages and therefore patience adherence and compliance issues, topical microbicide loaded gel formulation, such as CAPRISA 004, have shown their lack of effectiveness against HIV⁸⁶. Vaginal films which are less untidy than gels are fast dissolving with rapid drug clearance by mucus renewal cycle⁴⁶. Moreover,

the ASPIRE study states that the silicone based vaginal ring Dapivirine, although promising, still has to address compliance issues with undesirable drug release kinetics. In fact, the major concern of a ring-based delivery system is a constant drug release even in absence of HIV virus, which will eventually lead to drug waste, drug resistance issues, and potential side effects. To address this problem, the present study hypothesizes that a Concanavalin A (Con A) based topical vaginal and rectal nanomedicine formulation is capable of the safe and effective release of a pre-encapsulated HIV microbicide "on-demand". Nanoparticles can serve not only to protect the active agent but also facilitate penetration into the vaginal and ectocervical mucosa, allowing drug to reach HIV target cells⁴⁶. Such a delivery system will ultimately protect women since more than half of all new HIV infections worldwide occur in females.

Carbohydrate-binding agents (CBAs) are a class of proteins that have high affinities for sugar moieties. They have been shown to be highly effective against HIV as microbicides⁸⁷⁻⁸⁹. Lectins, which represent a subclass of CBAs, are proteins that specifically recognize carbohydrate (glycan) structures⁹⁰. One of the most studied lectins is *Canavalia ensiformis* (Concanavalin A (Con A)) extracted from jack beans. Con A is known to bind sugars, glycoproteins, and glycolipids, containing internal and nonreducing terminal α -D-mannosyl and α -D-glucosyl groups^{91,92}. Like most lectins, Con A is a homotetramer with each subunit composed of 235 amino acids and having a molecular weight of 26.5 kDa. At pH below 6, Con A exists as a dimer and is in its tetrameric form at pH above 6. Con A has an isoelectric point (PI) that ranges from 4.5 to 5.5 depending on its isoforms. Like most proteins, above its PI, Con A is negatively charged and bears a positive charge at pH values below the PI value. Con A's binding activity requires metal

ions. Agrawal and Goldstein have shown that each Con A subunit has one Ca^{2+} and Mn^{2+} binding site^{91,93}. Con A has previously been shown to bind HIV-1 and HIV-2 viruses' envelope glycoprotein 120 (HIV-gp120)⁹⁴. More recently, Con A-immobilized polystyrene nanospheres were successfully designed for HIV-1 virions captured through Con A/HIV-1 gp120 binding interactions⁹⁵. HIV-gp120 plays a critical role in HIV infection. In fact, the binding of HIV-gp120 (on HIV virus surface) to the CD4 receptors (on host cells surface) represents the first step in the course of HIV infection that leads to the fusion of both membranes and the incorporation of the virus material into the host cell cytoplasm⁹⁶. This process ultimately leads to the production of new viruses and the spreading of the disease.

In the last few decades, HIV-gp120 has been extensively studied. To date, more is known about its structure than ever before. Indeed, several groups have shown that HIV-gp120 is composed of high proportions of carbohydrates. It is estimated that 50% of the apparent molecular mass of HIV-gp120 is composed of carbohydrates⁹⁷. More specifically, Mizuochi et al. found that about 40% of the total oligosaccharide structures released from HIV-gp120 are hybrid and/or high mannose-type oligosaccharides and 60% are of the complex type^{98,99}. This study also highlighted the unique and high mannose oligosaccharides content in HIV-1 gp120 compared to other Chinese hamster ovary-cell-derived glycoproteins. Furthermore, Geyer et al.¹⁰⁰ found that high mannose-type oligosaccharides account for approximately 50% of the carbohydrate structures of HIV-gp120. More recently, Bonomelli et al.¹⁰¹ found that HIV-gp120 derived from a virus prepared by infection of peripheral blood mononuclear cells (PBMCs) with viruses from clade A (92RW009), clade B (JRCSF), and clade C 93IN905, show a predominantly

oligomannose glycan composition (62–79%) $\text{Man}_{5-9}\text{GlcNAc}_2$ with a predominant population of $\text{Man}_5\text{GlcNAc}_2$. These oligo-mannoses bind to Con A with equilibrium dissociation constant (K_D) values ranging from 0.05 μM to 1.5 μM ¹⁰². Binding of Con A to HIV-gp120 glycans either prevent HIV virus binding to receptors on the cells or affect alterations of gp120 following binding¹⁰³. Our group recently published Con A binding affinities to glycogen from Oyster (0.25 μM) and mannan from *Saccharomyces cerevisiae* (2.89 μM)¹⁰⁴. In this study, it is hypothesized that a mannose sensitive Con A cross linked-polysaccharide nanoparticle can be designed to target HIV-gp120 and deliver a pre-encapsulated microbicide drug “on-demand”. We envisaged the HIV-gp120 responsive drug delivery system to address deficiencies shown by previous approaches in HIV prevention including retention, effectiveness and undesired drug release. One of the potential advantages of this delivery system is stopping the virus before the propagation of the infection. Thus, HIV virus migration is stopped in the vaginal or rectal cavity before it diffuses through the mucus layer and infects the immune cells and ultimately spreads to the entire body.

Material and Methods

1] Material

Concanavalin A (Con A) from *Canavalia ensiformis* (Jack bean) type VI, glycogen from Oyster, polyethylenimine (PEI) 50 wt. % solution in water, poly(sodium 4-styrenesulfonate) (PSS) average Mw ~70.000 powder, calcium chloride dehydrate ($\text{CaCl}_2 \cdot 2\text{H}_2\text{O}$, ACS reagent, $\geq 99\%$), sodium carbonate anhydrous ($\geq 99\%$), fluorescein isothiocyanate labeled Concanavalin A (FITC-Con A), type IV, lyophilized powder, tetramethylrhodamine isothiocyanate–Dextran (TRITC-Dextran), manganese (II) chloride

tetrahydrate ($\text{MnCl}_2 \cdot 4\text{H}_2\text{O}$, Reagent Plus, $\geq 99\%$), methyl α -D-mannopyranoside ($\geq 99\%$), and Tris Buffer Saline (TBS) pH 8.0 are purchased from Sigma-Aldrich (St. Louis, MO, USA). Ethylenediaminetetraacetic acid (EDTA free acid) is purchased from Fisher Scientific (Pittsburgh, PA, USA) and Human Immunodeficiency Virus type 1 recombinant envelope glycoprotein (HIV-1 rgp120) was purchased from Sino Biological Inc. (Beijing, P. R. China).

2] Methods

2.1] Mannose sensitive nanoparticles synthesis

Mannose sensitive nanoparticles (MSN) are synthesized via the “layer-by-layer” method by alternatively coating a core template with the mannose specific lectin (Con A) and a polysaccharide (Glycogen)^{105,106}. In this study, the core (calcium carbonate (CaCO_3)) is prepared by mixing equal volume (15 ml) of 0.2 M calcium chloride (CaCl_2) and 0.2 M sodium carbonate (Na_2CO_3) in presence of a dispersant (PSS) under vigorous stirring at 13,500 rpm for 2 minutes with the IKA Ultra-Turax model T25 homogenizer (Wilmington, NC, USA). A preliminary screening test has led to the selection of PSS as the optimal dispersant at a concentration of 4 mg/ml. To encapsulate Tenofovir in the core particle, the drug is dissolved in CaCl_2 at 3 mg/ml prior to the addition of Na_2CO_3 -PSS solution. Particles prepared in the presence of PSS depict a net negative charge and are subsequently dispersed in a positively charged initiator solution (4 mg/ml PEI in 0.5 M NaCl, pH 8.0) for at least 30 minutes in order to achieve a net positive charge. This allows the negatively charged lectin (1 mg/l Con A in TBS, pH 8.0) to adhere to the previous molecular assembly after a 1-hour exposition time. After three washing steps in deionized water (DI water) and centrifugation (1000 rpm), Con A coated nanoparticles are re-dispersed in a glycogen

solution (1 mg/ml in TBS, pH 8.0) for 1 hour to allow the addition of the first polysaccharide layer. After a washing step, glycogen coated nanoparticles are dispersed in Con A solution and the process is repeated until a desired number of layers is reached. In this study, the core particle is coated with 5 alternating layers of Con A and glycogen excluding the layer initiator. In order to visualize the particles in confocal microscopy, FITC-Con A is used for the first lectin layer addition and TRITC- Dextran for the last polysaccharide layer. Figure 8, summarizes the layer-by-layer synthesis procedure of core dissolved (C^- MSN) and core containing (C^+ MSN) MSN. The first lectin layer successfully adheres to the assembly through electrostatic interaction between the positively charged PEI and the negatively charged Con A whereas the glycogen layer is successfully added through the specific binding property of Con A to α -D-glucose based polysaccharides⁹¹. After this first phase of preparation, part of the layer-by-layer assembled nanoparticles are dispersed in 0.1 M EDTA solution under gentle stirring to dissolve the $CaCO_3$ core. Core dissolved nanoparticles are then washed twice with DI water to remove residual EDTA and are then freeze dried for 12 hours (Labconco FreeZone 1 Liter Benchtop Freeze Dry System, Kansas City, MO).

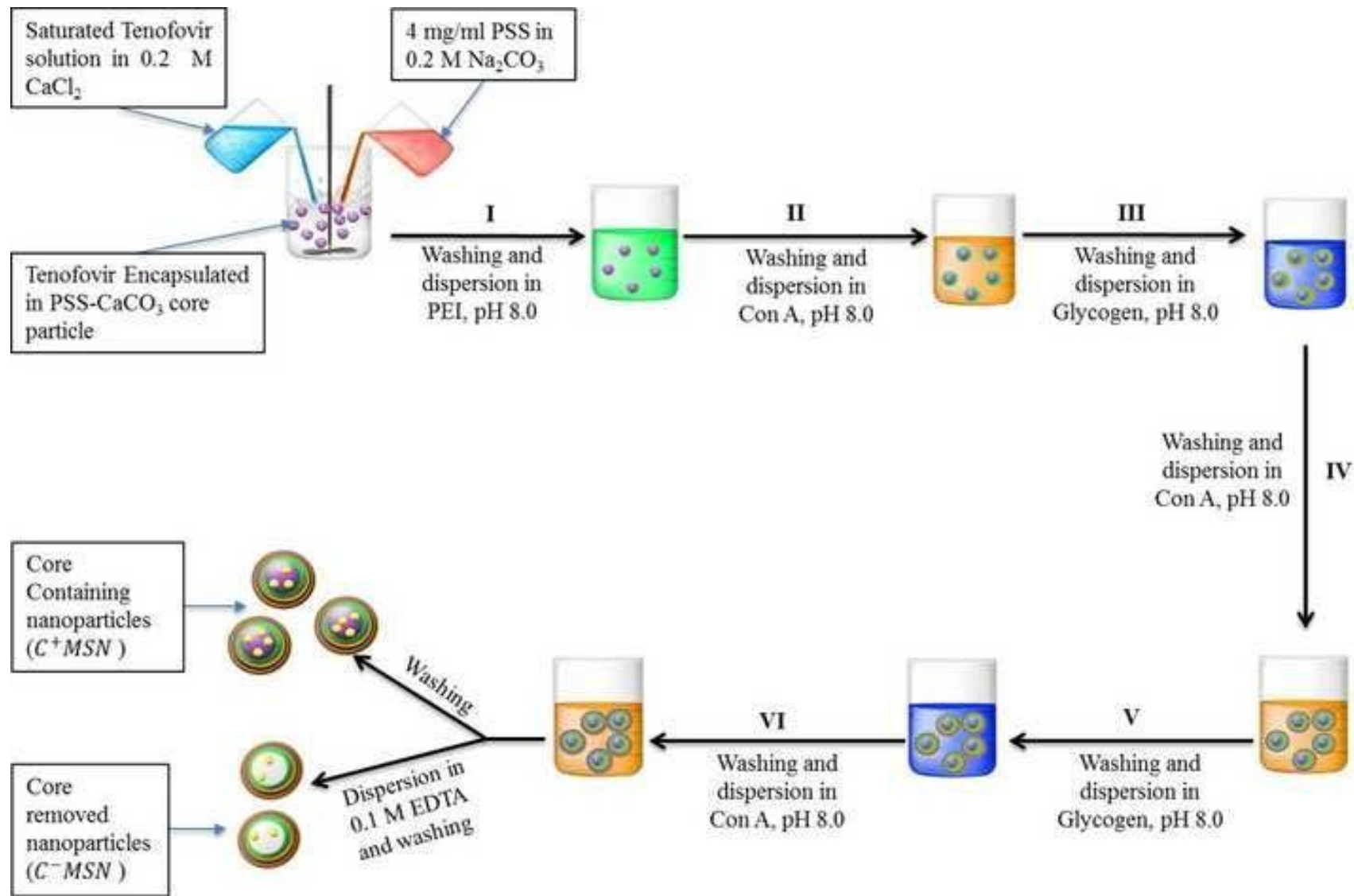


Figure 2.8. Illustration of the layer by layer preparation of core dissolved (C^-MSN) and core containing (C^+MSN) mannose sensitive nanoparticles (MSN). CaCO_3 core particle is coated with 6 layers including a PEI layer initiator.

2.2] Encapsulation and loading efficiency determination

Tenofovir encapsulation efficiency (EE%) and loading efficiency (LD%) in MSN are estimated by liquid state and solid state phosphorus (^{31}P) Nuclear magnetic resonance, respectively.

^{31}P solution state NMR: Tenofovir %EE is measured by quantifying the drug amount in the supernatant by ^{31}P Solution State NMR. Equation 1 is then used to compute %EE.

$$\text{Equation 1: \%EE} = \frac{\text{Total amount of TFV-Free TFV}}{\text{Total amount of TFV}} * 100$$

^{31}P solution state NMR experiment is carried out on a Varian (Palo Alto, California) 400 MHz spectrometer with a Varian two channel probe and operated by Vnmrj 2.2. Typically, the spectra are acquired with a 45° pulse length of 5.05 μs . The relaxation delay and the number of scans are 5 and 256 seconds, respectively. The spin-lattice relaxation time (T_1) of the target phosphorous in Tenofovir is 5 s and typically requires up to 25 s ($5 \times T_1$) for relaxation. Shimming is applied to every sample in order to obtain a similar linewidth in each spectrum. Baseline correction, phase adjustment, and integral calculations are carried out using MestReNova Lite 5.2.5-4731 software (Escondido, CA, USA) and Matlab 6.1 (Natick, MA, USA) and all experimental measurements are conducted at 37°C . To determine Tenofovir amount in the supernatant, a standard curve is performed across a concentration range of 0-500 $\mu\text{g/ml}$ in DI water. Equation 2, that describes the calibration curve is $Y = 9675.2X - 29.677$. The coefficient of determination is $R^2 = 0.9999$, indicating a very good correlation between ^{31}P NMR peak area (Y) and Tenofovir concentration (X).

^{31}P Solid State NMR: After freeze drying, Tenofovir LD% in and is determined by comparing their ^{31}P solid state NMR peak area to a pure Tenofovir standard of same mass.

Thus, solid state NMR spectra for 30 mg of C⁺MSN, C⁻MSN, and pure Tenofovir samples are taken at room temperature in triplicates and the signals are represented as chemical shift value δ : ppm. Equation 3 is used to compute the loading efficiency.

$$\text{Equation 3: \%LD} = \frac{\text{31P NMR Peak Area of 30 mg MSN}}{\text{31P NMR Peak Area of 30 mg TFV standard}} * 100$$

Practically, ³¹P-P90 Solid-State Magic Angle Spinning (MAS SS) NMR spectra are acquired on a Tecmag Apollo console (Houston, TX, USA) operated by NTNMR software package (v.2.4.29, Houston, TX, USA) with 8.45 T magnet and a 3 mm homebuilt, 2-channel, wide-bore NMR probes. The ¹H and ³¹P Larmor frequencies are 357.2 MHz and 144.596 MHz, respectively. The MAS spinning frequency and 45° pulse length are 8 KHz and 2 μ s, respectively.

2.3] Fourier Transform Infrared Spectroscopy

The Agilent Cary 630 FTIR instrument (Newark, DE, USA) equipped with a diamond crystal having a single reflection and a nominal angle of 45° is used in its Attenuated Total Reflectance (ATR) mode for IR spectra acquisition. A resolution of 4 cm⁻¹, a sample scan of 32 per second and an effective pathlength of 1.1 μ m are set as parameters. IR spectra are acquired between 4000 and 400 cm⁻¹. For better spectral resolution, all samples are allowed to make an intimate contact with the ATR diamond crystal surface by pressing them with a built-in pressure clamp. FTIR spectra are collected and analyzed with MicroLab PC and MicroLab Lite softwares (versions 4.0, Newark, DE, USA), respectively.

Results and Discussion

1] Drug Encapsulation and Loading Efficiencies

Tenofovir encapsulation efficiency in CaCO₃-PSS core particle is 74.4%. Likewise, Tenofovir loading efficiency in C⁻MSN (6.0 % ± 0.1 w/w; n=3) is about 3 fold lower than the loading efficiency obtained for C⁺MSN (16.3% ± 0.1 w/w; n=3). The difference in loading efficiency is probably due to a loss in Tenofovir during core dissolution because of its relatively high water solubility (13.4 mg/mL). Figure 9 shows the ³¹P solid state NMR spectra. Tenofovir encapsulation in CaCO₃-PSS particles is possible due to two major factors. Firstly, after the nucleation phase, leading to the formation of the CaCO₃-PSS crystal precursors, the crystal growth phase involved a co-precipitation. Thus, drug molecule can be entrapped in the CaCO₃-PSS particles during the crystallization process. Secondly, co-precipitation alone does not explain the overall drug entrapment level. In fact, along with aluminum hydroxide [Al(OH)₃], calcium acetate [Ca(C₂H₃O₂)₂], lanthanum carbonate [La₂(CO₃)₃], magnesium carbonate [MgCO₃], calcium carbonate [CaCO₃] is a member of the phosphate binders family¹⁰⁷⁻¹⁰⁹. As can be expected from their denomination, phosphate binders bind to phosphorus atoms through ionic interactions. In CaCO₃, it is the calcium ion (Ca²⁺) that binds the phosphate group. Therefore, it is expected that Tenofovir, which structure contains a phosphate group, will be entrapped in the core particles. Ueno et al. were able to reach a 90% loading of betamethasone phosphate in nano-CaCO₃ particles¹¹⁰.

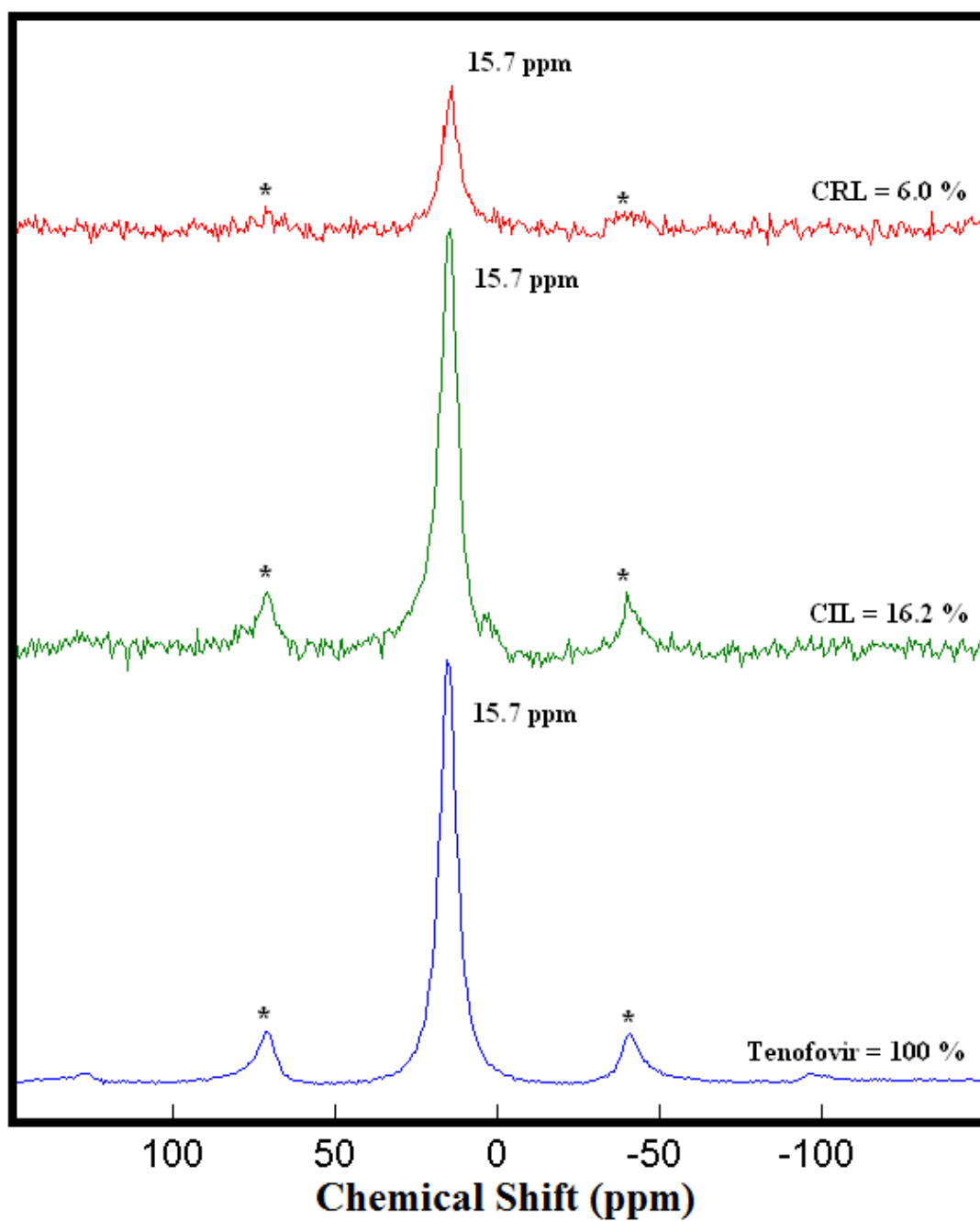


Figure 2.9. ^{31}P solid state NMR spectra of C⁻MSN, C⁺MSN. Tenofovir appears at 15.7 ppm and the spinning side bands are indicated by asterisks.

2] FTIR Analysis

In order to further characterize MSN and confirm the composition of the coating layers; FTIR spectra of C⁻MSN, C⁺MSN, glycogen, Con A, CaCO₃-PSS core particle and Con A/Glycogen agglutinate have been acquired in Figure 10. Glycogen IR spectrum shows distinctive weak peaks at 1160 cm⁻¹ and 1080 cm⁻¹ and a strong absorption at 1000 cm⁻¹ characteristic of polysaccharides C-O-C, C-O and C-H stretches^{111,112}. The bands at 3300 cm⁻¹ and 2900 cm⁻¹ are due to OH and CH₂ stretches in glycogen, respectively. Con A spectrum shows strong bands at 1620 cm⁻¹ and 1520 cm⁻¹ attributed to amide I and II, respectively¹¹³. Spectrum obtained for CaCO₃-PSS core particle shows a strong peak at 870 cm⁻¹ characteristic of carbonate band in calcium carbonate¹¹⁴. Features at 1400 cm⁻¹ - 1480 cm⁻¹ are attributed to S=O asymmetric stretching vibration mode in PSS¹¹⁵. C⁺MSN spectrum shows Con A amide I band at around 1620 cm⁻¹ confirming the presence of the lectin in the assembly. The bands between 1400 cm⁻¹-1480 cm⁻¹ as well as the strong absorption at 870 cm⁻¹ in C⁺MSN spectrum confirm the presence of CaCO₃-PSS core particle in the assembly. As expected, bands attributed to the carbonate band are not seen in C⁻MSN FTIR spectrum. The band at 1000 cm⁻¹ and the amide I stretching band at 1620 cm⁻¹ further confirm the presence of Con A-Glycogen agglutinate in C⁻MSN assembly. The absorption band at 3300 cm⁻¹ in Con A-Glycogen agglutinate spectrum is due to water residue in the preparation.

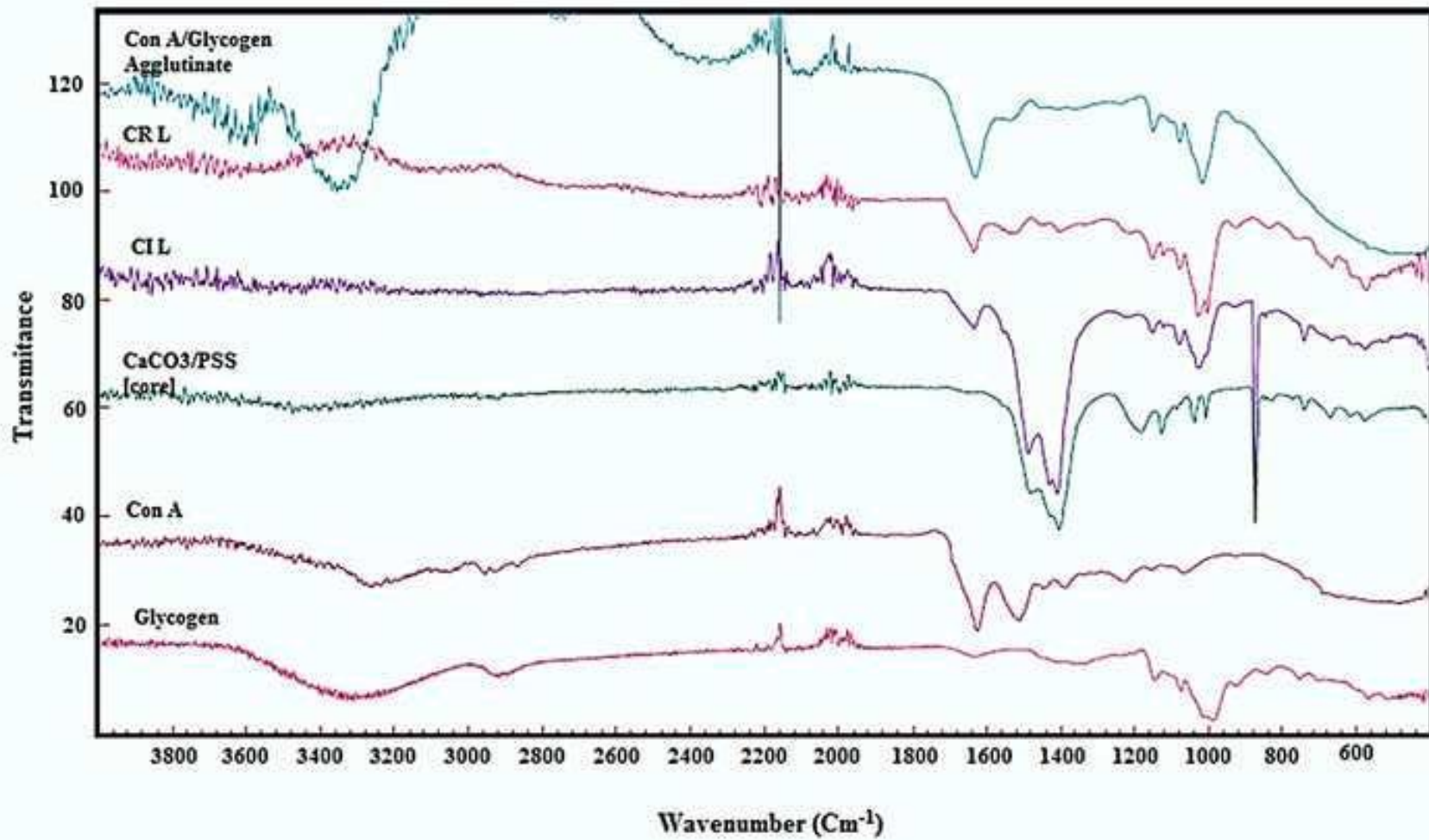


Figure 2.10. FTIR spectra of glycogen, Con A, CaCO₃-PSS core particle, C+MSN, C-MSN and Con A/glycogen agglutinate.

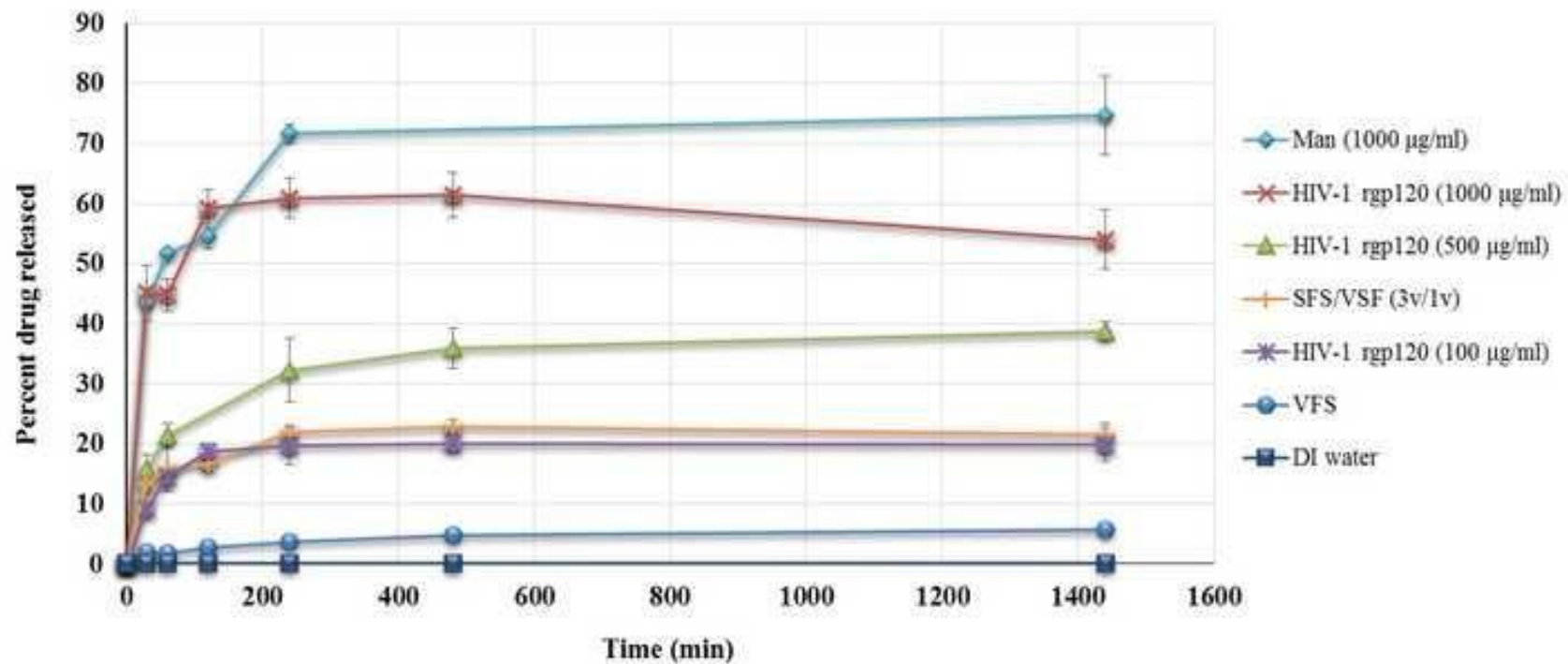


Figure 2.11. Tenofovir release profile from C+MSN in the presence of methyl α -D-mannopyranoside (1000 $\mu\text{g/ml}$) and HIV-1 rgp120 (100-1000 $\mu\text{g/ml}$). Data from each time point is triplicated ($n=3$).

3] Drug Release from MSN

The mannose responsive property of MSN is tested by monitoring Tenofovir release from up to 24h in the presence of methyl α -D-mannopyranoside as well as mannose-rich HIV-1 recombinant envelope glycoprotein (HIV-1 rgp120) (Figure 11). In general, a maximum drug release is reached within 4h. An increasing dose response effect is also observed with increasing concentration of HIV-1 rgp120. HIV-1 virus is known to cross the mucosal barrier in 2 to 6 hours and, during the first 3 to 6 days, disseminates locally and reaches draining lymph nodes¹¹⁶. Thus, might offer the unique advantage of neutralizing HIV-1 virus in the vaginal or rectal track before the completion of its migration through the mucosal barrier. The maximum drug release (75%) is observed in the presence of methyl α -D-mannopyranoside (1000 μ g/ml) while HIV-1 rgp120 induces 61% and 39% drug release at 1000 μ g/ml and 500 μ g/ml, respectively. The maximal drug release observed in methyl α -D mannopyranoside might be due in part to a higher binding affinity of Con A for the oligosaccharide a previously shown by Goldstein et al.⁹². Although 22% of Tenofovir is released from when exposed to 100 μ g/ml of HIV-1 rgp120, this is, however, not significantly different from the drug release observed in the control conditions [SFS:VSF/(3v:1v)].

PROJECT-3

Spray Dried Thiolated Chitosan Coated Sodium Alginate Multilayer Microparticles for Vaginal Anti-HIV Microbicide Delivery

Introduction

An ideal vaginal drug delivery system should be easy to administer, not cause discomfort to improve patient compliance and have a reduced number of doses required to the treatment¹¹⁷. To meet these requirements, various vaginal drug carriers have been developed^{69,73,74,118}. However, in most of these formulations, the encapsulation of a water-soluble small molecular drug is a serious problem associated with drug %payload. Recently, a special attention has been focused on the development of spray dried microparticles (MPs) as an alternative solution⁶³. Spray drying is a rapid and simple process based on the solvent evaporation. The atomized polymeric droplets containing the drug are transformed in solid particles by a stream of heated air¹¹⁹. The spray drying method not only typically produces spherical MPs with a narrow size distribution, but also enables the encapsulation of both hydrophilic and hydrophobic drugs with relatively high efficiency and yield^{120,121}.

The main advantages of MPs over traditional vaginal dosage forms such as gels, creams, rings, and films are: the generation of a sustained drug release profile following the application of a single dose, a proper spreading over the vaginal epithelium, the protection of the drugs and ability to reduce drug toxicity. To further prolong the residence time on the site of the treatment, a thiolated chitosan (TCS) is used to coat the MPs. It has been shown to possess high mucoadhesive properties due to the thiol groups present on the

chitosan backbone, which can form disulfide bonds with the thiol groups present on the mucus substructures¹²².

In this study, a hydrophilic anti-HIV microbicide, tenofovir (TFV) (water solubility 1.87 mg.ml, logP -1.5), is encapsulated within the spray dried alginate MPs. The MPs are coated with TCS based on the charge-charge interaction between alginate and TCS. It is postulated that these MPs may prolonge the drug retention time as well as controlled release profile, and could be a potential vaginal drug delivery system with increased encapsulation efficiency of water-soluble small molecule drugs, such as TFV.

Materials and Methods

1] Materials

Sodium alginate, chitosan with the weight molecular weight of 50-190 KDa, mucin, periodic acid, Schiff reagent kit and benzalkonium chloride (BZK, 2 % w/v) are purchased from Sigma Aldrich (St. Louis, MO, USA). Tenofovir (TFV) is purchased from Zhongshuo Pharmaceutical Co. Ltd. (Beijing, China). Sodium triphosphate pentabasic (TPP) is supplied by Fisher Scientific (Pittsburgh, PA, USA). The CytoTox-ONE™ and CellTiter 96™ Aqueous kits are purchased from Promega (Madison, WI, USA).

2] Method

2.a] Formulation of Spray Dried MPs

To prepare TFV loaded alginate MPs, different amounts of sodium alginate and TFV (Table 6) are dissolved in 40 ml of deionized water, the ratio of sodium alginate to TFV is 5:1 (w/w). The solution is then spray dried using a Buchi Mini Spray Dryer, Model 290 (Buchi Laboratories - Technik AG, Flawil, Switzerland). Then, the formulated MPs are stored at 4°C for further analysis.

In order to optimize the preparation conditions, a custom design with 3 factors and 16 run is used to study the effect of the formulation parameters on the yield. The independent variables, molecular weight of sodium alginate, concentration of the sodium alginate solution, and inlet temperature, are represented by X_1 , X_2 and X_3 , respectively. The percent (%) yield, which is the dependent variable is represented by Y . These variables and their coded factors are listed in Table 1. All independent variables in this work are selected based on preliminary experiments performed (data not shown). The yield is calculated using Equation 1 below:

$$\text{Yield}(\%) = \frac{\text{Total mass of MP powder collected}}{\text{Total mass of initial components in the formulation}} \times 100\% \quad (1)$$

2.b] Preparation of the Multilayered MPs

For the preparation of MPs by layer-by-layer is adapted from Li, et al. method¹²³. The multilayer MPs are obtained by alternately coating alginate and TCS on the surface of the particles (Figure 12). Briefly, 40 mg of CaCl_2 and 2 mg of TCS are dissolved in 1 ml of acidic acid solution (pH 5). A total of 1 mg of spray dried alginate MPs are subsequently suspended into the above solution. After the resulting suspension is stirred for 2 h. The product is collected by centrifugation at 10,000 rpm for 10 min (Beckman Coulter Inc., Pasadena, CA, USA) and washed thoroughly with water once. This product is TCS coated single layer MPs (SLMPs). To prepare the double layer MPs (DLMPs), alginate and TCS are dissolved in 0.1% acetic acid solution (pH 5) at a concentration of 2 mg/ml, respectively. At this pH, both TCS (weak acid, pKa 6.5) and alginate (weak base, pKa 4.2) mainly exist in ionized form¹²⁴. Then the SLMPs are suspended in 1 ml of alginate solution, stirred, centrifuged, and washed as described above, followed by suspending in

1 ml of TCS solution for 10 min. The resulting DLMPs are collected by centrifugation. The triple layer MPs (TLMPs) could thus be obtained by repeating the above operations of DLMPs. The percent drug loading is determined using ^{31}P SS NMR as follows.

70

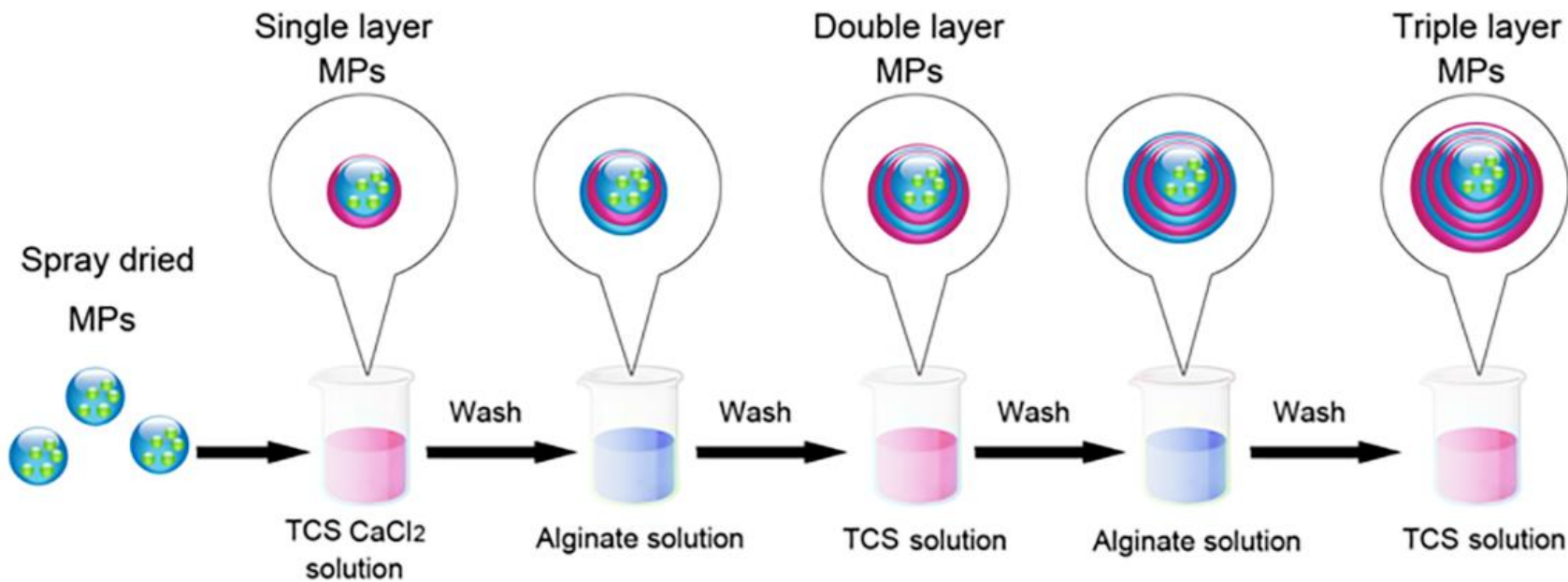


Figure 2.12. Schematic preparation scheme of the TCS coated multilayer MPs.

2.c] Percent Drug Loading Determination using ^{31}P SS NMR

^{31}P MAS SS NMR spectra are acquired on a Tecmag Apollo console (Houston, TX) with 8.45 T magnet and homebuilt, 2-channel, wide-bore NMR probes. The ^1H and ^{31}P Larmor frequencies were 357.2 MHz and 144.596 MHz respectively. ^{31}P spectra are acquired on 3 mm probe with MAS spinning frequency and 45° pulse length is 8 KHz and 2 μs , respectively and signals are represented as chemical shift value; δ : ppm. About 40 mg of the MPs sample is taken for each analysis. All experiments are performed at ambient temperature without any corrections for sample heating.

2.d] Surface Characteristics Determination using FT-IR Spectroscopy

The surface chemistry is determined by FT-IR spectroscopy. Before analyzing each sample, the background spectrum is collected at ambient conditions. The MPs are then scanned over the range of 650 and 4000 cm^{-1} . The FT-IR spectra are recorded by OMNIC V 7.0 spectra software.

Table 2.6. Independent and dependent variables and their levels in custom design.

Variables		Value	
Independent	Molecular weight of sodium alginate (X1)	Low	High
	Concentration of sodium alginate (X2)	5 mg/ml	15 mg/ml
	Inlet temperature (X3)	100 $^\circ\text{C}$	150 $^\circ\text{C}$
Dependent	Yield (Y)		

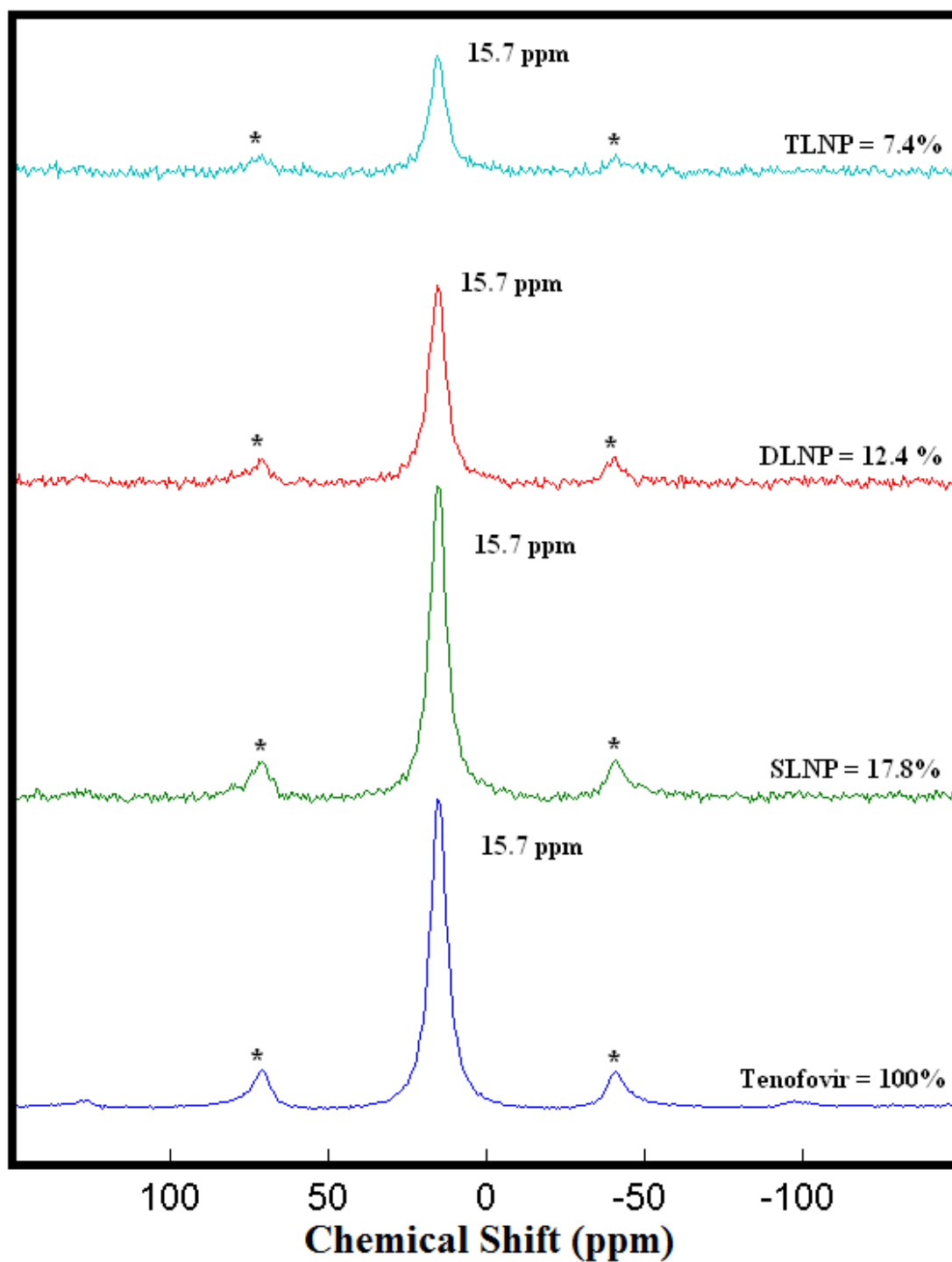


Figure 2.13. Drug Loading Analysis of MPs using ^{31}P SS NMR Spectroscopy. A single peak for TFV appears at 15.7 ppm. Spinning side bands are shown by Asterisks.

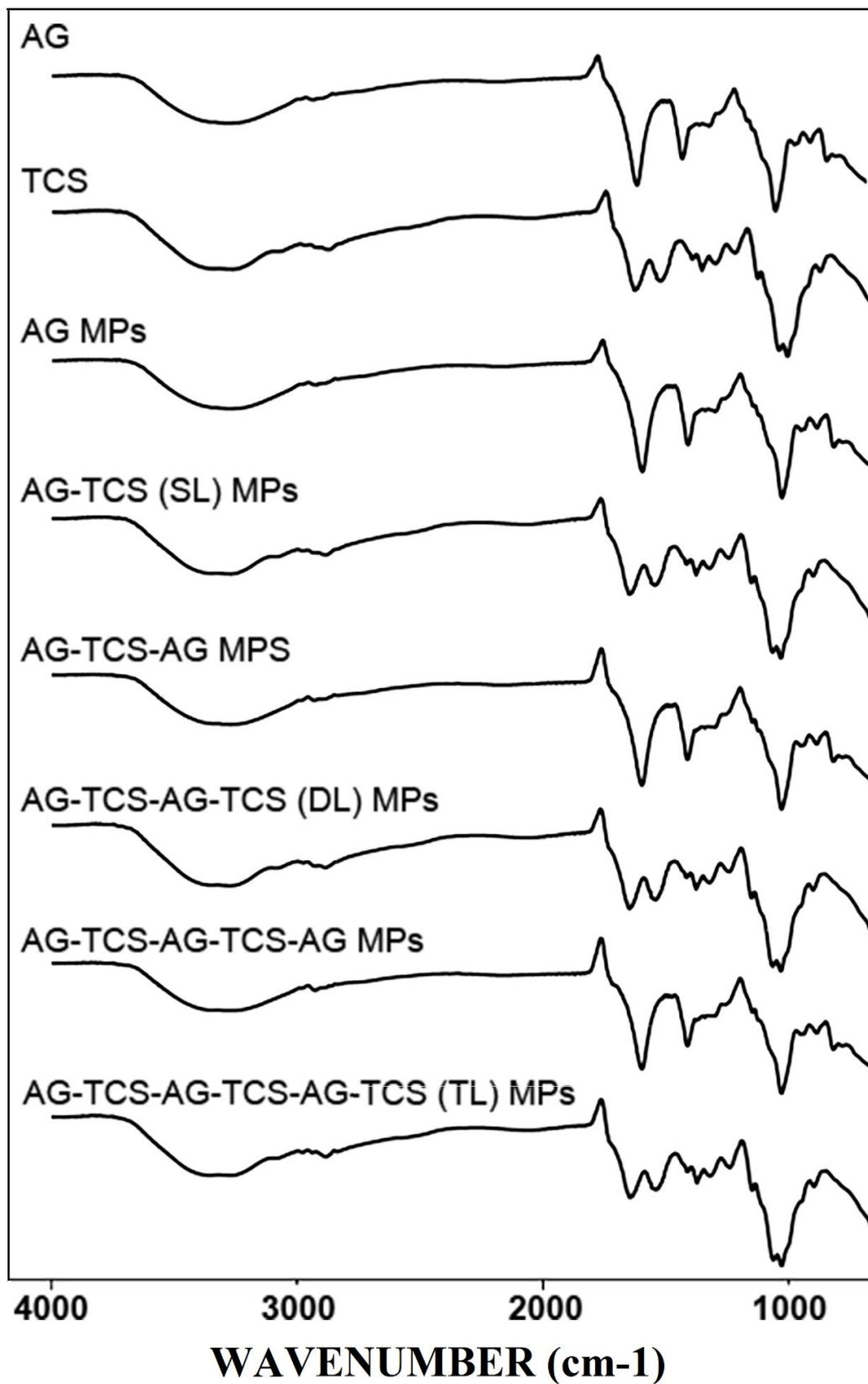


Figure 2.14. FT-IR spectra of oppositely charged TCS and Alginate coatings (n=3).

Results and Discussion

1] Characterization of MPs using ^{31}P SS NMR Spectroscopy

The amount of TFV encapsulated in MPs with different layers was detected by implementing ^{31}P SS NMR spectroscopy (Figure 13). The amount is presented as a percentage, in comparison with pure TFV (considered as 100 %). Three trials for each type of MPs are carried out in order to be able to calculate the standard deviation by utilizing ^{31}P solid state NMR spectroscopic technique. The drug loading slightly decreases when a new layer, which increases the total mass of polymer, is coated. The MPs are washed after each coating step, this may also lead to the loss of drug dye to the high water solubility of TFV. The percent drug loading slightly decreases due to new layers that increase the total mass of polymer, and drug loss during washing.

2] Characterization of MPs using FT-IR Spectroscopy

Layer by layer deposition also results in a slight increase in the particle size. The coating by these different layers is further confirmed by FT-IR spectroscopy (Figure 14). Both native alginate and native TCS exhibit a broad absorption peak at around 3100 to 3650 cm^{-1} and weak absorption peaks at 2890 cm^{-1} , attributed to their hydrogen bond stretching vibration and the CH stretch, respectively. TCS shows two characteristic peaks at 1520 and 1650 cm^{-1} , due to the amide (CO-NH-) and the amine (-NH₂) absorption band, respectively. The native alginate reveals two sharp and characteristic peaks at 1610 and 1415 cm^{-1} assigned to the carboxylic acids (COO⁻). After coating by either TCS or alginate, the main component on the MPs surface exhibit relative FT-IR spectra.

References

- (1) Nevozhay, D.; Kańska, U.; Budzyńska, R.; Boratyński, J. *Postep. Hig Med Dosw.* **2007**, *61*, 350.
- (2) Suri, S. S.; Fenniri, H.; Singh, B. *J Occup Med Toxicol.* **2007**, *2*, 16.
- (3) Brigger, I.; Dubernet, C.; Couvreur, P. *Adv Drug Deliv Rev.* **2002**, *54*, 631.
- (4) Marchesan, S.; Prato, M. *ACS Med. Chem. Lett.* **2013**, *4*, 147.
- (5) McCarron, P. A.; Hall, M. *Encycl. Nanosci. Nanotechnol.* **2004**, *8*, 469.
- (6) Mei, L.; Zhang, Z.; Zhao, L.; Huang, L.; Yang, X.-L.; Tang, J.; Feng, S.-S. *Adv. Drug Deliv. Rev.* **2012**, *65*, 880.
- (7) Musacchio, T.; Torchilin, V. P. *Front. Biosci., Landmark Ed.* **2011**, *16*, 1388.
- (8) Smith, H. J.; Williams, H. *Smith and Williams' Introduction to the Principles of Drug Design and Action*, 4th ed.
- (9) Henriksen, I.; Sande, S. A.; Smistad, G.; Agren, T.; Karlsen, J. *Int. J. Pharm.* **1995**, *119*, 231.
- (10) Wallace, S. J.; Li, J.; Nation, R. L.; Boyd, B. J. *Drug Deliv. Transl. Res.* **2012**, *2*, 284.
- (11) Levy, M. Y.; Benita, S. *Int. J. Pharm.* **1990**, *66*, 29.
- (12) Moreno-Bautista, G.; Tam, K. C. *Colloids. Surf. A.* **2011**, *389*, 299.
- (13) Friedman, D.; Benita, S. *Drug Dev. Ind. Pharm.* **1987**, *13*, 2067.
- (14) Washington, C. *Int. J. Pharm.* **1989**, *56*, 71.
- (15) Washington, C. *Int. J. Pharm.* **1990**, *58*, 1.
- (16) Calvo, P.; Vila-Jato, J. L.; Alonso, M. J. *J. Pharm. Sci.* **1996**, *85*, 530.
- (17) Xu, X.; Khan, M. A.; Burgess, D. J. *Int. J. Pharm.* **2012**, *426*, 211.
- (18) Agrahari, V.; Youan, B.-B. *AAPS. Pharm. Sci. Tech.* **2012**, *13*, 202.
- (19) Sentenac, S.; Fernandez, C.; Thuillier, A.; Lechat, P.; Aymard, G. *J. Chromatogr B. Anal. Technol. Biomed. Life Sci.* **2003**, *793*, 317.
- (20) Takahashi, M.; Kudaka, Y.; Okumura, N.; Hirano, A.; Banno, K.; Kaneda, T. *Biol. Pharm. Bull.* **2007**, *30*, 1784.
- (21) Yadav, M.; Mishra, T.; Singhal, P.; Goswami, S.; Shrivastav, P. S. *J. Chromatogr. Sci.* **2009**, *47*, 140.
- (22) Modi, S.; Anderson, B. D. *Mol. Pharm.* **2013**, *10*, 3076.
- (23) Yang, M.; Wang, J.; Kong, L. *J. Pharm. Biomed. Anal.* **2012**, *70*, 87.
- (24) Pieri, V.; Belancic, A.; Morales, S.; Stuppner, H. *J. Agric. Food. Chem.* **2011**, *59*, 4378.
- (25) Staneva, J.; Denkova, P.; Todorova, M.; Evstatieva, L. *J. Pharm. Biomed. Anal.* **2011**, *54*, 94.
- (26) Pinheiro, G. M.; Basso, E. A.; Fiorin, B. C.; Cendes, F.; Rittner, R.; Oliveira, A. N.; Hoehr, N. F. *Clin. Chim. Acta.* **2009**, *404*, 166.
- (27) Shoolery, J. N. *Prog. NMR Spectrosc.* **1977**, *11*, 79.
- (28) Greenhalgh, R.; Shoolery, J. N. *Anal. Chem.* **1978**, *50*, 2039.
- (29) Jungnickel, J. L.; Forbes, J. W. *Anal. Chem.* **1963**, *35*, 938.
- (30) Hollis, D. P. *Anal. Chem.* **1963**, *35*, 1682.
- (31) Otsuka, M.; Matsumoto, T.; Kaneniwa, N. *J. Pharm. Pharmacol.* **1989**, *41*, 665.
- (32) Connors, K. A.; Amidon, G. L.; Stella, V. J. New York John Wiley Sons. **1986**.
- (33) Pauli, G. F.; Godecke, T.; Jaki, B. U.; Lankin, D. C. *J. Nat. Prod.* **2012**, *75*, 834.

- (34) Malz, F.; Jancke, H. *J. Pharm. Biomed. Anal.* **2005**, *38*, 813.
- (35) Maniara, G.; Rajamoorthi, K.; Rajan, S.; Stockton, G. W. *Anal. Chem.* **1998**, *70*, 4921.
- (36) *United States Pharmacopoeia, USP XXII; United States Pharmacopoeia Conv. Inc. Rockville, MD* **1992**, *7*, 3140.
- (37) *Br. Pharmacopoeia, Her Majesty's Station. Off. London.* **1988**, *2*.
- (38) Zhang, C.; Zhang, T.; Oyler, N.; Youan, B.-B. *J. Pharm. Sci.* **2014**, *103*, 1170.
- (39) "Fact Sheets". *UNAIDS.org* **2013**.
- (40) "Guidelines Use Antiretrovir. Agents HIV-1-Infected Adults Adolesc. US Dep. Heal. Hum. Serv.
- (41) *New York Times.* March 21, 1987.
- (42) Emau, P.; Jiang Y.; Agy, M. B.; Tian, B.; Bekele, G.; Tsai, C.-C. *AIDS Res. Ther.* **2006**, *3*, 29.
- (43) "Prescribing Information". Gilead Sci. Inc.
- (44) Kearney, B. P.; Flaherty, J. F.; Shah, J. *Clin. Pharmacokinet.* **2004**, *43*, 606.
- (45) *Tenofovir disoproxil fumarate tablets Prescr. information. Foster City Gilead Sci. Inc.* **2003**.
- (46) Rohan, L. C.; Sassi, A. B. *AAPSJ* **2009**, *11*, 78.
- (47) Ndesendo, V. M.; Pillay, V.; Choonara, Y. E.; Buchmann, E.; Bayever, D. N.; Meyer, L. C. *AAPS Pharm. Sci. Tech.* **2008**, *9*, 505.
- (48) das Neves, J.; Michiels, J.; Arien, K. K.; Vanham, G.; Amiji, M.; Bahia, M. F.; Sarmiento, B. *Pharm. Res.* **2011**, *2012*, 1468.
- (49) Mbopi-Keou, F. X.; Trottier, S.; Omar, R. F.; Nkele, N. N.; Fokoua, S.; Mbu, E. R.; Domingo, M. C.; Giguere, J. F.; Piret, J.; Mwatha, A.; Masse, B.; Bergeron, M. G. *Contraception.* **2010**, *81*, 79.
- (50) McCormack, S.; Ramjee, G.; Kamali, A.; Rees, H.; Crook, A. M.; Gafos, M.; Jentsch, U.; Pool, R.; Chisembele, M.; Kapiga, S.; Mutemwa, R.; Vallely, A.; Palanee, T.; Sookrajh, Y.; Lacey, C. J.; Darbyshire, J.; Grosskurth, H.; Profy, A.; Nunn, A.; Hayes, R.; Weber, J. *Lancet.* **2010**, *376*, 1329.
- (51) Wan, L.; Pooyan, S.; Hu, P.; Leibowitz, M. J.; Stein, S.; Sinko, P. J. *Pharm. Res.* **2007**, *24*, 2110.
- (52) Abdool Karim, Q.; Abdool Karim, S. S.; Frohlich, J. A.; Grobler, A. C.; Baxter, C.; Mansoor, L. E.; Kharsany, A. B.; Sibeko, S.; Mlisana, K. P.; Omar, Z.; Gengiah, T. N.; Maarschalk, S.; Arulappan, N.; Mlotshwa, M.; Morris, L.; Taylor, D. *Science.* **2010**, *329*, 1168.
- (53) Rohan, L. C.; Moncla, B. J.; Kunjara, N.; Ayudhya, R. P.; Cost, M.; Huang, Y. *PLoS One.* **2010**, *5*, 1.
- (54) Alukda, D.; Sturgis, T.; Youan, B.-B. *J. Pharm. Sci.* **2011**, *100*, 3345.
- (55) Mayer, K. H.; Maslankowski, L. A.; Gai, F.; El-Sadr, W. M.; Justman, J.; Kwiecien, A. *AIDS.* **2006**, *20*, 543.
- (56) Rosen, R. K.; Morrow, K. M.; Carballo-Dieiguez, A.; Mantell, J. E.; Hoffman, S.; Gai, F. *J Womens Heal. (Larchmt).* **2008**, *17*, 383.
- (57) Saxena, B. B.; Han, Y. A.; Fu, D.; Rathnam, P.; Singh, M.; Laurence, J.; Lerner, S. *AIDS.* **2009**, *23*, 917.
- (58) Gupta, K. M.; Barnes, S. R.; Tangaro, R. A.; Roberts, M. C.; Owen, D. H.; Katz, D. F.; Kiser, P. F. *J. Pharm. Sci.* **2007**, *96*, 670.

- (59) Mahalingam, A.; Jay, J. I.; Langheinrich, K.; Shukair, S.; McRaven, M. D.; Rohan, L. C.; Herold, B. C.; Hope, T. J.; Kiser, P. F. *Biomaterials*. **2011**, *32*, 8343.
- (60) Clark, M. R.; Aliyar, H. A.; Lee, C. W.; Jay, J. I.; Gupta, K. M.; Watson, K. M.; Stewart, R. J.; Buckheit, R. W.; Kiser, P. F. *Int. J. Pharm.* **2011**, *413*, 10.
- (61) Zhang, T.; Sturgis, T. F.; Youan, B.-B. *Eur. J. Pharm. Biopharm.* **2011**, *79*, 526.
- (62) Cilurzo, F.; Selmin, F.; Minghetti, P.; Rimoldi, I.; Demartin, F.; Montanari, L. *Eur. J. Pharm. Sci.* **2005**, *24*, 355.
- (63) Zhang, T.; Zhang, C.; Agrahari, V.; Murowchick, J. B.; Oyler, N. A.; Youan, B.-B. *Antivir. Res.* **2013**, *97*, 334.
- (64) Modi, S.; Anderson, B. D. *Mol. Pharm.* **2013**, *10*, 3076.
- (65) Zambito, Y.; Pedreschi, E.; Di Colo, G. *Int. J. Pharm.* **2012**, *434*, 28.
- (66) Xie, L.; Beyer, S.; Vogel, V.; Wacker, M. G.; Mantele, W. *Int. J. Pharm.* **2015**, *488*, 108.
- (67) Clendinen, C. S.; Stupp, G. S.; Ajredini, R.; Lee-McMullen, B. *Front. Plant Sci.* **2015**, *6*, 611.
- (68) Maltsev, S.; Hudson, S. M.; Sahu, I. D.; Liu, L.; Lorigan, G. A. *J. Phys. Chem. B* **2014**, *118*, 4370.
- (69) Agrahari, V.; Zhang, C.; Zhang, T.; Gounev, T. K.; Oyler, N. A.; Youan, B.-B. *AAPSJ* **2014**, *16*, 181.
- (70) Agrahari, V.; Putty, S.; Mathes, C.; Murowchick, J. B.; Youan, B.-B. *Drug Test Anal.* **2015**, *7*, 207.
- (71) Hu, X.; Liu, S.; Zhou, G.; Huang, Y.; Xie, Z.; Jing, X. *J. Control. Release* **2014**, *185*, 12.
- (72) Zamani, M.; Prabhakaran, M. P.; Ramakrishna, S. *Int. J. Nanomedicine* **2013**, *8*, 2997.
- (73) Meng, J.; Zhang, T.; Agrahari, V.; Ezoulin, M. J.; Youan, B.-B. *Nanomedicine (London)* **2014**.
- (74) Meng, J.; Sturgis, T. F.; Youan, B.-B. *Eur. J. Pharm. Sci.* **2011**, *44*, 57.
- (75) Owen, D. H.; Katz, D. F. *Contraception*. **1999**, *59*, 91.
- (76) Owen D.H.; Katz, D. F. *J. Androl.* **2005**, *26*, 459.
- (77) *Harmon. ICo. Geneva, Switzerland.* **2005**.
- (78) Costa, P.; Sousa Lobo, J. M. *Eur. J. Pharm. Sci.* **2001**, *13*, 123.
- (79) Zhang, Y.; Huo, M.; Zhou, J.; Zou, A.; Li, W.; Yao, C.; Xie, S. *AAPSJ* **2010**, *12*, 263.
- (80) Sullentrop, F.; Moka, D.; Neubauer, S.; Haupt, G.; Engelmann, U.; Hahn, J.; Schicha, H. *NMR Biomed.* **2002**, *15*, 60.
- (81) Dash, S.; Murthy, P. N.; Nath, L.; Chowdhury, P. *Acta Pol. Pharm.* **2010**, *67*, 217.
- (82) Agrahir, V.; Meng, J.; Zhang, T.; Youan, B. B. *J. Anal. Bioanal. Tech.* **2014**, *5*, 1.
- (83) Pelillo, M.; Cuvelier, M. E.; Biguzzi, B.; Gallina, Toschi, T.; Berset, C.; Lercker, G. *J. Chromatogr. A* **2004**, *1023*, 225.
- (84) Royce, R. A.; Sena, A.; Cates, W.; Cohen, M. S. *J. N Engl J Med* **1997**, *336*, 1072.
- (85) Hunter, D. J. *Epidemiology* **1993**, *4*, 63.
- (86) Valley-Omar, Z.; Sibeko, S.; Anderson, J.; Goodier, S.; Werner, L.; Arney, L.; Naranbhai, V.; Treurnicht, F.; Abrahams, M. R.; Bandawe, G.; Swanstrom, R.; Karim, Q. A.; Karim, S. S.; Williamson, C. *J Infect Dis* **2012**, *206*, 35.
- (87) Balzarini, J. *Antivir Chem Chemother* **2007**, *18*, 1.

- (88) Balzarini, J.; Van Laethem, K.; Hatse, S.; Froeyen, M.; Peumans, W.; Van Damme, E.; Schols, D. *J Biol Chem* **2005**, *280*, 41005.
- (89) Pollicita, M.; Schols, D.; Aquaro, S.; Peumans, W. J.; Van Damme, E. J.; Perno, C. F.; Balzarini, J. *Virology* **2008**, *370*, 382.
- (90) Balzarini, J. *Nat Rev Microbiol* **2007**, *5*, 583.
- (91) Brewer, F. *Einstein Q. J. Biol. Med.* **1985**, *3*, 55.
- (92) Goldstein, I. J.; Hollerman, C. E.; Smith, E. E. *Biochemistry* **1965**, *4*, 876.
- (93) Agrawal, B. B.; Goldstein, I. J. *Arch Biochem Biophys* **1968**, *124*, 218.
- (94) Hansen, J. E.; Nielsen, C. M.; Nielsen, C.; Heegaard, P.; Mathiesen, L. R.; Nielsen, J. O. *Aids* **1989**, *3*, 635.
- (95) Hayakawa, T.; Kawamura, M.; Okamoto, M.; Baba, M.; Niikawa, T.; Takehara, S.; Serizawa, T.; Akashi, M. *J Med Virol* **1998**, *56*, 327.
- (96) Mondor, I.; Moulard, M.; Ugolini, S.; Klasse, P. J.; Hoxie, J.; Amara, A.; Delaunay, T.; Wyatt, R.; Sodroski, J.; Sattentau, Q. J. *Virology* **1998**, *248*, 394.
- (97) Leonard, C. K.; Spellman, M. W.; Riddle, L.; Harris, R. J.; Thomas, J. N.; Gregory, T. J. *J Biol Chem* **1990**, *265*, 10373.
- (98) Mizuochi, T.; Spellman, M. W.; Larkin, M.; Solomon, J.; Basa, L. J.; Feizi, T. *Biochem J* **1988**, *254*, 599.
- (99) Mizuochi, T.; Spellman, M. W.; Larkin, M.; Solomon, J.; Basa, L. J.; Feizi, T. *Biomed Chromatogr* **1988**, *2*, 260.
- (100) Geyer, H.; Holschbach, C.; Hunsmann, G.; Schneider, J. *J Biol Chem* **1988**, *263*, 11760.
- (101) Bonomelli, C.; Doores, K. J.; Dunlop, D. C.; Thaney, V.; Dwek, R. A.; Burton, D. R.; Crispin, M.; Scanlan, C. N. *PLoS One* **2011**, *6*, e23521.
- (102) Bhattacharyya, L.; Brewer, C. F. *Eur J Biochem* **1989**, *178*, 721.
- (103) Akkouh, O.; Ng, T. B.; Singh, S. S.; Yin, C.; Dan, X.; Chan, Y. S.; Pan, W.; Cheung, R. C. *Molecules* **2015**, *20*, 648.
- (104) Coulibaly, F. S.; Youan, B.-B. *Biosens Bioelectron* **2014**, *59*, 404.
- (105) Wohl, B. M.; Engbersen, J. F. *J Control Release* **2012**, *158*, 2.
- (106) Richardson, J. J.; Bjornmalm, M.; Caruso, F. *Science (80-.)*. **2015**, *348*, aaa2491.
- (107) Locatelli, F.; Del Vecchio, L.; Violo, L.; Pontoriero, G. *Expert Opin Drug Saf* **2014**, *13*, 551.
- (108) Friedman, E. A. *Clin J Am Soc Nephrol* **2006**, *1*, 704.
- (109) Friedman, E. A. *Kidney Int Suppl* **2005**, S2.
- (110) Ueno, Y.; Futagawa, H.; Takagi, Y.; Ueno, A.; Mizushima, Y. *J Control Release* **2005**, *103*, 93.
- (111) Gilberto Íñiguez, A. V.; Manríquez, R.; Moreno, M. V. *Rev. Int. Contam. Ambie.* **2011**, *27*, 61.
- (112) Grube, E. Z. M.; Gromozova, E.; Fomina, M. *Vib. Spectrosc.* **1999**, *19*, 301.
- (113) Deflores, L. P.; Ganim, Z.; Nicodemus, R. A.; Tokmakoff, A. *J Am Chem Soc* **2009**, *131*, 3385.
- (114) Ni, M.; Ratner, B. D. *Surf Interface Anal* **2008**, *40*, 1356.
- (115) Borba, A.; Gomez-Zavaglia, A.; Simoes, P. N.; Fausto, R. *Spectrochim Acta A Mol Biomol Spectrosc* **2005**, *61*, 1461.
- (116) Haynes, B. F.; Shattock, R. J. *J Allergy Clin Immunol* **2008**, *122*, 3.
- (117) Poelvoorde, N.; Verstraelen, H.; Verhelst, R.; saerens, B.; De Backer, B.; dos

- Santosn Santiago, G. L. *Off. J. Arbeitsgemeinschaft fur Pharm. Verfahrenstechnik eV.* **2009**, 73, 280.
- (118) Alukda, D.; Sturgis, T.; Youan, B.-B. *J. Pharm. Sci.* **2011**, 100, 3345.
- (119) Bilancetti L; Poncelet, D.; Loisel, C.; Mazzitelli, S.; Nastruzzi, C. *AAPS Pharm. Sci. Tech.* **2010**, 11, 1257.
- (120) Li, X.; Anton, N.; Arpagaus, C.; Belleiteix, F.; Vandamme, T. F. *J. Control Release* **2010**, 147, 304.
- (121) Peltonen, L.; Valo, H.; Kolakovic, R.; Laaksonen, T.; Hirvonen, J. *Expert Opin. Drug Deliv.* **2010**, 7, 705.
- (122) Leitner, V.; Walker, G.; Bernkop-Schnurch, A. *Off. J. Arbeitsgemeinschaft fur Pharm. Verfahrenstechnik eV.* **2003**, 56, 207.
- (123) Li, X.; Kong, X.; Shi, S.; Zheng, X.; Guo, G.; Wei, Y. *BMC Biotechnol.* **2008**, 8, 89.
- (124) Shinde, U. A.; Nagarsenker, M. S. *Indian J. Pharm. Sci.* **2009**, 71, 313.

Chapter 3

ANALYSIS OF CALCINED CLAY AS A SUPPLEMENTARY CEMENTITIOUS MATERIAL: A CASE STUDY OF CLAY FROM GHANA

Introduction

Calcined clay is an important and well-researched material which is used as a supplementary cementitious material (SCM) in concrete production. The construction industry around the globe has embraced SCMs as cement substitutes in promoting sustainable construction. SCMs reduce harmful anthropogenic gases contributed by cement manufacturing plants¹, reduce the dependence on natural resources for cement production², as well as significantly reducing cost of concrete production³. SCMs are classified into three categories namely; fillers, pozzolanic and hydraulic materials. Fillers are inert materials which contribute little to the hydration of cement. Pozzolanic materials are typically fine alumino-silicates that chemically react with calcium hydroxide to form additional calcium silicate hydrate and other cementitious compounds. Hydraulic materials chemically reacts with water to form cementitious compounds⁴. Examples of filler materials are chalk and limestone and that of pozzolanic materials include fly ash, silica fume, calcined clays, while steel slag and ground granulated blast furnace slag (slag cement) are primarily characterized as hydraulic materials.

Clay minerals undergo thermal activation to become reactive with Portland cement during hydration. The thermal activation process is usually achieved through calcination. At appropriate calcination temperatures these thermally activated clays become more reactive with cement and can improve strength and durability of concrete. Generally it has been found that temperatures between 500°C and 900°C are suitable to produce reactive

clays⁵. However, the exact calcination temperature suitable to activate clay thermally is dependent on the clay origin, chemistry, and amount and type of impurities. Clays are classified into kaolinitic, smectite and the illite groups⁶. Kaolinitic group includes kaolinite, nacrite, and nickite whereas the smectite group includes montmorillonite, nontronite, biedelollite. The illite group are made of Illite and Glauconite⁷. Fundamentally a clay mineral has different structures and compositions, however the basic building blocks are all the same⁸. The building blocks form sheets of tetrahedral and octahedral layer which defines the atomic structure of every clay mineral. The kaolinitic group are made of a 1:1 layer, i.e. a tetrahedral sheet and an octahedral sheet. Both the smectite and the illitic group also consist of a 2:1 layer, i.e. an octahedral sheet in-between two opposing tetrahedral sheets⁷. In a clay mineral, tetrahedral sheet is always combined with octahedral sheet.

During heating, three processes occur which are dehydroxylation, calcination, and crystallization. During dehydroxylation octahedral sheets lose water and transform into a meta-stable state⁹. In the metastable state amorphous materials are produced which are more reactive to free calcium hydroxide present during hydration. The end of the dehydroxylation process marks the calcination temperature. The calcination temperature also influences the environment of the layered silicate which is also an indicative of the reactivity of calcined clays¹⁰. At high temperature the clay minerals begin to crystallize which decreases reactivity. At about 600°C kaolinitic clays becomes fully dehydroxylize, whilst the smectite and the illitic groups dehydroxylizes above 600°C¹¹. Hydroxyls are not as strongly bound in kaolinite clays compared to smectites and illites which explains the differences in the calcination temperature. Qualitative techniques such as Thermal Gravimetric Analysis (TGA) and Fourier Transform Infrared Spectroscopy (FTIR), and

quantitative tools like Nuclear Magnetic Resonance (NMR) are able to provide meaningful characterizing of thermally activated clays. TGA determines the extent of dehydroxylation whereas FTIR determines the anionic functional groups^{11,12}. Solid state NMR is clearly a very powerful technique capable of looking at a variety of materials. It does not require crystalline materials like diffraction techniques, and can still determine local molecular environments. SS NMR helps in quantifying the structural features of amorphous materials¹⁰. NMR probes into the isotropic chemical shift of Silicon tetrahedral and Aluminum octahedral in either a calcined clay or a binder hydrate. Both qualitative and quantitative techniques uniquely support each other to limit the level of uncertainties in the characterization techniques and pozzolanic activity.

Ghana, a West African nation, and other neighboring countries do not have an abundance of commonly used SCMs such as fly ash, silica fume, metakaolin, and slag. However, the abundance of clay minerals in the country could provide a sustainable alternative with respect to SCMs application³. Previous research has characterized the strength performance of thermally activated clay^{13,14}. However there is little information on the phase transformation of thermally activated Ghanaian clay and their relation with strength activity. In this study, clay from Ghana was thermally activated at temperatures of 600, 700, 800, 900 and 1000°C. The main objective was to characterize calcined clay using TGA, FTIR, NMR, and their relation to pozzolanic activity to best understand the potential of this abundant resource to alleviate cement supply burdens.

Materials

The materials used for the study were clay, cement, silica sand, polycarboxylate high range water reducer (HRWR), and potable water. The clay was obtained from

Nyamebekyere in the Ashanti Region area of Ghana. Portland cement conformed to ASTM C150 both Type I and Type II and was obtained from Ashgrove cement plant in Chanute, Kansas. Graded silica sand used conformed to ASTM. A polycarboxylate HRWR, obtained from BASF Chemical Company conforming to ASTM C595 was used.

Methods

1] Thermal Analysis

TGA results were obtained using a Mettler Toledo TGA/ SDTA 851 e analyzer heated to 1200°C, ramping 15°C per minute in N₂ gas.

2] Clay Calcination

Calcination of clay samples were performed in a laboratory furnace (Barnstead Thermolyne 6000 furnace). A known mass was placed in ceramic bowls and heated at different temperatures of 600°C, 700°C, 800°C, 900°C and 1000°C for three hours. The calcined samples were then allowed to cool in the furnace to room temperature.

3] FTIR

Attenuated total reflectance infra-red spectroscopy was conducted using NICOLET iS10 FT-IR spectrometer equipped with a fast recovery deuterated triglycine sulfate (DTGS) detector and an extended KBr beamsplitter. Infra-red spectrum were obtained from 4000 to 600 cm⁻¹ and 512 acquisitions were added at a spectral resolution of 2 cm⁻¹. All spectral measurements were carried out at room temperature.

4] ²⁷Al and ²⁹Si Solid State MAS NMR

Tecmag Apollo Console (Houston, TX) with 8.45 T magnet and homebuilt, single channel, 4 mm wide-bore NMR probe was used to determine ²⁷Al and ²⁹Si spectra. About 90 mg of sample was taken for each analysis and signals are represented as chemical shift

value; δ : ppm. The ^{27}Al and ^{29}Si Larmor frequencies were 93.074 MHz and 70.958 MHz respectively. ^{27}Al spectra were acquired with MAS spinning frequency, last delay and 90° pulse length of 8 KHz, 1 s and 2.5 μs , respectively. ^{29}Si spectra were acquired with MAS spinning frequency, last delay and 60° pulse length of 8 KHz, 20 s and 5.5 μs , respectively. Aluminum nitrate [$\text{Al}(\text{NO}_3)_3$] and tetramethyl silane (TMS) were used as reference compounds for ^{27}Al and ^{29}Si NMR spectra respectively. All experiments were performed at ambient temperature without any corrections for sample heating.

5] Pozzolanic Activity

The pozzolana activity was determined according to the description of ASTM C618 and ASTM C311. This standard explains the determination of pozzolanic activity using the strength activity index (SAI) as well as pozzolana replacement dosage. SAI were determined on mortar samples. Mortar samples were prepared in accordance with ASTM C109 and cured in lime water bath for a period of 7 and 28 days. As per the ASTM C311, cement were replaced with calcined clay at 20%. The water-to-cement ratio was maintained at 0.485 and the ratio of cementitious material (Portland cement plus calcined clay) to sand was set at a ratio of 2.75 to 1. To achieve the desired flow according to ASTM C1437, the polycarboxylate HRWR was used. SAI was measured on an average of three mortar specimens. The SAI was calculated based on this formula-

$$SAI = [1 - (\frac{CS_o - CS_i}{CS_o})] \times 100\%$$

Where: CS_o is the compressive strength without pozzolan, CS_i is the compressive strength with calcined clay.

Results and Discussions

Calcined Clay Characterization

1] Thermal Analysis

Figure 1 presents the TGA results of the clay powder showing that four different processes occurred. The first two peaks, A and B that preceded the dehydroxylation peak C represented the evaporation of adsorbed water and decomposition of organic particles. The dehydroxylation of the clay started from 325°C to approximately 731°C. Figure 1, shows that the effective calcination temperature was at 731°C. The temperatures between 731°C and 905°C showed a complete dehydroxylation of the clay material. Complete dehydroxylation of clay mineral, indicated between 731°C and 904°C, shows that octahedral aluminium sheets dehydroxylized into a metastable disordered state, collapsing a higher quantity of crystalline clay minerals to produce a more reactive calcined clay⁹. The temperature between 905°C and 1036°C labelled as D also showed the formation of crystal growth of mullite phases. The growth of crystals shown between 905°C and 1036°C support the argument of Fernandez et al¹¹ that at higher temperatures a metastable state transforms from amorphous condition into crystalline units which inhibits reactivity of calcined clays.

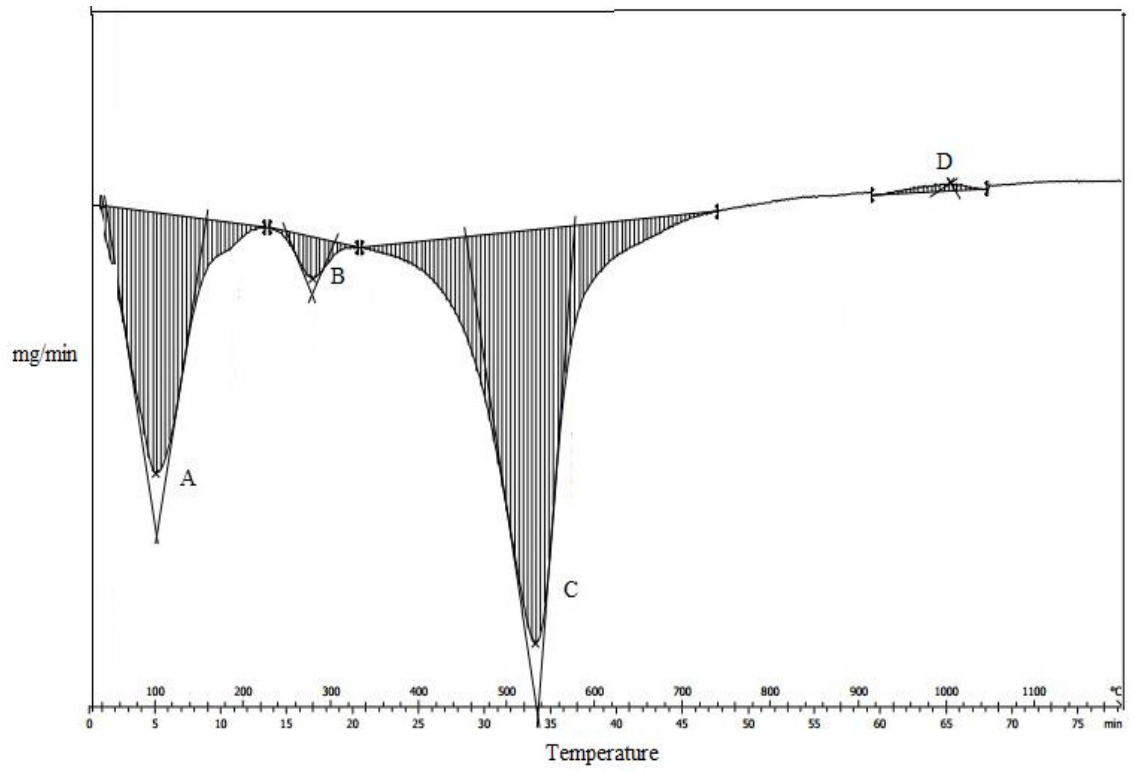


Figure 3.1. DTA results of powdered clay.

2] FTIR Analysis

Figure 2, presents the FTIR results of the raw and clay calcined between 600°C and 1000°C. The figure shows vibration band occurring between approximately 690 and 1800 cm^{-1} and molecular vibration from 1800 to 3700 cm^{-1} . The raw clay showed distinctive vibration bands at 3693, 3651 and 3619 cm^{-1} conforming a metal bonded to hydroxide group. This is most likely to be a kaolinite structure¹⁵. Absorption bands corresponding to Al-O and Si-O were also observed at 1162, 1109, 1025, 999, 910, 777 and 692 cm^{-1} ¹⁶. The clay calcined between 600-1000°C showed the disappearance of the kaolinite structures as well as the water molecules. This indicates a change from a crystalline structure to an amorphous or metastable structure¹⁷. The vibrational atoms that corresponded to Al/Si-O at 1162, 1109, 1025, 999 and 910 cm^{-1} were seen disappearing after calcination, whilst absorption bands at 777 and 692 cm^{-1} . The disappearance of the absorption bands meant a change from octahedral coordination of Al^{+3} to a tetrahedral coordinated environment¹⁸.

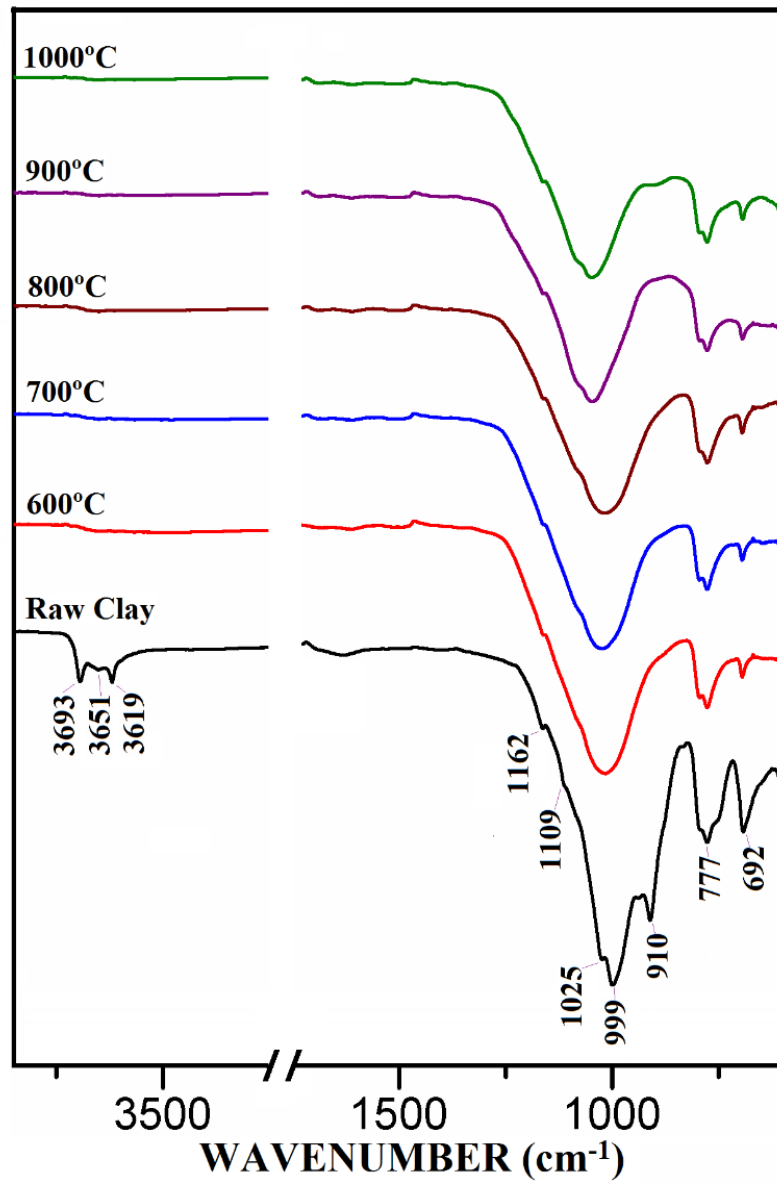


Figure 3.2. FTIR spectra of raw clay and clays calcined at temperatures 600-1000°C.

3] ^{27}Al SS MAS NMR

^{27}Al (spin = 5/2) is quite sensitive nucleus to perform SS NMR studies on and hence can be readily detected and hence, ^{27}Al SS MAS NMR spectroscopy is widely used to characterize aluminate phases. One must also understand the disadvantage of using ^{27}Al MAS NMR spectroscopy for ^{27}Al is a quadrupolar nucleus which can pose difficulties in spectral interpretation as ^{27}Al nucleus is affected by the quadrupolar interaction. Quadrupolar interaction is additionally affected by electric field gradients within the sample and leads to a field-dependent shift in resonance position and a broadening of the peaks. In the presence of overlapping quadrupolar resonances from several sites, the spectra can be very difficult to deconvolute, especially in the case of disordered solids where line shapes are not well defined.

Solution state NMR of quadrupolar nuclei is often fashioned with complications, mainly because of the rapid relaxation of the quadrupolar nucleus due to the large quadrupolar interaction (which may be on the order of MHz). At best, very broad peaks are observed. NMR of half-integer quadrupolar nuclei has become quite commonplace, and allowed investigation of a broad array of materials. Recent technological advancements and new pulse sequences have opened up the periodic table (73% of NMR active nuclei are quadrupolar nuclei) to solid-state NMR. The strange broadening effects of quadrupolar nuclei, once viewed as a hindrance to performing such experiments in the solid state, are now exploited to provide invaluable information on solid state chemistry, structure and dynamics. Although, 4-coordinate and 6-coordinated aluminum can readily be distinguished it is rather essential to discuss the theoretical aspects of NMR of quadrupolar nucleus in order to be able to interpret its spectra.

Quadrupolar nuclei have a spin $> 1/2$, and an asymmetric distribution of nucleons giving rise to a non-spherical positive electric charge distribution; this is in contrast to spin- $1/2$ nuclei, which have a spherical distribution of positive electric charge. The asymmetric charge distribution in the nucleus is described by the nuclear electric quadrupole moment, eQ , which is measured in barn (which is ca. 10^{-28} m^2). eQ is an intrinsic property of the nucleus, and is the same regardless of the environment. Quadrupolar nuclei interact with electric field gradients in the molecule. Electric field gradients are spatial changes in electric field in the molecule. Like the dipolar interaction, the quadrupolar interaction is a ground state interaction, but is dependent upon the distribution of electric point charges in the molecule and resulting electric field gradients. For a quadrupolar nuclei in the center of a spherically symmetric molecule, electric field gradients cancel one another resulting in a very small final electric field gradient at the quadrupolar nucleus. As the spherical symmetry breaks down, the electric field gradients at the quadrupolar nucleus grow in magnitude.

The ^{27}Al solid state magic angle spinning (MAS) nuclear magnetic resonance (NMR) spectra of raw and calcined clay from 600°C - 1000°C are presented in figure 3. The raw clay showed two distinct peaks which resonated at 68 ppm and -0.8 ppm respectively and indicated a 1:1 kaolinite group of clay. As it has already been explained from literature, a 1:1 group represents an octahedral and a tetrahedral sheets¹⁹, confirmed that tetrahedral sheet resonates from 50 ppm to 80 ppm whereas the octahedral sheet resonates from -20 ppm to 20 ppm.

Calcined clays exhibited an increase in the intensities of $\text{Al}^{(\text{iv})}$ and decrease in the intensities at the $\text{Al}^{(\text{vi})}$ environment with reference to the raw clay which indicated greater

reactivity of calcined clays^{20,21}. It was observed that calcined clays at 900°C and 1000°C had low and similar intensities at the Al^(vi) environment. Again, from the results of the TGA shown in Figure 1, the most appropriate temperature that may give higher amorphousness or disorderliness of calcined clay could be attained either at 700°C or 800°C. The intensities of the results at the four-coordinated environment of ²⁷Al were very difficult to attain because of the nature of the reference clay peak. The nature of the peak shown at 68 ppm on the spectra of the reference clay is subjected to produce higher error of margin being merged with the adjacent spinning side band (indicated by Asterisk). This limitation hindered our interest in calculating the respective peak areas of all the peaks at 68 ppm at various temperatures of calcination.

Table 3.1 Solid State NMR spectra indicating position and peak areas of respective peaks of ²⁷Al and ²⁹Si. Peak areas are calculated considering Raw Clay as a control.

<u>Dry Cement</u>	<u>²⁷Al SS NMR</u>		<u>²⁹Si SS NMR</u>	
	ppm	Peak Area (%)	ppm	Peak Area (%)
Raw Clay	-0.8	100	-126	100
600°C	-0.3	13	-126	320
700°C	-1.8	6	-126	328
800°C	-0.3	9	-126	335
900°C	-2.8	2	-126	800
1000°C	-6.3	2	-126	726

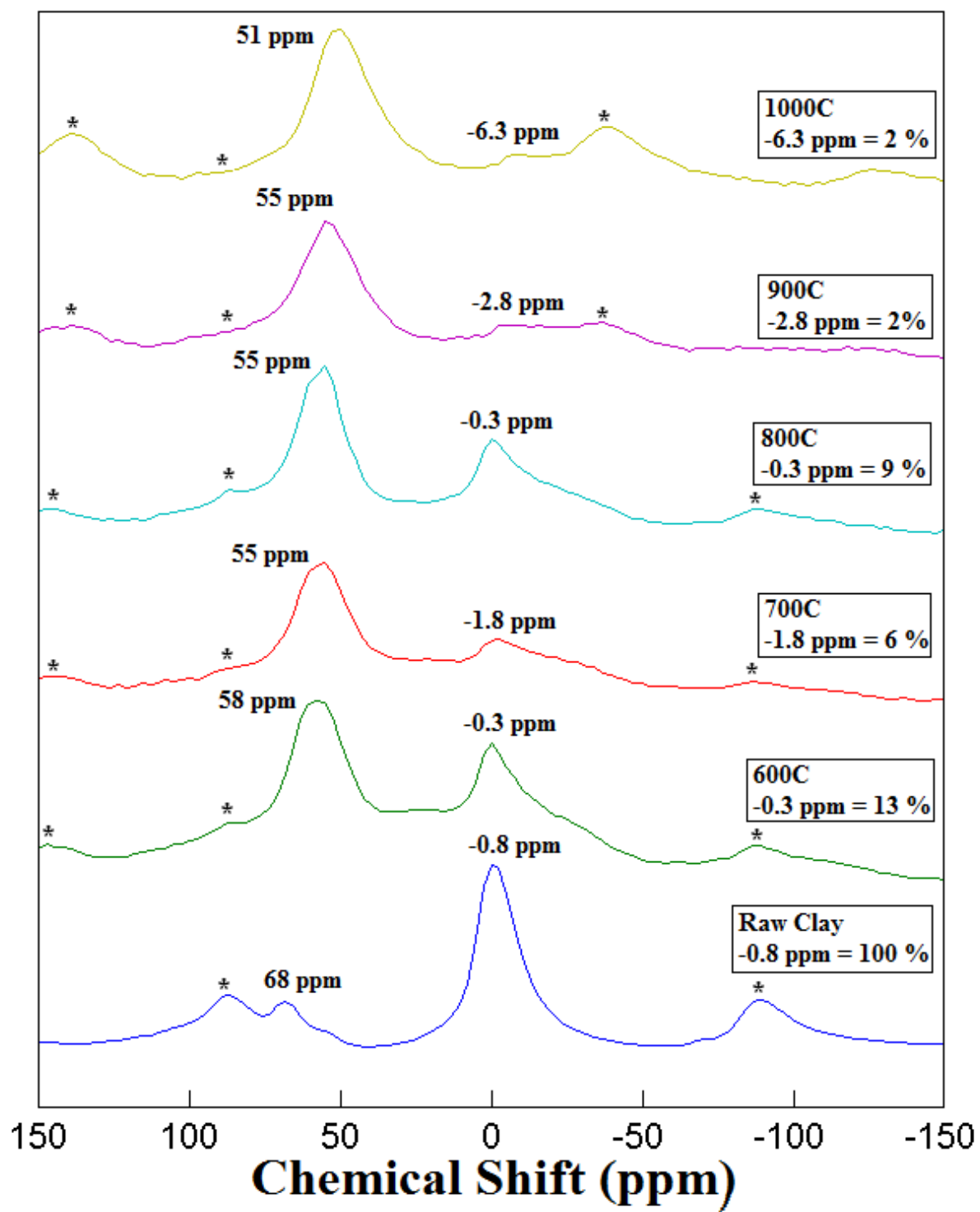


Figure 3.3. ^{27}Al SS MAS NMR spectra of raw clay and clays calcined at temperatures 600-1000°C. The spinning side-bands are indicated by Asterisk.

4] ^{29}Si SS MAS NMR

^{29}Si NMR spectra are normally interpreted in terms of the different silicon Q environments, where n denotes the number of bridging oxygens for each Q (SiO_n) unit and hence, ^{29}Si SS MAS NMR spectroscopy has proven to be extremely useful in the structural characterization of silicates and typical ordinary Portland cements, and also to investigate the hydration of pure C_3S and $\beta\text{-C}_2\text{S}$ phases. In hydrated cements, these show the presence of Q^0 units due to orthosilicate groups, Q^1 units from Si-O-SO_3 groups in dimers or terminating polymers, and Q^2 units from Si-O-Si-O-Si groups in trimers and higher polymers.

Figure 4, presents the ^{29}Si solid state mass angle spinning (MAS) nuclear magnetic resonance (NMR) of raw and calcined clay from 600°C - 1000°C . Raw clay showed a chemical shift at -110 ppm and -126 ppm. This shift corresponds to Q^4 silicon coordinated environment²². The process of calcination collapsed one of the Q^4 population in the raw clay remaining another one Q^4 population which increased progressively in intensities as calcined temperatures increased. Calcined temperatures at 900 and 1000°C indicated a higher intensities which could be due to the presence of recrystallized quartz shown in the TGA graph. TGA results have already shown that calcined clay between 900 and 1000°C may be less reactive because of crystalline products. Moreover the TGA has also shown that calcined materials at 700 and 800°C may be more reactive. However, Figure 4 confirms that calcined clay at 800°C could possess more reactive phases than calcined materials at 700°C due to the high intensity obtained at the Q^4 silicon population.

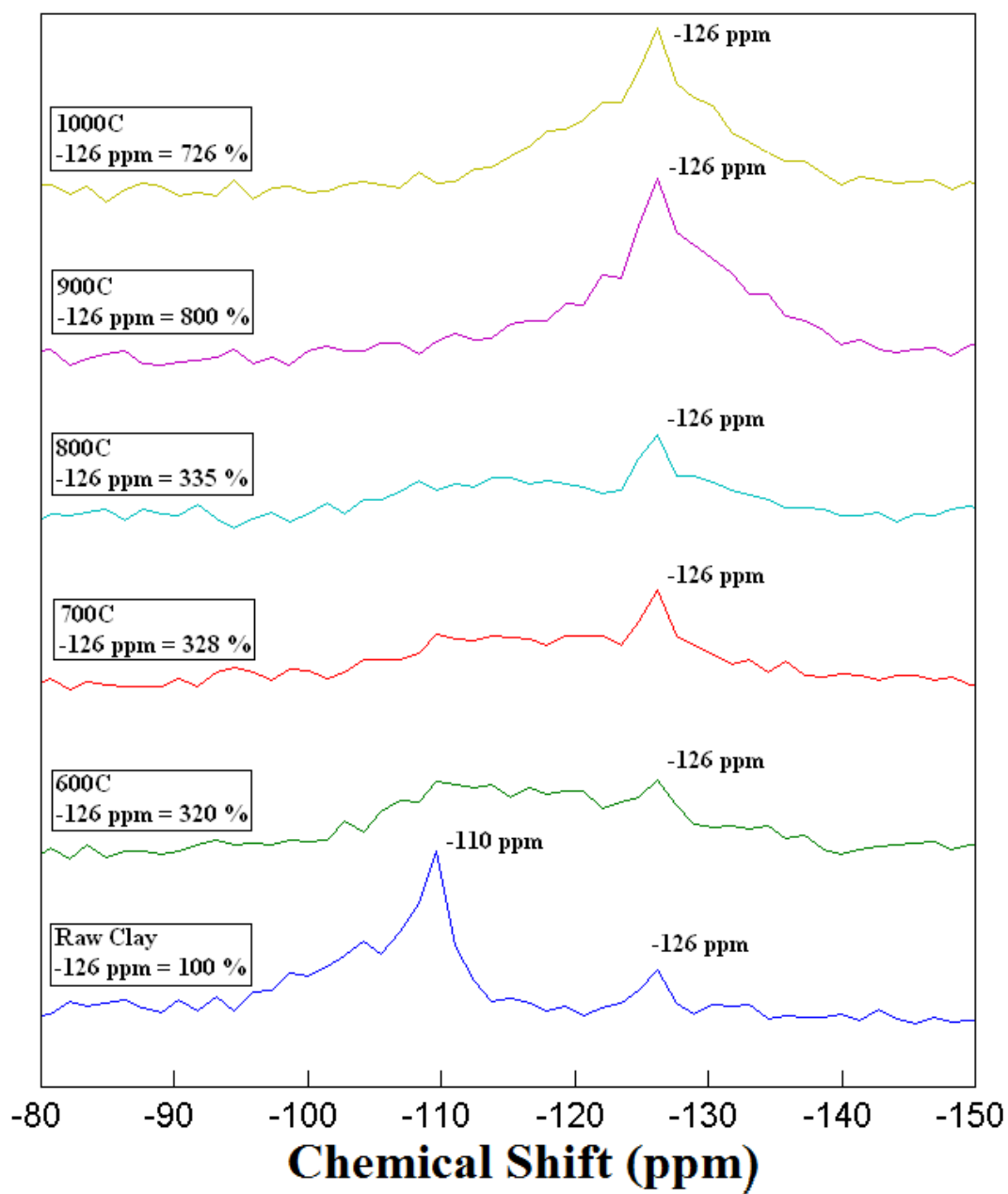


Figure 3.4. ^{29}Si SS MAS NMR spectra of raw and calcined clays.

5] Pozzolanic Activity

Table 2, shows the mortar mixture proportions of calcined clay pozzolan. The table shows that the flow for the mortar mixtures were between 106 and 116 which was within the acceptable range specified in the ASTM C1437. HRWR content reduced at temperatures of 900°C and 1000°C compared with materials calcined from 600°C-800°C. The reduction of HRWR at 900°C and 1000°C indicate a reduction in the particle surface area and absorption properties of the powder materials which is confirmed from the TGA results. The formation of crystalline substances reduces the two, surface area and porosity^{23,24}.

Figure 5, provides the results of the SAI of the calcined clay pozzolan. Calcined clay at 800°C attained the maximum strength at 7 and 28 days as compared to the control mortar mixture. This shows that at 800°C, the clay powder was completely calcined forming active pozzolanic phases which are very reactive with cement than the other temperatures used to calcine the clay. Tironi et al¹⁷, indicated that at optimum calcination temperature strength improves due to the pozzolanic active phases (amorphous phases) formed.

Table 3.2. Mortar mix proportion for strength activity index of calcined clays at 7 and 28 days.

Temp (°C)	Mix Name	Mass (g)					w/b	HRWR (%)	Flow (%)
		Cement	Clay	Sand	Water				
Control	C	500	0	1375	242	0.485	0	106	
600	20P600	400	100	1375	242	0.485	0.4	111	
700	20P700	400	100	1375	242	0.485	0.4	110	
800	20P800	400	100	1375	242	0.485	0.4	110	
900	20P900	400	100	1375	242	0.485	0.3	115	
1000	20P1000	400	100	1375	242	0.485	0.2	116	

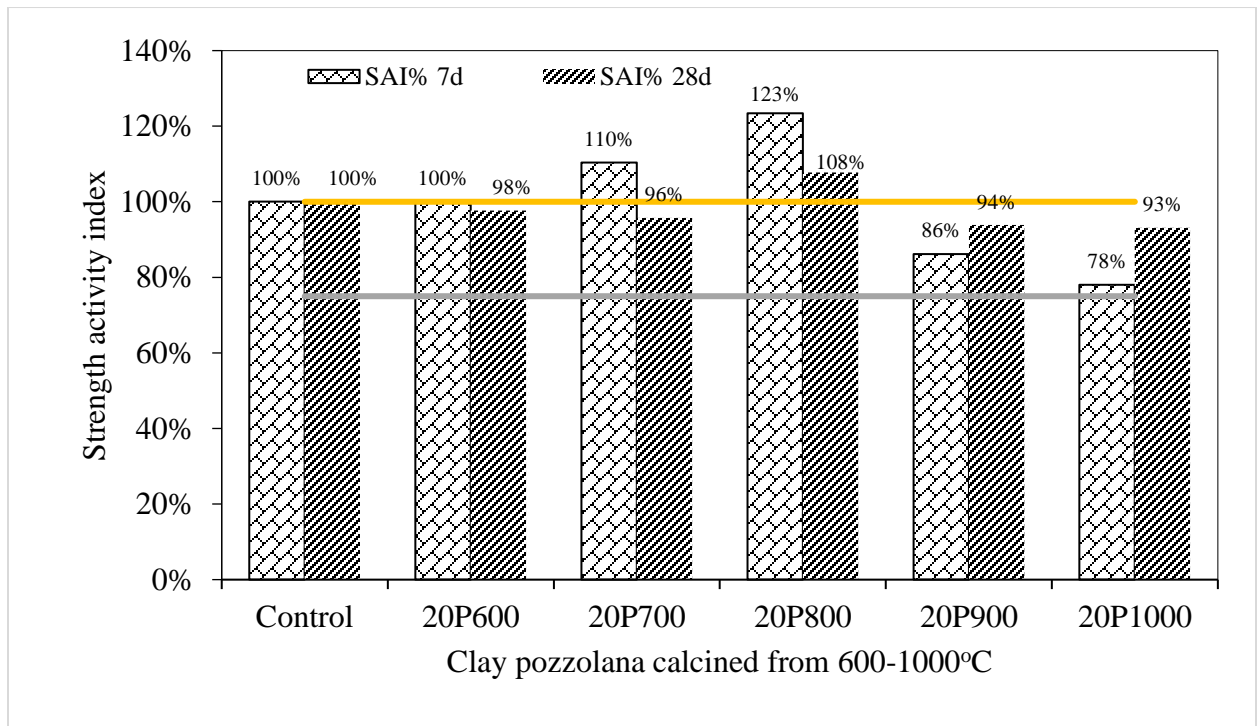


Figure 3.5. Strength activity index of calcined pozzolan.

6] Influence of Calcined Clay (800°C) on Cement Hydration using ^{27}Al SS MAS NMR Spectroscopic Technique

Figures 6,7,8, presents the ^{27}Al SS MAS NMR results of hydrated binder paste mixture of the unblended cement as well as blended mixtures between cement and calcined clay at 800°C. Figures 6,7,8, presents hydration at 3, 7 and 28 days respectively showing two distinct peaks. The studies^{25,26} have shown that chemical shift between 8 and 11.8 ppm corresponds to monosulphates whereas chemical shifts between 66 and 72 ppm corresponds to Al environment replacing Silicon in the tetrahedral environment of Aluminum. The diffused peaks around 8 ppm shown in Figures 6,7,8, represents monosulphate (AFm) present in the aluminosilicate hydrates or stratlingite formed whereas around 68 ppm, it could be seen that Al substituted Silicon in the tetrahedral environment. The peak relating to Afm grew with age from 3 days to 28 days and this is indicative of more Aluminum passing into cement solution forming stratlingite containing Afm phases¹¹. The intensity of the cement and calcined clay at 3 days which gave 114% as against 100% of the control, showed that the material was very reactive at early ages and even at the 7 day period of hydration.

The performance of the cement blended mixture at early ages indicated that the calcined clay behaved as a filler material. At 28 days, the cement blended material showed the highest intensity of 194% as compared to 100% intensity of plain cement. This shows that pozzolanic reaction occurred at the late stage of 28 days forming more of the stratlingite phases. The figure also indicated that the presence of the Afm phases virtually diminished the presence of ettringite phases (AFm). This is very important because

expansion due to ettringite was seen to be eliminated with the case of using cement and calcined clay as alternative binder materials.

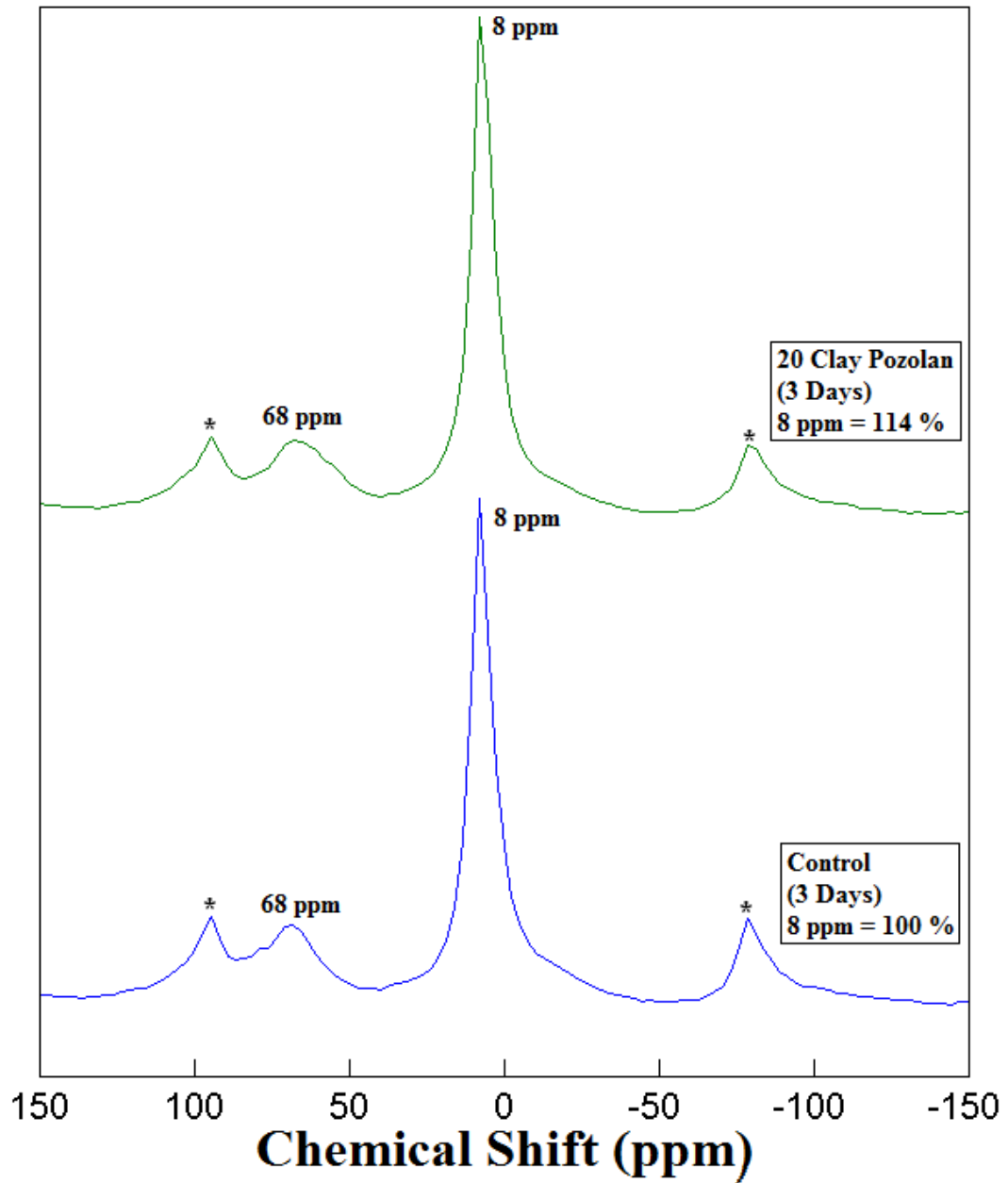


Figure 3.6. ^{27}Al SS MAS NMR spectra of hydrated cement '20 Clay Pozzolan' at 3 days.

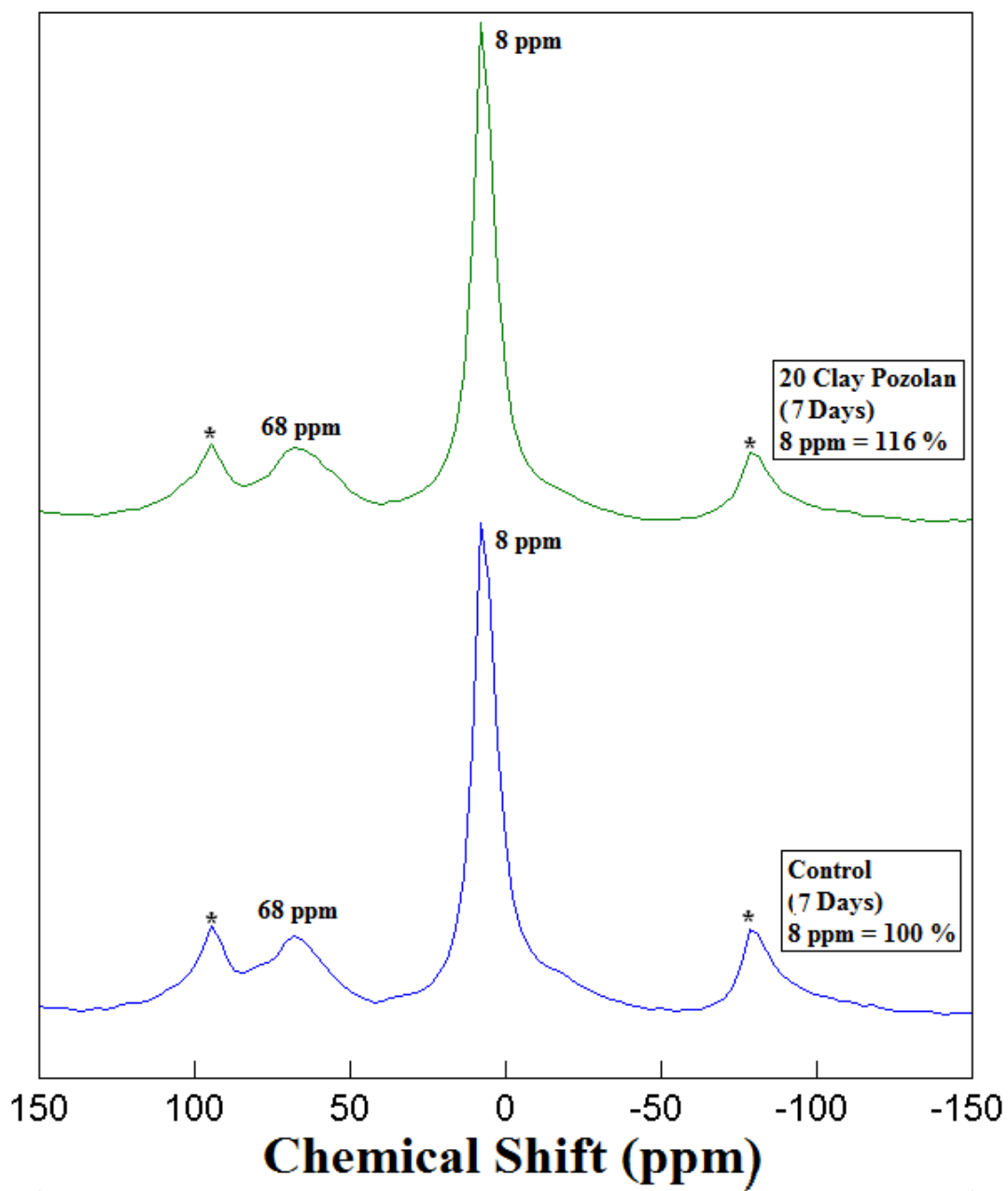


Figure 3.7. ^{27}Al SS MAS NMR spectra of hydrated cement '20 Clay Pozzolan' at 7 days.

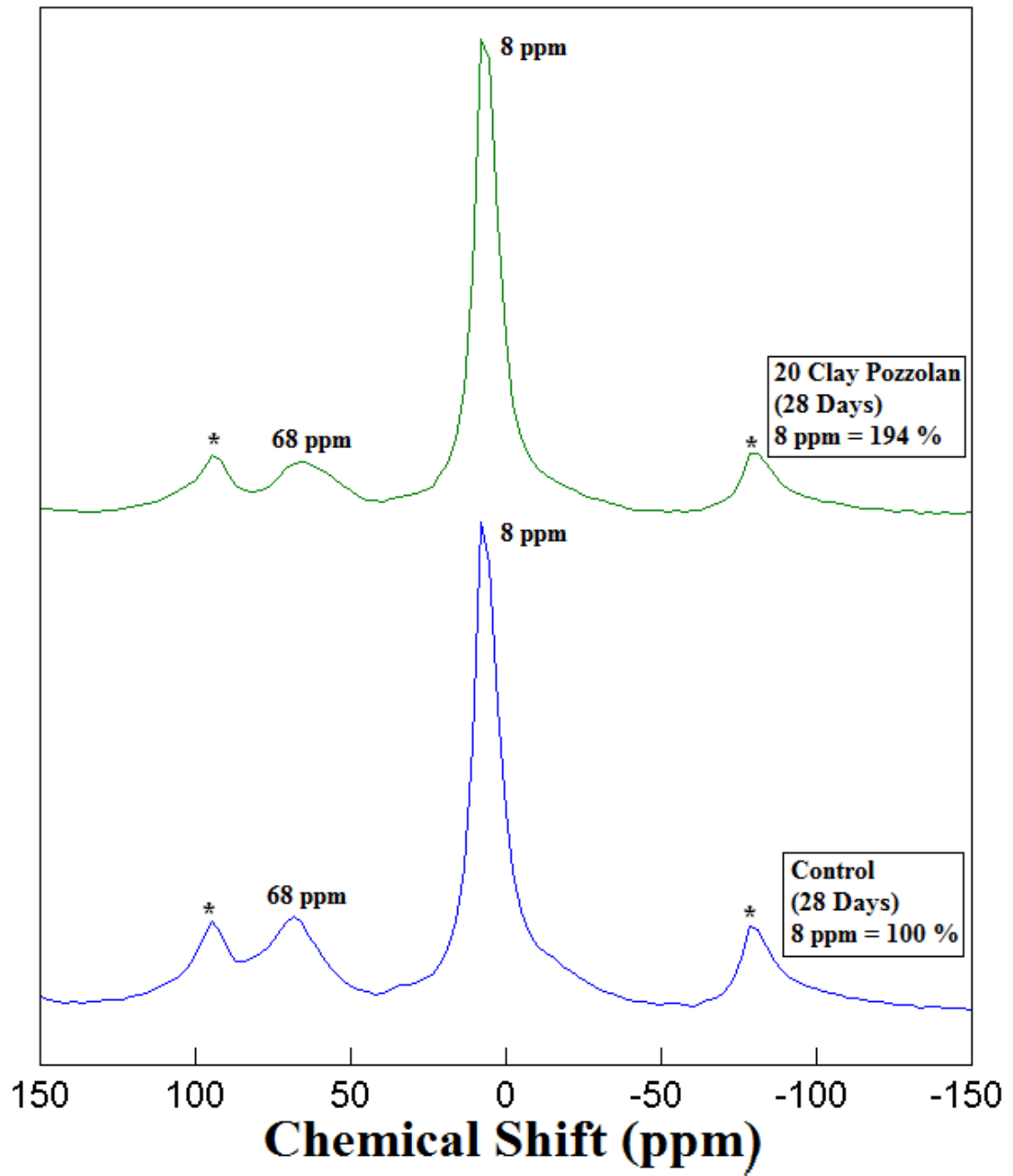


Figure 3.8. ^{27}Al SS MAS NMR spectra of hydrated cement '20 Clay Pozzolan' at 28 days.

Overall in conclusion, there is a growing interest on the use of calcined clays as suitable supplementary cementitious materials (SCMs) for construction in recent times. However, the origin of clay presents some form of variations which therefore influences their use as supplementary cementitious material. This study seeks to analyze clay obtained from the Nyamebikyere area of Ghana. The Ghanaian clay was calcined at temperatures of 600, 700, 800, 900 and 1000°C in a laboratory furnace. The properties of the raw and calcined clay were characterized using thermal gravimetric analysis (TGA) and, ^{27}Al and ^{29}Si solid state magic angle spinning nuclear magnetic resonance (SS MAS NMR) and Fourier transformed infrared (FTIR) spectroscopic techniques. Pozzolanic strength activity indices (PSAI) were determined by replacing Portland cement with 20% of the calcined materials. The results from the ^{27}Al SS MAS NMR showed that the clay was a 1:1 kaolinitic clay type. The PSAI results were corroborated with the TGA, ^{27}Al and ^{29}Si SS MAS NMR and the FTIR spectra results to achieve the optimum calcination temperature, which indicated that clay calcined at 800°C attained a more reactive pozzolanic phases which consequently influenced positively on the strength activity index. The study recommends calcination temperature of 800°C as the most appropriate temperature for the Nyamebikyere clay in Ghana.

Nyamebikyere clay used for the study could be classified as a 1:1 kaolinitic clay type from the ^{27}Al SS MAS NMR studies. The optimum temperature that yielded more reactive pozzolanic phases was obtained at 800°C. The influence of calcined clay in the cement blended material showed that the calcined material behaved partly as a filler and partly as a pozzolanic material. The filler effect accelerates portlandite growth which enhances early strength whereas the pozzolanic effect enhances late strength. Calcined

clays at 800°C used to replace Portland cement at 20% gave the maximum strength. This was attributed to the influence of the calcined clay which produced more stable aluminate phases including calcium aluminate hydrate (CAH), and stable form of monosulphate (AFm).

References

- (1) Sabir, B. B.; Wild, S.; Bai, J. *Cem. Concr. Compos.* **2001**, *23*, 441.
- (2) Samet, B.; Mnif, T.; Chaaboni, M. *Cem. Concr. Compos.* **2007**, *29*, 741.
- (3) Bediako, M.; Gawu, S. K. Y.; Adjaottor, A. A. *Constr. Build. Mater.* **2012**, *29*, 667.
- (4) Kosmatka, S. H.; Kerkhoff, B.; Panarese, W. C. *14th Ed. Portl. Cem. Assoc. Skokie*, **2002**, 39.
- (5) Hellar-Kallai, L. *Bergaya Theng, B.K.G.; Leg. G. (Eds), Handb. clay Sci. Dev. clay Sci. Elsevier* **2006**, 289.
- (6) Guggenheim, S.; Martin, R. T. *Clay. Clay. Miner.* **1995**, *43*, 255.
- (7) Guggenheim, S.; Adams, J. M.; Bain, D. C.; Bergaya, F.; Brigatti, M. F.; Drits, V. A.; Formoso, M. L. L.; Galan, E.; Kogure, T.; Stanjek, H. *Clay. Clay. Miner.* **2006**, *54*, 761.
- (8) Zhou, C. H.; Keeling, J. *Appl. Clay. Sci.* **2013**, *74*, 3.
- (9) Mendelovici, E. *J. Therm. Anal.* **1997**, *49*, 1385.
- (10) Mendess, A.; Gates, W. P.; Sanjayan, J. G.; Collins, F. *Mater. Struct.* **2011**, *44*, 1773.
- (11) Fernandez, R.; Martinez, F.; Scrivener, K. L. *Cem. Concr. Res.* **2011**, *41*, 113.
- (12) Ylmen, R.; Wadso, L.; Panas, I. *Cem. Concr. Res.* **2010**, *40*, 1541.
- (13) Bediako, M.; Frimpong, A. O. *Mater. Sci. Appl.* **2013**, *4*, 20.
- (14) Bediako, M.; Atiemo, E. *J. Sci. Res. Reports* **2014**, *3*, 3017.
- (15) Van der Marel, H. Elsevier, Amsterdam **1976**.
- (16) Russel, J. D. Wiley, New York **1987**.
- (17) Tironia, A.; Trezza, M. A.; Irassar, E. F.; Scian, A. N. *Procedia Mater. Sci.* **2012**, *1*, 343.
- (18) Ilic, B. R.; Mitrovic, A. A.; Milicic, L. R. *Hem. Ind.* **2010**, *64*, 351.
- (19) Hanna, R. A.; Barrie, P. J.; Cheeseman, C. R.; Hills, C. D.; Buchler, P. M.; Perry, R. *Cem. Concr. Res.* **1995**, *25*, 1435.
- (20) Klimesch, D. S.; Lee, G.; Ray, A.; Wilson, M. A. *Adv. Cem. Res.* **1998**, *30*, 93.
- (21) Pena, P.; Rivas-Mercury, J. M.; de Aza, A. H.; Turrillas, X.; Sobrados, I.; Sanz, J. *J. Solid State Chem.* **2008**, *181*, 1744.
- (22) Stebbins, J. F.; Kanzaki, M. *Science (80-.)*. **1991**, *251*, 294.
- (23) Kartina, K. *Appl. Sci. Tech.* **2011**, *1*, 169.
- (24) Moodi, F.; Ramezani-pour, A. A.; Safavizadeh, A. *Scintia Iran. A* **2011**, *18*, 906.
- (25) Skibsted, J.; Henderson, E.; Jakobsen H.J. *Inorg. Chem.* **1993**, *32*, 1013.
- (26) Anderson, M. W.; Teisl, M.; Noblet, C. *Ecol. Econ.* **2012**, *84*, 1.

Chapter 4

INFRARED AND RAMAN SPECTRAL STUDIES TO OBTAIN STRUCTURAL PARAMETERS, CONFORMATIONAL STABILITY, VIBRATIONAL ASSIGNMENTS AND *AB INITIO* CALCULATIONS OF ORGANIC MOLECULES CONTAINING FIVE MEMBERED RING AND PHOSPHOROUS

Introduction

The physiochemical properties of a molecule of interest are usually obtained from its molecular structure, and it involves the orientation of one part of the molecule about a particular bond with respect to the rest of the molecule. These properties depend mainly upon the three-dimensional arrangement of one part of the molecule in space with respect to the other and, additionally, the way the molecule will react chemically and its available reaction pathways are often critically dependent upon the orientation of the reactant molecule. The energy differences of various conformations generally strongly couple or interact by way of non-bonded interactions which even though are individually too weak to determine, any single geometric feature may nevertheless act together to uniquely determine the spatial structures of large and complicated molecules such as proteins and DNA. Therefore, conformational analysis can lead to significant improvement in the understanding of more complex system.

The field of biochemistry and nano-chemistry has caused a great deal of interest in conformational stability due to its effects on binding sites of proteins in biochemistry and the use of conformer interchange to drive molecular motions and shapes in nano-chemistry. Examples of substituted five-membered rings are the backbone sugar groups of DNA and RNA. In the case of DNA and RNA the five-membered ring has an oxygen in the ring and

so it adopts a planar conformation which helped to determine the structure of both DNA and RNA.

The saturated five-membered ring molecules are structurally interesting, since they can be in one or more of the three stable conformers, i.e. *twisted*, *envelope*, and *planar* forms. Several monosubstituted cyclopentanes were determined to have two conformations at ambient temperature where the substituent occupies the *axial* and *equatorial* positions at the tip of the C_s symmetric *envelope* form of the five-membered ring¹⁻⁵. For many of the molecules the vibrational spectra were used to first identify the two forms before they were identified by microwave spectra and electron diffraction investigations. Furthermore, the energy difference between these forms can be very small with the barrier for the molecule to go from one form to another also quite small. Thus, instead of going through the planar form, the molecule may go through a series of twisted forms where one atom moves perpendicular to a hypothetical plane of the rest of the atoms. This concept which was first proposed by Pitzer and he called it pseudorotation.

Professor Pitzer's reason for proposing the pseudo rotations for the five-membered rings was based on his thermodynamic information but this concept certainly was not accepted. Nevertheless, the five-membered saturated ring is an important unit in Organic Chemistry. It is also particularly interesting because the torsional forces about the single bonds are in opposition to the forces tending to retain tetrahedral bond angles. Thus the later forces tend to keep all five carbon atoms co-planar while the torsional forces tend to pucker the ring. To support the concept of pseudo rotations of the five-membered ring, Pitzer measured the heat capacity of gaseous cyclopentane in 1947⁶. The experimental results were analyzed by the vibrational spectra of cyclopentane and the fundamental

vibrational assignments were provided from which the enthalpy was then evaluated. In the similar paper⁷ the pseudo rotations of ring puckering were investigated by utilizing the potential energy. It was shown that the potential energy curve is the function of deviation from planarity and it was proved to be the same for molecules with C_2 or C_s symmetry. From this information it was concluded that the puckering suggested very probable intermediate types of motion which also shows the same potential curves.

This paper⁷ was then followed by an additional study⁸ of the conformational strain energy of cyclopentane and its derivatives. Since there were considerable questions concerning the idea of pseudo rotation there was little research that followed. However, the experimental determination of pseudo rotation was eventually proved by a vibrational study published in 1968⁹ i.e. more than 30 years after the motion was proposed. However, even at this time there is still a large amount of questions concerning why some molecules prefer the *twisted* form, over *axial* or *equatorial* forms, and additionally what affects the substitution of different elements in the ring or on the ring have on pseudo rotational motion of the substituted cyclopentane molecules. Therefore, I decided to undertake the research that involves investigations of various substitutions on the ring or in the ring to determine what factors most strongly affect pseudo rotations on the five-membered ring molecules.

Currently, the factors that are the major contributors to the interchange and/or the structural stabilities of substituted five-membered rings are not understood. The molecule pyrrolidine is an interesting example, which received significant scientific attention due to its presence in biologically important molecules such as peptides, proteins and amino acids. It has been the subject of several experimental and theoretical conformational studies. From the first microwave study¹⁰ it was reported that there was only one form present and it was

the *axial* conformer. In the following electron diffraction¹¹ study it was reported that a second conformer was observed and it was the *equatorial* conformer which was less stable than the *axial* form. Eventually, the *equatorial* form was reported in a later microwave study to be the more stable conformer than the *axial* form¹². However, this conclusion was shown to be incorrect¹³ and the second conformer was experimentally determined to be the *twist* form and not *axial* form from the vibrational spectra. This result has led interest to determine the stable conformations of other five-membered rings. Therefore, my studies of five-membered rings began with one of the carbon atoms replaced with a silicon atom with a halogen (Br) atom attached, i.e. 1-bromo-1-silacyclopentane. The second five-membered ring investigated was substituted cyclopentane, i.e. ethynylcyclopentane, C_5H_9CCH .

The conformational stability determination of 1,2-disubstituted ethane molecules have provided some interesting challenges for the structural scientists over the years. The 1,2-disubstituted ethane molecules of YCH_2CH_2X type are of main interest since most of them have two conformers *trans* (*anti*) and *gauche*, present in the fluid states and their relative stabilities are believed to depend on the electronegativity and size of the substituents. Also, it is frequently difficult to determine the conformer with the lowest energy (with possible solvent interference) spectroscopically because of the low symmetry of these molecules.

As a continuation of the studies of 1,2-substituted ethanes, we have investigated the conformational stability of 1,2-diaminoethane (ethylenediamine)¹⁴ and 1,2-diphosphinoethane (ethylenediphosphine) to determine whether there is a significant difference in the conformer stabilities of these two molecules since both ethylamine¹⁵ and

ethylphosphine¹⁶ have the *trans* conformer as the lower energy form. I was particularly interested in the phosphine molecule since some of the phosphines have anticancer/antitumor properties^{17,18} and, therefore, their conformational stabilities could be important in the selection of the compounds which could have the most potential as biochemical materials. Hence, 1,2-diphosphinoethane (XCH₂CH₂X type) and 2-cyanoethylphosphine (YCH₂CH₂X type) have received significant attention in my studies.

General Methodology

The findings of my spectroscopic, structural, and theoretical studies are based on infrared and/or Raman spectra of gas, liquid, solid as well as variable temperature xenon solutions, and microwave spectrum which are supported by *ab initio* and DFT calculations. The *ab initio* calculations are performed with the Gaussian 03 program¹⁹ with Gaussian-type basis functions. The energy minima with respect to nuclear coordinates are obtained by the simultaneous relaxation of all geometric parameters by the gradient method of Pulay²⁰. Several basis sets as well as the corresponding ones with diffuse functions are employed with the Møller-Plesset perturbation method²¹ to the second order with full electron correlation (MP2(full)) along with the density functional theory by the B3LYP method.

By utilizing the information, acquired through the experimental and theoretical studies carried out in the research laboratory, I have accomplished the following results for the molecules under study. Spectra obtained from infrared and Raman experiments are used in the vibrational studies to assign fundamental frequencies for all possible conformers as well as for the identification of the conformers. The MP2(full)/6-31G(d) calculations are used to predict the force constants, frequencies, infrared intensities, Raman

activities, band contours, potential energy distributions and depolarization values to support the vibrational assignment. Raman spectrum of liquid is used to obtain the experimental depolarization values. Determination of enthalpy difference values is carried out by using variable temperature, infrared or Raman spectra of xenon solutions or the liquid. From these experimentally obtained ΔH values, the order of the stability of the conformers are determined. The experimentally determined enthalpy values are used to evaluate the quality of the predicted values of energies by *ab initio* and density functional theory calculations obtained from various basis sets up to aug-cc-pVTZ. Also % abundance of each conformer are determined by experimentally obtained ΔH values. The r_0 structural parameters can be obtained from utilizing the experimentally determined rotational constants from previously published microwave data or data obtained from my research. The experimentally determined values are then compared with the estimated values obtained from adjusted MP2(full)/6-311+G(d,p) calculations for the respective conformers. These physiochemical data should provide significant trends and affects to better understand the major factors controlling the relative stabilities of the conformers as well as the relative values of the structural parameters.

PROJECT-1

Infrared and Raman Spectra, *ab initio* Calculations, Conformational Stability and Vibrational Assignment of 1-bromo-1-silacyclopentane

Introduction

Several monosubstituted cyclopentanes were determined to have two conformations at ambient temperature where the substituent occupies the *axial* and *equatorial* positions at the tip of the C_s -symmetric *envelope* form of the five-membered ring¹⁻⁵. For many of the molecules the vibrational spectra were used to first identify the two forms before they were identified by microwave spectra and/or electron diffraction investigations. The monohalocyclopentanes are interesting examples where initially the fluoride, chloride, and bromide¹ were all reported to have these forms from analyses of their infrared spectra. Later, from an investigation of the Raman spectrum²² of the liquid, it was concluded that there was only one conformer present in the fluid states and it was the *envelope-equatorial* conformer which was supported from the theoretical predictions²³ from CNDO predictions. More recently, we²⁴ have shown from the infrared spectra of the gas and variable temperature xenon solutions that there is, indeed, only one conformer in the fluid phases but it is the *twisted* (C_1 symmetry) form which was supported by structural parameters obtained from the rotational constants obtained from the microwave spectrum. For chlorocyclopentane there was only the *envelope-axial* conformer initially found from the microwave spectrum²⁵ and from a subsequent electron diffraction investigation²⁶ of it, the authors indicated that the data could be explained equally well by either a mixture of *axial* and *equatorial* conformers or a dynamic model involving nearly free pseudorotation which lead to doubts about a second conformer. However, from a later re-investigation of

the microwave spectrum of chlorocyclopentane²⁷, transitions for the *equatorial* conformer were observed and assigned.

There were no problems for bromocyclopentane concerning the early report²⁸ of the two forms since the observed microwave spectrum was assigned for the two conformers with estimated structural parameters consistent with the *axial* and *equatorial* forms. Therefore, we began our vibrational and conformational study of the corresponding five-membered rings with one of the carbon atoms replaced with a silicon atom which has a halogen atom attached, and for this study, the bromine atom, i.e. 1-bromo-1-silacyclopentane.

The infrared spectra (3500-300 cm^{-1}) of the gas and solid and the Raman spectrum (3500-60 cm^{-1}) of the liquid have been recorded of 1-bromo-1-silacyclopentane from which the conformational stability has been determined and a vibrational assignment of the fundamentals is reported. To support the conformational stability determination and aid in the vibrational assignment, *ab initio* MP2 with full electron correlation and density functional theory by the B3LYP method calculations have been carried out by using a variety of basis sets. The results of these spectroscopic and theoretical studies are reported herein.

Experimental and Theoretical Methods

The sample of 1-bromo-1-silacyclopentane was prepared in two steps. First, 1,1-dichloro-1-silacyclopentane was prepared by double Grignard of 1,4-dibromobutane and coupled with tetrachlorosilane. The product 1,1-dichloro-1-silacyclopentane was reduced with lithium aluminum hydride in dry dibutyl ether. The product 1-silacyclopentane was brominated with boron tribromide at 0°C for 18 hr. to produce 1-bromo-1-

silacyclopentane, which, was first purified using trap to trap distillation and finally by a low pressure, low temperature sublimation column. The sample was identified by IR and NMR spectroscopy.

The mid-infrared spectrum of the gas was obtained from 3500 to 300 cm^{-1} on a Perkin-Elmer model 2000 Fourier transform spectrometer equipped with a Ge/CsI beamsplitter and a DTGS detector. Atmospheric water vapor was removed from the spectrometer housing by purging with dry nitrogen. The theoretical resolution used to obtain the spectrum of the gas was 0.5 cm^{-1} and 128 interferograms were added and truncated with a boxcar function. For the spectrum of the solid the vapor was deposited on a CsI window cooled with boiling liquid nitrogen in a low temperature infrared cell. Typical spectra of the gas and solid are shown in Fig. 1.

The Raman spectra (Fig. 2) were recorded on a Spex model 1403 spectrophotometer equipped with a Spectra-Physics model 2017 argon ion laser operating on the 514.5 nm line. The laser power used was 1.5 W with a spectral bandpass of 3 cm^{-1} . The spectrum of the liquid was recorded with the sample sealed in a Pyrex glass capillary. Depolarization measurements were obtained for the liquid sample using a standard Ednalite 35 mm camera polarizer with 38 mm of free aperture affixed to the Spex instrument. Depolarization ratio measurements were checked by measuring the state of polarization of the Raman bands of CCl_4 immediately before depolarization measurements were made on the liquid sample. The measurements of the Raman frequencies are expected to be accurate to $\pm 2 \text{ cm}^{-1}$. All of the observed fundamental bands in the Raman spectrum of the liquid along with their proposed assignments and depolarization values are listed in Table 1.

The LCAO-MO-SCF restricted Hartree-Fock calculations were performed with the Gaussian-03 program¹⁹ by using Gaussian-type basis functions. The energy minima with respect to nuclear coordinates were obtained with the simultaneous relaxation of all geometric parameters by using the gradient method of Pulay²⁰. Several basis sets as well as the corresponding ones with diffuse functions up to the 6-311+G(2df,2pd) basis set were employed with the Møller-Plesset perturbation method²¹ to the second order (MP2(full)) as well as with the density functional theory by the B3LYP method. The predicted conformational energy differences are listed in Table 6.

In order to obtain a complete description of the molecular motions involved in the fundamental modes of *c*-C₄H₈SiBrH, a normal coordinate analysis has been carried out. The force field in Cartesian coordinates was obtained with the Gaussian 03 program¹⁹ at the MP2(full) level with the 6-31G(d) basis set. The internal coordinates used to calculate the **G** and **B** matrices are listed in Table 5 with the atomic numbering shown in Fig. 3. By using the **B** matrix²⁹, the force field in Cartesian coordinates was converted to a force field in internal coordinates. Subsequently, scaling factors of 0.88 for CH₂ stretches and deformations, and 0.90 for other coordinates except for the heavy atom bends were applied, along with the geometric average of the scaling factors for the interaction force constants, to obtain the fixed scaled force field and resultant wavenumbers. A set of symmetry coordinates was used (Table 6) to determine the corresponding potential energy distributions (P.E.D.s). A comparison between the observed and calculated wavenumbers, along with the calculated infrared intensities, Raman activities, depolarization ratios and potential energy distributions for the *twisted* conformer are listed in Table 1.

The vibrational spectra were predicted from the MP2(full)/6-31G(d) calculations. The predicted scaled frequencies were used together with a Lorentzian function to obtain the simulated spectra. Infrared intensities were obtained based on the dipole moment derivatives with respect to Cartesian coordinates. The derivatives were transformed with respect to normal coordinates by $(\partial\mu_u/\partial Q_i) = \sum_j (\partial\mu_u/\partial X_j)L_{ij}$, where Q_i is the i^{th} normal coordinate, X_j is the j^{th} Cartesian displacement coordinate, and L_{ij} is the transformation matrix between the Cartesian displacement coordinates and the normal coordinates. The infrared intensities were then calculated by $(N\pi)/(3c^2) [(\partial\mu_x/\partial Q_i)^2 + (\partial\mu_y/\partial Q_i)^2 + (\partial\mu_z/\partial Q_i)^2]$. A comparison of experimental and simulated infrared spectra of c-C₄H₈SiBrH is shown in Fig. 1. The predicted spectrum is in good agreement with the experimental spectrum which shows the utility of the scaled predicted frequencies and predicted intensities for supporting the vibrational assignment.

Additional support for the vibrational assignments was obtained from the simulated Raman spectrum. The evaluation of Raman activity by using the analytical gradient methods has been developed³⁰⁻³² and the activity S_j can be expressed as: $S_j = g_j(45\alpha_j^2 + 7\beta_j^2)$, where g_j is the degeneracy of the vibrational mode j , α_j is the derivative of the isotropic polarizability, and β_j is the anisotropic polarizability. To obtain the Raman scattering cross sections, the polarizabilities are incorporated into S_j by multiplying S_j with $(1-\rho_j)/(1+\rho_j)$ where ρ_j is the depolarization ratio of the j^{th} normal mode. The Raman scattering cross sections and calculated wavenumbers obtained from the Gaussian 03 program were used together with a Lorentzian function to obtain the simulated Raman spectra. Comparison of experimental Raman spectrum of the liquid and the predicted Raman spectrum are shown in Fig. 2.

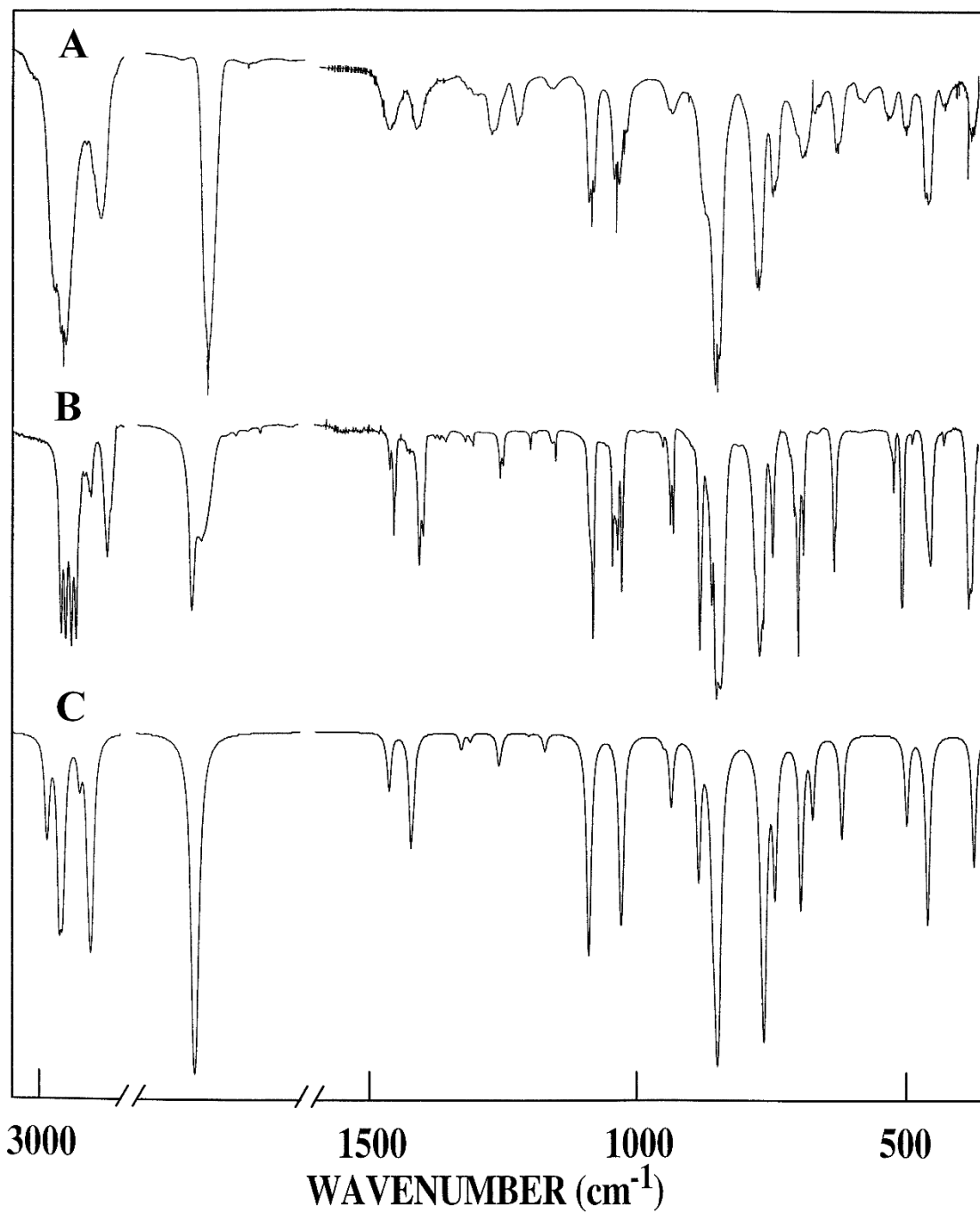


Figure 4.1. Comparison of experimental and calculated infrared spectra of 1-bromo-1-silacyclopentane: (A) observed IR spectrum of gas; (B) observed IR spectrum of solid; (C) simulated IR spectrum of *twist* (C_2) conformer.

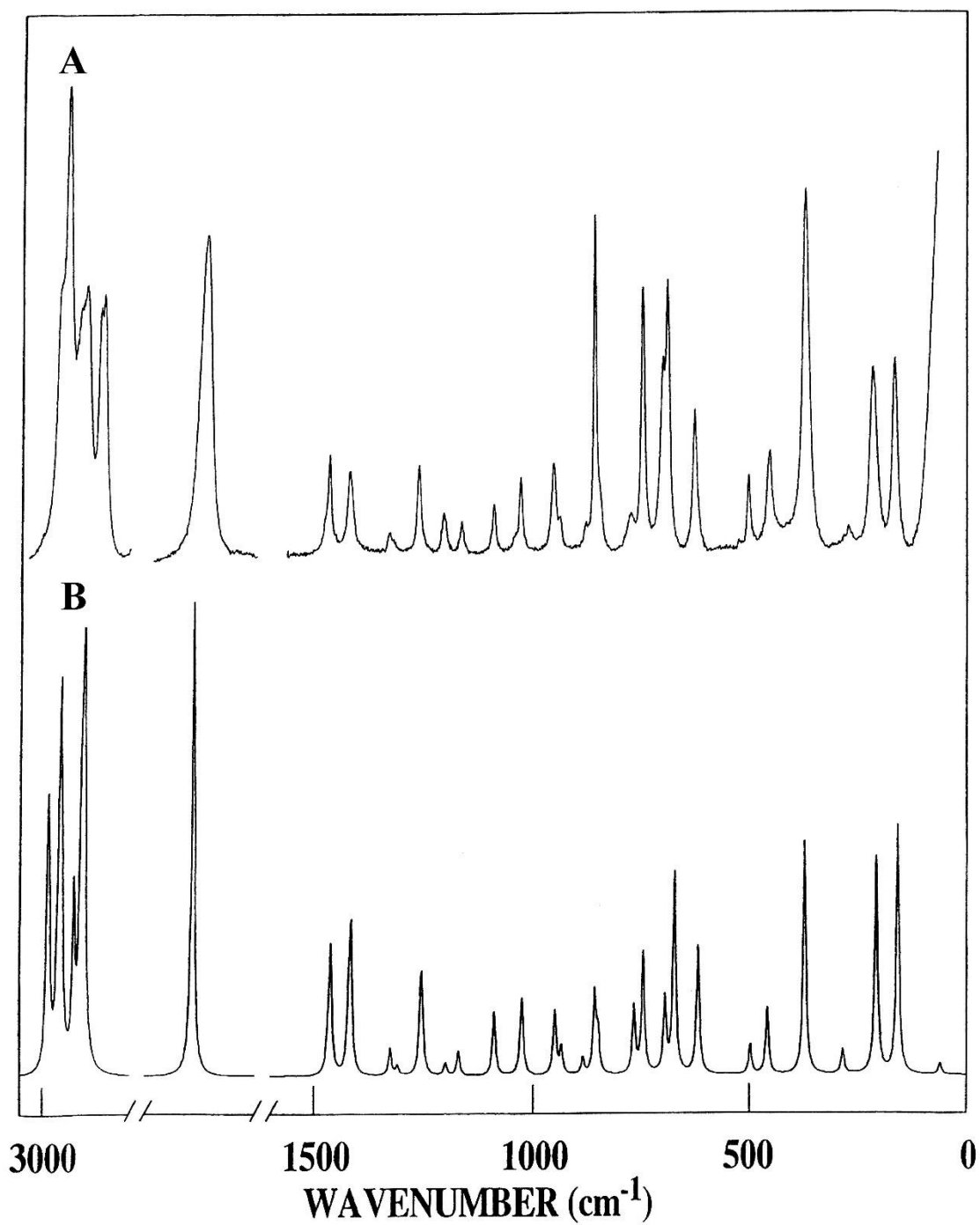


Figure 4.2. Comparison of experimental and calculated Raman spectra of 1-bromo-1-silacyclopentane: (A) observed Raman spectrum of liquid; (B) simulated Raman spectrum of *twist* (C_1) conformer.

Table 4.1. Calculated^a and observed frequencies (cm⁻¹) for 1-bromo-1-silacyclopentane *twist* (*C*₁) form.

Vib. No.	Approx. description	<i>ab initio</i>	fixed scaled ^b	B3LYP ^c	IR gas	Raman liquid	IR solid	P.E.D. ^d	Band Contour		
									A	B	C
v ₁	α-CH ₂ antisymmetric	3186	2988	3101	2	2981	-	47S ₁ ,39S ₂	5	15	30
v ₂	α-CH ₂ antisymmetric	318	2985	3095	2	2972	-	52S ₂ ,42S ₁	1	16	71
v ₃	β-CH ₂ antisymmetric	315	2963	3067	2	2960	2957	92S ₃	2	39	37
v ₄	β-CH ₂ antisymmetric	315	2957	3062	2	2944	2949	85S ₄ ,11S ₈	6	-	31
v ₅	α-CH ₂ symmetric	311	2926	3045	2	2915	-	50S ₅ ,46S ₆	3	62	3
v ₆	α-CH ₂ symmetric	310	2911	3024	2	2902	2911	42S ₆ ,39S ₅	-	2	98
v ₇	β-CH ₂ symmetric	309	2906	3020	2	2869	2900/	88S ₇	1	36	52
v ₈	β-CH ₂ symmetric	309	2903	3014	2	2862	2864/	82S ₈ ,11S ₄	9	-	3
v ₉	Si-H stretch	231	2193	2231	2	2173	2197/	100S ₉	2	3	95
v ₁₀	β-CH ₂ deformation	156	1470	1505	1	1463	1456	94S ₁₀	5	3	43
v ₁₁	β-CH ₂ deformation	155	1463	1496	1	1452	1448/	99S ₁₁	2	14	63
v ₁₂	α-CH ₂ deformation	151	1423	1456	1	1407	1402	78S ₁₂ ,19S ₁₃	1	74	25
v ₁₃	α-CH ₂ deformation	150	1418	1452	1	1402	1395	74S ₁₃ ,21S ₁₂	1	67	15
v ₁₄	β-CH ₂ wag	140	1329	1351	1	1325	1353	62S ₁₄ ,23S ₁₆	8	-	19
v ₁₅	β-CH ₂ wag	138	1312	1340	1	1318	1316	88S ₁₅	5	9	34
v ₁₆	β-CH ₂ twist	132	1259	(1284)	1	1262	1250	47S ₁₆ ,33S ₂₀	6	1	35
v ₁₇	β-CH ₂ twist	132	1255	(1280)	1	1250	1244	51S ₁₇ ,19S ₂₁ ,18S ₁₉	9	6	-
v ₁₈	α-CH ₂ twist	126	1202	1224	-	1195	1192	36S ₁₈ ,32S ₂₄ ,12S ₂₀	2	82	16
v ₁₉	α-CH ₂ wag	123	1172	1184	1	1153	1151/	54S ₁₉ ,17S ₃₃ ,10S ₂₃ ,10S ₂₁	1	73	11
v ₂₀	α-CH ₂ wag	114	1089	1108	1	1079	1078/	39S ₂₀ ,21S ₁₆ ,10S ₃₁ ,10S ₁₄	8	-	18
v ₂₁	α-CH ₂ twist	108	1029	1056	1	1033	1035/	50S ₂₁ ,26S ₁₇	6	1	38
v ₂₂	ring deformation	108	1026	1028	1	1019	1018	41S ₂₂ ,20S ₃₁ ,16S ₁₄	9	-	1
v ₂₃	ring deformation	996	950	957	-	945	941	32S ₂₃ ,20S ₁₉ ,13S ₃₃ ,10S ₂₅	2	98	-
v ₂₄	β-CH ₂ rock	985	935	949	9	930	927/9	39S ₂₄ ,39S ₁₈	1	90	9
v ₂₅	ring deformation	923	885	882	8	870	873/8	53S ₂₅ ,29S ₂₈	1	84	3
v ₂₆	ring breathing	898	857	(858)	8	851	849	41S ₂₆ ,20S ₃₁ ,14S ₂₂	7	17	6
v ₂₇	α-CH ₂ rock	891	849	(853)	8	840	840/8	36S ₂₇ ,16S ₃₀ ,13S ₃₇	7	17	13

ν_{28}	β -CH ₂ rock	805	764	776	7	765	761/7	13S ₂₈ ,33S ₃₂ ,19S ₃₀ ,14S ₂₉	5	45	3
ν_{29}	α -CH ₂ rock	780	743	744	7	738	736	21S ₂₉ ,23S ₃₀ ,12S ₂₆ ,11S ₃₁	9	5	2
ν_{30}	Si-H parallel bend*	729	694	699	6	693	695/6	19S ₃₀ ,22S ₂₇ ,14S ₂₃ ,10S ₃₂ ,10S ₁	70	19	
ν_{31}	ring deformation	704	672	673	6	682	680/6	21S ₃₁ ,22S ₂₆ ,17S ₂₅ ,10S ₂₃	6	13	19
ν_{32}	Si-H perpendicular	649	618	619	6	621	620/6	26S ₃₂ ,25S ₂₉ ,17S ₂₅ ,10S ₂₆	8	12	4
ν_{33}	ring deformation	512	498	499	4	496	495/4	53S ₃₃ ,18S ₂₈ ,15S ₃₉ ,10S ₂₃	6	15	23
ν_{34}	ring deformation	471	459	453	4	449	439	58S ₃₄ ,26S ₃₅	9	2	-
ν_{35}	Si-Br stretch	389	373	356	3	364	370	51S ₃₅ ,20S ₃₄ ,12S ₃₇	5	1	47
ν_{36}	ring twist	298	285	269	-	268	-	80S ₃₆	2	73	25
ν_{37}	Si-Br parallel bend*	215	208	205	-	210	-	36S ₃₇ ,19S ₃₉ ,13S ₃₅ ,12S ₃₀	6	6	34
ν_{38}	Si-Br perpendicular	159	158	150	-	160	-	87S ₃₈	1	91	8
ν_{39}	ring puckering	63	60	61	-	-	-	59S ₃₉ ,27S ₃₇	2	9	89

^aMP2(full)/6-31G(d) *ab initio* calculations, B3LYP/6-311+G(d,p) density functional theory calculations, scaled frequencies, potential energy distributions (P.E.D.s).

^b Scaled frequencies with scaling factors of 0.88 for CH₂ stretches and deformations and 0.90 for all other modes except heavy atom bends.

^c Values in parenthesis are reordered to match the MP2(full)/6-31G(d) *ab initio* values.

^d Symmetry coordinates with P.E.D. contribution less than 10% are omitted.

*Bend parallel and perpendicular to the ring, respectively.

Table 4.2. Calculated^a frequencies (cm⁻¹) for 1-bromo-1-silacyclopentane *twisted* (*C₁*) form.

Vib. No.	Approx. description	<i>ab initio</i>	fixed scaled ^b	IR int.	Raman act.	B3LYP 6-31G(d) ^c	IR int.	Raman act.	B3LYP 6-311+G(d,p) ^c	IR int.	Raman act.
v ₁	α -CH ₂ antisymmetric	3186	2988	6.8	60.0	3124	10.7	72.4	3101	9.9	77.7
v ₂	α -CH ₂ antisymmetric	3182	2985	9.0	73.7	3117	16.2	83.8	3095	15.2	88.3
v ₃	β -CH ₂ antisymmetric	3159	2963	27.0	57.8	3088	45.5	71.1	3067	42.7	73.1
v ₄	β -CH ₂ antisymmetric	3153	2957	25.6	148.0	3082	38.5	198.7	3062	38.3	259.5
v ₅	α -CH ₂ symmetric stretch	3119	2926	5.1	69.2	3065	10.2	67.1	3045	11.1	75.6
v ₆	α -CH ₂ symmetric stretch	3103	2911	10.6	68.7	3044	21.8	56.5	3024	23.1	60.2
v ₇	β -CH ₂ symmetric stretch	3098	2906	20.4	47.7	3039	19.7	81.8	3020	19.1	90.8
v ₈	β -CH ₂ symmetric stretch	3095	2903	22.9	146.4	3034	27.0	131.0	3014	24.4	185.6
v ₉	Si-H stretch	2311	2193	153.	125.1	2244	155.	126.5	2231	123.	178.7
v ₁₀	β -CH ₂ deformation	1564	1470	0.5	3.3	1534	0.2	4.4	1505	1.3	1.1
v ₁₁	β -CH ₂ deformation	1556	1463	7.4	18.6	1524	4.8	20.1	1496	6.8	11.1
v ₁₂	α -CH ₂ deformation	1513	1423	14.7	5.7	1484	9.1	8.2	1456	10.4	4.6
v ₁₃	α -CH ₂ deformation	1508	1418	4.9	19.8	1480	4.8	19.4	1452	6.6	8.7
v ₁₄	β -CH ₂ wag	1400	1329	2.1	3.5	1372	3.2	4.3	1351	1.4	1.7
v ₁₅	β -CH ₂ wag	1382	1312	1.0	1.2	1358	1.7	1.5	1340	0.8	0.7
v ₁₆	β -CH ₂ twist	1325	1259	3.6	6.1	(1295)	1.2	6.2	(1284)	2.4	3.7
v ₁₇	β -CH ₂ twist	1323	1255	1.1	9.3	(1297)	0.4	9.7	(1280)	0.6	5.1
v ₁₈	α -CH ₂ twist	1266	1202	0.3	1.4	1238	0.7	1.5	1224	0.6	1.8
v ₁₉	α -CH ₂ wag	1230	1172	2.2	2.7	1197	1.5	2.4	1184	1.9	2.0
v ₂₀	α -CH ₂ wag	1147	1089	41.5	6.4	1118	32.9	8.6	1108	30.4	4.3
v ₂₁	α -CH ₂ twist	1084	1029	24.9	1.5	1063	27.9	1.6	1056	25.9	0.8
v ₂₂	ring deformation	1081	1026	11.4	6.2	1038	8.8	4.8	1028	10.7	4.2
v ₂₃	ring deformation	996	950	0.8	5.4	964	0.4	5.1	957	0.4	4.5
v ₂₄	β -CH ₂ rock	985	935	9.4	2.2	958	8.2	1.9	949	8.2	1.9
v ₂₅	ring deformation	923	885	21.1	1.3	891	27.8	2.5	882	26.8	1.6
v ₂₆	ring breathing	898	857	17.8	5.9	(861)	2.6	6.7	(858)	1.5	9.2
v ₂₇	α -CH ₂ rock	891	849	120.	2.8	(870)	124.	2.1	(853)	126.	1.6
v ₂₈	β -CH ₂ rock	805	764	87.2	4.3	783	76.9	4.2	776	74.2	4.4

v ₂₉	α -CH ₂ rock	780	743	23.5	7.5	754	20.8	6.8	744	25.3	8.1
v ₃₀	Si-H parallel bend*	729	694	28.3	4.2	703	26.3	4.7	699	24.2	4.6
v ₃₁	ring deformation	704	672	10.6	11.0	674	13.0	11.5	673	13.9	11.8
v ₃₂	Si-H perpendicular bend*	649	618	14.7	6.3	621	14.3	6.2	619	14.8	7.4
v ₃₃	ring deformation	512	498	12.3	1.1	502	10.9	1.2	499	8.8	1.1
v ₃₄	ring deformation	471	459	32.6	2.2	461	35.9	2.6	453	38.3	2.3
v ₃₅	Si-Br stretch	389	373	19.7	5.8	368	15.5	6.2	356	23.8	7.7
v ₃₆	ring twist	298	285	0.3	0.4	277	0.2	0.4	269	0.2	0.4
v ₃₇	Si-Br parallel bend*	215	208	0.7	2.2	207	0.7	2.6	205	0.8	3.1
v ₃₈	Si-Br perpendicular bend*	159	158	1.1	1.6	153	0.9	1.8	150	1.0	2.1
v ₃₉	ring puckering	63	60	0.5	0.8	63	0.5	1.0	61	0.5	1.0

^a MP2(full)/6-31G(d) *ab initio* calculations, B3LYP/6-31G(d) and B3LYP/6-311+G(d,p) density functional theory calculations, scaled frequencies, infrared intensities (km/mol), Raman activities ($\text{\AA}^4/\text{u}$).

^b Scaled frequencies with scaling factors of 0.88 for CH₂ stretches and deformations and 0.90 for all other modes except heavy atom bends.

^c Values in parenthesis are reordered to match the MP2(full)/6-31G(d) *ab initio* values.

*Bend parallel and perpendicular to the ring, respectively.

Table 4.3. Calculated^a frequencies (cm⁻¹) for 1-bromo-1-silacyclopentane *twisted* (*C₁*) form.

Vib. No.	Approx. description	<i>ab initio</i>	fixed scaled ^b	P.E.D. ^c	B3LYP 6-31G(d) ^d	P.E.D. ^c	B3LYP 6-311+G(d,p) ^d	P.E.D. ^c
v ₁	α -CH ₂ antisymmetric	3186	2988	47S ₁ ,39S ₂	3124	41S ₁ ,37S ₂ ,11S ₆ ,10S ₅	3101	41S ₁ ,36S ₂ ,11S ₆ ,10S ₅
v ₂	α -CH ₂ antisymmetric	3182	2985	52S ₂ ,42S ₁	3117	49S ₂ ,44S ₁	3095	49S ₂ ,44S ₁
v ₃	β -CH ₂ antisymmetric	3159	2963	92S ₃	3088	89S ₃	3067	88S ₃
v ₄	β -CH ₂ antisymmetric	3153	2957	85S ₄ ,11S ₈	3082	71S ₄ ,19S ₈	3062	68S ₄ ,21S ₈
v ₅	α -CH ₂ symmetric	3119	2926	50S ₅ ,46S ₆	3065	43S ₅ ,41S ₆	3045	42S ₅ ,40S ₆
v ₆	α -CH ₂ symmetric	3103	2911	42S ₆ ,39S ₅	3044	32S ₆ ,31S ₅ ,16S ₇	3024	29S ₆ ,29S ₅ ,20S ₇
v ₇	β -CH ₂ symmetric	3098	2906	88S ₇	3039	65S ₇ ,10S ₈	3020	66S ₇ ,10S ₈
v ₈	β -CH ₂ symmetric	3095	2903	82S ₈ ,11S ₄	3034	64S ₈ ,18S ₄ ,17S ₇	3014	63S ₈ ,22S ₄ ,12S ₇
v ₉	Si-H stretch	2311	2193	100S ₉	2244	100S ₉	2231	100S ₉
v ₁₀	β -CH ₂ deformation	1564	1470	94S ₁₀	1534	91S ₁₀	1505	92S ₁₀
v ₁₁	β -CH ₂ deformation	1556	1463	99S ₁₁	1524	97S ₁₁	1496	98S ₁₁
v ₁₂	α -CH ₂ deformation	1513	1423	78S ₁₂ ,19S ₁₃	1484	70S ₁₂ ,27S ₁₃	1456	64S ₁₂ ,32S ₁₃
v ₁₃	α -CH ₂ deformation	1508	1418	74S ₁₃ ,21S ₁₂	1480	66S ₁₃ ,29S ₁₂	1452	60S ₁₃ ,35S ₁₂
v ₁₄	β -CH ₂ wag	1400	1329	62S ₁₄ ,23S ₁₆	1372	62S ₁₄ ,26S ₁₆	1351	61S ₁₄ ,28S ₁₆
v ₁₅	β -CH ₂ wag	1382	1312	88S ₁₅	1358	90S ₁₅	1340	90S ₁₅
v ₁₆	β -CH ₂ twist	1325	1259	47S ₁₆ ,33S ₂₀	1295	40S ₁₆ ,29S ₂₀	(1284)	44S ₁₆ ,32S ₂₀
v ₁₇	β -CH ₂ twist	1323	1255	51S ₁₇ ,19S ₂₁ ,18S ₁₉	1297	46S ₁₇ ,18S ₂₁ ,14S ₁₉	(1280)	52S ₁₇ ,21S ₂₁ ,15S ₁₉
v ₁₈	α -CH ₂ twist	1266	1202	36S ₁₈ ,32S ₂₄ ,12S ₂₀	1238	39S ₁₈ ,32S ₂₄ ,10S ₂₀ ,10S ₂	1224	40S ₁₈ ,31S ₂₄ ,10S ₂₀ ,10S ₂₉
v ₁₉	α -CH ₂ wag	1230	1172	54S ₁₉ ,17S ₃₃ ,10S ₂₃ ,10S ₂₁	1197	61S ₁₉ ,15S ₃₃	1184	62S ₁₉ ,15S ₃₃
v ₂₀	α -CH ₂ wag	1147	1089	39S ₂₀ ,21S ₁₆ ,10S ₃₁ ,10S ₁₄	1118	46S ₂₀ ,20S ₁₆ ,15S ₁₄	1108	48S ₂₀ ,20S ₁₆ ,17S ₁₄
v ₂₁	α -CH ₂ twist	1084	1029	50S ₂₁ ,26S ₁₇	1063	59S ₂₁ ,31S ₁₇	1056	59S ₂₁ ,32S ₁₇
v ₂₂	ring deformation	1081	1026	41S ₂₂ ,20S ₃₁ ,16S ₁₄	1038	54S ₂₂ ,28S ₃₁ ,11S ₁₄	1028	55S ₂₂ ,29S ₃₁
v ₂₃	ring deformation	996	950	32S ₂₃ ,20S ₁₉ ,13S ₃₃ ,10S ₂₅	964	31S ₂₃ ,19S ₂₈ ,18S ₁₉ ,17S ₃	957	31S ₂₃ ,20S ₂₈ ,19S ₃₃ ,17S ₁₉
v ₂₄	β -CH ₂ rock	985	935	39S ₂₄ ,39S ₁₈	958	43S ₂₄ ,38S ₁₈	949	43S ₂₄ ,37S ₁₈
v ₂₅	ring deformation	923	885	53S ₂₅ ,29S ₂₈	891	46S ₂₅ ,30S ₂₈ ,10S ₂₃	882	50S ₂₅ ,29S ₂₈ ,10S ₂₃
v ₂₆	ring breathing	898	857	41S ₂₆ ,20S ₃₁ ,14S ₂₂	(861)	46S ₂₆ ,22S ₃₁ ,15S ₂₂	(858)	46S ₂₆ ,23S ₃₁ ,16S ₂₂
v ₂₇	α -CH ₂ rock	891	849	36S ₂₇ ,16S ₃₀ ,13S ₃₇	(870)	37S ₂₇ ,19S ₃₀ ,14S ₃₇ ,11S ₂	(853)	39S ₂₇ ,19S ₃₀ ,14S ₃₇
v ₂₈	β -CH ₂ rock	805	764	13S ₂₈ ,33S ₃₂ ,19S ₃₀ ,14S ₂₉	783	13S ₂₈ ,33S ₃₂ ,18S ₃₀ ,15S ₂	776	13S ₂₈ ,33S ₃₂ ,18S ₃₀ ,15S ₂₉

v ₂₉ α-CH ₂ rock	780	743	21S ₂₉ ,23S ₃₀ ,12S ₂₆ ,11S ₃₁	754	20S ₂₉ ,26S ₃₀ ,13S ₂₇	744	18S ₂₉ ,28S ₃₀ ,12S ₂₇
v ₃₀ Si-H parallel bend*	729	694	19S ₃₀ ,22S ₂₇ ,14S ₂₃ ,10S ₃₂	703	13S ₃₀ ,19S ₂₇ ,12S ₂₃ ,12S ₃₂	699	14S ₃₀ ,20S ₂₇ ,13S ₃₂ ,11S ₂₃
v ₃₁ ring deformation	704	672	21S ₃₁ ,22S ₂₆ ,17S ₂₅ ,10S ₂₃	674	23S ₃₁ ,21S ₂₆ ,19S ₂₅ ,11S ₂	673	20S ₃₁ ,22S ₂₅ ,18S ₂₆ ,14S ₂₃
v ₃₂ Si-H perpendicular	649	618	26S ₃₂ ,25S ₂₉ ,17S ₂₅ ,10S ₂₆	621	24S ₃₂ ,25S ₂₉ ,20S ₂₅	619	22S ₃₂ ,28S ₂₉ ,18S ₂₅
v ₃₃ ring deformation	512	498	53S ₃₃ ,18S ₂₈ ,15S ₃₉ ,10S ₂₃	502	57S ₃₃ ,16S ₂₈ ,15S ₃₉ ,11S ₂	499	58S ₃₃ ,17S ₂₈ ,14S ₃₉ ,11S ₂₃
v ₃₄ ring deformation	471	459	58S ₃₄ ,26S ₃₅	461	56S ₃₄ ,30S ₃₅	453	66S ₃₄ ,23S ₃₅
v ₃₅ Si-Br stretch	389	373	51S ₃₅ ,20S ₃₄ ,12S ₃₇	368	48S ₃₅ ,23S ₃₄ ,12S ₃₇	356	56S ₃₅ ,14S ₃₄ ,13S ₃₇
v ₃₆ ring twist	298	285	80S ₃₆	277	83S ₃₆	269	83S ₃₆
v ₃₇ Si-Br parallel bend*	215	208	36S ₃₇ ,19S ₃₉ ,13S ₃₅ ,12S ₃₀	207	36S ₃₇ ,20S ₃₉ ,14S ₃₅ ,12S ₃	205	36S ₃₇ ,19S ₃₉ ,16S ₃₅ ,12S ₃₀
v ₃₈ Si-Br perpendicular	159	158	87S ₃₈	153	89S ₃₈	150	89S ₃₈
v ₃₉ ring puckering	63	60	59S ₃₉ ,27S ₃₇	63	59S ₃₉ ,28S ₃₇	61	60S ₃₉ ,27S ₃₇

^a MP2(full)/6-31G(d) *ab initio* calculations, B3LYP/6-31G(d) and B3LYP/6-311+G(d,p) density functional theory calculations, scaled frequencies, and potential energy distributions (P.E.D.s).

^b Scaled frequencies with scaling factors of 0.88 for CH₂ stretches and deformations and 0.90 for all other modes except heavy atom bends.

^c Symmetry coordinates with P.E.D. contribution less than 10% are omitted.

^d Values in parenthesis are reordered to match the MP2(full)/6-31G(d) *ab initio* values.

*Bend parallel and perpendicular to the ring, respectively.

Conformational Stability and Vibrational Assignment

To determine the conformational stabilities, we first determined whether there was more than one conformer present in the fluid states. A comparison of the infrared spectrum of the gas and solid indicated that there was only one conformer present in the gas since all of the bands observed in the spectrum of the gas were also present in the spectrum of the polycrystalline solid (Fig. 1) which was obtained by repeated annealing of the sample until no changes were observed in the spectrum. Also, a comparison of the Raman spectrum of the liquid with that of the infrared spectra indicated that there were no Raman lines present which were not observed in the infrared spectrum. Once it was ascertained that there was only one conformer present in all of the physical states, the structure of this conformer was determined.

The predicted spectra were plotted for each of the three most likely conformers, i.e. *envelope-axial* (C_s), *envelope-equatorial* (C_s) and *twisted* form (C_1) with the assumption that the planar conformer would be a high energy form. The simulated spectra from *ab initio* MP2(full)/6-31G(d) calculations with two scaling factors were compared with the spectrum of the solid and are shown in Fig. 4. The most definitive spectral region for determining the conformer(s) present is the region from 400 to 1000 cm^{-1} , where five or six of the ring vibrations are expected. It is clear from these data that the predicted spectrum of the *twisted* (C_1) conformer is the best fit to the observed spectrum of the solid as well as that for the gas (Fig. 1). This conclusion is also supported by the *ab initio* calculations where both of the *envelope* forms are predicted to be saddle points by a negative frequency. Therefore, it is concluded that the conformer present in all of the physical states is the *twisted* form. Since both *envelope-axial* and *-equatorial* forms have predicted lower

energies of ~ 1400 and ~ 900 cm^{-1} , respectively, than the planar form which shows that transitions from one *twisted* form to another will not be through the planar form.

Once the form of the stable conformer has been identified the vibrational assignment could be made which was aided significantly by the predicted information from the *ab initio* MP2(full)/6-31G(d) calculations. Of particular importance were the infrared band contours and intensities, the Raman activities and depolarization values, and of course the fundamental frequencies which were obtained with only two scaling factors of 0.88 for the CH_2 stretches and deformations and 0.90 for the remaining vibrations except for the heavy atom bends. A significant number of the fundamental vibrations could be initially assigned from well known “group frequencies” particularly in the fingerprint region. The most uncertain assignments are for the CH_2 stretches where eight normal modes are “bunched” together with significant Fermi resonance expected. More confident assignments could be made in this spectral region by utilizing deuterium substitution for the α - CH_2 groups and then the β - CH_2 groups.

Most of the CH_2 bending modes could be readily assigned with the predicted frequencies, band contours and intensities from the infrared spectra. The A-, C- or A/C- and B-type bands could be observed in the spectrum (Fig. 5). For example, the band at 1157 cm^{-1} is obviously a B-type band and a fundamental is predicted at 1172 cm^{-1} with 73% B-type contour which is due to a relatively weak α - CH_2 wag. The band at 1080 cm^{-1} is clearly an A-type band (predicted 82% A and 18% C), where, the α_{20} (α - CH_2 wag) fundamental is predicted to be at 1089 cm^{-1} with an intensity of 41.5 km/mol . The band at 1033 cm^{-1} has a pronounced shoulder at 1019 cm^{-1} with the latter one nearly a pure A-type band (99%) and the former one nearly an equal A/C type band (61% A and 38% C); these

bands are due to ν_{21} (\square -CH₂ twist, 50% S₂₁) and ν_{22} (ring deformation, 41% S₂₂, 20% S₃₁), respectively. These assignments illustrate how most of the CH₂ bends could be assigned but beginning at 1019 cm⁻¹ and lower frequencies to 400 cm⁻¹ the vibrations are due to heavy atom motions, the four CH₂ rocks, and two SiH bends. It is fairly easy to identify the fundamental frequencies but a significant number of them are extensively mixed with the CH₂ bends and heavy atom modes. Thus, the approximate descriptions are more for “bookkeeping” rather than the major molecular motion giving rise to the vibration.

The most interesting vibrations are the heavy atom modes particularly the ring vibrations. Four of these modes are expected to be between 850 and 1030 cm⁻¹ and the other modes in this spectral range are CH₂ rocking modes. The ring deformation (ν_{25}) is predicted to have the largest infrared intensity of these modes and is assigned at 871 cm⁻¹ with a weaker band (17.8 km/mol) at 851 cm⁻¹ which is the ring breathing mode (41% S₂₆). In addition to the first ring mode assigned earlier there is another very weak one at 941 cm⁻¹ (solid; 32% S₂₃, 13% S₃₃, 10% S₂₅, all ring modes). Three other ring deformations are expected in the region from 700 to 400 cm⁻¹ and two of them could readily be assigned at 493 (53% S₃₃) and 452 (58% S₃₄) cm⁻¹ but the other one is difficult to assign although the band at 685 cm⁻¹ (21% S₃₁) seems to be the best choice. The two SiH bends can be assigned at 620 and 694 cm⁻¹ with the latter one having contributions from five symmetry coordinates with only 19% S₃₀ and the former one with contributions from four symmetry coordinates with only 26% of S₃₂. Even though both of these modes are extensively mixed they are reasonable “group frequencies”.

Three of the five fundamentals predicted below 400 cm^{-1} were observed in the Raman spectrum (Fig. 2) of the liquid with the ring twisting mode at 268 cm^{-1} (80% S_{36}) and the two SiBr bends are observed as distinct Raman lines at 210 and 160 cm^{-1} with predicted frequencies of 208 and 158 cm^{-1} , respectively. The \square_{37} mode is extensively mixed with contributions of greater than 10% from four symmetry coordinates.

Table 4.4. Calculated electronic energies (hartree) and energy differences (cm^{-1}) for the *twisted* (C_1), *envelope-axial* (C_s), *envelope-equatorial* (C_s), and *planar* (C_s) forms of 1-bromo-1-silacyclopentane.

Method/Basis Set	# of Basis Functi ons	<i>Twist</i> (C_1)	<i>Axial</i> (C_s) ^a	<i>Equatorial</i> (C_s) ^a	<i>Planar</i> (C_s) ^a
RHF/6-31G(d)	127	-3015.591261	1364	1630	2319
RHF/6-31+G(d)	151	-3015.605360	1448	1569	2284
MP2(full)/6-31G(d)	127	-3016.363603	1364	1722	2778
MP2(full)/6-31+G(d)	151	-3016.386375	1351	1631	2606
MP2(full)/6-311G(d,p)	196	-3019.536273	1363	1694	2494
MP2(full)/6-311+G(d,p)	220	-3019.541142	1258	1667	2479
MP2(full)/6-311G(2d,2p)	253	-3019.619863	1233	1678	2659
MP2(full)/6-311+G(2d,2p)	277	-3019.622927	1187	1683	2643
MP2(full)/6-311G(2df,2pd)	340	-3019.744369	1254	1703	2637
MP2(full)/6-311+G(2df,2pd)	364	-3019.746926	1216	1715	2630
MP2(full) average			1252 ± 61	1690 ± 17	2590 ± 81

B3LYP/6-31G(d)	127	-3019.113573	1245	1453	2077
B3LYP/6-31+G(d)	151	-3019.131730	1310	1394	2012
B3LYP/6-311G(d,p)	196	-3021.616934	1221	1385	1860
B3LYP/6-311+G(d,p)	220	-3021.618264	1215	1381	1860
B3LYP/6-311G(2d,2p)	253	-3021.622659	1115	1288	1759
B3LYP/6-311+G(2d,2p)	277	-3021.624140	1170	1358	1831
B3LYP/6-311G(2df,2pd)	340	-3021.631479	1200	1363	1833
B3LYP/6-311+G(2df,2pd)	364	-3021.632497	1188	1363	1829
B3LYP/aug-cc-pVTZ	500	-3021.722449	1205	1367	1845
B3LYP average			1188 ± 36	1358 ± 32	1831 ± 34

^a Energy differences are relative to the *twist* conformer.

Table 4.5. Structural parameters (Å and degree), rotational constants (mhz) and dipole moment (debye) for 1-⁷⁹bromo-1-silacyclopentane *twisted* (C₁) form.

Structural Parameters	Internal Coordinates	RHF/ 6-31G(d)	MP2(full)/ 6-311+G(d, p)	B3LYP/ 6-311+G(d, p)	Estimated r ₀
r (Si ₁ -C ₂)	X ₁	1.892	1.883	1.894	1.882(5)
r (Si ₁ -C ₃)	X ₂	1.889	1.878	1.892	1.877(5)
r (C ₂ -C ₄)	Y ₁	1.548	1.546	1.551	1.549(5)
r (C ₃ -C ₅)	Y ₂	1.546	1.543	1.549	1.546(5)
r (C ₄ -C ₅)	Z	1.538	1.536	1.544	1.536(5)
r (Si ₁ -Br ₆)	r ₁	2.236	2.242	2.270	2.232(5)
r (Si ₁ -H ₇)	r ₂	1.471	1.474	1.483	1.482(2)
r (C ₂ -H ₈)	r ₃	1.086	1.095	1.094	1.095(2)
r (C ₃ -H ₉)	r ₄	1.089	1.098	1.097	1.098(2)
r (C ₂ -H ₁₀)	r ₅	1.085	1.094	1.092	1.094(2)
r (C ₃ -H ₁₁)	r ₆	1.084	1.092	1.092	1.092(2)
r (C ₅ -H ₁₂)	r ₇	1.088	1.097	1.096	1.097(2)
r (C ₄ -H ₁₃)	r ₈	1.088	1.097	1.097	1.097(2)
r (C ₅ -H ₁₄)	r ₉	1.086	1.095	1.094	1.095(2)
r (C ₄ -H ₁₅)	r ₁₀	1.085	1.094	1.094	1.094(2)

$\angle \text{C}_3\text{Si}_1\text{C}_2$	θ	96.5	96.5	96.5	96.8(5)
$\angle \text{Si}_1\text{C}_2\text{C}_4$	ψ_1	102.9	103.1	103.2	103.3(5)
$\angle \text{Si}_1\text{C}_3\text{C}_5$	ψ_2	102.7	102.1	103.1	102.3(5)
$\angle \text{C}_2\text{C}_4\text{C}_5$	φ_1	108.9	108.4	109.0	108.3(5)
$\angle \text{C}_3\text{C}_5\text{C}_4$	φ_2	108.6	107.7	108.8	107.6(5)
$\angle \text{Br}_6\text{Si}_1\text{H}_7$	α	105.5	106.1	105.2	106.1(5)
$\angle \text{H}_8\text{C}_2\text{H}_{10}$	γ_1	107.1	107.4	107.2	107.4(5)
$\angle \text{H}_9\text{C}_3\text{H}_{11}$	γ_2	107.2	107.8	107.3	107.8(5)
$\angle \text{H}_{13}\text{C}_4\text{H}_{15}$	ε_1	106.7	107.2	106.7	107.2(5)
$\angle \text{H}_{12}\text{C}_5\text{H}_{14}$	ε_2	106.9	107.3	106.8	107.3(5)
$\angle \text{Br}_6\text{Si}_1\text{C}_2$	β_1	112.3	111.2	112.0	111.2(5)
$\angle \text{Br}_6\text{Si}_1\text{C}_3$	β_2	112.7	110.9	112.6	110.9(5)
$\angle \text{H}_7\text{Si}_1\text{C}_3$	β_3	115.3	116.0	115.7	116.0(5)
$\angle \text{H}_7\text{Si}_1\text{C}_2$	β_4	114.9	116.2	115.0	116.2(5)
$\angle \text{H}_8\text{C}_2\text{Si}_1$	π_1	110.1	109.5	109.4	109.5(5)
$\angle \text{H}_9\text{C}_3\text{Si}_1$	π_5	109.2	109.5	108.5	109.5(5)
$\angle \text{H}_{10}\text{C}_2\text{Si}_1$	π_3	114.2	114.2	113.7	114.2(5)
$\angle \text{H}_{11}\text{C}_3\text{Si}_1$	π_7	115.1	114.5	114.5	114.5(5)
$\angle \text{H}_8\text{C}_2\text{C}_4$	π_2	110.2	110.1	110.6	110.1(5)
$\angle \text{H}_9\text{C}_3\text{C}_5$	π_6	110.0	109.5	110.3	109.5(5)
$\angle \text{H}_{10}\text{C}_2\text{C}_4$	π_4	112.3	112.5	112.7	112.5(5)
$\angle \text{H}_{11}\text{C}_3\text{C}_5$	π_8	112.6	113.2	113.0	113.2(5)
$\angle \text{H}_{13}\text{C}_4\text{C}_2$	σ_1	109.5	109.7	109.5	109.7(5)
$\angle \text{H}_{13}\text{C}_4\text{C}_5$	σ_2	108.9	108.5	109.0	108.5(5)
$\angle \text{H}_{15}\text{C}_4\text{C}_2$	σ_3	111.5	111.5	111.4	111.5(5)
$\angle \text{H}_{15}\text{C}_4\text{C}_5$	σ_4	111.3	111.5	111.2	111.5(5)
$\angle \text{H}_{12}\text{C}_5\text{C}_3$	σ_5	109.4	109.6	109.3	109.6(5)
$\angle \text{H}_{12}\text{C}_5\text{C}_4$	σ_6	109.2	109.0	109.1	109.0(5)
$\angle \text{H}_{14}\text{C}_5\text{C}_3$	σ_7	111.7	111.8	111.6	111.8(5)
$\angle \text{H}_{14}\text{C}_5\text{C}_4$	σ_8	111.2	111.4	111.1	111.4(5)
$\tau \text{Si}_1\text{C}_2\text{C}_4\text{C}_5$	τ_1	-35.5	-34.6	-35.0	-34.6(5)
$\tau \text{C}_2\text{C}_4\text{C}_5\text{C}_3$	τ_2	50.4	52.1	49.1	52.1(5)
A		4144.99	4197.99	4118.94	4039.24
B		972.91	1545.68	953.27	1000.16
C		904.20	1380.76	886.96	935.94
$ \mu_a $		2.387	2.554	2.535	
$ \mu_b $		0.038	0.071	0.022	
$ \mu_c $		0.356	0.477	0.290	
$ \mu_t $		2.414	2.599	2.552	

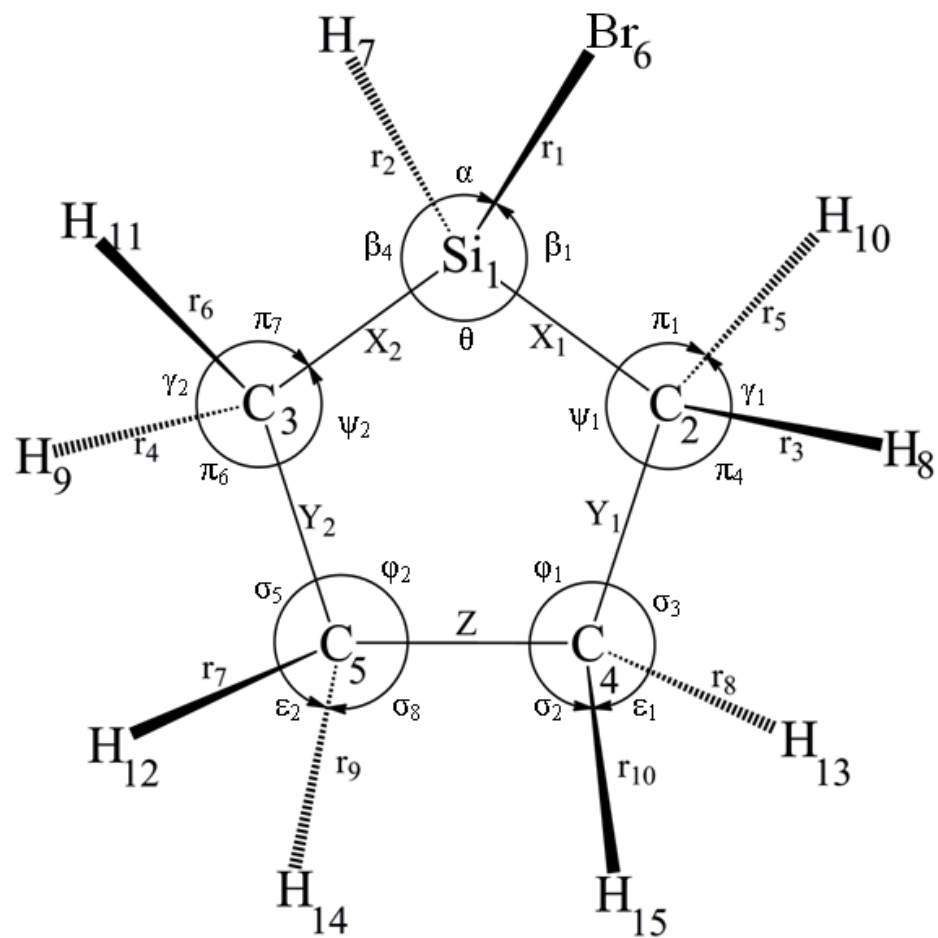


Figure 4.3. Planar (C_s) conformer of 1-bromo-1-silacyclopentane showing atom numbering and internal coordinates.

Table 4.6. Symmetry coordinates of 1-bromo-1-silacyclopentane.

Description	Symmetry Coordinate ^a
α -CH ₂ antisymmetric stretch	$S_1 = r_3 - r_5 + r_4 - r_6$
α -CH ₂ antisymmetric stretch	$S_2 = r_3 - r_5 - r_4 + r_6$
β -CH ₂ antisymmetric stretch	$S_3 = r_7 - r_9 - r_8 + r_{10}$
β -CH ₂ antisymmetric stretch	$S_4 = r_7 - r_9 + r_8 - r_{10}$
α -CH ₂ symmetric stretch	$S_5 = r_3 + r_5 + r_4 + r_6$
α -CH ₂ symmetric stretch	$S_6 = r_3 + r_5 - r_4 - r_6$
β -CH ₂ symmetric stretch	$S_7 = r_7 + r_9 + r_8 + r_{10}$
β -CH ₂ symmetric stretch	$S_8 = r_7 + r_9 - r_8 - r_{10}$
Si-H stretch	$S_9 = r_2$
β -CH ₂ deformation	$S_{10} = 4\varepsilon_1 - \sigma_1 - \sigma_2 - \sigma_3 - \sigma_4 + 4\varepsilon_2 - \sigma_5 - \sigma_6 - \sigma_7 - \sigma_8$
β -CH ₂ deformation	$S_{11} = 4\varepsilon_1 - \sigma_1 - \sigma_2 - \sigma_3 - \sigma_4 - 4\varepsilon_2 + \sigma_5 + \sigma_6 + \sigma_7 + \sigma_8$
α -CH ₂ deformation	$S_{12} = 4\gamma_1 - \pi_1 - \pi_2 - \pi_3 - \pi_4 + 4\gamma_2 - \pi_5 - \pi_6 - \pi_7 - \pi_8$
α -CH ₂ deformation	$S_{13} = 4\gamma_1 - \pi_1 - \pi_2 - \pi_3 - \pi_4 - 4\gamma_2 + \pi_5 + \pi_6 + \pi_7 + \pi_8$
β -CH ₂ wag	$S_{14} = \sigma_1 - \sigma_2 + \sigma_3 - \sigma_4 - \sigma_5 + \sigma_6 - \sigma_7 + \sigma_8$
β -CH ₂ wag	$S_{15} = \sigma_1 - \sigma_2 + \sigma_3 - \sigma_4 + \sigma_5 - \sigma_6 + \sigma_7 - \sigma_8$
β -CH ₂ twist	$S_{16} = \sigma_1 - \sigma_2 - \sigma_3 + \sigma_4 + \sigma_5 - \sigma_6 - \sigma_7 + \sigma_8$
β -CH ₂ twist	$S_{17} = \sigma_1 - \sigma_2 - \sigma_3 + \sigma_4 - \sigma_5 + \sigma_6 + \sigma_7 - \sigma_8$
α -CH ₂ twist	$S_{18} = \pi_1 - \pi_2 - \pi_3 + \pi_4 - \pi_5 + \pi_6 + \pi_7 - \pi_8$
α -CH ₂ wag	$S_{19} = \pi_1 - \pi_2 + \pi_3 - \pi_4 + \pi_5 - \pi_6 + \pi_7 - \pi_8$
α -CH ₂ wag	$S_{20} = \pi_1 - \pi_2 + \pi_3 - \pi_4 - \pi_5 + \pi_6 - \pi_7 + \pi_8$
α -CH ₂ twist	$S_{21} = \pi_1 - \pi_2 - \pi_3 + \pi_4 + \pi_5 - \pi_6 - \pi_7 + \pi_8$
ring deformation	$S_{22} = 4Z - X_1 - X_2 - Y_1 - Y_2$
ring deformation	$S_{23} = X_1 - X_2 - Y_1 + Y_2$
β -CH ₂ rock	$S_{24} = \sigma_1 + \sigma_2 - \sigma_3 - \sigma_4 + \sigma_5 + \sigma_6 - \sigma_7 - \sigma_8$
ring deformation	$S_{25} = X_1 - X_2 + Y_1 - Y_2$
ring breathing	$S_{26} = Z + X_1 + X_2 + Y_1 + Y_2$
α -CH ₂ rock	$S_{27} = \pi_1 + \pi_2 - \pi_3 - \pi_4 - \pi_5 - \pi_6 + \pi_7 + \pi_8$
β -CH ₂ rock	$S_{28} = \sigma_1 + \sigma_2 - \sigma_3 - \sigma_4 - \sigma_5 - \sigma_6 + \sigma_7 + \sigma_8$
α -CH ₂ rock	$S_{29} = \pi_1 + \pi_2 - \pi_3 - \pi_4 + \pi_5 + \pi_6 - \pi_7 - \pi_8$
Si-H parallel bend*	$S_{30} = \beta_3 - \beta_4$
ring deformation	$S_{31} = 4\theta - \psi_1 - \psi_2 - \phi_1 - \phi_2$
Si-H perpendicular bend*	$S_{32} = 4\alpha - \beta_1 - \beta_2 - \beta_3 - \beta_4$
ring deformation	$S_{33} = X_1 + X_2 - Y_1 - Y_2$
ring deformation	$S_{34} = \psi_1 - \psi_2 + \phi_1 - \phi_2$
Si-Br stretch	$S_{35} = r_1$
ring twist	$S_{36} = \tau_1 + \tau_2$
Si-Br parallel bend*	$S_{37} = \beta_1 - \beta_2$
Si-Br perpendicular bend*	$S_{38} = \beta_1 + \beta_2 - \beta_3 - \beta_4$
ring puckering	$S_{39} = \tau_1 - \tau_2$

^a Not normalized.

*Bend parallel and perpendicular to the ring, respectively.

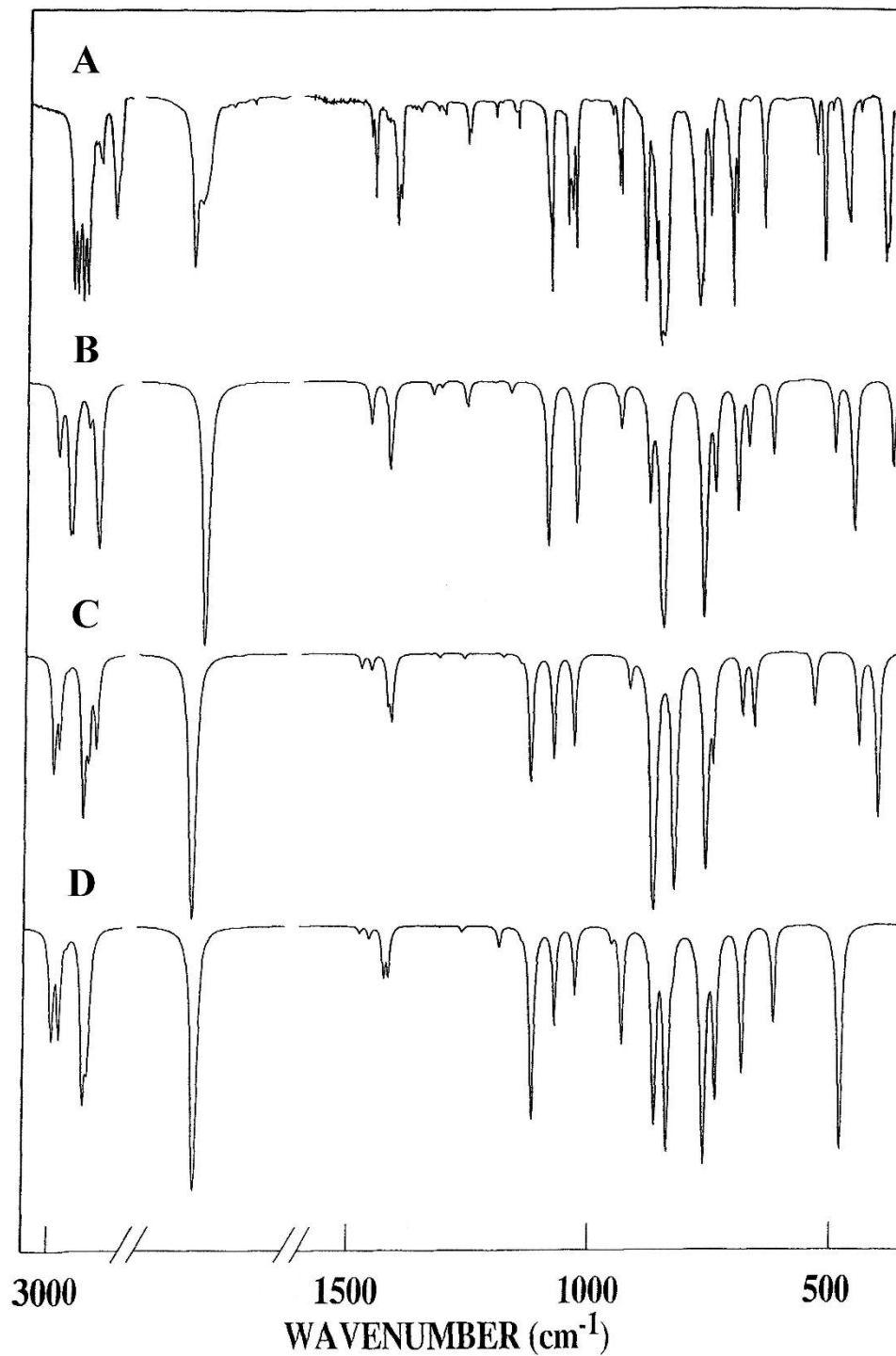


Figure 4.4. Comparison of experimental and calculated infrared spectra of 1-bromo-1-silacyclopentane: (A) observed infrared spectrum of solid; (B) simulated infrared spectrum of *twist* conformer; (C) simulated infrared spectrum of *envelope-axial* conformer; (D) simulated infrared spectrum of *envelope-equatorial* conformer.

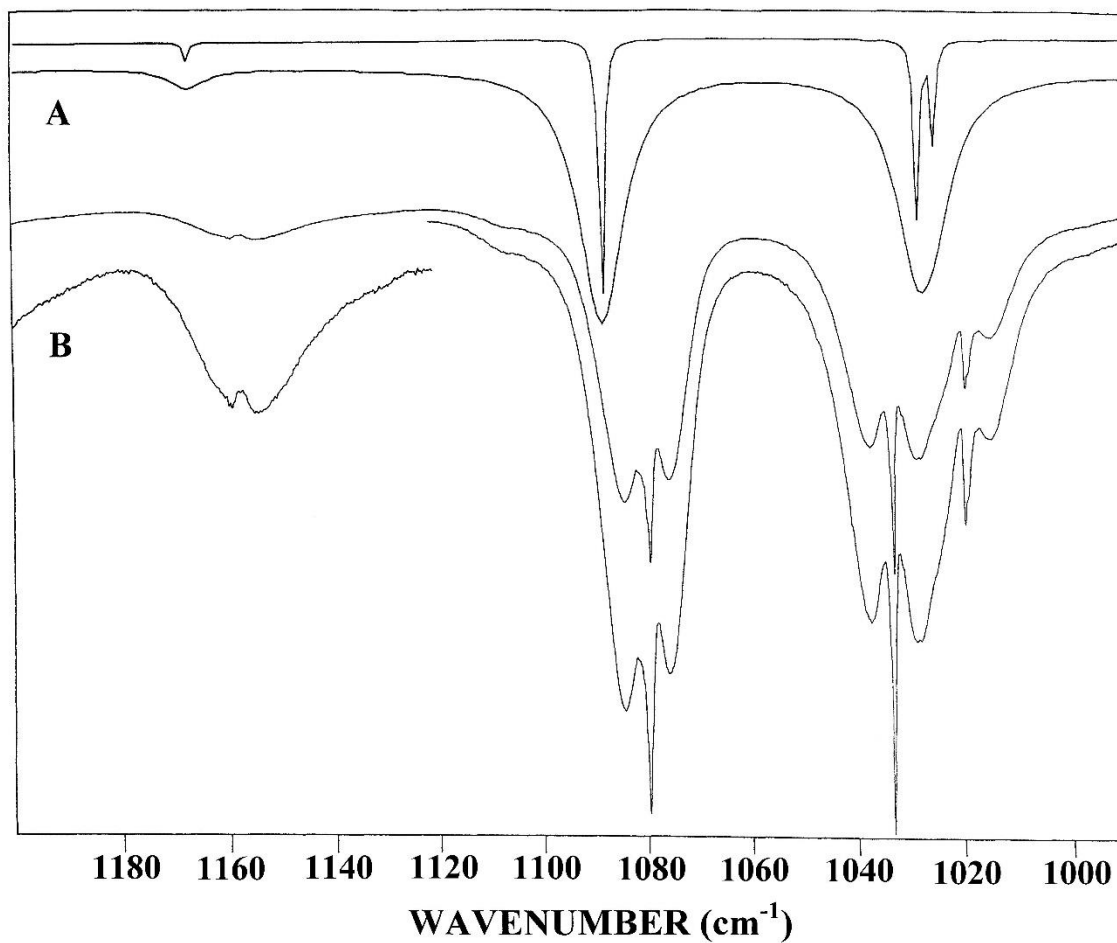


Figure 4.5. Comparison of experimental and calculated infrared spectra (990-1200 cm^{-1}) of 1-bromo-1-silacyclopentane: (A) simulated spectra of *twist* (C_1) conformer at 0.5 cm^{-1} and 4.0 cm^{-1} resolutions; (B) observed infrared spectrum of the gas showing typical B-, A- and A/C-type band contours at 1157, 1080 and 1033 cm^{-1} , respectively, measured at 0.5 cm^{-1} resolution.

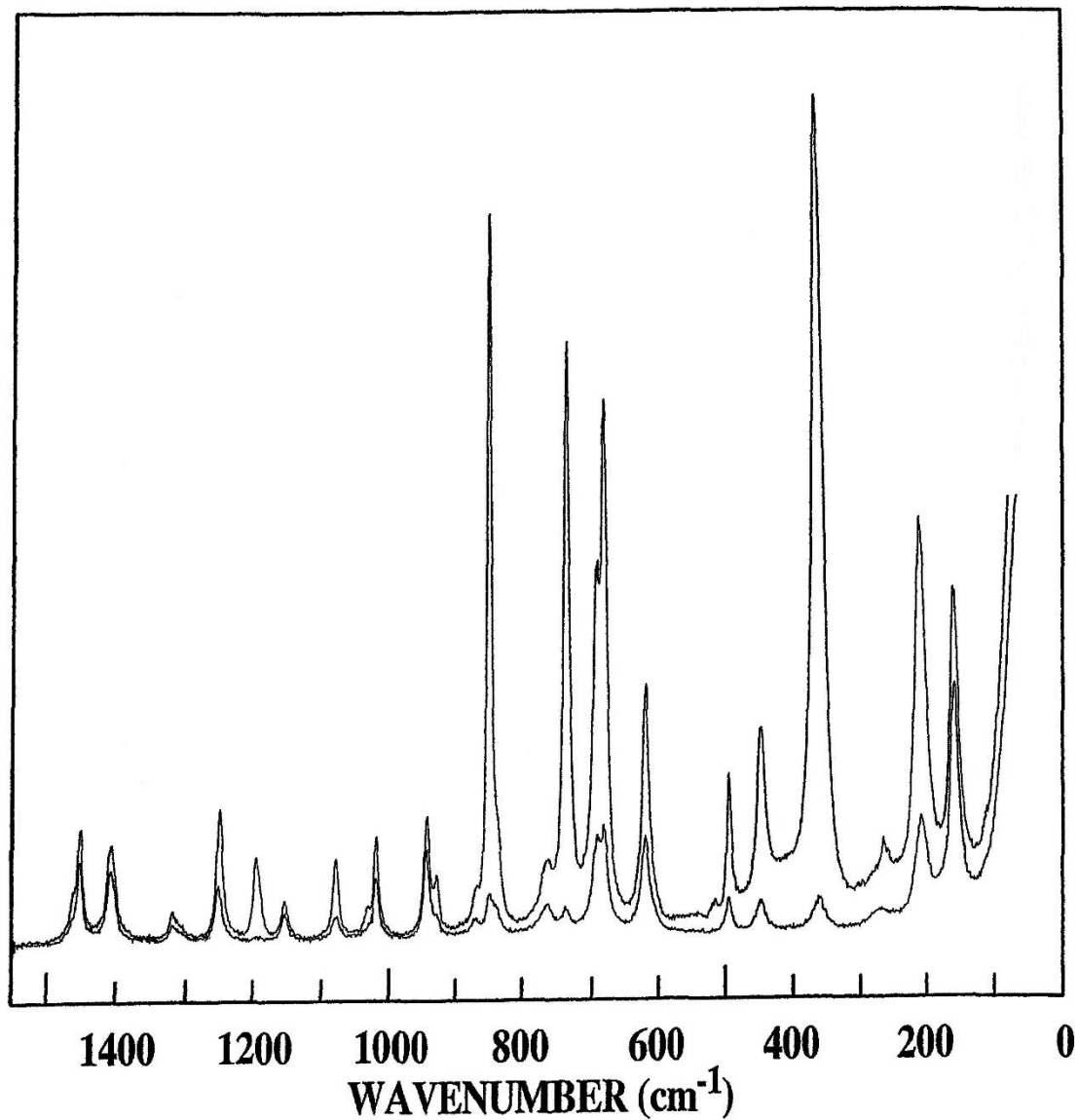


Figure 4.6. Raman spectra (0-1550 cm⁻¹) showing the polarized and the depolarized bands for 1-bromo-1-silacyclopentane.

Discussion

We investigated the changes in the predicted intensities of the infrared bands and the Raman activities when the basis set was increased, from 6-31G(d) to 6-311+G(d,p), by the B3LYP density functional theory method. In Table 6 the values are reported and many have very small changes but a few of them have rather large differences for Raman activities. For example, ν_8 has a Raman activity of $131.0 \text{ \AA}^4/\text{u}$ that increases to $185.6 \text{ \AA}^4/\text{u}$ when the basis set increases and for ν_9 (Si-H stretch) the Raman activity increases from 126.5 to $178.7 \text{ \AA}^4/\text{u}$. There are also significant differences such as ν_{11} which drops $\sim 50\%$ from 20.1 to $11.1 \text{ \AA}^4/\text{u}$ and ν_{13} which decreases from 19.4 to $8.7 \text{ \AA}^4/\text{u}$. However, as the vibrational frequencies decrease the differences decrease and are often nearly the same. The predicted intensities for the infrared bands are not nearly as varied as the Raman activities but they do follow the same trend to smaller differences at lower frequencies.

The predicted depolarization (dp) ratios do not vary significantly with the change in basis sets from B3LYP calculations and these are quite similar to the values obtained from the MP2(full)/6-31G(d) calculations (Table 6). The P.E.D.s are very similar for both B3LYP predicted values, which, are also similar to those predicted from the MP2(full)/6-31G(d) calculations (Table 5).

The predicted dp ratios are quite good as compared to the experimental spectra (Fig. 6). The predicted depolarization ratios differ significantly for only four of the fundamentals, $1250 (\nu_{17})$, $1079 (\nu_{20})$, $840 (\nu_{27})$, and $693 (\nu_{30}) \text{ cm}^{-1}$. The band at 1250 cm^{-1} assigned as the fundamental ν_{17} is predicted as having a dp ratio of 0.75 while the experimental ratio is 0.31 , the fundamental can be described as a β -CH₂ twist (51%) with some α -CH₂ twist (19%) and α -CH₂ wag (18%) character. At 1079 cm^{-1} the ν_{20} (39% α -

CH₂ wag and 21% β-CH₂ twist) fundamental has an experimental dp ratio of 0.25 as compared with 0.73 from the *ab initio* prediction. The fundamental at 840 cm⁻¹ (ν₂₇) has a predicted dp ratio of 0.64 as compared to the experimentally determined ratio of 0.24, this band has 36% α-CH₂ rock character with contributions of 16% Si-H parallel bend and 13% Si-Br parallel bend while the remaining 35% is composed of smaller (less than 10%) contributions. The fundamental ν₃₀ at 693 cm⁻¹ is highly mixed with contributions from five different modes, it is described as the Si-H parallel bend (19%) but this should be considered “bookkeeping” rather than a meaningful description of this complex vibrational motion. The experimentally determined dp ratio is 0.28 compared to 0.61 from the *ab initio* predictions. This shows good utility for the *ab initio* predictions with the predicted depolarization ratios matching reasonably well with the experimentally observed depolarization ratios.

The *ab initio* predicted frequencies are in good agreement with the observed fundamentals of the *twist* form with an average difference of 8 cm⁻¹ which is 0.5% error where these errors arise mainly from the β-CH₂ symmetric stretches, α-CH₂ deformations, the α-CH₂ wag, and the ring deformations. The fundamental frequencies were also calculated using the B3LYP density functional theory method at two different basis sets. The 6-31G(d) and 6-311+G(d,p) basis sets were used and gave an average difference of 32 cm⁻¹ (3.1% error) and 20 cm⁻¹ (2.0% error), respectively, where the carbon-hydrogen stretching modes were not included as they differed by over a hundred wavenumbers from the observed frequencies. As noted the B3LYP calculations do significantly worse at predicting the fundamental frequencies. This is partially due to the B3LYP predicted frequencies having values that are sometimes higher and sometimes lower than the

observed values so any effort to scale the predictions becomes complicated at best. This highlights the advantage of the *ab initio* MP2(full)/6-31G(d) predictions in that the predicted frequencies are usually higher than the observed values or relatively close to the observed values.

The *twist* conformer is relatively rigid with the predicted energy difference to the *envelope-axial* form (saddle point) of 1216 cm^{-1} from the MP2 calculations by utilizing the largest basis set with a similar value of $1188 \pm 36\text{ cm}^{-1}$ from the average of all the B3LYP calculations which agrees with the value of 1205 cm^{-1} from the B3LYP/aug-cc-pVTZ (500 basis functions). The next higher energy saddle point which is the *envelope-equatorial* form, has a predicted value nearly 500 cm^{-1} greater than the *axial* form from the MP2 calculations with those from the B3LYP calculations only about 300 cm^{-1} higher. The energy difference at the planar position is about 900 cm^{-1} higher than the *equatorial* form from the MP2 calculations and about 500 cm^{-1} higher from the B3LYP calculations. These energy differences are relatively large compared to those of the corresponding carbon compounds. From the limited data that is currently available one would expect that 1-X-1-silacyclopentane molecules will have the *twisted* form as the most stable conformer for this molecule which is very different from the carbon analogues.

It should be possible to estimate structural parameters for the *twist* conformer of 1-bromo-1-silacyclopentane by adjusting the MP2(full)/6-311+G(d,p) calculated structural parameters using similar molecules as a guideline. The CH bond distances predicted by MP2(full)/6-311+G(d,p) *ab initio* calculations can be used as a good prediction without any adjustment as we³³ have shown that *ab initio* MP2/6-311+G(d,p) calculations predict the r_0 CH distances for more than fifty substituted hydrocarbons to better than $\pm 0.002\text{ \AA}$

compared to the experimentally determined values from isolated CH stretching frequencies which were compared³⁴ to previously reported values from earlier microwave studies. Therefore, all of the carbon-hydrogen distances can be taken from the MP2(full)/6-311+G(d,p) predicted values for 1-bromo-1-silacyclopentane. The heavy atom ring parameters can be estimated by using the corresponding parameters in silacyclopentane³⁵ to adjust the MP2(full)/6-311+G(d,p) calculated parameters. For silacyclopentane the adjusted r_0 Si-C distance is 0.005 Å shorter than the predicted value whereas the two side C-C distances are 0.003 Å longer and the unique “bottom” C-C distance has the same value as predicted. Therefore, we have predicted the two C-C distances for 1-bromo-1-silacyclopentane to be 0.003 Å longer than the *ab initio* predicted value with the same value for the “bottom” C-C distance as predicted. The Si-C distance for silacyclopentane, while interesting for comparison purposes to 1-bromo-1-silacyclopentane, was not used to find the estimated r_0 structural parameters as the parameters from trimethylbromide should give a more consistent value. The differences in the angle values with those obtained from the adjusted values to the predicted values for silacyclopentane were retained for the bromosubstituted molecule. This leaves the Si-Br and Si-C distances to be obtained from the values reported for trimethyl bromosilane³⁶ and bromosilane³⁷, while the Si-H distance can be obtained using the frequency of the isolated SiH stretching mode.

It has been shown that SiH distances can be obtained from the frequencies of the isolated SiH stretching modes³⁸. Therefore, from the observed frequency of 2176 cm^{-1} for the SiH stretch we have obtained a value of 1.482 Å for the SiH distance (Table 5) which is 0.008 Å longer than the corresponding distance from the *ab initio* predicted parameter. We believe that this value has at most an uncertainty of ± 0.002 Å. This longer distance

compared to the *ab initio* predicted value is the same difference found for many SiH distances in other organosilanes^{39,40}.

In the microwave study³⁶ of trimethyl bromosilane the structure was determined though only the SiBr is a true r_s parameter while the carbon parameters are approximate r_s parameters. Therefore, we have again determined the structural parameters for trimethyl bromosilane by utilizing the three B rotational constants previously reported³⁶. We have found that good structural parameters for hydrocarbons and many substituted ones can be determined by adjusting the structural parameters obtained from the *ab initio* MP2(full)/6-311+G(d,p) calculations to fit the rotational constants obtained from microwave experimental data by using a computer program “A&M” (*Ab initio* and Microwave) developed⁴¹ in our laboratory. In order to reduce the number of independent variables, the structural parameters are separated into sets according to their types where bond distances in the same set keep their relative ratio, and bond angles and torsional angles in the same set keep their difference in degrees. This assumption is based on the fact that errors from *ab initio* calculations are systematic. Therefore, we obtained “adjusted r_0 ” structural parameters using the previously reported rotational constants. The determined heavy atom structural parameters for trimethyl bromosilane are: the distances with MP2(full)/6-311+G(d,p) values in brackets (Å) Si-C = 1.863(3) [1.864], Si-Br = 2.244(3) [2.252], and the angle in degrees (°) \angle BrSiC = 106.9(5) [107.3]. These parameters give differences of -0.001 and -0.008 Å for the Si-C and Si-Br bonds, respectively, and -0.4° for the \angle BrSiC angle. The Si-C distances were then obtained using the MP2(full)/6-311+G(d,p) calculations and adjusting them by -0.001 Å. This leaves the Si-Br distance to be determined.

The microwave study of bromosilane³⁷ determined the r_0 structural parameters for Si-Br and Si-H to be 2.2123(1) and 1.4743(2) Å, respectively. The corresponding MP2(full)/6-311+G(d,p) parameters were predicted to be 2.225 and 1.468 Å from which the differences of -0.013 and 0.006 Å can be determined. The Si-H bond distance determined from the frequency of the SiH isolated stretching mode compares favorably with this prediction again showing the systematic nature of *ab initio* errors. The Si-Br value was adjusted using the average of the difference between the r_0 parameters and the corresponding MP2(full)/6-311+G(d,p) parameter for bromosilane and trimethyl bromosilane. This average gives an adjustment of -0.010 Å, thereby, giving the bond distance listed in Table 5.

For the angles, we retained the values from the *ab initio* calculation since the adjusted values of the angles of silacyclopentane differed by 0.3, 0.2, 0.1 and 0.1° and with the listed uncertainties of 0.5 we believe they should be within the experimentally determined values. All of these estimated parameters are listed in Table 5 along with those predicted from RHF/6-31G(d) and B3LYP/6-311+G(d,p) and those from the MP2 calculations from which the adjusted parameters were obtained. It should be noted that the predictions from the RHF calculation provided good estimates for the C-C distances but the Si-C distances are very long. The B3LYP predictions for the Si-C distances are even longer than those from the RHF calculation and those for the C-C are also slightly too long. It is believed that the estimated r_0 parameters reported herein for 1-bromo-1-silacyclopentane have listed uncertainty values that should be within the experimentally determined parameters. Thus, the listed rotational constants given in Table 5 for the ⁷⁹Br

atom should make it relatively easy to assign the microwave spectrum from which the experimental parameters could be obtained.

It is clear that additional work to determine Si-Br distances would be of value where it would be interesting to see if the predicted parameter is consistent for several different types of Si-Br molecules. Also of interest would be a microwave study of a 5-membered ring which contains a silicon atom and four carbon atoms to obtain structural parameters by utilizing isotopic Si and ^{13}C data which should give accurate heavy atom distances of the 1-X-1-silacyclopentane molecules.

PROJECT-2

Infrared and Raman Spectra, Structural Parameters, Conformational Stability, Vibrational Assignment and *ab initio* Calculations of 2-cyanoethylphosphine

Introduction

The conformational stability determination of 1,2-disubstituted ethylene molecules have provided some interesting challenges for the structural scientists over the years. The 1,2-dihaloethane molecules provided good examples where it was shown by infra-red gas phase studies⁴² that the *gauche* conformer of 1,2-difluoroethane has lower energy than the *trans* form by $280 \pm 30 \text{ cm}^{-1}$ ($3.35 \pm 0.36 \text{ kJ mol}^{-1}$). However the *trans* conformer of 1,2-dichloroethane, has lower energy than the *gauche* form by⁴³ $323 \pm 7 \text{ cm}^{-1}$ ($3.87 \pm 0.09 \text{ kJ mol}^{-1}$). This value was obtained by Turner et al. from variable temperature infrared studies of xenon solutions. By utilizing an average of four *gauche/trans* conformer pairs. Eight years later the enthalpy difference was again determined⁴⁴ for 1,2-dichloroethane for both the gas and two different noble gas solutions from variable temperature infrared studies. For the liquid xenon solution two conformer pairs were utilized⁴⁴ which differed from those used earlier⁴³ and a value of $272 \pm 11 \text{ cm}^{-1}$ ($3.26 \pm 0.13 \text{ kJ mol}^{-1}$) was obtained. However from the krypton solution a value of $318 \pm 25 \text{ cm}^{-1}$ ($3.81 \pm 0.30 \text{ kJ mol}^{-1}$) was obtained from only one conformer pair which differed from the two used for the xenon study. This value was much lower than the value of $410 \pm 13 \text{ cm}^{-1}$ ($4.90 \pm 0.15 \text{ kJ mol}^{-1}$) obtained for the gas from one conformational pair. These results indicate that more than one conformer pair should be used to obtain enthalpy differences of conformers since underlining overtones and/or combination bands of the fundamentals can significantly affect the intensities when the temperature is varied.

Instead of XCH_2CH_2X ($X = F, Cl$) molecules, the XCH_2CH_2Y molecules are of even more interest since it is frequently difficult to determine the conformer with the lowest energy spectroscopically because of the low symmetry of the molecules. Also, the energy difference can be very small with 1,2-chlorofluoroethane as an example. The conformational stability of FCH_2CH_2Cl was obtained⁴⁴ from variable temperature infrared studies of both krypton and xenon solutions. The *trans* form was found to have lower energy by $17 \pm 8 \text{ cm}^{-1}$ ($0.20 \pm 0.10 \text{ kJ mol}^{-1}$) from the krypton solution and the *gauche* form was determined to have lower energy by $20 \pm 10 \text{ cm}^{-1}$ ($0.24 \pm 0.12 \text{ kJ mol}^{-1}$) from the xenon solution. These differences are so small that it is not possible to determine which form has the lower energy with possible solvent interference. From variable temperature infrared studies of the gas the *trans* form was reported⁴⁴ to have lower energy by $126 \pm 8 \text{ cm}^{-1}$ ($1.51 \pm 0.09 \text{ kJ mol}^{-1}$). These values indicate the variations that have been reported for these types of molecules with different solutions.

Of particular scientific interest, has been the conformational stability of the 2-substituted ethylamines, $XCH_2CH_2NH_2$, since a large number of molecules containing amines are very important biochemical materials. Therefore, we began such studies with an investigation⁴⁵ of 2-fluoroethylamine where all five possible stable conformers were identified and their relative conformational stabilities determined. Additionally, the r_0 structural parameters were determined for the two conformers with permanent dipole moments and their rotational constants were determined from a previous microwave study⁴⁶. We continued these studies with an investigation of the infrared spectra of the gas and variable temperature xenon solutions of ethylenediamine¹⁴ from which only three of the possible ten conformers were identified and their relative enthalpy differences obtained.

We have broadened our studies to include phosphines since some of the phosphines have been shown to have antitumor activity^{17,18} and, therefore, their conformational stabilities could be important in the selection of the compounds which could have the most potential as biochemical materials.

The first organophosphine molecule initially studied was 2-cyanoethylphosphine, $\text{NCCH}_2\text{CH}_2\text{PH}_2$. The infrared spectra of the gas, liquid and solid and the Raman spectrum of the liquid and solid of 2-cyanoethylphosphine have been recorded from which the conformational stability has been determined and a vibrational assignment of the fundamentals is reported. To support the conformational stability determination and aid in the vibrational assignment, predictions from calculation by ab initio MP2 level with full electron correlation and density functional theory by the B3LYP method have been obtained by using a variety of basis sets. The results of these spectroscopic and theoretical studies are reported herein.

Experimental Methods

The sample of 2-cyanoethylphosphine was purchased from Strem Chemical Company. The purity was determined by gas chromatography to be greater than 96%. The sample was subjected to trap-to-trap transfers under vacuum prior to recording the spectra and stored at -78°C .

Infrared spectra of the solid from $3200 - 400 \text{ cm}^{-1}$ were obtained from a Perkin-Elmer 283B grating spectrophotometer and a liquid-nitrogen-cooled sampling cell with a CsI substrate. The spectra of the solids were recorded at a resolution of 2.0 cm^{-1} . Infrared spectra of the crystalline solid was obtained by the process of annealing which was achieved by repetitive evaporation of the liquid nitrogen completely from the reservoir in

the solid cell, which resulted in a gradual increase in the temperature, which was then followed by sudden freezing of the sample by the addition of liquid nitrogen. This warming process allowed the molecules to form a crystalline structure. The spectrum of the liquid was obtained by sandwiching a drop of the sample between two KBr windows. The infrared spectra of the gas was recorded on a Nicolet 7199 Fourier transform interferometer equipped with a Ge/KBr beamsplitter and a liquid-nitrogen-cooled MCT detector with the sample contained in a 10 cm cell with KBr windows. The instrument was purged to remove the water and carbon dioxide by a commercial two column dryer with one column to remove the water and the other CO₂. The resolution for the spectra of the gas was 0.5 cm⁻¹ at ambient pressure of the gas. Typical spectra are shown in Fig. 7 and the wavenumbers of the observed bands from the spectra of the gas, liquid and solid are listed in Tables 7, 8, 9 and 10.

Raman spectra were recorded from 3050 to 50 cm⁻¹ on a Spex Ramalog DUV spectrometer with the 4880 Å line of a Spectra-Physics model 171 argon ion laser as the excitation source with laser power of 200 mW. Liquid samples were sealed in Pyrex capillaries under vacuum, and spectra of solid and variable temperature liquids were obtained by using a cell similar to one described by Miller and Harney⁴⁷. All the Raman spectra were recorded at 3 cm⁻¹ spectral bandwidths and frequencies are expected to be accurate to be better than 2 cm⁻¹. Typical spectra are shown in Fig. 8.

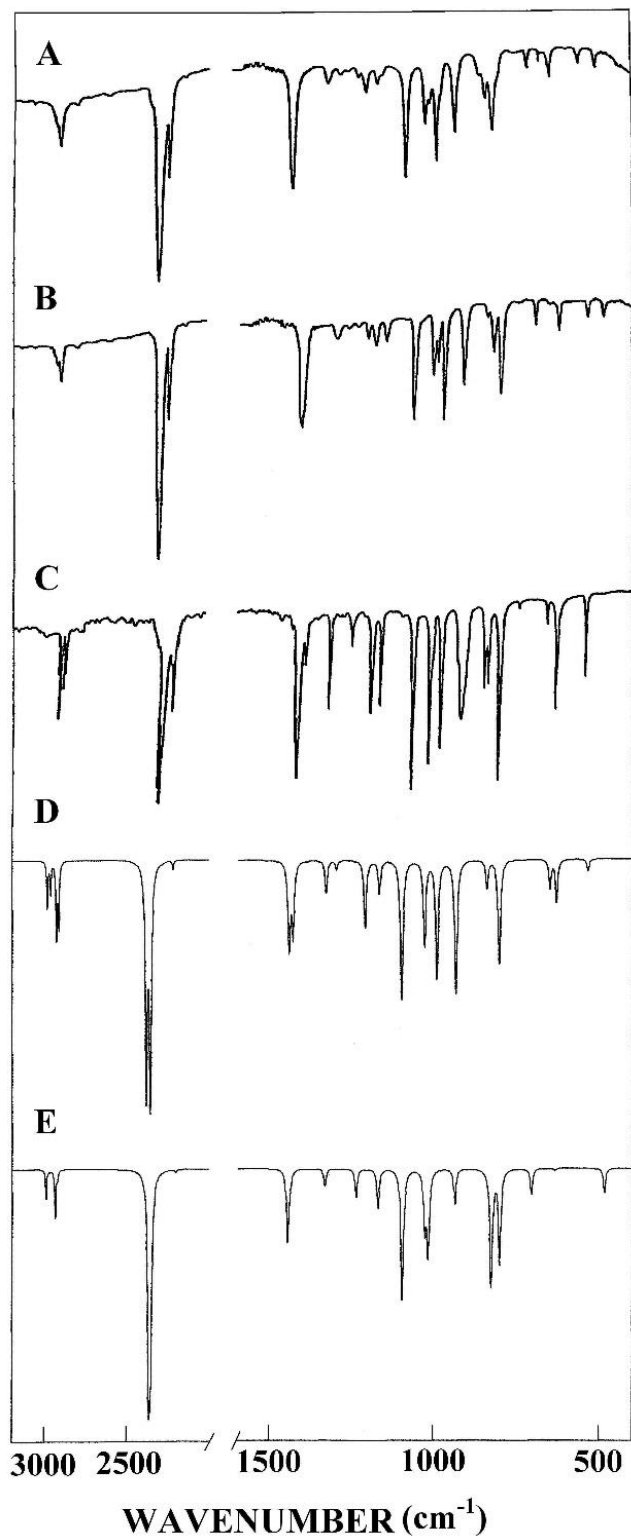


Figure 4.7. Infrared spectra (3200-400 cm^{-1}) of 2-cyanoethylphosphine: (A) liquid; (B) amorphous solid; (C) crystalline solid; (D) simulated IR spectrum of *Gauche-trans* conformer; (E) simulated IR spectrum of *Trans-trans* conformer.

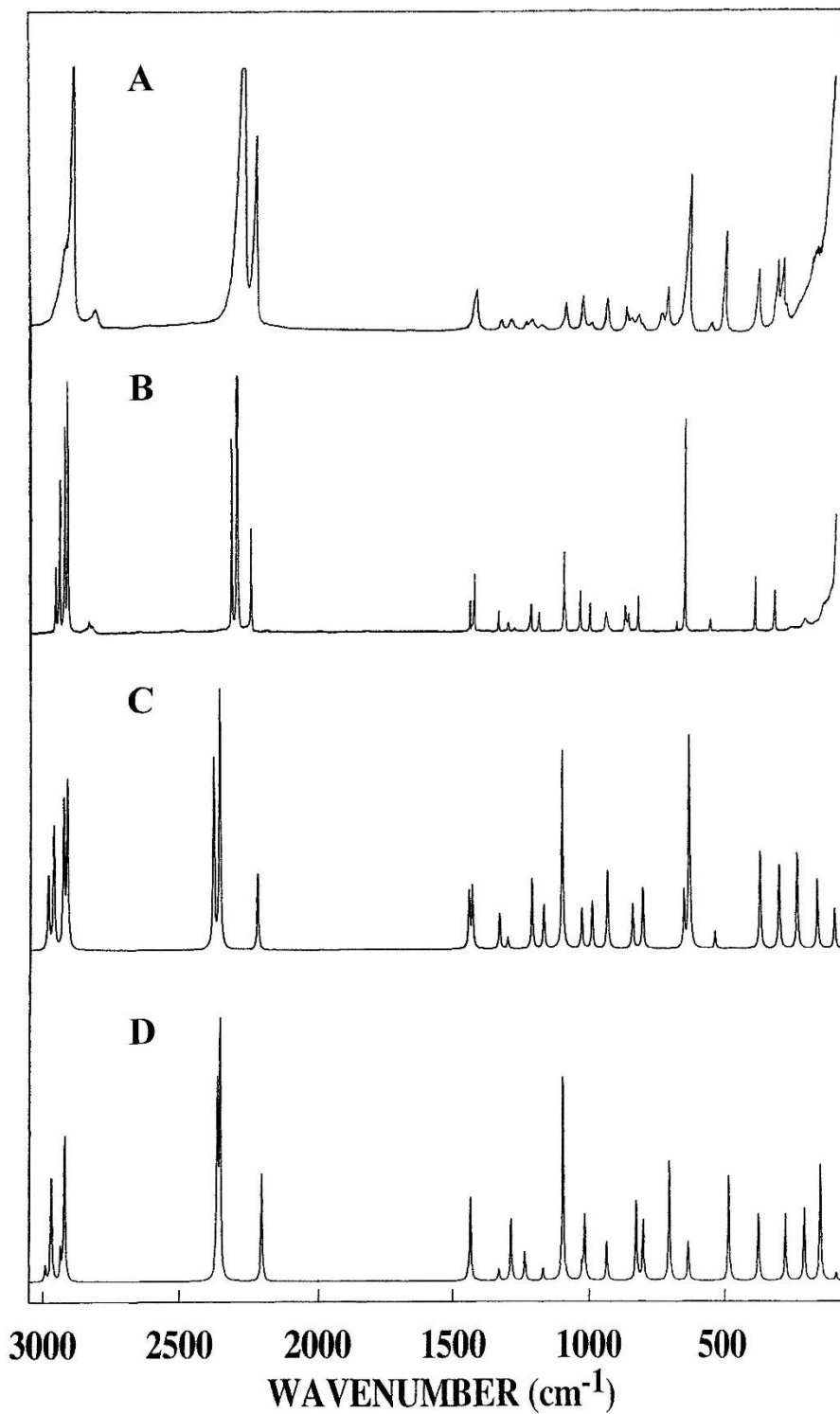


Figure 4.8. Raman spectra ($3050\text{-}50\text{cm}^{-1}$) of 2-cyanoethylphosphine: (A) liquid; (B) solid; (C) simulated Raman spectrum of *Gauche-trans* conformer; (D) simulated Raman spectrum of *Trans-trans* conformer.

Table 4.7. Observed and calculated^a frequencies (cm⁻¹) and potential energy distributions (P.E.D.s) for the *Gt* (C₁) conformer of 2-cyanoethylphosphine.

Vib. no.	Approximate description	AB		IR				Raman		P.E.D. ^c	Contour		
		<i>INITIO</i>	Fixed scaled ^b	gas	liquid	amorphous	crystalline	liquid	solid		A	B	C
v ₁	CH ₂ antisymmetric stretch	3182	2985	2970					2963	93S ₁	21	19	60
v ₂	CH ₂ antisymmetric stretch	3161	2965	2949	2946	2948	2949	2950		92S ₂	15	56	28
v ₃	CH ₂ symmetric stretch	3122	2929					2930		98S ₃	12	68	20
v ₄	CH ₂ symmetric stretch	3108	2916	2922	2920	2917	2922	2917		97S ₄	26	57	17
v ₅	PH ₂ antisymmetric stretch	2511	2315	2303		2310		2314		74S ₅ , 26S ₆	26	59	15
v ₆	PH ₂ symmetric stretch	2486	2292	2298	2300	2297	2295	2296	2295	74S ₆ , 26S ₅	-	2	98
v ₇	C≡N stretch	2222	2222	2247	2246	2243	2246	2243		89S ₇ , 11S ₁₈	33	65	2
v ₈	CH ₂ deformation	1534	1443	1436		1435		1435		97S ₈	8	37	54
v ₉	CH ₂ deformation	1522	1431	1430	1425	1422	1420	1420	1420	99S ₉	8	33	59
v ₁₀	CH ₂ rock	1402	1331	1324	1322	1330	1325	1329		69S ₁₀ , 16S ₁₃	63	2	35
v ₁₁	CH ₂ rock	1370	1300	1288	1288		1285	1290		65S ₁₁ , 24S ₁₂	80	8	12
v ₁₂	CH ₂ twist	1275	1211	1209	1207	1205	1207	1207	1204	30S ₁₂ , 27S ₁₃ , 17S ₁₁ , 12S ₁₀	49	47	4
v ₁₃	CH ₂ twist	1230	1168	1173	1175	1176	1171	1175		40S ₁₃ , 40S ₁₂	2	55	43
v ₁₄	PH ₂ deformation	1159	1100	1084	1081	1081		1082	1083	95S ₁₄	1	60	39
v ₁₅	C-C(P) stretch	1082	1030	1024	1020	1021	1023	1018	1020	44S ₁₅ , 15S ₁₇ , 10S ₁₆	9	44	47
v ₁₆	CH ₂ wag	1042	993	988	987	988	987	985	987	21S ₁₆ , 21S ₂₀ , 20S ₁₈ , 13S ₁₅	16	49	35
v ₁₇	CH ₂ wag	979	936	927	928	928	927	927	928	36S ₁₇ , 19S ₁₉	99	-	1
v ₁₈	C-C(N) stretch	883	842	856	855	855	855	853	856	48S ₁₈ , 16S ₂₀ , 10S ₁₅	69	-	31
v ₁₉	PH ₂ rock	847	805	812	813	811	810	812	809	58S ₁₉ , 22S ₁₇	26	2	72

v ₂₀	PH ₂ twist	684	652	669	666	666	669	669	36S ₂₀ , 36S ₁₆	-	94	6
v ₂₁	C-P stretch	665	632	633	634	638	631	640	78S ₂₁	48	39	13
v ₂₂	C-C≡N in-plane bend	546	537	544	546	548	541	548	33S ₂₂ , 33S ₂₆ , 14S ₁₆	53	47	-
v ₂₃	C-C≡N out-of-plane bend	373	371				373	378	76S ₂₃ , 13S ₂₇	24	5	71
v ₂₄	C-C-P bend	303	299				301	301	67S ₂₄ , 16S ₂₆	68	-	31
v ₂₅	PH ₂ torsion	233	233					242	57S ₂₅ , 15S ₂₆ , 13S ₂₇	36	49	15
v ₂₆	C-C-C bend	159	159				190	191	31S ₂₆ , 24S ₂₂ , 35S ₂₅	5	21	74
v ₂₇	C-C(P) torsion	97	97					119	67S ₂₇	53	20	27

^a MP2(full)/6-31G(d) ab initio calculations, frequencies from scaled force constants and potential energy distributions (P.E.D.s).

^b Scaling factors of 0.88 for CH₂ stretches and CH₂ deformations, 0.85 for PH₂ stretches and 0.90 for all other modes except torsions, heavy atom bends, and C≡N stretch.

^c Symmetry coordinates with P.E.D. contribution less than 10% are omitted.

Table 4.8. Observed and calculated^a frequencies (cm⁻¹) and potential energy distributions (P.E.D.s) for the *Tt* (C_s) conformer of 2-cyanoethylphosphine.

Sym block	Vib. no.	Approximate description	AB		IR				Raman		P.E.D. ^c	Contour		
			<i>INITIO</i>	Fixed scaled ^b	gas	liquid	amorphous	crystalline	liquid	solid		A	B	
A'	v ₁	CH ₂ symmetric stretch	3129	2936	2930				2929			87S ₁ , 13S ₂	4	96
	v ₂	CH ₂ symmetric stretch	3115	2922								87S ₂ , 13S ₁	7	93
	v ₃	PH ₂ symmetric stretch	2482	2288								100S ₃	3	97
	v ₄	C≡N stretch	2219	2205				2235				89S ₄ , 11S ₁₁	90	10
	v ₅	CH ₂ deformation	1537	1445								76S ₅ , 22S ₆	4	96
	v ₆	CH ₂ deformation	1527	1435	1430	1425			1427			76S ₆ , 23S ₅	34	66
	v ₇	CH ₂ rock	1403	1332								60S ₇ , 30S ₈	29	71
	v ₈	CH ₂ rock	1302	1236			1229	1229		1229		62S ₈ , 32S ₇	50	50
	v ₉	PH ₂ deformation	1155	1096	1094				1075	1076	1076	94S ₉	22	78
	v ₁₀	C-C(P) stretch	1079	1027								78S ₁₀	56	44
	v ₁₁	C-C(N) stretch	975	937								55S ₁₁ , 11S ₁₆ , 10S ₁₂	38	62
	v ₁₂	PH ₂ rock	870	827		835	834			833		59S ₁₂ , 16S ₁₁ , 15S ₁₃	53	47
	v ₁₃	C-P stretch	737	706		705	706			703		51S ₁₃ , 19S ₁₂ , 15S ₁₆	98	2
	v ₁₄	C-C≡N in-plane bend	493	484		496	494			493		45S ₁₄ , 21S ₁₆ , 20S ₁₃	95	5
	v ₁₅	C-C-P bend	281	276						282		64S ₁₅ , 11S ₁₄ , 10S ₁₃	72	28
	v ₁₆	C-C-C bend	149	148						160		45S ₁₆ , 36S ₁₄ , 18S ₁₅	7	93
A''	v ₁₇	CH ₂ antisymmetric stretch	3189	2992								80S ₁₇ , 20S ₁₈	-	-
	v ₁₈	CH ₂ antisymmetric stretch	3166	2970	2964				2962			80S ₁₈ , 20S ₁₇	-	-
	v ₁₉	PH ₂ antisymmetric stretch	2493	2298								100S ₁₉	-	-
	v ₂₀	CH ₂ twist	1355	1286						1285		49S ₂₀ , 42S ₂₁	-	-
	v ₂₁	CH ₂ twist	1231	1170								41S ₂₁ , 44S ₂₀	-	-
	v ₂₂	PH ₂ twist	1070	1017		1008	1008			~1010		29S ₂₂ , 32S ₂₃ , 31S ₂₄	-	-
	v ₂₃	CH ₂ wag	843	802					755		755	42S ₂₃ , 35S ₂₂ , 10S ₂₁	-	-
	v ₂₄	CH ₂ wag	666	635								53S ₂₄ , 31S ₂₂	-	-

ν_{25}	C-C≡N out-of-plane bend	377	376		84S ₂₅ , 11S ₂₇	-	-
ν_{26}	PH ₂ torsion	207	207		95S ₂₆	-	-
ν_{27}	C-C(P) torsion	91	91		77S ₂₇	-	-

^a MP2(full)/6-31G(d) ab initio calculations, frequencies from scaled force constants and potential energy distributions (P.E.D.s).

^b Scaling factors of 0.88 for CH₂ stretches and CH₂ deformations, 0.85 for PH₂ stretches and 0.90 for all other modes except torsions, heavy atom bends, and C≡N stretch.

^c Symmetry coordinates with P.E.D. contribution less than 10% are omitted.

Table 4.9. Observed and calculated^a frequencies (cm⁻¹) and potential energy distributions (P.E.D.s) for the *Tg* (C₁) conformer of 2-cyanoethylphosphine.

Vib. no.	Approximate description	AB		IR		Raman liquid	P.E.D. ^c	Contour		
		<i>INITIO</i>	Fixed scaled ^b	gas	liquid			A	B	C
ν_1	CH ₂ antisymmetric stretch	3199	3001				93S ₁	3	1	96
ν_2	CH ₂ antisymmetric stretch	3163	2967				93S ₂	8	19	74
ν_3	CH ₂ symmetric stretch	3135	2941				95S ₃	6	94	-
ν_4	CH ₂ symmetric stretch	3112	2919				96S ₄	-	95	5
ν_5	PH ₂ antisymmetric stretch	2510	2314				83S ₅ , 17S ₆	26	69	5
ν_6	PH ₂ symmetric stretch	2491	2297				83S ₆ , 17S ₅	17	1	81

v ₇	C≡N stretch	2222	2222			89S ₇ , 11S ₁₇	93	7	-
v ₈	CH ₂ deformation	1542	1450			56S ₈ , 41S ₉	4	95	1
v ₉	CH ₂ deformation	1534	1443			57S ₉ , 42S ₈	41	47	12
v ₁₀	CH ₂ rock	1407	1336			66S ₁₀ , 23S ₁₂	21	70	9
v ₁₁	CH ₂ twist	1354	1285			55S ₁₁ , 34S ₁₃	79	19	2
v ₁₂	CH ₂ rock	1290	1224		1229	69S ₁₂ , 25S ₁₀	14	85	1
v ₁₃	CH ₂ twist	1219	1159		1155	44S ₁₃ , 37S ₁₁ , 11S ₁₆	44	7	49
v ₁₄	PH ₂ deformation	1156	1096	1091		95S ₁₄	72	2	25
v ₁₅	C-C(P) stretch	1087	1035			73S ₁₅	8	92	-
v ₁₆	CH ₂ wag	1058	1005	992/996		29S ₁₆ , 31S ₂₁ , 17S ₁₉	41	4	55
v ₁₇	C-C(N) stretch	983	944	934		57S ₁₇	54	45	1
v ₁₈	PH ₂ twist	846	803			37S ₁₈ , 20S ₁₆ , 14S ₂₀	-	34	66
v ₁₉	PH ₂ rock	836	794	798	796	44S ₁₉ , 18S ₁₆	30	35	35
v ₂₀	C-P stretch	755	722	727	725	40S ₂₀ , 12S ₂₆ , 12S ₁₉ , 11S ₁₈	53	3	44
v ₂₁	CH ₂ wag	716	684			40S ₂₁ , 15S ₁₈ , 14S ₁₉	77	23	-
v ₂₂	C-C≡N in-plane bend	496	487			46S ₂₂ , 21S ₂₆ , 19S ₂₀	95	5	-
v ₂₃	C-C≡N out-of-plane bend	375	374			85S ₂₃	9	1	91
v ₂₄	C-C-P bend	267	262		267	61S ₂₄ , 12S ₂₂ , 11S ₂₀	-	62	38
v ₂₅	PH ₂ torsion	174	173			84S ₂₅	30	60	10
v ₂₆	C-C-C bend	146	145			38S ₂₆ , 29S ₂₂ , 23S ₂₄	25	74	1
v ₂₇	C-C(P) torsion	88	87			81S ₂₇	1	4	95

^aMP2(full)/6-31G(d) ab initio calculations, frequencies from scaled force constants and potential energy distributions (P.E.D.s).

^bScaling factors of 0.88 for CH₂ stretches and CH₂ deformations, 0.85 for PH₂ stretches and 0.90 for all other modes except torsions, heavy atom bends, and C≡N stretch.

^cSymmetry coordinates with P.E.D. contribution less than 10% are omitted.

Table 4.10. Observed and calculated^a frequencies (cm⁻¹) for the *Gg* (C₁) conformer of 2-cyanoethylphosphine.

Vib. No.	Approximate Description	<i>AB</i>		IR int.	Raman act.
		<i>INITIO</i>	Fixed scaled ^b		
v ₁	CH ₂ antisymmetric stretch	3193	2995	5.0	53.2
v ₂	CH ₂ antisymmetric stretch	3167	2971	1.4	75.7
v ₃	CH ₂ symmetric stretch	3127	2933	9.6	96.6
v ₄	CH ₂ symmetric stretch	3115	2922	4.6	91.9
v ₅	PH ₂ symmetric stretch	2516	2387	70.9	95.5
v ₆	PH ₂ antisymmetric stretch	2501	2373	72.1	157.4
v ₇	C≡N stretch	2220	2220	0.7	31.2
v ₈	CH ₂ deformation	1534	1439	7.8	9.5
v ₉	CH ₂ deformation	1531	1436	7.6	16.0
v ₁₀	CH ₂ rock	1402	1330	1.1	7.3
v ₁₁	CH ₂ rock	1362	1292	7.5	1.5
v ₁₂	CH ₂ twist	1268	1203	0.7	11.8
v ₁₃	CH ₂ twist	1215	1153	8.3	5.7
v ₁₄	PH ₂ deformation	1160	1100	16.1	34.7
v ₁₅	C-C(P) stretch	1083	1027	6.3	5.2
v ₁₆	C-C(N) stretch	1032	979	22.0	7.1
v ₁₇	CH ₂ wag	984	934	5.7	11.2
v ₁₈	CH ₂ wag	881	836	1.4	7.3
v ₁₉	PH ₂ twist	831	788	14.2	6.3
v ₂₀	PH ₂ rock	734	696	2.7	3.7
v ₂₁	C-P stretch	672	638 ^c	4.5	17.1
v ₂₂	C-C-C bend	547	547	1.5	0.8
v ₂₃	C-C≡N out-of-plane bend	372	372	0.1	2.9
v ₂₄	C-C-P bend	289	289	4.7	2.5
v ₂₅	C-C≡N in-plane bend	219	219	1.4	1.9
v ₂₆	PH ₂ torsion	160	160	9.8	1.4
v ₂₇	C-C torsion	88	88	3.8	1.0

^aMP2(full)/6-31G(d) ab initio calculations, frequencies from scaled force constants, infrared intensities (km mol⁻¹), Raman activities (Å⁴ u⁻¹).

^bScaling factors of 0.88 for CH₂ stretches and CH₂ deformations, 0.85 for PH₂ stretches and 0.90 for all other modes except torsions, heavy atom bends, and C≡N stretch.

^cOnly one band was observed for *Gg* form at 638 cm⁻¹ in the Raman liquid.

Theoretical Methods

The ab initio calculations were performed with the Gaussian 03 program¹⁹ with Gaussian-type basis functions. The energy minima with respect to nuclear coordinates were obtained by the simultaneous relaxation of all geometric parameters by the gradient method of Pulay²⁰. Several basis sets as well as the corresponding ones with diffuse functions were employed with the Møller-Plesset perturbation method²¹ to the second order (MP2(full)) as well as with the density functional theory by the B3LYP method.

In order to obtain a complete description of the molecular motions involved in the fundamental modes of 2-cyanoethylphosphine, normal coordinate analyses were carried out. The force field in Cartesian coordinates was obtained with the Gaussian 03 program¹⁹ with the 6-31G(d) basis set. The internal coordinates used to calculate the **G** and **B** matrices are given in Table 11 with the atomic numbering shown in Fig. 9. By using the **B** matrix²⁹, the force field in Cartesian coordinates was converted to a force field in internal coordinates. Subsequently, scaling factors of 0.88 for CH₂ stretches and CH₂ deformations, 0.85 for PH₂ stretches and 0.90 for other coordinates except for the heavy atom bends, torsions, and C≡N stretch which were not scaled were used, along with the geometric average of the scaling factors for the interaction force constants, to obtain the fixed scaled force field and resultant wavenumbers. A set of symmetry coordinates was utilized (Table 15) to determine the corresponding potential energy distributions (P.E.D.s). The calculated infrared intensities, Raman activities, depolarization ratios and potential energy distributions for the *Gt*, *Tt*, *Tg* and *Gg* conformers are listed in Tables 7, 8, 9 and 10, respectively. Rotation about the C-C bond gives rise to *Trans* (*T*) and *Gauche* (*G*) forms which are indicated by capital letters and rotation around the C-P bond also results in *trans*

(*t*) and *gauche* (*g*) forms indicated by lower case letters. There are a total of five possible stable conformers that can exist for the NCCH₂CH₂PH₂ molecule which are *Gauche-trans* (*Gt*), *Trans-trans* (*Tt*), *Trans-gauche* (*Tg*), *Gauche-gauche* (*Gg*) and *Gauche-gauche'* (*Gg'*) as shown in Fig. 10.

The frequencies from the scaled force constants were used together with a Lorentzian function to obtain the simulated spectra. Infrared intensities were obtained based on the dipole moment derivatives with respect to Cartesian coordinates. The derivatives were transformed with respect to normal coordinates by $(\partial\mu_u/\partial Q_i) = \sum_j (\partial\mu_u/\partial X_j)L_{ij}$, where Q_i is the i^{th} normal coordinate, X_j is the j^{th} Cartesian displacement coordinate, and L_{ij} is the transformation matrix between the Cartesian displacement coordinates and the normal coordinates. The infrared intensities were then calculated by $(N\pi)/(3c^2) [(\partial\mu_x/\partial Q_i)^2 + (\partial\mu_y/\partial Q_i)^2 + (\partial\mu_z/\partial Q_i)^2]$. A comparison of experimental and simulated infrared spectra of 2-cyanoethylphosphine is shown. Infrared spectra of the liquid, amorphous solid, crystalline solid and the predicted infrared spectra for the pure *Gt* and *Tt* conformers are shown in Fig. 7 (A-E), respectively. The predicted spectrum, which included the frequencies and intensities, greatly aided in making the initial assignment of the fundamentals for each conformer.

Additional support for the vibrational assignments was obtained from the simulated Raman spectra. The evaluation of Raman activity by using the analytical gradient methods has been developed³⁰⁻³² and the activity S_j can be expressed as: $S_j = g_j(45\alpha_j^2 + 7\beta_j^2)$, where g_j is the degeneracy of the vibrational mode j , α_j is the derivative of the isotropic polarizability, and β_j is the anisotropic polarizability. To obtain the Raman scattering cross sections, the polarizabilities are incorporated into S_j by multiplying S_j with $(1-\rho_j)/(1+\rho_j)$

where ρ_j is the depolarization ratio of the j^{th} normal mode. The Raman scattering cross sections and calculated wavenumbers obtained from the Gaussian 03 program were used together with a Lorentzian function to obtain the simulated Raman spectra. Comparison of experimental Raman spectra of the liquid, solid and the predicted Raman spectra for the pure *Gt* and *Tt* conformers are shown in Fig. 8 (A-D). The predicted spectrum is in reasonable agreement with the experimental spectrum which indicates the utility of the predicted Raman spectra for aiding the vibrational assignments.

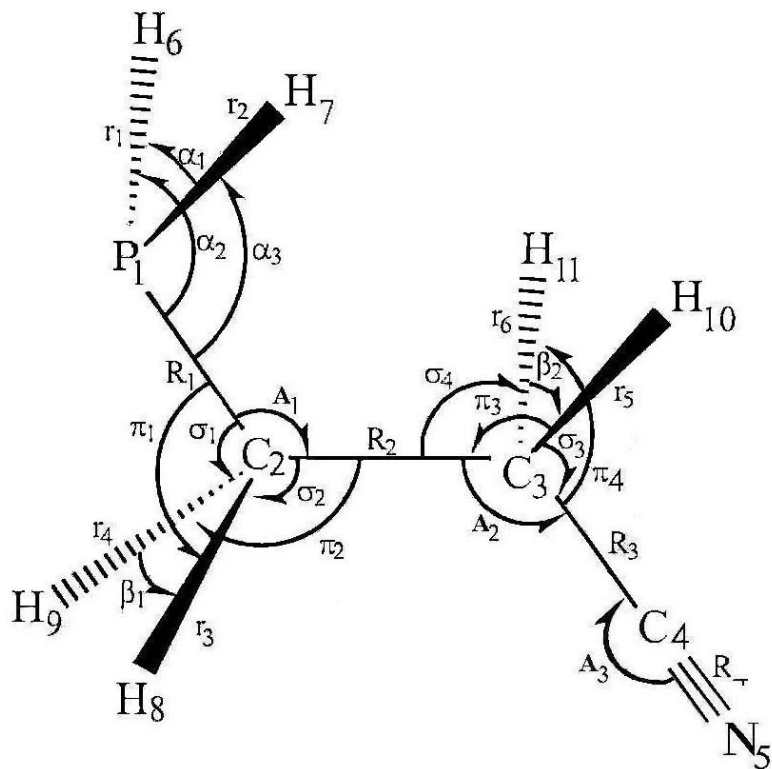


Figure 4.9. *Trans-trans* (C_s) conformer of 2-cyanoethylphosphine showing atom numbering and internal coordinates.

Vibrational Assignment

The assignment of the vibrational spectra is essential in order to be able to obtain the enthalpy difference among the conformers. The fundamentals for at least the three conformers having lowest energies need to be assigned since the microwave spectra have been assigned for all three. For the conformer having the lowest energy the predicted amount is 62% from ab initio calculations. It will give the most dominant spectra, in most cases, except where the molar absorption coefficients predict the intensities to be significantly different for either the second or the third conformer. The most interesting vibrational frequencies will be for the P-H motions as well as the heavy atom modes. The frequencies for the CH₂ stretching vibrations are well known from “group frequencies”. The PH₂ antisymmetric and symmetric stretches are clearly identified in the infrared spectra of the gas and also as overlapping bands in the spectra of the liquid and amorphous solid. The predicted frequencies of the PH₂ stretches for the conformers with higher energies have essentially the same frequencies and it is not possible to distinguish them. The other vibration in this region is the C≡N stretch which has a significantly lower frequency and is well characterized with no question of its assignment. The CH₂ bending modes, for the most part, are also readily assigned based on the predictions from the ab initio calculations as well as from well known “group frequencies” particularly for the deformations and CH₂ wagging modes. One of the CH₂ twisting modes is extensively mixed with the CH₂ rock but both the twists were readily assigned. The PH₂ deformation is nearly a pure mode at 1084 cm⁻¹. Even though the corresponding PH₂ deformations for the other two conformers are predicted to be near the same frequencies as that for the *Gt* conformer, distinct frequencies could be assigned for them.

The assignments of the most interest are the heavy atom vibrations, especially the stretches. The C-C(P) stretch is readily assigned at 1024 cm^{-1} in the spectrum of the gas with similar frequencies for the amorphous and crystalline solids. The other C-C(N) stretch is assigned at 856 cm^{-1} with the two CH_2 wags falling between the C-C stretches. One of the CH_2 wags is so mixed that the band at 988 cm^{-1} although appropriately assigned as this mode, has equal contributions from a PH_2 motion and a C-C stretch. The other two PH_2 bending modes are assigned at 812 cm^{-1} as the PH_2 rock which is a relatively strong band and the weaker one at 669 cm^{-1} to the PH_2 twist in the infrared spectra. The C-P stretch is a very strong band in the Raman spectra and it is observed at 631 cm^{-1} with the C-C \equiv N bends at 541 and 373 cm^{-1} . Four of the remaining fundamentals are readily assigned based upon the predicted frequencies and the Raman data provide the most definitive bands for their assignments. Once the assignments had been made for the *Gt* conformer the next task was to obtain bands that could be used for the determination of the enthalpy differences. Consequently, their assignment was to relatively strong bands in the region where the fundamentals are expected based upon their predicted values. Of particular interest were the C-P stretches which was relatively easily assigned for the *Gt* conformer and are assigned at 703 and 725 cm^{-1} for the *Tt* and *Tg* conformers, respectively. This fundamental for the *Tt* form was readily assigned at similar frequencies in the infrared spectra of the liquid and solid.

Once the fundamentals had been assigned for the *Gt* conformer the assignments for the other conformers were fairly limited to the region below 800 cm^{-1} since it was almost impossible to obtain well defined bands above this spectral region for the other conformers. After the C-P stretching band for the *Gt* form, the second band utilized for the enthalpy

determination was the 541 cm^{-1} which is a weak band and the corresponding fundamental for the *Tt* form is a pronounced band at 493 cm^{-1} which can be confidently assigned. The C-C≡N bend for the *Tg* conformer is predicted to be at a slightly higher frequency and appears as a weak shoulder on the high frequency side of the 493 cm^{-1} band but does not interfere with obtaining the intensity of this band for the determination of the enthalpy difference.

There was one additional band at 669 cm^{-1} which was sufficiently away from any other bands and not predicted for the other conformers so it could be assigned as the PH₂ twist for the *Gt* form. Thus, there are three fundamentals for the *Gt* conformer that could be used for the determinations of the enthalpy differences. For the most part other fundamentals for the two *Trans* conformers are significantly overlapped by the fundamentals from the *Gt* conformer so that individual frequencies were difficult to measure or obtain for these *Trans* conformers. Therefore, the vibrational assignment is primarily for the *Gt* conformer and the lower frequency bands were identified based upon their significant change in intensities and the predicted frequencies.

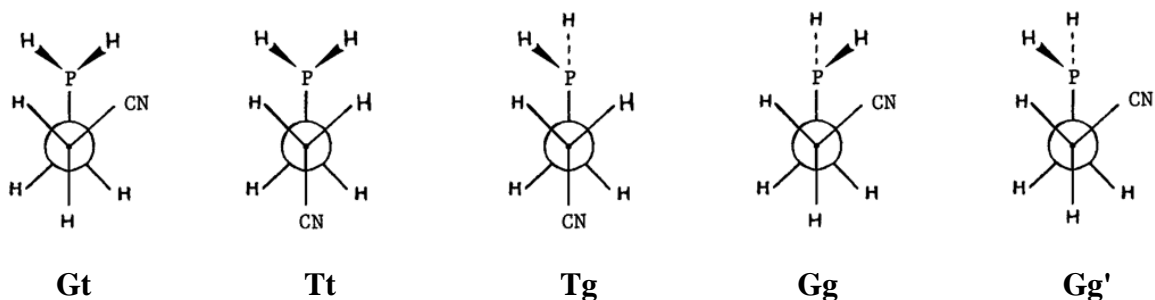


Figure 4.10. Newmann projections of the five conformers of 2-cyanoethylphosphine.

Table 4.11. Structural parameters (Å and °) and rotational constants (mhz) for the *Gt*, *Tt* and *Tg* conformer of 2-cyanoethylphosphine.

Structural parameters	Internal coordinates	<i>Gt</i>				<i>Tt</i>		<i>Tg</i>	
		MP2(full)/ 6-311+G(d,p)	B3LYP/ 6-311+G(d,p)	Microwave ^a	Adjusted r_0	MP2(full)/ 6-311+G(d,p)	Adjusted r_0	MP2(full)/ 6-311+G(d,p)	Adjusted r_0
r (P ₁ -C ₂)	R ₁	1.859	1.877	1.880	1.860(3)	1.858	1.858(3)	1.864	1.864(3)
r (C ₂ -C ₃)	R ₂	1.535	1.543	1.530	1.535(3)	1.533	1.535(3)	1.535	1.535(3)
r (C ₃ -C ₄)	R ₃	1.464	1.462	1.474	1.464(3)	1.465	1.465(3)	1.463	1.463(3)
r (C ₄ -N ₅)	R ₄	1.174	1.153	1.157	1.160(3)	1.174	1.160(3)	1.174	1.160(3)
r (P ₁ -H ₆)	r ₁	1.410	1.422	1.414	1.410(3)	1.412	1.412(3)	1.412	1.412(3)
r (P ₁ -H ₇)	r ₂	1.413	1.425	1.414	1.413(3)	1.412	1.412(3)	1.410	1.410(3)
r (C ₂ -H ₈)	r ₃	1.094	1.093	1.093	1.094(2)	1.094	1.094(2)	1.092	1.092(2)
r (C ₂ -H ₉)	r ₄	1.095	1.093	1.093	1.095(2)	1.094	1.094(2)	1.094	1.094(2)
r (C ₃ -H ₁₀)	r ₅	1.094	1.094	1.093	1.094(2)	1.094	1.094(2)	1.095	1.095(2)
r (C ₃ -H ₁₁)	r ₆	1.095	1.096	1.093	1.095(2)	1.094	1.094(2)	1.095	1.095(2)
∠ P ₁ C ₂ C ₃	A ₁	116.6	118.1	117.0(15) ^b	117.1(5)	114.9	114.9(5)	110.2	110.0(5)
∠ C ₂ C ₃ C ₄	A ₂	112.3	113.5	110.5	112.5(5)	112.1	112.1(5)	111.8	111.8(5)
∠ H ₆ P ₁ C ₂	α ₂	96.7	97.4	95.5	96.7(5)	96.2	96.2(5)	96.4	96.4(5)
∠ H ₇ P ₁ C ₂	α ₃	96.0	96.9	95.5	96.0(5)	96.2	96.2(5)	96.7	96.7(5)
∠ H ₈ C ₂ P ₁	π ₁	107.8	107.0	108.0	107.8(5)	107.8	107.8(5)	112.2	112.2(5)
∠ H ₉ C ₂ P ₁	σ ₁	107.2	106.5	106.6	107.2(5)	107.8	107.8(5)	107.9	107.9(5)
∠ H ₈ C ₂ C ₃	σ ₂	109.6	109.9	109.5	109.6(5)	109.7	109.7(5)	109.5	109.5(5)
∠ H ₉ C ₂ C ₃	π ₂	108.5	108.3	109.5	108.5(5)	109.7	109.7(5)	109.1	109.1(5)
∠ H ₁₀ C ₃ C ₂	π ₃	110.4	110.4	109.5	110.4(5)	110.3	110.3(5)	110.6	110.6(5)
∠ H ₁₀ C ₃ C ₄	σ ₃	108.1	108.2	109.5	108.1(5)	108.4	108.4(5)	108.1	108.1(5)
∠ H ₁₁ C ₃ C ₂	σ ₄	110.5	110.0	109.5	110.5(5)	110.3	110.3(5)	110.6	110.6(5)
∠ H ₁₁ C ₃ C ₄	π ₄	107.9	107.7	109.5	107.9(5)	108.4	108.4(5)	108.3	108.3(5)
∠ H ₆ P ₁ H ₇	α ₁	94.4	93.8	93.4	94.4(5)	94.0	94.0(5)	94.6	94.6(5)
∠ H ₈ C ₂ H ₉	β ₁	106.7	106.4	109.5	106.7(5)	106.5	106.5(5)	107.9	107.9(5)
∠ H ₁₀ C ₃ H ₁₁	β ₂	107.5	106.9	109.5	107.5(5)	107.1	107.1(5)	107.2	107.2(5)
∠ C ₃ C ₄ N ₅	A ₃	178.8	179.4	180.0	178.8(5)	178.3	178.3(5)	178.6	178.6(5)

τ P ₁ C ₂ C ₃ C ₄	τ_1	64.5	65.6	66(3) ^c	63.4(5)	180.0	180.0(5)	176.8	176.8(5)
--	----------	------	------	--------------------	---------	-------	----------	-------	----------

^a Ref.⁴⁸.

^b Structural parameters kept fixed for *Gt*, *Tt* and *Tg* conformers except for \angle P₁C₂C₃ which is 114.0(15) for *Tt* and 109.0(15) for *Tg* conformer.

^c Fitted PCCC dihedral angle for *Gt* conformer.

Table 4.12. Temperature and intensity ratios of the conformational bands of 2-cyanoethylphosphine from the Raman spectra of the liquid.

T(°C)	1/T (×10 ⁻³ K ⁻¹)	<i>Gt</i> / <i>Tr</i> ^a				<i>Tt</i> / <i>Tg</i> ^a		<i>Gt</i> / <i>Tg</i> ^a		
		I ₆₃₁ /I ₄₉₃	I ₅₄₁ /I ₇₀₃	I ₅₄₁ /I ₄₉₃	I ₆₆₉ /I ₄₉₃	I ₇₀₃ /I ₇₂₅	I ₄₉₃ /I ₇₂₅	I ₆₃₁ /I ₇₂₅	I ₅₄₁ /I ₇₂₅	I ₆₆₉ /I ₇₂₅
29.0	3.311	2.07	0.17	0.12	0.07	2.07	3.00	6.21	0.36	0.21
10.0	3.533	2.26	0.15	0.12	0.12	2.79	3.50	7.92	0.42	0.42
-5.0	3.731	2.31	0.15	0.13	0.11	3.20	3.80	8.80	0.50	0.40
-10.0	3.802	2.33	0.16	0.12	0.10	3.37	4.31	10.05	0.53	0.42
-29.0	4.098	2.41	0.19	0.15	0.13	3.65	4.59	11.06	0.71	0.59
-50.0	4.481	2.43	0.19	0.17	0.11	4.57	5.00	12.14	0.86	0.57
-70.0	4.926	2.85	0.21	0.20	0.13	4.40	4.73	13.47	0.93	0.60
-85.0	5.319	2.55	0.18	0.17	0.11	7.10	7.80	19.90	1.30	0.90
-95.0	5.618	2.68	0.19	0.18	0.13	6.73	7.09	19.00	1.27	0.91
-100.0	5.775	2.69	0.19	0.19	0.17	7.40	7.20	19.40	1.40	1.20
-108.0	6.060	2.75	0.19	0.19	0.14	7.90	7.70	21.20	1.50	1.10
ΔH , cm ⁻¹		61 ± 10	53 ± 19	130 ± 21	113 ± 37	309 ± 24	228 ± 23	289 ± 22	357 ± 23	347 ± 42
ΔH average, cm ⁻¹ (kJmol ⁻¹)		89 ± 12 (1.07 ± 0.15)			268 ± 19 (3.21 ± 0.22)		331 ± 18 (3.96 ± 0.21)			

^a The average values of ΔH and the statistical uncertainty (1 σ) was obtained by utilizing all of the data as a single set.

Conformational Stability

To determine the enthalpy differences among the three conformers with the lowest energies of $\text{NCCH}_2\text{CH}_2\text{PH}_2$, the Raman spectra of the liquid sample was recorded as a function of different temperatures from 29 to -108°C . When the sample was cooled to -118°C it crystallized and only one conformer was observed which is consistent with the *Gt* form. Once confident assignment for the three conformers having the lowest energies, $Gt < Tt < Tg$, were made, the next step was in finding a pair or pairs of bands from which the enthalpy determination could be carried out. For this determination, it is desirable to have the lowest frequency pair(s) in the spectra to minimize the effect of combination and overtone bands. The bands should also be sufficiently resolved to allow for accurate intensity measurements. After taking into consideration these requirements, a good selection of band pairs could be made relatively easily as most of the peaks that were used for the enthalpy determinations are heavy atom stretching and bending modes. The C-P stretch which is a relatively strong band in the Raman spectra but is of a medium or weak intensity in the infrared spectra was of primary interest. This fundamental which appears at 631, 703 and 725 cm^{-1} in the spectra and was assigned to the *Gt*, *Tt* and *Tg* conformers, respectively, were used. Additionally, the C-C \equiv N in-plane bends at 541 and 493 cm^{-1} for the *Gt* and *Tt* forms, respectively, were also used. Apart from the heavy atom vibrations, the shoulder at 669 cm^{-1} which is due to the PH_2 twisting mode for the *Gt* conformer was also considered for possible use in the enthalpy determination. By combining these peaks, a total of nine pairs were obtained with four of them for *Gt/Tt*, three for *Gt/Tg* and remaining two for *Tt/Tg* conformer pairs.

Initially, the relative intensities of the above indicated pairs for the three stable conformers were measured as a function of temperature and their ratios were determined. Eleven temperatures were chosen to obtain the spectral data for these pairs and by application of the van't Hoff equation, $-\ln K = \Delta H/(RT) - \Delta S/R$, the enthalpy differences were determined from a plot of $-\ln K$ versus $1/T$, where, $\Delta H/R$ is the slope of the line and K is substituted with the appropriate intensity ratios, i.e. $I_{\text{conf-1}}/I_{\text{conf-2}}$. It was assumed that ΔH , ΔS and the ratio of the molar absorption coefficients $\epsilon_{\text{conf-1}}/\epsilon_{\text{conf-2}}$ are not a function of temperature in the range studied.

After utilizing the four band pairs for the *Gt/Tt* conformers, the enthalpy differences ranged from a low value of $53 \pm 19 \text{ cm}^{-1}$ ($0.63 \pm 0.23 \text{ kJ mol}^{-1}$) to a high value of $130 \pm 21 \text{ cm}^{-1}$ ($1.55 \pm 0.25 \text{ kJ mol}^{-1}$) (Table 12). The average of the uncertainties is 25%. However, by utilizing the data from all the pairs as a single set and by using the statistical standard deviation of one sigma the enthalpy difference is $89 \pm 12 \text{ cm}^{-1}$ ($1.07 \pm 0.15 \text{ kJ mol}^{-1}$).

To determine the enthalpy difference between the lowest energy conformer *Gt* and the *Tg* form having third lowest energy, the three band pairs that were used give enthalpy differences that ranged from $289 \pm 22 \text{ cm}^{-1}$ ($3.46 \pm 0.26 \text{ kJ mol}^{-1}$) to $357 \pm 23 \text{ cm}^{-1}$ ($4.27 \pm 0.27 \text{ kJ mol}^{-1}$), with the average of the uncertainties being 9%. Similar to the *Gt/Tt* conformers when the data from all the pairs of the *Gt/Tg* conformers were utilized as a single set with a statistical deviation of one sigma for the error limits a ΔH value of $331 \pm 18 \text{ cm}^{-1}$ ($3.96 \pm 0.21 \text{ kJ mol}^{-1}$) was obtained. Similarly, for the determination of the ΔH value between the *Tt* conformer having second lowest energy and *Tg* form, the two pairs that were utilized gave an average value of $268 \pm 19 \text{ cm}^{-1}$ ($3.21 \pm 0.22 \text{ kJ mol}^{-1}$) as the enthalpy

difference (Table 12). The predicted conformational energy differences from ab initio calculations employing the MP2(full) and B3LYP methods are listed in Table 13, which can be compared to the experimentally determined ΔH values.

Table 4.13. Calculated energies (hartree) and energy differences^a (cm⁻¹) for the five conformers of 2-cyanoethylphosphine.

Method / basis set	# of basis sets	<i>Gt</i>	<i>Tt</i> ΔE	<i>Tg</i> ΔE	<i>Gg</i> ΔE	<i>Gg'</i> ΔE
MP2(full)/6-31G(d)	91	-512.923708	-85	119	108	487
MP2(full)/6-31+G(d)	111	-512.936135	-126	159	127	496
MP2(full)/6-311G(d,p)	134	-513.235293	-77	255	190	514
MP2(full)/6-311+G(d,p)	154	-513.241668	-70	298	225	542
MP2(full)/6-311G(2d,2p)	177	-513.305911	2	361	281	566
MP2(full)/6-311+G(2d,2p)	197	-513.311170	-24	346	303	596
MP2(full)/6-311G(2df,2pd)	242	-513.391002	18	355	276	578
MP2(full)/6-311+G(2df,2pd)	262	-513.395502	2	346	294	604
MP2(full)/aug-cc-pVTZ	372	-513.323508	77	313	240	551
B3LYP/6-31G(d)	91	-514.007178	-168	92	229	532
B3LYP/6-31+G(d)	111	-514.015706	-239	23	191	498
B3LYP/6-311G(d,p)	134	-514.084163	-166	102	208	496
B3LYP/6-311+G(d,p)	154	-514.087487	-178	99	219	502
B3LYP/6-311G(2d,2p)	177	-514.092537	-158	128	233	487
B3LYP/6-311+G(2d,2p)	197	-514.095918	-185	103	242	500
B3LYP/6-311G(2df,2pd)	242	-514.100039	-164	114	228	476
B3LYP/6-311+G(2df,2pd)	262	-514.103178	-189	93	238	491
B3LYP/aug-cc-pVTZ	372	-514.110133	-188	69	212	467

^a Energy differences with respect to the *Gt* conformer.

Table 4.14. Symmetry coordinates for 2-cyanoethylphosphine w.r.t. *Tt* conformer.

Sym. Block	Description	Symmetry Coordinate ^a
A'	CH ₂ symmetric stretch	$S_1 = r_3 + r_4$
	CH ₂ symmetric stretch	$S_2 = r_5 + r_6$
	PH ₂ symmetric stretch	$S_3 = r_1 + r_2$
	CN stretch	$S_4 = R_4$
	CH ₂ deformation	$S_5 = 4\beta_1 - \pi_1 - \pi_2 - \sigma_1 - \sigma_2$
	CH ₂ deformation	$S_6 = 4\beta_2 - \pi_3 - \pi_4 - \sigma_4 - \sigma_3$
	CH ₂ rock	$S_7 = \pi_1 - \pi_2 + \sigma_1 - \sigma_2$
	CH ₂ rock	$S_8 = \pi_3 - \pi_4 + \sigma_4 - \sigma_3$
	PH ₂ deformation	$S_9 = \alpha_1$
	CC(P) stretch	$S_{10} = R_2$
	CC(N) stretch	$S_{11} = R_3$
	PH ₂ rock	$S_{12} = \alpha_2 + \alpha_3$
	CP stretch	$S_{13} = R_1$
	CCN in-plane bend	$S_{14} = A_3$
	CCP bend	$S_{15} = A_1$
	CCC bend	$S_{16} = A_2$
A''	CH ₂ asymmetric stretch	$S_{17} = r_3 - r_4$
	CH ₂ asymmetric stretch	$S_{18} = r_5 - r_6$
	PH ₂ asymmetric stretch	$S_{19} = r_1 - r_2$
	CH ₂ twist	$S_{20} = \pi_1 + \pi_2 - \sigma_1 - \sigma_2$
	CH ₂ twist	$S_{21} = \pi_3 + \pi_4 - \sigma_4 - \sigma_3$
	PH ₂ twist	$S_{22} = \alpha_2 - \alpha_3$
	CH ₂ wag	$S_{23} = \pi_1 - \pi_2 - \sigma_1 + \sigma_2$
	CH ₂ wag	$S_{24} = \pi_3 - \pi_4 - \sigma_4 + \sigma_3$
	CCN out-of-plane bend	$S_{25} = \tau_3$
	PH ₂ torsion	$S_{26} = \tau_2$
	CC torsion	$S_{27} = \tau_1$

^a Not normalized.

Structural Parameters

In the initial microwave study⁴⁸ only one angle ($\angle\text{PCC}$) for each conformer and the dihedral angle (τPCCC) for the *Gt* form were determined for the three identified conformers. The remaining structural parameters were estimated from the corresponding ones from related compounds. Thus, there were only four structural parameters determined from the earlier microwave study so more extensive determination of the structural parameters of these three molecules is desirable. Therefore, we embarked upon a study to determine all of the structural parameters for all three conformers.

We have found that good structural parameters for hydrocarbons and many substituted ones can be determined by adjusting the structural parameters obtained from the ab initio MP2(full)/6-311+G(d,p) calculations to fit the rotational constants obtained from microwave experimental data by using a computer program “A&M” (*Ab initio* and Microwave) developed⁴¹ in our laboratory. In order to reduce the number of independent variables, the structural parameters are separated into sets according to their types where bond distances in the same set keep their relative ratio and bond angles in the same set keep their difference in degrees. This assumption is based on the fact that errors from ab initio calculations are systematic⁴⁹. Additionally, we have also shown that the differences in predicted distances and angles from the ab initio calculations for different conformers of the same molecule can usually be used as one parameter with the ab initio predicted differences except for some dihedral angles.

We³³ have also shown that ab initio MP2(full)/6-311+G(d,p) calculations predict the r_0 structural parameters for more than fifty carbon-hydrogen distances in substituted hydrocarbons to at least 0.002 Å compared to the experimentally determined values from

isolated CH stretching frequencies³⁴. Therefore, all of the carbon-hydrogen distances can be taken from the MP2(full)/6-311+G(d,p) predicted values for *Gt*, *Tt* and *Tg* conformers of 2-cyanoethylphosphine. Therefore, it should be possible to obtain “adjusted r_0 ” structural parameters for heavy atoms for all three conformers of 2-cyanoethylphosphine by utilizing the previously reported seven well determined rotational constants from the earlier microwave study⁴⁸. For the *Tt* and *Tg* forms only the B and C rotational constants were well determined and the A rotational constants could not be used for obtaining the adjusted r_0 parameters due to their large uncertainties.

The fit of the seven determined rotational constants (Table 15) by the structural parameters for the *Gt*, *Tt* and *Tg* conformers is remarkably good with six of the differences having values of 0.4 and 0.3 MHz and the other one 0.02 MHz. The only adjusted heavy atom parameter which required a significant adjustment for all three conformers was the C≡N distance which is always predicted much larger from MP2 ab initio calculations than the experimental value. The B3LYP calculations, on the other hand, predicted a slightly smaller value. Bond distances for triple bonds seldom vary significantly with substitutions. The other three heavy atom distances vary a maximum of 0.002 Å from the ab initio predicted values. Only two of the angles, ∠PCC and ∠CCC were adjusted to slightly larger values than the MP2 calculations for the *Gt* form. For the *Tg* form ∠PCC got smaller by just 0.2°.

The heavy atom distances along with the P-H distances have estimated accuracies to ± 0.003 Å and the angles should be within $\pm 0.5^\circ$. The resulting adjusted parameters are listed in Table 11. Therefore, it is believed that the suggested uncertainties are realistic values and the determined structural parameters are probably as accurate as can be obtained

for the molecule in the gas phase by either electron diffraction or microwave substituted methods.

Table 4.15. Comparison of rotational constants (MHz) obtained from ab initio MP2(full)/6-311+G(d,p) predictions, experimental values from microwave spectra, and from the adjusted r_0 structural parameters for 2-cyanoethylphosphine.

Isotopomer	Rotational constants	MP2(full)/6-311+G(d,p)	Experimental ^a	Adjusted r_0	$ \Delta $
<i>Gt</i>	A	7545.8	7555.25(1)	7554.9	0.3
	B	2252.1	2257.927(6)	2257.5	0.4
	C	1867.6	1868.707(6)	1869.1	0.4
<i>Tt</i>	A	22697.3	22607 (117)	22708.3	-
	B	1443.7	1448.061(6)	1447.8	0.3
	C	1396.9	1400.310(6)	1400.7	0.4
<i>Tg</i>	A	22922.6	23271 (1274)	22946.5	-
	B	1453.5	1459.52(3)	1459.5	0.0
	C	1404.2	1410.16(4)	1409.9	0.3

^a Ref.⁴⁸.

Discussion

It was possible to confidently assign the P-C stretch at 638 cm^{-1} for the *Gg* conformer having fourth lowest energy which was predicted and observed on the high frequency side of the lowest energy *Gt* form at 631 cm^{-1} in the Raman spectra of the liquid. The band at 638 cm^{-1} was observed to be a weak shoulder on the band at 631 cm^{-1} which made it difficult to obtain the relative intensity as a function of temperature particularly as the temperature of the sample was lowered. Nevertheless, this region of the Raman spectrum did not have other fundamentals interfering with the observation of this vibration at ambient temperature. Based on the relative intensity also at ambient temperature, *Gg* is estimated to be 5% abundant with an enthalpy difference of 387 cm^{-1} (4.63 kJ mol^{-1}) with respect to *Gt*. The abundance of the *Gt* form itself is calculated to be 62% with the remainder values of 20% for the *Tt* and 13% for the *Tg* form at ambient temperature. The ab initio prediction was for *Gg* conformer to be having third lowest energy but the experimental data indicates that it has fourth lowest energy.

There were slight discrepancies that were observed in the theoretical energy values involving MP2(full) and B3LYP methods. While the experimentally determined order of energies for 2-cyanoethylphosphine was $Gt < Tt < Tg < Gg < Gg'$, the predicted values from the MP2(full) calculations follow the order: $Gt < Tt < Gg < Tg < Gg'$, where, some of the basis sets predict the *Tt* form to be having lower energy than *Gt*. On the other hand, conformational stability obtained from the B3LYP calculations minimally varies with the size of the basis set and the order was predicted to be $Tt < Gt < Tg < Gg < Gg'$.

The predicted frequencies for the fundamental vibrations with three scaling factors compare favorably with the observed values with an average error of 10 cm^{-1} which

represents a percentage error of 0.8% for the *Gt* conformer. This error cannot be obtained for the *Tt* and *Tg* conformers since many of the vibrations of these conformers seem to be nearly the same as the corresponding ones for the *Gt* form or they simply could not be observed in the spectra; thus, only a few fundamentals for these two conformers were confidently identified. Nevertheless, it is clear from the few normal modes that were assigned that the error is probably similar for the predicted frequencies.

Since the fit of the seven rotational constants were excellent it is believed that the adjusted r_0 structural parameters for the *Tt* and *Tg* conformers should predict their A rotational constants to within a very few megahertz. It should be noted that the experimental value of 22607 ± 117 MHz is within the 22708.3 MHz obtained from the r_0 structural parameters of the *Tt* conformer. Similarly, for the *Tg* conformer the determined structural parameters predict the A rotational constant to within 324 MHz to the experimentally determined value which had an uncertainty of 1274 MHz.

In the microwave study, the P-C bond distance was fixed at 1.880 Å for all three isotopes which is quite long compared to the r_0 distances of 1.860(3) Å for the *Gt* conformer with similar values of 1.858(3) and 1.864(3) Å for the *Tt* and *Tg* forms, respectively. The estimated distance for the C-C(N) bond of 1.474 Å is also considerably longer than the corresponding values from this study where they differed with similar values of 1.463, 1.464, and 1.465 Å. However, the remaining estimated distances are as good as the determined ones in the current study.

The ab initio predicted heavy atom angles were adjusted by 0.5° and 0.2° for $\angle PCC$ and $\angle CCC$ for the fit of the rotational constants for the *Gt* conformer and no adjustment for the *Tt* form and a decrease of 0.2° for the PCC angle for the *Tg* conformer. Thus, only

minor adjustments were made from the ab initio MP2(full)/6-311+G(d,p) predicted parameters for the three conformers of 2-cyanoethylphosphine.

The experimentally determined values of $\angle\text{PCC}$ for the three conformers were 117.0, 114.0 and 109.0° for the *Gt*, *Tt*, and *Tg* conformers, respectively, which have differences of 0.1, 0.9, and 1.0 degrees, respectively, from the values of these angles obtained in this study. Since the listed uncertainties of the angles were reported to be 1.5° they all are in agreement with the experimentally determined values reported herein.

The results of this study indicate that the ab initio MP2(full)/6-311+G(d,p) calculations provide very good predictions of the structural parameters for the organophosphorus molecules which include both the heavy atoms and the PH₂ parameters. This is a small sample and it would be of interest to study a few more organophosphorus molecules to see if the predictions from these ab initio calculations also provide good values.

From early vibrational studies of some XCH₂CH₂Y molecules conformer having the lowest energy was determined where many of the results were obtained for all three physical states. Of particular interest in the current study was the results obtained when Y = CN and X = Cl, Br⁵⁰. These investigators concluded that when the X and Y groups were in the *trans* position for these molecules, the carbon-halogen bond stretching frequencies were significantly affected by the electronegativity of the Y group as the result of the inductive effect. This relationship was further developed by an empirical relationship in which the force constants were found to be proportional to the electronegativity product of the bound atoms⁵¹. Thus, from these results it was possible to identify the *trans* and *gauche* conformers of the ClCH₂CH₂CN and BrCH₂CH₂CN molecules⁵². With this background we

investigated whether the conformations of the $\text{NCCH}_2\text{CH}_2\text{PH}_2$ molecule obeyed these C-C(N) stretching frequencies for the two conformers, and they did. Therefore, these frequencies of the C-X and C-Y stretches can be used to identify the conformer when the electronegativities of these substituents are utilized which provides a rather simple method for identifying the conformation. Although this method does not indicate which conformer has the lowest energy, it should be very useful for identifying the spectral bands for $\text{XCH}_2\text{CH}_2\text{Y}$ molecules with *trans* and *gauche* conformers. For example, the $\text{H}_2\text{PCH}_2\text{CH}_2\text{PH}_2$ molecule will have ten possible conformers with four of them being *trans* conformers and the remaining six being *gauche* forms and it should be possible to vibrationally distinguish them. There are several other $\text{XCH}_2\text{CH}_2\text{PH}_2$ molecules where this method could be valuable for the identification of *trans* and *gauche* conformers.

PROJECT-3

Conformational Stabilities from Variable Temperature Raman Spectra, ro

Structural Parameters and Vibrational Assignments of

1,2-diphosphinoethane

Introduction

The 1,2-disubstituted ethane ($\text{YCH}_2\text{CH}_2\text{X}$) molecules are of interest since most of them have two conformers *trans* (*anti*) and *gauche*, present in the fluid states and their relative stabilities are believed to depend on the electronegativity and size of the substituents. For example, 1,2-difluoroethane has the *gauche* conformer lower in energy than the *trans* form by $280 \pm 30 \text{ cm}^{-1}$ ($3.35 \pm 0.36 \text{ kJ mol}^{-1}$)⁴², whereas, 1,2-dichloroethane has the *trans* conformer lower in energy than the *gauche* form⁴³ by $323 \pm 7 \text{ cm}^{-1}$ ($3.87 \pm 0.09 \text{ kJ mol}^{-1}$) from variable temperature infrared studies of xenon solutions. When Y is a methyl group and X is a fluorine atom (1-fluoropropane) the *gauche* conformer has lower energy⁵³ than the *trans* form by $104 \pm 6 \text{ cm}^{-1}$ ($1.24 \pm 0.07 \text{ kJ mol}^{-1}$). One might expect the 1-chloro-2-fluoroethane molecule to have the *gauche* conformer with lower energy since the fluorine and chlorine atoms are highly electronegative and the chlorine atom has a van der Waal's radius nearly the same as that of the methyl group. However, it has been reported that the 1-chloro-2-fluoroethane molecule has the *trans* form with lower energy than the *gauche* by $287 \pm 58 \text{ cm}^{-1}$ ($3.43 \pm 0.69 \text{ kJ mol}^{-1}$) from a determination of the enthalpy difference from the variable temperature Raman spectra of the gas⁵⁴ as well as from a variable temperature study of rare gas solutions⁴⁴. Thus, it is clear that there are additional factors than just size and electronegativity that determines which conformer has the lowest energy.

As a continuation of our studies of 1,2-substituted ethanes, we have investigated the conformational stability of 1,2-diaminoethane (ethylenediamine)¹⁴ and 1,2-diphosphinoethane (ethylenediphosphine) to determine whether there is a significant difference in the conformer stabilities of these two molecules since both ethylamine¹⁵ and ethylphosphine⁵⁵ have the *trans* conformers as the lower energy forms. We were particularly interested in the phosphine molecule since some of the phosphines have been shown to have anticancer properties^{17,18}.

We initiated the investigation of the vibrational spectra of 1,2-diphosphinoethane with a study of the infrared spectra of the gas, amorphous and crystalline solid. Additionally, we have investigated the Raman spectra of the liquid and solid. Variable temperature Raman spectra of the liquid have been obtained from which enthalpy differences between the various conformers were determined. Rotation about the C-C bond gives rise to *Trans* (*T*) and *Gauche* (*G*) forms which are indicated by capital letters and rotation around both of the C-P bonds also results in *trans* (*t*) and *gauche* (*g*) forms which are indicated by lower case letters. There are a total of ten possible stable conformers that can exist for the H₂PCH₂CH₂PH₂ molecule which are shown in Fig. 11.

To support the vibrational study, we have carried out *ab initio* calculations with basis sets up to aug-cc-pVTZ as well as those with diffuse functions up to 6-311+G(2df,2pd). We have also carried out density functional theory (DFT) calculations by the B3LYP method with the same basis sets. We have calculated optimized geometries, conformational stabilities, harmonic force constants, infrared intensities and Raman activities. By utilizing the previously reported⁵⁶ microwave rotational constants along with *ab initio* MP2(full)/6-311+G(d,p) predicted structural values, adjusted r_0 parameters have

been obtained for two C-C *Trans* and two C-C *Gauche* conformers. The results of these spectroscopic, structural, and theoretical studies are reported herein.

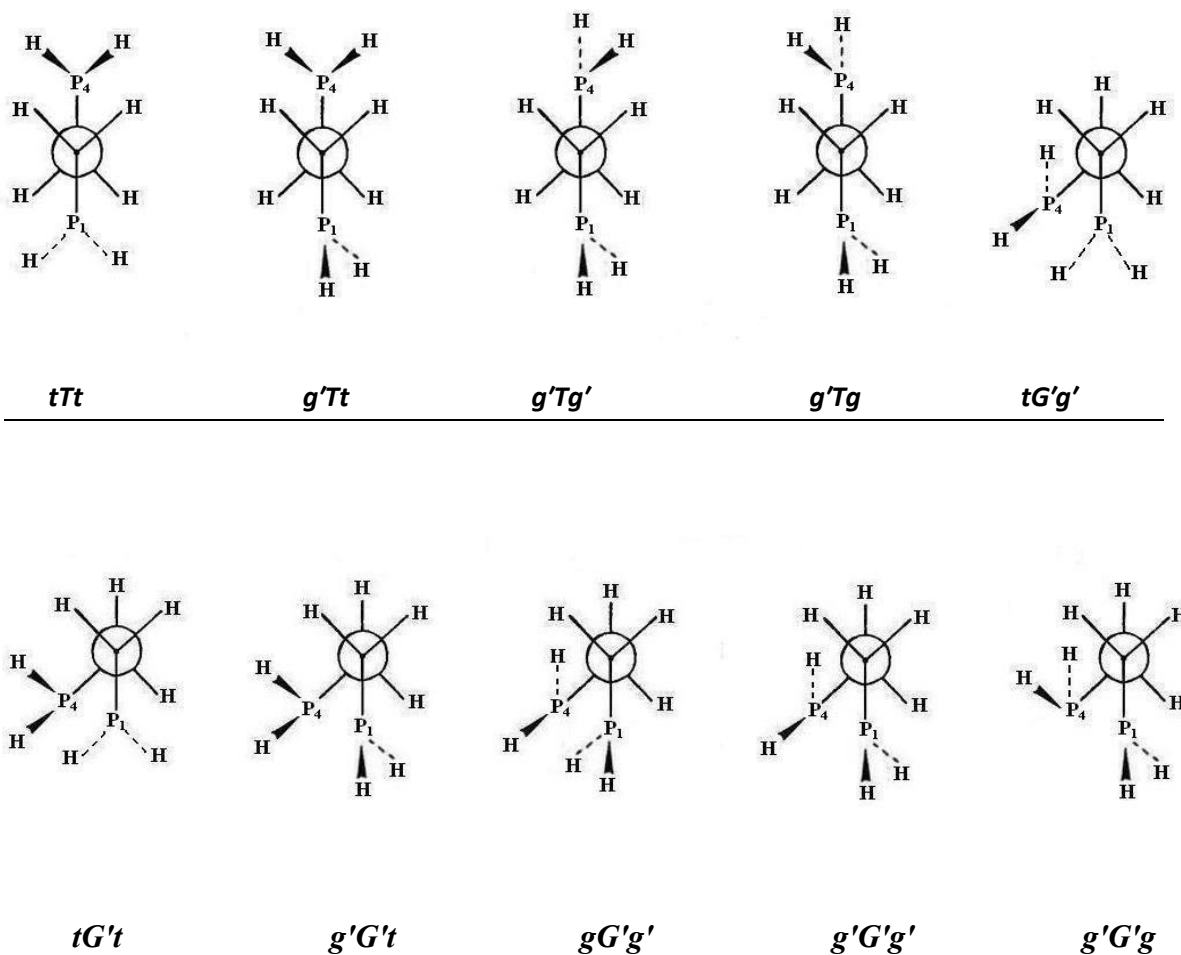


Figure 4.11. Newmann projections of the ten conformers of 1,2-diphosphinoethane.

Experimental Methods

The sample of 1,2-diphosphinoethane was purchased from Strem Chemicals, Inc., Newburyport, MA. The purity was determined by gas chromatography to be greater than 96%. The sample was subjected to trap-to-trap transfers under vacuum prior to recording spectra and stored at -78°C .

Infrared spectra of the solid in the $3600\text{-}500\text{ cm}^{-1}$ region were obtained with a Perkin-Elmer 283B grating spectrophotometer and a liquid-nitrogen-cooled sampling cell with a CsI substrate. The spectra of the solids were recorded at a resolution of 2.0 cm^{-1} . Infrared spectrum of the crystalline solid was obtained by the process of annealing which was achieved by repetitive evaporation of the liquid nitrogen completely from the reservoir in the solid cell, which resulted in a gradual increase in the temperature, which was then followed by sudden freezing of the sample by the addition of liquid nitrogen. This warming process allowed the molecules to form a crystalline structure. Gaseous phase infrared samples were contained in a 10 cm cell fitted with KBr windows, and the spectra were recorded on a Nicolet 7199 Fourier transform interferometer equipped with a Ge/KBr beamsplitter and a liquid-nitrogen-cooled MCT detector. The instrument was purged to remove the water and carbon dioxide by a commercial two column dryer with one column to remove water and the other carbon dioxide. The resolution for the spectra of the gas was 0.5 cm^{-1} at ambient pressure of the gas. The infrared spectra of the gas, amorphous and crystalline solid are shown in Fig. 12(A-C), respectively.

Raman spectra were recorded from $3000\text{-}200\text{ cm}^{-1}$ on a Spex Ramalog DUV spectrometer set to use the 4880 \AA line of a Spectra-Physics model 171 argon ion laser as the excitation source with a laser power of 200 mW. Liquid samples were sealed in Pyrex

capillaries under vacuum, and spectra of solids and variable temperature liquids were obtained by using a cell similar to one described by Miller and Harney⁴⁷. All of the Raman spectra were recorded at 3 cm⁻¹ spectral bandwidths and frequencies are expected to be accurate to better than 2 cm⁻¹. The Raman spectra of the liquid and the solid are shown in Fig. 13A and 13B, respectively.

Table 4.16. Observed and calculated^a frequencies (cm⁻¹) and potential energy distributions (P.E.D.s) for the *tTt* (C_{2h}) conformer of 1,2-diphosphinoethane.

Sym. Block	Vib. No.	Approximate Description	AB		IR gas	IR amorphous	IR annealed	Raman liquid	Raman solid	contour			P.E.D. ^c
			<i>INITIO</i>	fixed scaled ^b						A	B	C	
A _g	v ₁	CH ₂ symmetric stretch	3106	2914				2899	2896	5	95	-	100S ₁
	v ₂	PH ₂ symmetric stretch	2481	2287				2284	2283	2	98	-	100S ₂
	v ₃	CH ₂ deformation	1523	1429				1415	1415	5	95	-	99S ₃
	v ₄	CH ₂ wag	1373	1303				-	1313	84	5	11	93S ₄
	v ₅	PH ₂ deformation	1158	1099				1078	1075	13	87	-	91S ₅
	v ₆	CC stretch	1090	1037				1037	1035	79	19	2	76S ₆
	v ₇	PH ₂ wag	918	876				863	865	22	77	1	58S ₇ , 19S ₈ , 15S ₉
	v ₈	CP stretch	696	666				655	656	98	2	-	43S ₈ , 29S ₇ , 21S ₉
	v ₉	CCP bend	290	282				283	291	-	7	93	55S ₉ , 35S ₈
A _u	v ₁₀	CH ₂ antisymmetric stretch	3176	2980	2948	2929	2931			-	-	100	100S ₁₀
	v ₁₁	PH ₂ antisymmetric stretch	2493	2298	2302	2284	2286			-	-	100	100S ₁₁
	v ₁₂	CH ₂ twist	1214	1151	1143	1129	1129			-	-	100	84S ₁₂ , 13S ₁₃
	v ₁₃	PH ₂ twist	883	838	838	838	838			-	-	100	63S ₁₃ , 21S ₁₄ , 16S ₁₂
	v ₁₄	CH ₂ rock	647	613	621	611	611			-	-	100	78S ₁₄ , 22S ₁₃
	v ₁₅	PH ₂ torsion	195	195	-	-	-			-	-	100	93S ₁₅
	v ₁₆	CC torsion	103	103						-	-	100	94S ₁₆
B _g	v ₁₇	CH ₂ antisymmetric stretch	3156	2961				2940	-	-	-	100	100S ₁₇
	v ₁₈	PH ₂ antisymmetric stretch	2492	2297				2297	2292	-	-	100	100S ₁₈
	v ₁₉	CH ₂ twist	1354	1285				1264	1260	-	1	99	89S ₁₉ , 11S ₂₀
	v ₂₀	CH ₂ rock	1070	1015				1028	1027	16	9	75	51S ₂₀ , 45S ₂₁
	v ₂₁	PH ₂ twist	699	664				655	656	8	1	91	55S ₂₁ , 36S ₂₀
	v ₂₂	PH ₂ torsion	227	227						9	90	1	99S ₂₂
B _u	v ₂₃	CH ₂ symmetric stretch	3115	2922	2920	2901	2902			5	95	-	100S ₂₃
	v ₂₄	PH ₂ symmetric stretch	2481	2287	2302	2276	2278			2	98	-	100S ₂₄
	v ₂₅	CH ₂ deformation	1528	1433	1430	1410	1410			5	95	-	100S ₂₅
	v ₂₆	CH ₂ wag	1283	1218	1190	1192	1192			52	48	-	93S ₂₆

v ₂₇	PH ₂ deformation	1152	1093	1082	1064	1064	12	88	-	97S ₂₇
v ₂₈	PH ₂ wag	856	812	815	806	805	56	44	-	90S ₂₈
v ₂₉	CP stretch	716	680	676	672	674	89	11	-	96S ₂₉
v ₃₀	CCP bend	204	202				15	85	-	99S ₃₀

^aMP2(full)/6-31G(d) *ab initio* calculations, frequencies from scaled force constants, and potential energy distributions (P.E.D.s)

^bScaling factors of 0.88 for CH₂ stretches and CH₂ deformations, 0.85 for PH₂ stretches, 0.90 for all other modes except torsions and heavy atom bends.

^cSymmetry coordinates with P.E.D. contribution less than 10% are omitted.

Table 4.17. Observed and calculated^a frequencies (cm⁻¹) for the *g'Tt* (*C₁*) conformer of 1,2-diphosphinoethane.

Vib. No.	Approx. Description	<i>AB</i>		IR gas	IR amorphous	Raman	
		<i>INITIO</i>	fixed scaled ^b			liquid	Raman solid
v ₁	CH ₂ antisymmetric stretch	3183	2986	2979	2968		
v ₂	CH ₂ antisymmetric stretch	3158	2962				
v ₃	CH ₂ symmetric stretch	3120	2927		2901		
v ₄	CH ₂ symmetric stretch	3106	2913			2919	2916
v ₅	PH ₂ antisymmetric stretch	2497	2302				
v ₆	PH ₂ antisymmetric stretch	2493	2298				
v ₇	PH ₂ symmetric stretch	2485	2291				
v ₈	PH ₂ symmetric stretch	2481	2287				
v ₉	CH ₂ deformation	1536	1441				
v ₁₀	CH ₂ deformation	1528	1433				
v ₁₁	CH ₂ wag	1374	1305				1263
v ₁₂	CH ₂ twist	1353	1284				
v ₁₃	CH ₂ wag	1274	1209				
v ₁₄	CH ₂ twist	1200	1144				
v ₁₅	PH ₂ deformation	1157	1097	~1086	1071	1081	1082
v ₁₆	PH ₂ deformation	1154	1095	~1086	1071	1081	1082
v ₁₇	CC stretch	1096	1043				
v ₁₈	CH ₂ rock	1061	1022			1000	995
v ₁₉	PH ₂ wag	915	874	869			
v ₂₀	PH ₂ twist	878	836	838			
v ₂₁	PH ₂ wag	847	804	~815		808	
v ₂₂	PH ₂ twist	749	721	716			697
v ₂₃	CP stretch	715	682				
v ₂₄	CP stretch	691	660				
v ₂₅	CH ₂ rock	665	635				
v ₂₆	CCP bend	282	275			276	
v ₂₇	CC torsion	221	221				
v ₂₈	CCP bend	199	197				
v ₂₉	PH ₂ torsion	170	170				
v ₃₀	PH ₂ torsion	99	99				

^aMP2(full)/6-31G(d) *ab initio* calculations, frequencies from scaled force constants,.

^bScaling factors of 0.88 for CH₂ stretches and CH₂ deformations, 0.85 for PH₂ stretches, 0.90 for all other modes except torsions and heavy atom bends.

Table 4.18. Observed and calculated^a frequencies (cm⁻¹) for the *g'Tg'* (C₂) form of 1,2-diphosphinoethane.

Sym. block	Vib. No.	Approximate Description	AB		IR gas	IR amorphous	Raman liquid	Raman solid
			<i>INITIO</i>	fixed scaled ^b				
A	v ₁	CH ₂ antisymmetric stretch	3184	2987	2979	2968		
	v ₂	CH ₂ symmetric stretch	3112	2919				
	v ₃	PH ₂ antisymmetric stretch	2497	2302				
	v ₄	PH ₂ symmetric stretch	2485	2291				
	v ₅	CH ₂ deformation	1537	1442				
	v ₆	CH ₂ wag	1350	1302				
	v ₇	CH ₂ twist	1188	1127				
	v ₈	PH ₂ deformation	1158	1099				
	v ₉	CC stretch	1100	1047				
	v ₁₀	PH ₂ twist	915	873				
	v ₁₁	PH ₂ wag	872	828	824		826	
	v ₁₂	CH ₂ rock	717	681			673	676
	v ₁₃	CP stretch	693	661				
	v ₁₄	CCP bend	270	263			265	
	v ₁₅	PH ₂ torsion	171	171				
	v ₁₆	CC torsion	96	96				
B	v ₁₇	CH ₂ antisymmetric stretch	3166	2970				
	v ₁₈	CH ₂ symmetric stretch	3120	2927				
	v ₁₉	PH ₂ antisymmetric stretch	2497	2302				
	v ₂₀	PH ₂ symmetric stretch	2483	2289				
	v ₂₁	CH ₂ deformation	1539	1444	1382	1382		
	v ₂₂	CH ₂ twist	1371	1281	1276	1270		
	v ₂₃	CH ₂ wag	1265	1201	1168	1168	1169	
	v ₂₄	PH ₂ deformation	1154	1095				
	v ₂₅	CH ₂ rock	1052	998	986		990	
	v ₂₆	PH ₂ twist	844	801				
	v ₂₇	PH ₂ wag	759	720				
	v ₂₈	CP stretch	714	677				
	v ₂₉	PH ₂ torsion	216	215				
	v ₃₀	CCP bend	176	175				

^aMP2(full)/6-31G(d) *ab initio* calculations, frequencies from scaled force constants.

^bScaling factors of 0.88 for CH₂ stretches and CH₂ deformations, 0.85 for PH₂ stretches, 0.90 for all other modes except torsions and heavy atom bends.

Table 4.19. Observed and calculated^a frequencies (cm⁻¹) for the *g'Tg* (*C_i*) form of 1,2-diphosphinoethane.

Sym. block	Vib. No.	Approximate Description	<i>AB</i> <i>INITIO</i>	fixed scaled ^b	IR gas	IR amorphous	Raman liquid
<i>A_g</i>	v ₁	CH ₂ antisymmetric stretch	3170	2974			
	v ₂	CH ₂ symmetric stretch	3109	2917			
	v ₃	PH ₂ antisymmetric stretch	2500	2305			
	v ₄	PH ₂ symmetric stretch	2487	2293			
	v ₅	CH ₂ deformation	1535	1456			
	v ₆	CH ₂ wag	1372	1302			
	v ₇	CH ₂ twist	1352	1283			
	v ₈	PH ₂ deformation	1158	1099			
	v ₉	CC stretch	1101	1045			
	v ₁₀	CH ₂ rock	1052	998			990
	v ₁₁	PH ₂ twist	903	857			
	v ₁₂	PH ₂ wag	752	713			714
	v ₁₃	CP stretch	683	648			
	v ₁₄	CCP bend	275	275			276
	v ₁₅	PH ₂ torsion	197	197			
<i>A_u</i>	v ₁₆	CH ₂ antisymmetric stretch	3188	2991			
	v ₁₇	CH ₂ symmetric stretch	3118	2925	2948		
	v ₁₈	PH ₂ antisymmetric stretch	2501	2306			
	v ₁₉	PH ₂ symmetric stretch	2486	2292			
	v ₂₀	CH ₂ deformation	1537	1458	1393		
	v ₂₁	CH ₂ wag	1268	1203			
	v ₂₂	CH ₂ twist	1183	1122	1130	1114	
	v ₂₃	PH ₂ deformation	1154	1095			
	v ₂₄	PH ₂ wag	872	827			
	v ₂₅	PH ₂ twist	841	798			
	v ₂₆	CH ₂ rock	740	702			
	v ₂₇	CP stretch	697	661			
	v ₂₈	CCP bend	181	181			
	v ₂₉	PH ₂ torsion	147	147			
	v ₃₀	CP torsion	96	96			

^aMP2(full)/6-31G(d) *ab initio* calculations, frequencies from scaled force constants.

^bScaling factors of 0.88 for CH₂ stretches and CH₂ deformations, 0.85 for PH₂ stretches, 0.90 for all other modes except torsions and heavy atom bends.

Table 4.20. Observed and calculated^a frequencies (cm⁻¹) for the *tG'g'* (*C_i*) form of 1,2-diphosphinoethane.

Vib. No.	Approximate Description	<i>AB</i>		IR gas	IR amorphous	Raman liquid
		<i>INITIO</i>	fixed scaled ^b			
v ₁	CH ₂ antisymmetric stretch	3172	2976			
v ₂	CH ₂ antisymmetric stretch	3159	2964			
v ₃	CH ₂ symmetric stretch	3109	2917			
v ₄	CH ₂ symmetric stretch	3103	2911			
v ₅	PH ₂ antisymmetric stretch	2510	2314			
v ₆	PH ₂ antisymmetric stretch	2498	2303			
v ₇	PH ₂ symmetric stretch	2495	2300			
v ₈	PH ₂ symmetric stretch	2481	2287			
v ₉	CH ₂ deformation	1529	1434	1361	1369	
v ₁₀	CH ₂ deformation	1521	1427	1350	1346	
v ₁₁	CH ₂ wag	1372	1302			
v ₁₂	CH ₂ wag	1364	1295	1290		
v ₁₃	CH ₂ twist	1263	1200			1176
v ₁₄	CH ₂ twist	1197	1139	1134		1130
v ₁₅	PH ₂ deformation	1166	1107			
v ₁₆	PH ₂ deformation	1153	1094			
v ₁₇	CC stretch	1089	1039			
v ₁₈	CH ₂ rock	1014	973			982
v ₁₉	CH ₂ rock	985	943	944		
v ₂₀	PH ₂ wag	864	821			
v ₂₁	PH ₂ twist	844	802			
v ₂₂	PH ₂ wag	755	720			
v ₂₃	CP stretch	711	677			
v ₂₄	PH ₂ twist	647	626			
v ₂₅	CP stretch	631	601			593
v ₂₆	CCP bend	358	352			348
v ₂₇	PH ₂ torsion	267	266			
v ₂₈	CCP bend	218	216			
v ₂₉	PH ₂ torsion	172	172			
v ₃₀	CP torsion	100	100			

^aMP2(full)/6-31G(d) *ab initio* calculations, frequencies from scaled force constants.

^bScaling factors of 0.88 for CH₂ stretches and CH₂ deformations, 0.85 for PH₂ stretches, 0.90 for all other modes except torsions and heavy atom bends.

Table 21. Observed and calculated^a frequencies (cm⁻¹) for the *tG't* (C₂) form of 1,2-diphosphinoethane.

Sym. block	Vib No.	Approximate Description	AB		IR gas	IR amorphous	Raman liquid
			<i>INITIO</i>	fixed scaled ^b			
A	v ₁	CH ₂ antisymmetric stretch	3152	2956			
	v ₂	CH ₂ symmetric stretch	3103	2910			
	v ₃	PH ₂ antisymmetric stretch	2512	2316			
	v ₄	PH ₂ symmetric stretch	2484	2290			
	v ₅	CH ₂ deformation	1523	1429			
	v ₆	CH ₂ wag	1367	1296			
	v ₇	CH ₂ twist	1272	1206			1188
	v ₈	PH ₂ deformation	1163	1104			
	v ₉	CC stretch	1086	1031			
	v ₁₀	CH ₂ rock	1020	967			959
	v ₁₁	PH ₂ wag	865	819			
	v ₁₂	PH ₂ twist	707	671			
	v ₁₃	CP stretch	621	589			601
	v ₁₄	PH ₂ torsion	281	277			
	v ₁₅	CCP bend	193	191			
	v ₁₆	CC torsion	94	94			
B	v ₁₇	CH ₂ antisymmetric stretch	3161	2964			
	v ₁₈	CH ₂ symmetric stretch	3097	2905			
	v ₁₉	PH ₂ antisymmetric stretch	2501	2306			
	v ₂₀	PH ₂ symmetric stretch	2484	2290			
	v ₂₁	CH ₂ deformation	1520	1426	1350	1346	
	v ₂₂	CH ₂ wag	1371	1301			
	v ₂₃	CH ₂ twist	1215	1151	1156	1152	
	v ₂₄	PH ₂ deformation	1156	1097			
	v ₂₅	PH ₂ twist	989	941	939	929	
	v ₂₆	PH ₂ wag	869	824			
	v ₂₇	CP stretch	711	674			
	v ₂₈	CH ₂ rock	629	597			~604
	v ₂₉	CCP bend	363	356			
	v ₃₀	PH ₂ torsion	174	174			

^aMP2(full)/6-31G(d) *ab initio* calculations, frequencies from scaled force constants.

^bScaling factors of 0.88 for CH₂ stretches and CH₂ deformations, 0.85 for PH₂ stretches, 0.90 for all other modes except torsions and heavy atom bends.

Theoretical Methods

The *ab initio* calculations were performed with the Gaussian 03 program¹⁹ with Gaussian-type basis functions. The energy minima with respect to nuclear coordinates were obtained by the simultaneous relaxation of all geometric parameters by the gradient method of Pulay²⁰. Several basis sets as well as the corresponding ones with diffuse functions were employed with the Møller-Plesset perturbation method²¹ to the second order (MP2(full)) as well as with the density functional theory (DFT) by the B3LYP method.

In order to obtain a complete description of the molecular motions involved in the fundamental vibrations of 1,2-diphosphinoethane, normal coordinate analyses were carried out. The force field in Cartesian coordinates was obtained with the Gaussian 03 program¹⁹ with the 6-31G(d) basis set. The internal coordinates used to calculate the **G** and **B** matrices along with the atomic numbering are shown in Fig. 14. By using the **B** matrix²⁹, the force field in Cartesian coordinates was converted to a force field in internal coordinates. Subsequently, scaling factors were applied of 0.88 for the force constants of the CH₂ stretches and CH₂ deformations, 0.85 for the force constants of the PH₂ stretches and 0.90 for all other force constants except for the heavy atom bends, torsions, and C≡N stretch which were not scaled. For the interaction force constants, the geometric average of the scaling factors was used. From the fixed scaled force field the predicted wavenumbers were obtained and a set of symmetry coordinates was used (Table 25) to determine the corresponding potential energy distributions (P.E.D.s). The calculated infrared intensities, Raman activities and potential energy distributions for the *tTt*, *g'Tt*, *g'Tg'*, *g'Tg*, *tG'g'* and *tG't* conformers are listed in Tables 10, 8S-12S, respectively.

The vibrational spectra were predicted from the MP2(full)/6-31G(d) calculations. The predicted frequencies from the scaled force constants were used together with a Lorentzian

function to obtain the simulated spectra. Infrared intensities were obtained based on the dipole moment derivatives with respect to Cartesian coordinates. The derivatives were transformed with respect to normal coordinates by $(\partial\mu_w/\partial Q_i) = \sum_j (\partial\mu_w/\partial X_j)L_{ij}$, where Q_i is the i^{th} normal coordinate, X_j is the j^{th} Cartesian displacement coordinate, and L_{ij} is the transformation matrix between the Cartesian displacement coordinates and the normal coordinates. The infrared intensities were then calculated by $(N\pi)/(3c^2) [(\partial\mu_x/\partial Q_i)^2 + (\partial\mu_y/\partial Q_i)^2 + (\partial\mu_z/\partial Q_i)^2]$. A comparison of experimental infrared spectra of the gas, amorphous and crystalline solid and simulated infrared spectra of *tTt* and *g'Tt* forms of 1,2-diphosphinoethane are shown in Fig. 12 (A-E), respectively. The predicted spectrum is in good agreement with the experimental spectrum which shows the utility of the predicted frequencies from the scaled force constants and predicted intensities for supporting the vibrational assignment.

Additional support for the vibrational assignments was obtained from the simulated Raman spectra. The evaluation of Raman activity by using the analytical gradient methods has been developed³⁰⁻³² and the activity S_j can be expressed as: $S_j = g_j(45\alpha_j^2 + 7\beta_j^2)$, where g_j is the degeneracy of the vibrational mode j , α_j is the derivative of the isotropic polarizability, and β_j is the anisotropic polarizability. To obtain the Raman scattering cross sections, the polarizabilities are incorporated into S_j by multiplying S_j with $(1-\rho_j)/(1+\rho_j)$ where ρ_j is the depolarization ratio of the j^{th} normal mode. The Raman scattering cross sections and calculated wavenumbers obtained from the Gaussian 03 program were used together with a Lorentzian function to obtain the simulated Raman spectra. A comparison of experimental Raman spectra of the liquid and solid and simulated Raman spectra of *tTt* and *g'Tt* forms of 1,2-diphosphinoethane are shown in Fig. 13 (A-D), respectively. The predicted spectra are in reasonable agreement with the experimental spectrum but there are a few bands where the predicted bands are significantly weaker than the

corresponding experimental bands. Nevertheless, the relative activities of the Raman bands can provide some support for making the vibrational assignments.

Vibrational Assignment

To be able to obtain the enthalpy differences of the conformers it is necessary to assign fundamentals for each conformer which has a reasonable amount present at ambient temperature. Since four conformers have been identified from the microwave spectra⁵⁶ and two additional conformers, without a permanent dipole, are predicted to have relatively small energy differences from the *ab initio* calculations, there should be six conformers that can be identified for enthalpy difference determinations. Additionally, the *ab initio* calculations performed on 1,2-diphosphinoethane support this estimate as the energies of these six conformers are predicted within $\sim 560\text{ cm}^{-1}$. Thus, searches were made initially for the fundamentals of the conformers with C_{2h} and C_i symmetry, which were not identified from the microwave study⁵⁶.

The infrared and Raman spectra of the solid are quite simple and there is obvious mutual exclusion between the two spectra, so there is a center of symmetry for the conformer remaining in the solid. Of the ten possible conformers, only the $g'Tg$ (C_i) and tTt (C_{2h}) forms have symmetry centers and the $g'Tg$ conformer is predicted to be 489 cm^{-1} higher in energy, so the conformer in the crystal must be the tTt form. The predicted infrared and Raman spectra for this conformer are shown in Fig. 12 and Fig. 13, respectively, and the agreement clearly supports the conclusion that these bands are due to the tTt form.

Once the fundamentals that were observed in the infrared and Raman spectra of the solid arising from the tTt form were assigned, it was relatively simple to make complete assignments for all of the fundamentals for this conformer. With the predicted frequencies from *ab initio* calculations along with the predicted intensities for the infrared and Raman bands, the

corresponding fundamental bands in the spectrum of the gas and amorphous solid were also readily assigned. The complete assignment of the fundamentals for the tTt conformer is listed in Table 16.

After the bands from the Raman spectra of the solid were identified for the tTt form, a few bands remained due to the solid not being able to be completely annealed, unlike the infrared spectrum of the solid, which were then assigned to the other lower energy forms. Thus, the Raman spectrum of the solid did not correspond solely to the C_{2h} symmetry form.

The assignment for the C_i conformer ($g'Tg$) was then attempted since a second group of bands should have mutual exclusion but they are expected to be relatively weak compared to the corresponding bands of the C_{2h} form. To obtain the enthalpy difference between the C_{2h} conformer and the C_i form, at least one band of the C_i form needs to be confidently assigned which is free from extensive overlap from bands of the other conformers. Fortunately, there is a band at 714 cm^{-1} in the Raman spectrum of the liquid which does not have a corresponding infrared band and disappears from the Raman spectrum of the solid. Therefore, this Raman band is assigned as ν_{12} of the C_i conformer. Further fundamentals of this conformer were difficult to confidently assign except for the bands at 990 and 276 cm^{-1} . However, these bands could not be used for enthalpy difference determination since the former band was too weak and the latter band was not well separated.

With the complete assignment of the conformer with lowest energy it seems most pertinent to attempt to assign as many fundamentals as possible for the two lowest energy conformers identified from the microwave study. Both of these are *Trans* conformers and vibrational assignments of these were made with assistance from the predicted frequencies as well as the infrared and Raman intensities but not the infrared band contours which provide little information. Also, since we were mainly interested in obtaining bands that are not significantly overlapped or

readily assigned without other fundamentals affecting the intensities, we emphasized the region below 1000 cm^{-1} . For the *g'Tt* conformer, the PH_2 wag (ν_{21}) was predicted to be at 804 cm^{-1} and there was a clear Raman band at 808 cm^{-1} which has an activity consistent with the $4.6\text{ \AA}^4\text{ u}^{-1}$ predicted value from the *ab initio* calculations (Table 17). The bands for the next *Trans* form were also readily assignable in this spectral region. For example, the PH_2 wag (ν_{11}) for the *g'Tg'* form was predicted at 828 cm^{-1} and to have a strong infrared band and weak Raman band. This was consistent with both the observed intensities of the infrared and Raman band.

The in-plane C-P stretches for the two *Gauche* conformers are predicted to be about 60 cm^{-1} lower than the corresponding values for any of the *Trans* forms. Additionally, they are expected to have significantly pronounced Raman activity. Therefore, they were expected to be observed within that difference in the Raman spectrum of the liquid and were observed at 593 and 601 cm^{-1} . With the exception of the two *Trans* forms with lowest energy, very few fundamentals were observed for the remaining four conformers and they are listed in Tables 18-21.

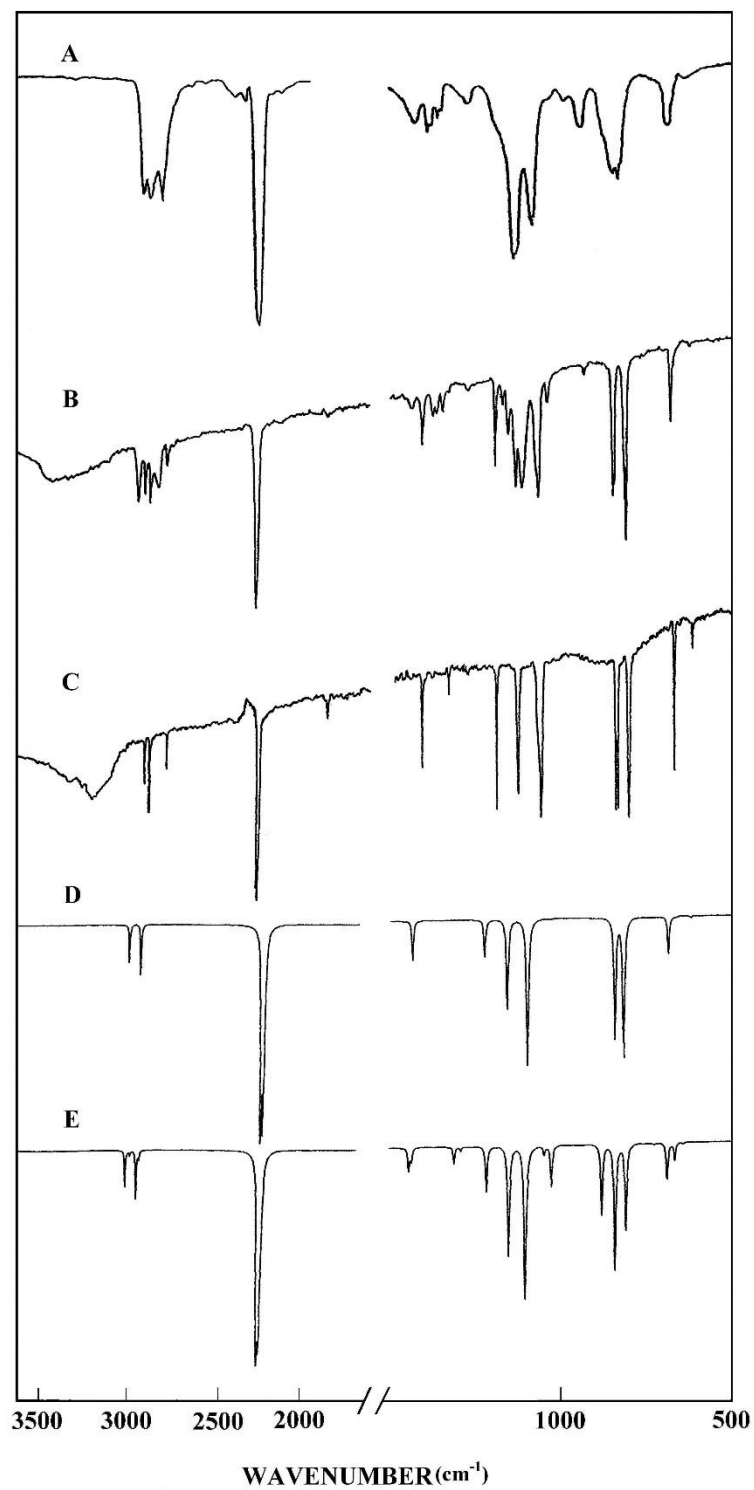


Figure 4.12. Comparison of experimental and calculated infrared spectrum of 1,2-diphosphinoethane: (A) observed spectrum of gas; (B) observed spectrum of amorphous solid; (C) observed spectrum of crystalline solid; (D) simulated spectrum of *tTt* form; (E) simulated spectrum of *g'Tt* form.

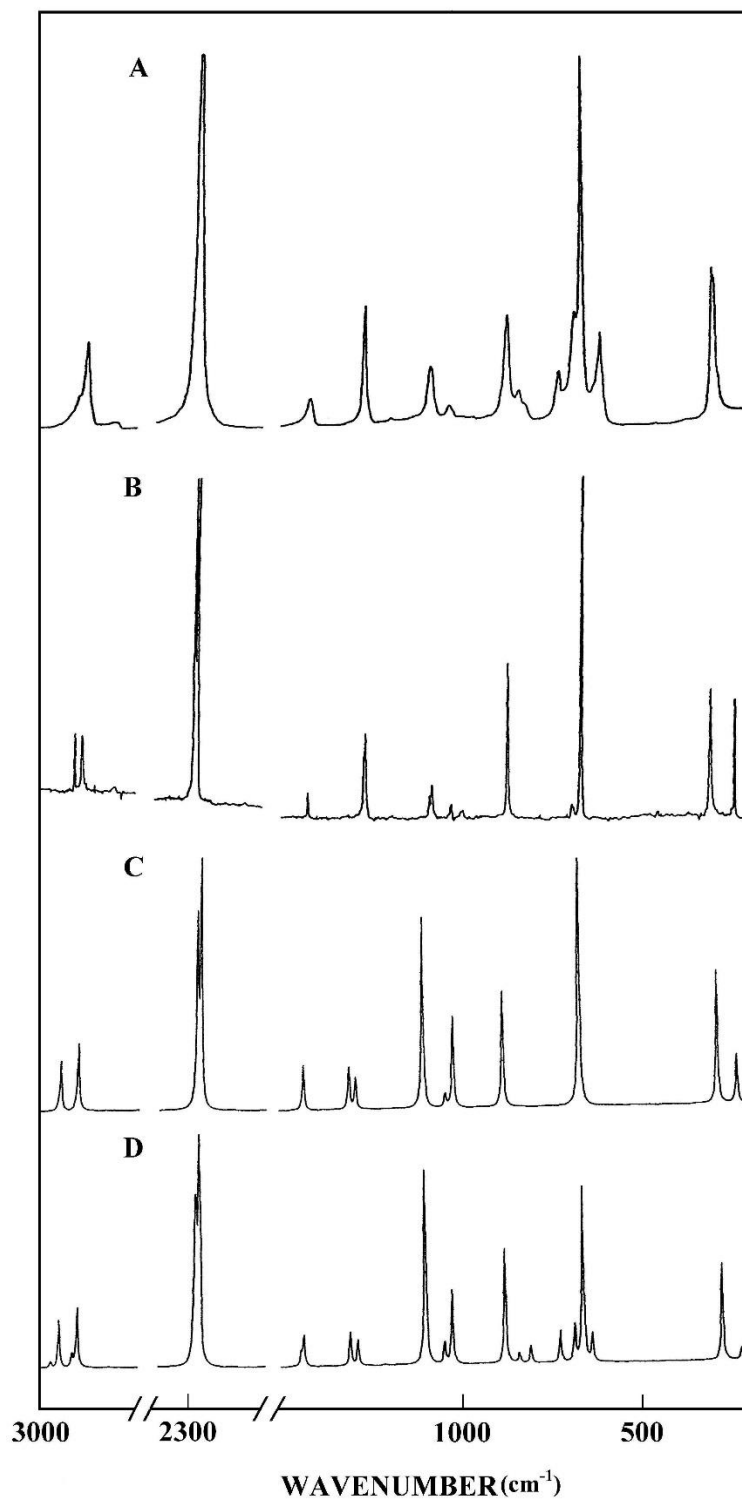


Figure 4.13. Comparison of experimental and calculated Raman spectrum of 1,2-diphosphinoethane: (A) observed spectrum of liquid; (B) observed spectrum of solid; (C) simulated spectrum of *tTt* form; (D) simulated spectrum of *g'Tt* form.

Conformational Stability

After all of the fundamentals that could be assigned for the six conformers, the next step was to find a pair or pairs of bands from which the enthalpy difference determination could be carried out. For this study, it is desirable to have the lower frequency pair(s) in the spectra to minimize the effect of combination and overtone bands. Also, the bands should be sufficiently resolved to allow for accurate intensity measurements. By identifying six of the ten possible conformers, the resulting vibrational spectra were complex. But the task of selecting band pairs for ΔH determinations was not as arduous as expected, since the heavy atom stretching and bending modes were used. With combining the peaks of the lowest energy *tTt* conformer with each of the remaining five lower energy forms (*g'Tt*, *g'Tg'*, *g'Tg*, *tG'g'*, *tG't*), a total of ten pairs of bands were obtained, with each combination contributing two pairs.

Six temperatures (-38 to 30°C) were chosen to obtain the spectral data for these pairs and by application of the van't Hoff equation, $-\ln K = \Delta H/(RT) - \Delta S/R$, the enthalpy differences were determined from a plot of $-\ln K$ versus $1/T$, where, $\Delta H/R$ is the slope of the line and K is substituted with the appropriate intensity ratios, i.e. $I_{\text{conf-1}}/I_{\text{conf-2}}$. It was assumed that ΔH , ΔS and the ratio of the molar absorption coefficients $\epsilon_{\text{conf-1}}/\epsilon_{\text{conf-2}}$ are not a function of temperature in the range studied.

With the utilization of two band pairs of the *g'Tt* and *tTt* conformers, the ΔH values obtained were $210 \pm 63 \text{ cm}^{-1}$ ($2.51 \pm 0.75 \text{ kJ mol}^{-1}$) and $333 \pm 33 \text{ cm}^{-1}$ ($3.98 \pm 0.39 \text{ kJ mol}^{-1}$). However, by utilizing these data from both band pairs as a single set, and by using the statistical standard deviation of one sigma for this conformer pair, the enthalpy difference obtained was $272 \pm 39 \text{ cm}^{-1}$ ($3.25 \pm 0.47 \text{ kJ mol}^{-1}$). The determination of the ΔH values was also carried out in a similar manner between the remaining two *Trans* and two *Gauche* conformers. The results

obtained for each band pair as well as those when treated as a single set of data, are reported in Table 22.

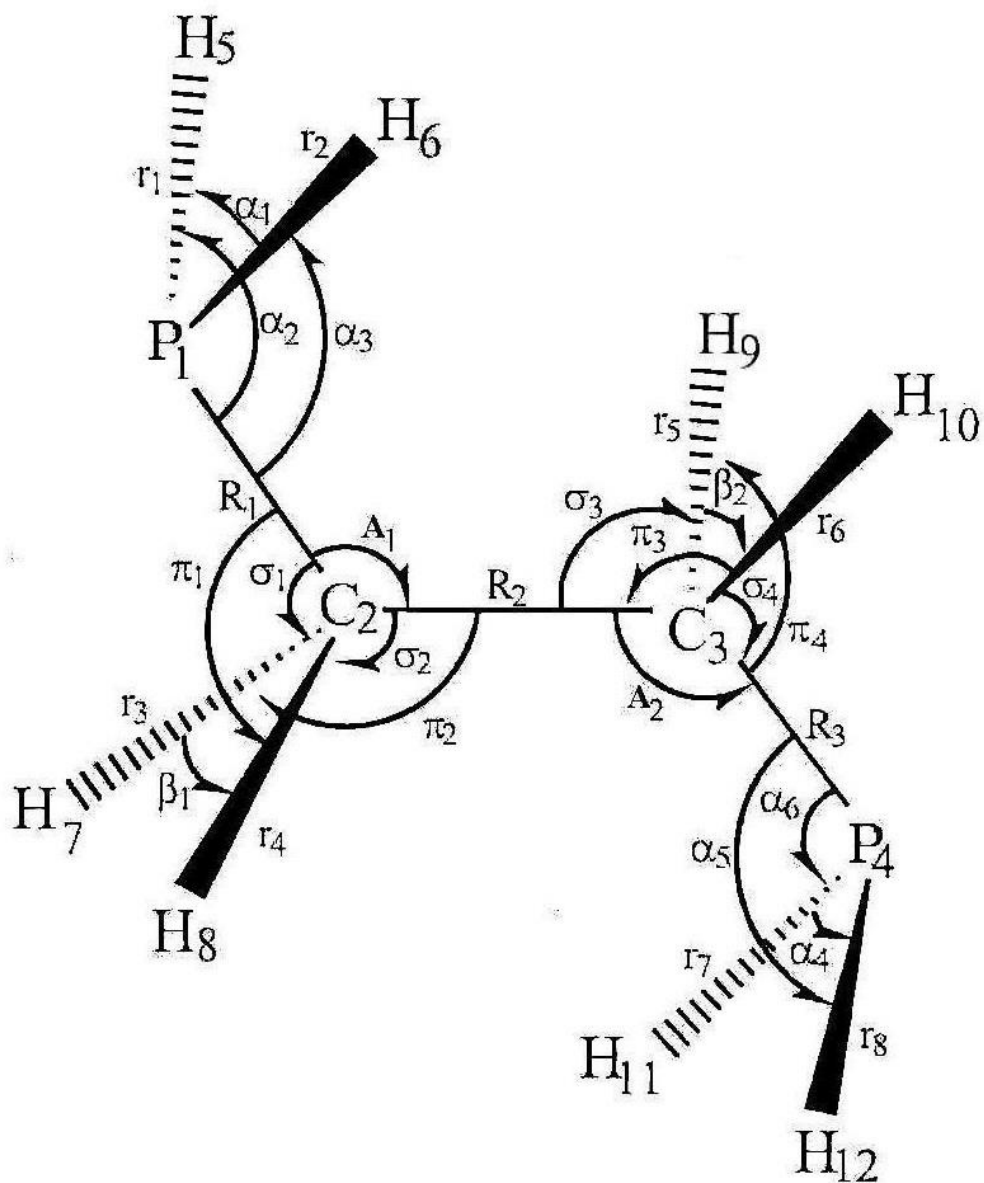


Figure 4.14. *tTt* conformer of 1,2-diphosphinoethane showing atom numbering and internal coordinates.

Table 4.22. Temperature and intensity ratios of the conformational bands of 1,2-diphosphinoethane from the Raman spectra of the liquid.

T(°C)	1/T ($\times 10^3 \text{ K}^{-1}$)	$g'Tt / tTt$		$g'Tg'/tTt$		$g'Tg/tTt$		$tG'g'/tTt$		$tG't/tTt$	
		I ₈₀₈ /I ₆₅₅	I ₈₀₈ /I ₈₆₃	I ₆₇₃ /I ₈₆₃	I ₆₇₃ /I ₆₅₅	I ₇₁₄ /I ₈₆₃	I ₇₁₄ /I ₆₅₅	I ₅₉₃ /I ₆₅₅	I ₅₉₃ /I ₈₆₃	I ₆₀₁ /I ₆₅₅	I ₆₀₁ /I ₈₆₃
-38.0	4.2526	0.030	0.078	0.516	0.200	0.234	0.091	0.055	0.141	0.103	0.266
-30.0	4.1127	0.034	0.090	0.522	0.200	0.254	0.097	0.057	0.149	0.114	0.299
-15.0	3.8737	0.037	0.094	0.594	0.232	0.281	0.110	0.073	0.188	0.140	0.359
0.0	3.6610	0.043	0.113	0.663	0.252	0.325	0.124	0.076	0.200	0.167	0.438
15.0	3.4704	0.041	0.117	0.833	0.296	0.400	0.142	0.112	0.317	0.201	0.567
30.0	3.2987	0.040	0.125	1.025	0.325	0.475	0.151	0.119	0.375	0.238	0.750
$\Delta H, \text{ cm}^{-1}$		210 ± 63	333 ± 33	496 ± 66	373 ± 31	505 ± 45	382 ± 13	602 ± 71	725 ± 95	609 ± 14	733 ± 56
ΔH average, cm^{-1}		272 ± 39		434 ± 40		443 ± 30		663 ± 60		671 ± 34	

^aThe average values of ΔH and the statistical uncertainty (1σ) was obtained by utilizing all of the data as a single set.

Table 4.23. Calculated energies (hartree) and energy differences^a (cm⁻¹) for the ten conformers of 1,2-diphosphinoethane.

Method / Basis set	# of Basis Sets	<i>tTt</i>	<i>g'Tt</i> ΔE	<i>g'Tg'</i> ΔE	<i>g'Tg</i> ΔE	<i>tG'g'</i> ΔE	<i>tG't</i> ΔE	<i>g'G't</i> ΔE	<i>gG'g'</i> ΔE	<i>g'G'g'</i> ΔE	<i>g'G'g</i> ΔE
MP2/6-31G(d)	84	-762.3111661	206	353	343	584	606	690	619	644	929
MP2/6-31+G(d)	100	-762.3207757	269	476	477	703	677	834	797	825	1078
MP2/6-311G(d,p)	136	-762.7277772	288	523	528	674	619	773	807	859	1129
MP2/6-311+G(d,p)	152	-762.7315808	297	546	542	682	594	797	836	911	1165
MP2/6-311G(2d,2p)	180	-762.8027328	306	549	558	567	504	686	760	835	1042
MP2/6-311+G(2d,2p)	196	-762.8052335	310	559	564	578	507	701	760	849	1064
MP2/6-311G(2df,2pd)	248	-762.8813122	283	502	512	494	453	626	674	759	992
MP2/6-311+G(2df,2pd)	264	-762.8835243	285	510	516	504	457	638	677	769	1004
MP2/aug-cc-pVTZ	376	-762.7336880	209	351	359	286	372	447	416	499	732
MP2 average			273	485	489	563	532	688	705	772	1015
B3LYP/6-31G(d)	84	-763.7118653	291	509	503	762	612	811	908	942	1152
B3LYP/6-31+G(d)	100	-763.7172045	283	491	496	803	689	867	919	958	1179
B3LYP/6-311G(d,p)	136	-763.7941691	272	476	484	733	604	794	866	904	1135
B3LYP/6-311+G(d,p)	152	-763.7952159	269	472	479	725	594	785	853	899	1130
B3LYP/6-311G(2d,2p)	180	-763.8034707	270	471	481	694	584	773	845	895	1094
B3LYP/6-311+G(2d,2p)	196	-763.8043915	267	466	476	696	587	776	838	898	1102
B3LYP/6-311G(2df,2pd)	248	-763.8097777	264	456	468	680	573	760	830	876	1079
B3LYP/6-311+G(2df,2pd)	264	-763.8106750	262	455	465	685	578	766	831	884	1089
B3LYP/ aug-cc-pVTZ	376	-763.8164273	243	413	425	668	592	749	789	844	1048
B3LYP average			269	468	475	716	601	787	853	900	1112

^a Energy differences with respect to the *tTt* conformer.

Table 4.24. Structural parameters (Å and °) and rotational constants (mhz) for the *g'tt*, *g'tg'*, *tg'g'*, and *tg't* conformer of 1,2-diphosphinoethane.

Structural parameters	Internal coordinates	<i>g'Tt</i>			<i>g'Tg'</i>		<i>tG'g'</i>		<i>tG't</i>	
		MP2(full)/	B3LYP/	Adjusted	MP2(full)/	Adjusted	MP2(full)/	Adjusted	MP2(full)/	Adjusted
		6- 311+G(d,p)	6- 311+G(d,p)	r ₀						
r (P ₁ -C ₂)	R ₁	1.865	1.887	1.870(3)	1.862	1.866(3)	1.858	1.858(3)	1.864	1.859(3)
r (C ₂ -C ₃)	R ₂	1.527	1.531	1.535(3)	1.530	1.536(3)	1.531	1.534(3)	1.537	1.536(3)
r (C ₃ -P ₄)	R ₃	1.858	1.878	1.863(3)	1.862	1.866(3)	1.865	1.866(3)	1.864	1.859(3)
r (P ₁ -H ₅)	r ₁	1.412	1.425	1.412(3)	1.412	1.412(3)	1.411	1.411(3)	1.402	1.402(3)
r (P ₁ -H ₆)	r ₂	1.412	1.424	1.412(3)	1.412	1.412(3)	1.413	1.413(3)	1.405	1.405(3)
r (C ₂ -H ₇)	r ₃	1.095	1.094	1.095(2)	1.095	1.095(2)	1.096	1.096(2)	1.086	1.086(2)
r (C ₂ -H ₈)	r ₄	1.093	1.092	1.093(2)	1.094	1.094(2)	1.096	1.096(2)	1.088	1.088(2)
r (C ₃ -H ₉)	r ₅	1.096	1.095	1.096(2)	1.095	1.095(2)	1.094	1.094(2)	1.086	1.086(2)
r (C ₃ -H ₁₀)	r ₆	1.096	1.095	1.096(2)	1.094	1.094(2)	1.096	1.096(2)	1.088	1.088(2)
r (P ₄ -H ₁₁)	r ₇	1.412	1.425	1.412(3)	1.412	1.412(3)	1.411	1.411(3)	1.402	1.402(3)
r (P ₄ -H ₁₂)	r ₈	1.412	1.425	1.412(3)	1.412	1.412(3)	1.410	1.410(3)	1.405	1.405(3)
∠ P ₁ C ₂ C ₃	A ₁	110.9	111.7	110.5(5)	110.7	110.4(5)	117.5	117.0(5)	119.1	118.5(5)
∠ C ₂ C ₃ P ₄	A ₂	115.9	116.8	115.5(5)	110.7	110.4(5)	113.2	113.7(5)	119.1	118.5(5)
∠ H ₅ P ₁ H ₆	α ₁	94.5	93.5	94.5(5)	94.5	94.5(5)	94.1	94.1(5)	108.0	108.0(5)
∠ H ₅ P ₁ C ₂	α ₂	96.5	97.2	96.5(5)	97.7	97.7(5)	97.3	97.3(5)	119.1	119.1(5)
∠ H ₆ P ₁ C ₂	α ₃	97.6	97.2	97.6(5)	96.5	96.5(5)	96.4	96.4(5)	100.1	100.1(5)
∠ H ₇ C ₂ H ₈	β ₁	107.3	107.2	107.3(5)	107.4	107.4(5)	106.1	106.1(5)	114.7	114.7(5)
∠ H ₇ C ₂ P ₁	σ ₁	107.5	106.4	106.4(5)	107.4	107.4(5)	106.9	106.9(5)	108.8	108.8(5)
∠ H ₈ C ₂ P ₁	π ₁	111.6	110.9	113.0(5)	111.3	111.3(5)	106.1	106.1(5)	105.8	105.8(5)
∠ H ₇ C ₂ C ₃	π ₂	109.6	109.9	109.6(5)	109.8	109.8(5)	110.1	110.1(5)	98.4	98.4(5)
∠ H ₈ C ₂ C ₃	σ ₂	109.9	110.5	109.9(5)	110.1	110.1(5)	109.4	109.4(5)	110.4	110.4(5)
∠ H ₉ C ₃ H ₁₀	β ₂	106.0	105.9	106.0(5)	107.4	107.4(5)	109.2	109.2(5)	114.7	114.7(5)
∠ H ₉ C ₃ C ₂	σ ₃	110.4	110.6	110.4(5)	109.8	109.8(5)	110.2	110.2(5)	98.4	98.4(5)
∠ H ₁₀ C ₃ C ₂	π ₃	110.3	110.7	110.3(5)	110.1	110.1(5)	108.8	108.8(5)	110.4	110.4(5)

$\angle \text{H}_9\text{C}_3\text{P}_4$	π_4	107.0	106.2	106.0(5)	107.4	107.4(5)	111.5	111.5(5)	108.8	108.8(5)
$\angle \text{H}_{10}\text{C}_3\text{P}_4$	σ_4	106.7	105.9	108.1(5)	111.3	111.3(5)	105.7	105.7(5)	105.8	105.8(5)
$\angle \text{H}_{11}\text{P}_4\text{H}_{12}$	α_4	93.9	93.3	93.9(5)	94.5	94.5(5)	94.4	94.4(5)	108.0	108.0(5)
$\angle \text{H}_{11}\text{P}_4\text{C}_3$	α_6	96.5	97.3	96.5(5)	97.7	97.7(5)	96.3	96.3(5)	119.1	119.1(5)
$\angle \text{H}_{12}\text{P}_4\text{C}_3$	α_5	96.4	97.2	96.4(5)	96.5	96.5(5)	98.8	98.8(5)	100.1	100.1(5)
$\tau \text{P}_1\text{C}_2\text{C}_3\text{P}_4$	τ_1	176.8	177.1	175.3(5)	174.0	171.1(5)	68.1	66.9(5)	60.9	74.6(5)

Table 4.25. Symmetry coordinates for the *tTt* conformer of 1,2-diphosphinoethane.

Sym. Block	Description	Symmetry Coordinate ^a
A _g	CH ₂ symmetric stretch	S ₁ = r ₃ + r ₄ + r ₅ + r ₆
	PH ₂ symmetric stretch	S ₂ = r ₁ + r ₂ + r ₇ + r ₈
	CH ₂ deformation	S ₃ = γ ₁ + γ ₂
	CH ₂ wag	S ₄ = π ₁ + π ₂ - σ ₁ - σ ₂ - θ ₁ - θ ₂ + φ ₁ + φ ₂
	PH ₂ deformation	S ₅ = α ₁ + α ₂
	CC stretch	S ₆ = R ₂
	PH ₂ wag	S ₇ = β ₁ + β ₂ + β ₃ + β ₄
	CP stretch	S ₈ = R ₁ + R ₃
	CCP bend	S ₉ = ε ₁ + ε ₂
A _u	CH ₂ antisymmetric stretch	S ₁₀ = r ₃ - r ₄ + r ₅ - r ₆
	PH ₂ antisymmetric stretch	S ₁₁ = r ₁ - r ₂ + r ₇ - r ₈
	CH ₂ twist	S ₁₂ = π ₁ - π ₂ - σ ₁ + σ ₂ - θ ₁ + θ ₂ + φ ₁ - φ ₂
	PH ₂ twist	S ₁₃ = β ₁ - β ₂ + β ₃ - β ₄
	CH ₂ rock	S ₁₄ = π ₁ - π ₂ + σ ₁ - σ ₂ + θ ₁ - θ ₂ + φ ₁ - φ ₂
	PH ₂ torsion	S ₁₅ = τ ₁ + τ ₂
	CC torsion	S ₁₆ = τ ₃
B _g	CH ₂ antisymmetric stretch	S ₁₇ = r ₃ - r ₄ - r ₅ + r ₆
	PH ₂ antisymmetric stretch	S ₁₈ = r ₁ - r ₂ - r ₇ + r ₈
	CH ₂ twist	S ₁₉ = π ₁ - π ₂ - σ ₁ + σ ₂ + θ ₁ - θ ₂ - φ ₁ + φ ₂
	CH ₂ rock	S ₂₀ = π ₁ - π ₂ + σ ₁ - σ ₂ - θ ₁ + θ ₂ - φ ₁ + φ ₂
	PH ₂ twist	S ₂₁ = β ₁ - β ₂ - β ₃ + β ₄
	PH ₂ torsion	S ₂₂ = τ ₁ - τ ₂
B _u	CH ₂ symmetric stretch	S ₂₃ = r ₃ + r ₄ - r ₅ - r ₆
	PH ₂ symmetric stretch	S ₂₄ = r ₁ + r ₂ - r ₇ - r ₈
	CH ₂ deformation	S ₂₅ = γ ₁ - γ ₂
	CH ₂ wag	S ₂₆ = π ₁ + π ₂ - σ ₁ - σ ₂ + θ ₁ + θ ₂ - φ ₁ - φ ₂
	PH ₂ deformation	S ₂₇ = α ₁ - α ₂
	PH ₂ wag	S ₂₈ = β ₁ + β ₂ - β ₃ - β ₄
	CP stretch	S ₂₉ = R ₁ - R ₃
	CCP bend	S ₃₀ = ε ₁ - ε ₂

^a Not normalized.

Structural Parameters

From the microwave study⁵⁶ carried out on H₂PCH₂CH₂PH₂, rotational constants for two *Trans* ($g'Tt$, $g'Tg'$) and two *Gauche* ($tG'g'$, $tG't$) conformers out of the ten stable forms were obtained, but no structural parameters were estimated for any of these forms. This made an extensive determination of the structural parameters of these four conformers of primary interest. Thus, we embarked on this study to determine all of the structural parameters for these four conformers.

We have found that good structural parameters for hydrocarbons and many substituted ones can be determined by adjusting the structural parameters obtained from the *ab initio* MP2(full)/6-311+G(d,p) calculations to fit the rotational constants obtained from microwave experimental data by using a computer program “A&M” (*Ab initio* and Microwave) developed⁴¹ in our laboratory. In order to reduce the number of independent variables, the structural parameters are separated into sets according to their types where bond distances in the same set keep their relative ratio and bond angles in the same set keep their difference in degrees. This assumption is based on the fact that errors from *ab initio* calculations are systematic. Additionally, we have also shown that the differences in predicted distances and angles from the *ab initio* calculations for different conformers of the same molecule can usually be used as one parameter with the *ab initio* predicted differences except for some dihedral angles.

We³³ have also shown that *ab initio* MP2(full)/6-311+G(d,p) calculations predict the C-H r_0 structural parameters for more than fifty carbon-hydrogen distances in substituted hydrocarbons to at least 0.002 Å compared to the experimentally determined values from isolated C-H stretching frequencies³⁴. Therefore, all of the carbon-hydrogen distances can be taken from the MP2(full)/6-311+G(d,p) predicted values for the $g'Tt$, $g'Tg'$, $tG'g'$ and $tG't$ conformers of 1,2-

diphosphinoethane. Thus, it should be possible to obtain “adjusted r_0 ” structural parameters for heavy atoms for all four conformers of 1,2-diphosphinoethane by utilizing the twelve well determined rotational constants from the previously reported microwave study⁵⁶.

The three heavy atom distances vary a maximum of 0.008 Å from the *ab initio* predicted values. The P-C and C-C distances were adjusted to be longer than those from MP2 calculations for all four conformers except for *tG't* which had slightly smaller values. On the other hand, $\angle P_1C_2C_3$ and $\angle C_2C_3P_4$ were adjusted to slightly smaller values than the MP2 calculations for *g'Tt*, *g'Tg'*, *tG't* conformers except *tG'g'* form which was adjusted to a slightly smaller value for $\angle P_1C_2C_3$ and a slightly larger value for $\angle C_2C_3P_4$, whereas, two angles of $\angle HCP$ for only *g'Tt* conformer were adjusted to slightly larger values than the MP2 calculations. The heavy atom distances along with the P-H distances have uncertainties of ± 0.003 Å and the angles should be accurate within $\pm 0.5^\circ$. The resulting adjusted parameters are listed in Table 24.

The fit of the twelve determined rotational constants (Table 26) by the structural parameters for the *g'Tt*, *g'Tg'*, *tG'g'* and *tG't* conformers is remarkably good with values of 0.2, 0.3 and 0.4 MHz for eleven of the differences and one with 0.7 MHz. Therefore, it is believed that the suggested uncertainties are realistic values and the determined structural parameters are probably as accurate as can be obtained for the molecule in the gas phase by either electron diffraction or microwave r_s substitution methods.

Table 4.26. Comparison of rotational constants (MHz) obtained from ab initio MP2(full)/6-311+G(d,p) predictions, experimental values from microwave spectra, and from the adjusted r_0 structural parameters for 1,2-diphosphinoethane.

Isotopomer	Rotational Constants	MP2(full)/6-311+G(d,p)	Experimental ^a	Adjusted r_0	$ \Delta $
<i>g'Tt</i>	A	20915.4	20731.28(3)	20732.0	0.7
	B	1414.4	1409.968(1)	1410.3	0.3
	C	1375.5	1371.259(1)	1370.9	0.4
<i>g'Tg'</i>	A	20966.6	20778.23(2)	20778.4	0.2
	B	1429.7	1427.185(3)	1427.6	0.4
	C	1387.5	1385.593(3)	1385.2	0.4
<i>tG'g'</i>	A	8668.3	8596.864(4)	8597.1	0.2
	B	2061.1	2071.659(1)	2072.0	0.3
	C	1797.8	1802.283(1)	1801.9	0.4
<i>tG't</i>	A	9330.4	9244.29(1)	9244.1	0.2
	B	1898.8	1904.980(8)	1904.8	0.2
	C	1708.2	1709.118(8)	1709.3	0.2

^a Ref.⁵⁶.

Discussion

The predicted frequencies of the fundamental vibrations for the *tTt* conformer, from which a complete vibrational assignment was obtained from force constants with three scaling factors, compare favorably with the observed values with an average error of 12 cm^{-1} which represents a percentage error of 0.8%. This error cannot be obtained for the remaining five observed forms since many of the vibrations of these conformers are nearly the same as the corresponding ones for the *tTt* form or they simply could not be observed in the spectra. Thus, only a few fundamentals for these five conformers were confidently identified. Nevertheless, it is clear from the few fundamental modes that were assigned for the other conformers that the error for the predicted frequencies is similar to that for the *tTt* form.

In the infrared spectrum of the crystalline solid of the *tTt* conformer two of the fundamentals, 1064 cm^{-1} (ν_{27} , PH_2 deformation) and 805 cm^{-1} (ν_{28} , PH_2 wag) have distinctive doublets at 1071 cm^{-1} and 802 cm^{-1} , respectively. The differences in frequencies are consistent with factor group splitting which indicate that there are at least two molecules per unit cell. There is a third doublet at 844 cm^{-1} and 838 cm^{-1} (ν_{13} , PH_2 twist) which is well separated and was observed very early in the crystallization of the sample. Initially, it was thought that it could be due to Fermi resonance but with further crystallizing and the observation of the other fundamentals being doublets and the small frequency differences, it was clear that it was also due to factor group splitting. It is rather interesting that only the fundamentals of the PH_2 group show observable factor group splitting.

Based on the relative intensities at ambient temperature, the abundance of the *tTt* form was calculated to be $46 \pm 5\%$ with the remainder values of $25 \pm 2\%$ for the *g'Tt* form and $11 \pm 1\%$ each for the *g'Tg'* and *g'Tg* forms. Additionally, the abundances of the *tG'g'* and *tG't* forms are estimated

to be $4 \pm 1\%$ and 3% , respectively. There are no discrepancies observed in the theoretical energy values involving MP2(full) and B3LYP methods (Table 23). Thus, the experimentally determined order of energy for 1,2-diphosphinoethane was $tTt < g'Tt < g'Tg' \simeq g'Tg < tG'g' < tG't$, which was found to be in accordance with the *ab initio* and DFT predictions.

The only structural parameters previously reported for 1,2-diphosphinoethane was from the earlier microwave studies⁵⁶, where the parameters were predicted at the MP2/6-31G** (frozen core) level. Some of the heavy atom parameters calculated at this level were found to be in closer agreement with the corresponding r_0 parameters obtained in this study than at the MP2(full)/6-311+G(d,p) level. For example, the adjusted r_0 C-P distances and those from the microwave study vary by only 0.002 \AA on an average for the $g'Tt$, $g'Tg'$, and $tG't$ conformers. The C-C distances, on the other hand, were predicted more accurately with the higher level calculation. For the $g'Tg'$ form, it is interesting to note that despite this conformer having C_2 symmetry, the PCC angles were not predicted to be equal from the 6-31G** calculations.

The investigation of ethylenediamine¹⁴, from variable temperature xenon solutions, had indicated that the three lowest energy forms were identified as the *Gauche* conformers. This is remarkably different from the results for the phosphorus analogue in the current study, wherein, the *Trans* conformers are the lowest energy forms. One of the primary reasons for the lower energies of two of the *Gauche* forms of ethylenediamine is attributed to the presence of intramolecular hydrogen bonds which is not observed in the lower energy forms of 1,2-diphosphinoethane. The tendency for the P-C-C-P skeleton to prefer *Trans* conformations over the *Gauche* forms could possibly be due to the following reasons: (1) the “gauche effect” states that the tendency to prefer a X-C-C-X *Gauche* arrangement increases with the electronegativity of the substituent X. Since the nitrogen atom is significantly more electronegative than the phosphorus

atom, the *Gauche* forms has preferably lower energy than the *Trans* forms in ethylenediamine; (2) the large size of the phosphorus atom, the low polarity of the P-H bond makes the formation of hydrogen bond less favorable in 1,2-diphosphinoethane than in the nitrogen analogue.

From the conformational study of ethylphosphine⁵⁵, the enthalpy difference between the lower energy *trans* form and the *gauche* conformer was determined to be $196 \pm 21 \text{ cm}^{-1}$ ($2.34 \pm 0.25 \text{ kJ mol}^{-1}$). When the hydrogen atom is replaced by a methyl moiety for n-propylphosphine⁵⁷, the PH₂ form with lowest energy is the *trans* conformer but the enthalpy difference is a larger value of $351 \pm 20 \text{ cm}^{-1}$ ($4.20 \pm 0.24 \text{ kJ mol}^{-1}$) from variable temperature Raman studies for the liquid. In the current study on 1,2-diphosphinoethane, the *trans* form for PH₂ has lower energy than the *gauche* form by $272 \pm 39 \text{ cm}^{-1}$ ($3.25 \pm 0.47 \text{ kJ mol}^{-1}$). Thus, the replacement of a hydrogen atom on the methyl group in ethylphosphine did not seem to have any effect on the PH₂ conformational stability. It would be of interest to learn what the effect would be when the hydrogen atom is replaced by a halogen atom.

References

- (1) Ekejiuba, I. O. C.; Hallam, H. E. *Spectrochim. Acta Part A Mol. Spectrosc.* **1970**, *26* (1), 67.
- (2) Ekejiuba, I. O. C.; Hallam, H. E. *Spectrochim. Acta Part A Mol. Spectrosc.* **1970**, *26* (1), 59.
- (3) Durig, J. R.; Karriker, J. M.; Harris, W. C. *Spectrochim. Acta Part A Mol. Spectrosc.* **1971**, *27* (9), 1955.
- (4) Choe, J.-I.; Harmony, M. D. *J. Mol. Spectrosc.* **1980**, *81* (2), 480.
- (5) Nandi, R. N.; Harmony, M. D. *J. Mol. Spectrosc.* **1983**, *98* (1), 221.
- (6) Beckett, C. W.; Pitzer, K. S.; Spitzer, R. *J. Am. Chem. Soc.* **1947**, *69* (10), 2488.
- (7) Kilpatrick, J. E.; Pitzer, K. S.; Spitzer, R. **1947**, *69*, 2483.
- (8) Pitzer, K. S.; Donath, W. E. *J. Am. Chem. Soc.* **1959**, *81*, 3213.
- (9) Durig, J. R. *J. Chem. Phys.* **1968**, *49* (5), 2118.
- (10) Caminati, W.; Oberhammer, H.; Pfafferott, G.; Filgueira, R. R.; Gomez, C. H. *J. Mol. Spectrosc.* **1984**, *106* (1), 217–226.
- (11) Pfafferott, G.; Oberhammer, H.; Boggs, J. E.; Caminati, W. *J. Am. Chem. Soc.* **1985**, *107*, 2305.
- (12) Caminati, W.; Dell' Erba, A.; Maccaferri, G.; Favero, P. G. *J. Mol. Spectrosc.* **1998**, *191* (1), 45–48.
- (13) Durig, J. R.; El-Defrawy, A. M.; Ganguly, A.; Panikar, S. S.; Soliman, M. S. *J. Phys. Chem.* **2011**, *115*, 7473.
- (14) Durig, J. R.; Panikar, S. S.; Iwata, T.; Gounev, T. K. *J. Mol. Struct.* **2010**, *984*, 58.
- (15) Durig, J. R.; Zheng, C.; Gounev, T. K.; Herrebout, W. A.; van der Veken, B. J. *J. Phys. Chem.* **2006**, *110*, 5674.
- (16) Durig, J. R. *J. Chem. Phys.* **1976**, *64* (5), 1930.
- (17) Snyder, R. M.; Mirabelli, C. K.; Johnson, R. K.; Sung, C. M.; Faucette, L. F.; McCabe, F. L.; Zimmerman, J. P.; Whitman, M.; Hempel, J. C.; Crooke, S. T. *Cancer Res.* **1986**, *46*, 5054.
- (18) Caruso, F.; Rossi, M.; Tanski, J.; Pettinari, C.; Marchetti, F. *J. Med. Chem.* **2003**, *46*, 1737.
- (19) Frisch, M. J.; Trucks, G. W.; Schlegel, H. B.; Scuseria, G. E.; Robb, M. A.; Cheeseman, J. R.; Montgomery, Jr., J. A.; Vreven, T.; Kudin, K. N.; Burant, J. C.; Millam, J. M.; Iyengar, S. S.; Tomasi, J.; Barone, V.; Mennucci, B.; Cossi, M.; Scalmani, G.; Rega, N.; Petersson,

- G. A.; Nakatsuji, H.; Hada, M.; Ehara, M.; Toyota, K.; Fukuda, R.; Hasegawa, J.; Ishida, M.; Nakajima, T.; Honda, Y.; Kitao, O.; Nakai, H.; Klene, M.; Li, X.; Knox, J. E.; Hratchian, H. P.; Cross, J. B.; Bakken, V.; Adamo, C.; Jaramillo, J.; Gomperts, R.; Stratmann, R. E.; Yazyev, O.; Austin, A. J.; Cammi, R.; Pomelli, C.; Ochterski, J. W.; Ayala, P. Y.; Morokuma, K.; Voth, G. A.; Salvador, P.; Dannenberg, J. J.; Zakrzewski, V. G.; Dapprich, S.; Daniels, A. D.; Strain, M. C.; Farkas, O.; Malick, D. K.; Rabuck, A. D.; Raghavachari, K.; Foresman, J. B.; Ortiz, J. V.; Cui, Q.; Baboul, A. G.; Clifford, S.; Cioslowski, J.; Stefanov, B. B.; Liu, G.; Liashenko, A.; Piskorz, P.; Komaromi, I.; Martin, R. L.; Fox, D. J.; Keith, T.; Al-Laham, M. A.; Peng, C. Y.; Nanayakkara, A.; Challacombe, M.; Gill, P. M. W.; Johnson, B.; Chen, W.; Wong, M. W.; Gonzalez, C.; Pople, J. A. Gaussian 03, Revis. E.01, Gaussian, Inc., Wallingford, CT **2004**.
- (20) Pulay, P. *Mol. Phys.* **1969**, *17*, 197.
- (21) Møller, C.; Plesset, M. S. *Phys. Rev.* **1934**, *46*, 618.
- (22) Wertz, D. W.; Shasky, W. E. *J. Chem. Phys.* **1971**, *55* (5), 2422.
- (23) Carreira, L. A. *J. Chem. Phys.* **1971**, *55* (1), 181.
- (24) Durig, J. R.; El Defrawy A.M.; Ganguly, A.; Gounev T.K.; Guirgis, G. A. *J. Phys. Chem. A* **2009**, *113*, 9675.
- (25) Loyd, R. C.; Mathur, S. N.; Harmony, M. D. *J. Mol. Spectrosc.* **1978**, *72*, 359.
- (26) Hildebrandt, R. L.; Shen, Q. *J. Phys. Chem.* **1982**, *86*, 587.
- (27) Groner, P.; Lee, M. J.; Durig, J. R. *J. Chem. Phys.* **1991**, *94* (5), 3315.
- (28) Durig, J. R.; Zhao, W.; Zhu, X. *J. Mol. Struct.* **2000**, *521*, 25.
- (29) Guirgis, G. A.; Zhu, X.; Yu, Z.; Durig, J. R. *J. Phys. Chem. A* **2000**, *104*, 4383.
- (30) Frisch, M. J.; Yamaguchi, Y.; Gaw, J. F.; Schaefer, H. F.; Binkley, J. S. *J. Chem. Phys.* **1986**, *84* (1), 531.
- (31) Amos, R. D. *Chem. Phys. Lett.* **1986**, *124* (4), 376.
- (32) Polavarapu, P. L. *J. Phys. Chem.* **1990**, *94*, 8106.
- (33) Durig, J. R.; Ng, K. W.; Zheng, C.; Shen, S. *Struct. Chem.* **2004**, *15*, 149.
- (34) McKean, D. C. *J. Mol. Struct.* **1984**, *113*, 251.
- (35) Guirgis, G. A.; El Defrawy, A. M.; Gounev, T. K.; Soliman, M. S.; Durig, J. R. *J. Mol. Struct.* **2007**, *832*, 73.
- (36) Harmony, M. D.; Strand, M. R. *J. Mol. Spectrosc.* **1980**, *81*, 308.
- (37) Demaison, J.; Cosléou, J.; Bürger, H.; Mkadmi, E. B. *J. Mol. Spectrosc.* **1997**, *185*, 384.
- (38) Duncan, J. L.; Harvie, J. L.; McKean, D. C.; Cradock, S. *J. Mol. Struct.* **1986**, *145*, 225.

- (39) Durig, J. R.; Pan, C.; Guirgis, G. A. *Spectrochim. Acta Part A Mol. Biomol. Spectrosc.* **2003**, *59*, 979.
- (40) Durig, J. R.; Pan, C.; Guirgis, G. A. *J. Mol. Struct.* **2004**, *688*, 95.
- (41) van der Veken, B. J.; Herrebout, W. A.; Durig, D. T.; Zhao, W.; Durig, J. R. *J. Phys. Chem. A* **1999**, *103*, 1976.
- (42) Durig, J. R.; Liu, J.; Little, T. S.; Kalasinsky, V. F. *J. Phys. Chem.* **1992**, *96*, 8224.
- (43) Turner, J. J.; Poliakoff, M.; Howdle, S. M.; Jackson, S. A.; McLaughlin, J. G. *Faraday Discuss. Chem. Soc.* **1988**, *86*, 271.
- (44) Herrebout, W. A.; van der Veken, B. J. *J. Chem. Phys.* **1996**, *100*, 9671.
- (45) Durig, J. R.; Ganguly, A.; Zheng, C.; Gurigis, G. A.; Herrebout, W. A.; van der Veken, B. J.; Gounev, T. K. *J. Mol. Struct.* **2010**, *968*, 36.
- (46) Marstockk, K.-M.; Mollendal, H. *Acta. Chem. Scand. A* **1980**, *34*, 15.
- (47) Miller, F. A.; Harney, B. M. *Appl. Spectrosc.* **1970**, *24*, 291.
- (48) Marstokk, K.-M.; Mollendal, H. *Acta, Chem, Scand. A* **1983**, *37*, 755.
- (49) Parkanyi, C. *Theoretical Organic Chemistry*; Elsevier Science B.V.: Amsterdam, 1998.
- (50) Wyn-Jones, E.; Orville-Thomas, W. J. *J. Chem. Soc.* **1964**, 5853.
- (51) Gordy, W. *J. Chem. Phys.* **1946**, *14* (5), 305.
- (52) Wyn-Jones, E.; Orville-Thomas, W. J. *J. Chem. Soc.* **1996**, 101.
- (53) Guirgis, G. A.; Zhu, X.; Durig, J. R. *Struct. Chem.* **1999**, *10*, 445.
- (54) Durig, J. R.; Liu, J.; Little, T. S. *J. Phys. Chem.* **1991**, *95*, 4664.
- (55) Durig, J. R.; Cox, A. W. *J. Chem. Phys.* **1975**, *63*, 2303.
- (56) Marstokk, K.-M.; Molendall, H. *Acta Chem. Scand.* **1996**, *50*, 875.
- (57) Durig, J. R.; Gounev, T. K.; Lee, M. S.; Little, T. S. *J. Mol. Struct.* **1994**, *327*, 23.

VITA

Sudhaunshu Shrikant Purohit was born on February 09, 1982, in Mumbai, India to Mr. Shrikant Purohit (father) and Miss. Asha Gaikawaiari (mother) and is also an adopted son to Mr. Nitin Patwardhan (step-father) since year 1994. He graduated high school from 'IES Raja Shivaji Vidyalaya', Mumbai in 1998 and also subsequently completed two years of junior college at 'Ramnarain Ruia College' which is affiliated to the University of Mumbai. He later on chose Chemistry as a subject of career, pursued and earned Bachelor's of Science (B.Sc.) degree in year 2004 in Chemistry (with Industrial Chemistry as minor) from Ruia College. His inclination towards higher education compelled him towards next step and he earned Master's of Science (M.Sc.) degree in year 2006 in Inorganic Chemistry at Ramnarain Ruia College, University of Mumbai. While pursuing Master's degree in Ruia College, Sudhaunshu actively worked under the guidance of Prof. Kiran Mangaonkar and assisted one of the Ph.D. students in his research group and worked on a project that studied 'Syntheses, Characterization, Stability and Antimicrobial Activity of Transition Metal Complexes of Schiff Bases'.

After the completion of Master's degree, Sudhaunshu acquired a job as analytical chemist with Cipla LTD., a leading pharmaceutical company, in the Manufacturing and Research Division in Mumbai, India. His job responsibilities included routine analysis of active pharmaceutical ingredient samples using a variety of spectroscopic and chromatographic techniques such as GC, GCMS, HPLC, NMR, IR, UV/Visible spectroscopy. At Cipla, he gained technical expertise with handling a variety of analytical instruments.

The pursuit of greater knowledge further inspired him to take another leap in career and Sudhaunshu decided to come to United States of America for higher education in Chemistry. He attended graduate school at University of Kentucky, (Lexington, KY) and earned another Master's

degree in Chemistry in year 2010 while working on the ‘Syntheses and Characterization of Salen-Group I Metal Complexes’ under the guidance of Prof. David Atwood. Sudhaunshu also actively participated along with another graduate student and completed a project that explained a research on ‘Metal Ion Doped Flash Paper’ which was carried out under the guidance of Prof. Fitzgerald Bramwell.

The relentless desire to pursue innovative research and immense motivation to earn doctorate degree in Chemistry, brought Sudhaunshu to University of Missouri Kansas City, (Kansas City, MO). He choose the field of Spectroscopy and its applications as a wide nature of his Ph.D. career and began research under the guidance of Prof. James Durig, where he was exposed to the research projects that included an ‘Implementation of Infrared and Raman Spectral Studies to Obtain Structural Parameters, Conformational Stability, Vibrational Assignments and ab initio Calculations of Organic Molecules Containing Five Membered Ring and Phosphorous’. After successfully completing and co-authoring four projects in Durig research group within initial two years of Ph.D., Sudhaunshu went on to join a research group that involved Nuclear Magnetic Resonance Spectroscopy (NMR). He started working on various projects that requited utilization of both solid state and solution state NMR spectroscopic techniques in order to investigate both qualitative and quantitative aspects of samples under study. He has yet considerably contributed in research projects which were collaborative efforts between Department of Chemistry and Department of Physics, School of Pharmacy and Department of Civil and Mechanical Engineering at University of Missouri Kansas City under the invaluable guidance of Prof. Nathan Oyler.

Currently, Sudhaunshu is a candidate of Ph.D. in Chemistry at UMKC. During the course of Ph.D., he has also presented the accomplishments of his research in various conferences such as SciX (Reno, NV, 2014), Midwest American Chemical Society (St. Joseph, MO, 2015) and

Pittcon (Atlanta, GA, 2016) with upcoming Eastern Analytical Symposium (New Jersey, NY in November, 2016) for both oral and poster presentations. He has also been honored by prestigious scholarship of USD 2400 when he was selected for participating in ‘Preparing Future Faculty Program’ at UMKC for years 2013-2015. Sudhaunshu has also earned best poster presentation award of USD 100 at SciX conference held at Reno, NV, in year 2014 for presenting his research on ‘Solid State NMR Spectroscopic Analysis on Thiolated Chitosan Coated Sodium Alginate Core-Shell Microparticles for Enhanced Drug Loading Profile of Tenofovir’. He also worked under the guidance of Prof. Fedor Rudakov in the summer of 2014 to learn the basic techniques of Laser spectroscopy. Since, September 2016, Sudhaunshu has joined RTI Laboratories located in Livonia, MI in their Environmental Division and has been working on the analysis of soil, water and air samples from various streams.

Sudhaunshu began publishing soon after joining Durig research group and has also worked persistently since he has joined Oyler research group during the course of his Ph.D. where, he has co-authored the following peer-reviewed journal publications:

SCIENTIFIC PUBLICATIONS

❖ *(Published)*

- B.J. Nordell, C.L. Keck, T.D. Nguyen, A.N. Caruso, **S.S. Purohit**, W.A. Lanford, D. Dutta, David Gidley, P. Henry, S.W. King, M.M. Paquette, “Tuning the properties of a complex disordered material: Full factorial investigation of PECVD-grown amorphous hydrogenated boron carbide.” *Mater. Chem. Phys.* **2016**, *173*, 268-284.
- B.J. Nordell, S. Karki, T.D. Nguyen, P. Rulis, A.N. Caruso, **S.S. Purohit**, H. Li, S.W. King, D. Dutta, D. Gidley, W.A. Lanford, M.M. Paquette, “The influence of hydrogen on the chemical, mechanical, optical/electronic, and electrical transport properties of amorphous hydrogenated boron carbide.” *J. Appl. Phys.* **2015**, *118*, 035703(1-16).
- J.R. Durig, J.J. Klaassen, B.S. Deodhar, I.D. Darkhalil, W.A. Herrebut, J.J.J. Dom, B.J. van der Veken, **S.S. Purohit**, G.A. Guirgis, “Conformational and structural studies of ethynylcyclopentane from temperature dependent Raman spectra of xenon solution, infrared spectra and *ab initio* calculations.” *J. Mol. Struct.*, **2013**, *1044*, 10-20.
- J.R. Durig, S.S. Panikar, **S.S. Purohit**, T.H. Pai, V.F. Kalasinsky, “Conformational stabilities from variable temperature Raman spectra, r_0 structural parameters and vibrational assignments of 1,2-diphosphinoethane.” *J. Mol. Struct.*, **2013**, *1033*, 19-26.

- J.R. Durig, S.S. Panikar, T.H. Pai, C.X. Zhou, V.F. Kalasinsky, **S.S. Purohit**, “Infrared and Raman spectra, structural parameters, conformational stability, vibrational assignment and *ab initio* calculations of 2-cyanoethylphosphine.” *Chem. Phys.*, **2012**, 405, 1-8.
- G.A. Guirgis, S.S. Panikar, J.J. Klaassen, **S.S. Purohit**, M.D. Johnston, J.R. Durig, “Infrared and Raman spectra, *ab initio* calculations, conformational stability and vibrational assignment of 1-bromo-1-silacyclopentane.” *Spectrochim. Acta A*, **2011**, 79, 858-866.
- ❖ *(Submitted)*
- J. Meng, V. Agrahari, M.J. Ezoulin, C. Zhang, **S.S. Purohit**, A. Molteni, D. Dim, N.A. Oyler, B-B.C. Youan, “Electrospun Tenofovir Loaded Core/Shell Bioadhesive Chitosan Nanofibers: In Vitro and In Vivo Evaluations.” *Small*, **2016**.
- F.S. Coulibaly, M.J. Ezoulin, **S.S. Purohit**, N.J. Ayon, N.A. Oyler, B-B.C. Youan, “Layer by Layer Engineering of HIV-1 rgp120 Responsive Nanomicrobicide: Physico-Chemistry and Biological Responses.” *Nano Lett.*, **2016**.
- M. Bediako, **S.S. Purohit**, J.T. Kevern, N.A. Oyler, “Performance of calcined clay as a supplementary cementitious material: A case study of clay from Ghana.” *Adv. Mater. Sci. Eng.*, **2016**.
- **S.S. Purohit**, J. Meng, V. Agrahari, N.A. Oyler, B-B.C. Youan, “Real-Time Analysis of Tenofovir Release in Biological Fluids Using Quantitative Phosphorus (³¹P) Nuclear Magnetic Resonance Spectroscopy.” *JPS.*, **2016**.
- ❖ *(Under Preparation)*
- J. Meng, V. Agrahari, **S.S. Purohit**, T. Zhang, M.J. Ezoulin, A. Molteni, D. Dim, N.A. Oyler, B-B.C. Youan, “Spray Dried Thiolated Chitosan Coated Sodium Alginate Multilayer Microparticles for Vaginal Anti-HIV microbicide Delivery.” **2016**.
- B.J. Nordell, T.D. Nguyen, S. Dhungana, A.N. Caruso, **S.S. Purohit**, N.A. Oyler, W.A. Lanford, D. Gidley, J.T. Gaskins, P.E. Hopkins, D.R. Merrill, D.C. Johnson, L.L. Ross, P. Henry, S.W. King, M.M. Paquette, “Carbon-Enriched Amorphous Hydrogenated Boron Carbide Films for Very-Low-*k* Interlayer Dielectrics with Superior Mechanical Properties.” **2016**.
- **S.S. Purohit**, M. Bediako, J.T. Kevern, N.A. Oyler, “Hydration behavior of Portland cement and calcined clay incorporated with palm kernel shells: Pozzolanic activity of co-fired Ghanaian clay and palm kernel shell mixture.” **2016**.
- **S.S. Purohit**, M. Bediako, J.T. Kevern, N.A. Oyler, {3 more articles are under preparation}. “Study of Portland cement and calcined clay incorporated with- 1]Saw Dust, 2]Rice Husk, 3]Maize Cob etc.” **2016**.